



HAL
open science

Effect of biomolecules adsorption on oxide layers developed on metallic materials used in cooling water systems

Blanca E. Torres Bautista

► **To cite this version:**

Blanca E. Torres Bautista. Effect of biomolecules adsorption on oxide layers developed on metallic materials used in cooling water systems. Chemical Sciences. Université Pierre et Marie Curie, 2014. English. NNT: . tel-01087647v1

HAL Id: tel-01087647

<https://hal.science/tel-01087647v1>

Submitted on 26 Nov 2014 (v1), last revised 8 Jul 2015 (v2)

HAL is a multi-disciplinary open access archive for the deposit and dissemination of scientific research documents, whether they are published or not. The documents may come from teaching and research institutions in France or abroad, or from public or private research centers.

L'archive ouverte pluridisciplinaire **HAL**, est destinée au dépôt et à la diffusion de documents scientifiques de niveau recherche, publiés ou non, émanant des établissements d'enseignement et de recherche français ou étrangers, des laboratoires publics ou privés.

**THESE DE DOCTORAT DE
L'UNIVERSITE PIERRE ET MARIE CURIE**

Spécialité

Chimie Physique et Chimie Analytique

Présentée par

Blanca Estela TORRES-BAUTISTA

Pour obtenir le grade de

DOCTEUR DE L'UNIVERSITE PIERRE ET MARIE CURIE

Sujet de la thèse :

Effect of biomolecules adsorption on oxide layers developed on metallic materials used in cooling water systems

Soutenue le 7 juillet 2014

devant le jury composé de :

Mme. Christine Dupont-Gillain	Professeur, UCL	Rapporteur
Mme. Régine Basseguy	Directeur de Recherche, CNRS	Rapporteur
Mme. Audrey Allion	Chercheur, APERAM	Examineur
Mme. Xochitl Dominguez-Benetton	Chargée de recherche, VITO	Examineur
M. Bernard Tribollet	Directeur de recherche, CNRS	Examineur
Mme. Isabelle Frateur	Chargée de recherche, CNRS	Directeur de thèse
M. Philippe Marcus	Directeur de recherche, CNRS	Co-directeur de thèse

ACKNOWLEDGEMENTS

I am deeply grateful to my advisors Isabelle Frateur and Philippe Marcus. Working with them has been a real honour to me. They had oriented and supported me with care, and had always been patient and encouraging in times of difficulties. I appreciate it from all my heart.

I also want to thank to all current and former colleagues from the Research group Physical Chemistry of Surfaces, Chimie-Paristech, especially Sandrine Zanna and Antoine Seyeux. I appreciate her patience to read and correct my papers and the thesis manuscript repeatedly.

Special thanks also to Prof. Wolfgang Sand and the Biofilm Center, UDE, to have welcomed me during one month for training on EPS extraction. Thanks to Agata Wikel, Iaryna Datsenko and Mario Vera.

I will be forever thankful to Bernard Tribollet and the Laboratory of Interfaces and Electrochemical Systems (LISE) for the scientific advices, knowledge, many insightful discussions and suggestions.

The research leading to thesis results has received funding from the Marie Curie European Community's Seventh Framework Programme (FP7/2007–2013) under grant agreement n°238579, BIOCOR Initial Training Network (www.biocor.eu/ip8). The BIOCOR project gave me the opportunity to collaborate with research institutes across Europe and to work with the best scientists within the field of biocorrosion. I am very grateful for all BIOCOR network meetings, trainings and scientific discussions. I would like to thank also all BIOCOR students. I would particularly like to thank Regine Basseguy, Jenny Stephenson and Vincent Birrien for their effort to organize the BIOCOR meetings and summer school.

I also want to take this opportunity to express my thanks to my former supervisor in Mexico, Xochitl Dominguez Benetton, who introduced me to the EIS world, and for her encouragement and good advices.

Most important, a great thank to my parents, Roberto Torres and Roberta Bautista. Thank you for raising me, supporting me, encouraging me and loving me.

Finally, I would like to thank my boyfriend Oscar Mauricio, for his unlimited patience and support when times were rough, for sharing me his heart and every second of his life.

Table of Contents

Introduction	i
I. Background	1
I.1. Cooling water systems	1
I.1.1. Importance of cooling water systems	1
I.1.2. Types of cooling water systems and heat exchangers in power supply facilities.....	2
I.1.3. Materials	4
I.1.4. Operating problems in cooling water systems.....	6
I.1.4.1. Scaling.....	9
I.1.4.2. Fouling	9
I.1.4.3. Biofouling and Microbially Influenced Corrosion (MIC)	9
I.2. Biofilms.....	12
I.2.1. Introduction	12
I.2.2. Conditioning films.....	17
I.2.3. EPS and biofilm architecture	18
I.2.3.1. Exopolysaccharides.....	20
I.2.3.2. Extracellular proteins	23
I.2.3.3. Extracellular nucleic acids	23
I.2.3.4. Surfactants and lipids	24
I.2.3.5. Interaction of EPS with metals	24
I.3. Bovine Serum Albumin (BSA)	26
I.3.1. Composition and physico-chemical properties.....	26
I.3.2. Structure/conformation	28
I.4. Bacterial culture (<i>Pseudomonas NCIMB 2021</i>)	29
I.5. Conclusions	30
II. Experimental	32
II.1. Materials, electrolytes, biomolecules, and bacteria.....	32
II.1.1. Metallic materials	32
II.1.2. Electrolytes	34
II.1.3. Biomolecules	34
II.1.3.1. BSA.....	34
II.1.3.2. EPS extracted from <i>Pseudomonas NCIMB 2021</i>	34
II.2. Experimental techniques	41
II.2.1. Electrochemical measurements	41

Table of Contents

II.2.1.1.	Electrochemical cell.....	41
II.2.1.2.	Instrumentation	43
II.2.1.3.	E_{corr} vs time	44
II.2.1.4.	Polarisation curves	45
II.2.1.5.	Electrochemical Impedance Spectroscopy (EIS).....	46
II.2.1.5.1.	Principle	46
II.2.1.5.2.	Impedance data analysis.....	51
II.2.2.	Surface analysis	52
II.2.2.1.	X-ray Photoelectron Spectroscopy (XPS)	52
II.2.2.1.1.	Principle	52
II.2.2.1.2.	Instrumentation.....	55
II.2.2.1.3.	Data processing	56
II.2.2.2.	Time-of-Flight Secondary Ion Mass Spectrometry (ToF-SIMS)	58
II.2.2.2.1.	Principle	58
II.2.2.2.2.	Instrumentation.....	61
III.	Electrochemical behaviour and surface chemical composition of 70Cu-30Ni alloy after short-term immersion in artificial seawater and filtered natural seawater	63
III.1.	Results	63
III.1.1.	Static conditions.....	63
III.1.1.1.	Electrochemical measurements.....	63
III.1.1.2.	Surface analysis	65
III.1.2.	Effect of hydrodynamics.....	74
III.1.2.1.	Comparison static conditions/under flow and stirring.....	74
III.1.2.1.1.	Electrochemical measurements	75
III.1.2.1.2.	Surface analysis.....	76
III.1.2.2.	Electrochemical measurements using a RRE	79
III.1.2.2.1.	Theory for a Rotating Ring Electrode	79
III.1.2.2.2.	Experimental results obtained with a RRE	82
III.2.	Discussion.....	86
III.2.1.	Impedance model for 70Cu-30Ni	86
III.2.2.	Surface layers models (combined XPS and ToF-SIMS)	102
III.2.3.	Conclusions.....	104
IV.	Influence of biomolecules adsorption on the electrochemical behaviour and the surface chemical composition of 70Cu-30Ni alloy in seawater	106
IV.1.	Results	106
IV.1.1.	Bovine Serum Albumin (BSA).....	106
IV.1.1.1.	Static conditions.....	106
IV.1.1.1.1.	Electrochemical measurements	106

Table of Contents

IV.1.1.1.2. Surface analysis.....	108
IV.1.1.2. Effect of hydrodynamics.....	114
IV.1.1.2.1. Effect of hydrodynamics on the surface chemical composition (comparison static conditions/under flow and stirring).....	114
IV.1.1.2.2. Electrochemical measurements using a RRE.....	118
IV.1.2. EPS from <i>Pseudomonas NCIMB 2021</i>	121
IV.1.2.1. Electrochemical measurements.....	122
IV.1.2.2. Surface analysis	124
IV.2. Discussion.....	130
IV.2.1. Analysis of impedance data	130
IV.2.2. Surface layer models (combined XPS and ToF-SIMS).....	137
IV.2.3. Organic layers (XPS)	139
IV.3. Conclusions	144
V. Influence of biomolecules adsorption on the electrochemical behaviour and the surface chemical composition of passive materials (304L stainless steel, Ti)	145
V.1. Electrochemical measurements	145
V.1.1. Titanium.....	145
V.1.2. 304L stainless steel.....	148
V.2. Surface analysis.....	152
V.2.1. Titanium.....	152
V.2.2. 304L stainless steel.....	160
V.3. Discussion	167
V.3.1. Surface layers models (combined XPS and ToF-SIMS).....	167
V.3.2. Analysis of impedance data.....	169
V.3.3. Organic layer	176
V.4. Conclusions	181
VI. General conclusions and future work.....	183
References	188
Annex A	200
Annex B.....	201
B.1. 70Cu-30Ni.....	203
B.2. 304L stainless steel.....	209
B.3. Titanium	214
B.4. Organic layer	218
B.5. Discussion and conclusions.....	221
List of Figures.....	224
List of Tables.....	234

Introduction

This work was carried out in the frame of a European project (BIOCOR ITN -Initial Training Network on Biocorrosion); in close collaboration with the industrial partner RSE S.p.A. (Italy).

Power plants require cooling circuits with water as the cooling agent; therefore, they are generally located on seacoasts due to the immediate availability of abundant seawater. Tubes are the basic components of heat exchangers; they provide the heat transfer surface between one fluid flowing inside and another fluid flowing outside thereof. The selection of materials for heat exchangers is a difficult procedure. Cu-Ni alloys and titanium are often the choice for marine environments, whereas stainless steel 304 types are preferred for freshwaters (they suffer crevice attack, pitting, or stress-corrosion cracking in presence of brackish or seawater).

Cooling circuits of power plants are ideal incubators for microorganisms because they offer plenty of water, are maintained at temperatures between 30 and 60°C and pH between 6 and 9. They also have good aeration and provide a continuous source of organic and inorganic nutrients. Microorganisms are those organisms that cannot be seen individually with the unaided human eye. The microorganisms present in cooling water circuits can be divided into planktonic and sessile. Planktonic cells are free-floating microorganisms whose transport is mostly controlled by water movement, whereas sessile cells attach to surfaces and form what is known as biofilms. The development of a biofilm is considered to be a multistage process involving the following major steps: a) formation of an organic/inorganic conditioned film on a solid surface by adsorption of biomolecules such as proteins, salts and solvated ions, b) transport of microorganisms from the bulk water to the surface, c) adhesion of microorganisms onto the surface, d) replication of the attached cells and production of exopolymers, e) detachment of parts of the biofilm that are swept along by the flowing water to repeat the process of biofilm formation elsewhere. Biofouling is a consequence of biofilm formation and it is able to change the electrochemical properties of a metal/water interface, both in aerobic and anaerobic environments. The significant negative effects of biofouling are the blockage of water free flow in the cooling circuit and consequent mechanical damage to pumps, clogging of condenser tubes, reduction of the heat transfer efficiency (having a direct effect on the efficiency of the thermal cycle of power plants), and microbially induced corrosion (MIC) also called biocorrosion.

A wide variety of heat-exchanging metallic materials can be affected by MIC, including copper alloys and stainless steels. In some cases, using more noble materials such as titanium and superferritic stainless steel has solved corrosion problems. Controlling adsorption of biomolecules which is the first step in biofilm formation, by modifying the surface properties of the material, may represent a good strategy for inhibiting microbial growth. Thus, the objective of this work was to study the effect of the adsorption of biomolecules on the electrochemical behaviour of three metallic materials often used in heat exchangers (70Cu-30Ni (wt. %) alloy; 304L stainless steel; titanium), and the chemical composition of oxide layers in seawater environment. In order to achieve this objective the effect of bovine serum albumin (BSA) was studied in a first step, since it is a model protein often used to study protein-surface interactions, due to its low cost and to a good knowledge of its properties. Afterward, tightly bound (TB) and loosely bound (LB) extracellular polymeric substances (EPS) were extracted from a marine strain *Pseudomonas NCIMB 2021*, and their effect on the oxide layer was studied.

The selected solutions used in this work, representative of the environment of interest, were: a) filtered natural seawater (FNSW), b) artificial seawater (ASW), and c) a chloride-free solution with the same ionic strength as ASW (in 304L stainless steel the presence of chloride induces pitting corrosion).

In cooling circuits water is usually circulating but, frequently, plant outages cause provisional stagnant condition that can persist for hours or, at worst, for days. This condition is a particular risk concern for corrosion, especially at the beginning of plant operation. Therefore, hydrodynamics is one of the key parameters to be studied.

This thesis is divided in five main chapters. Chapter I presents a general background which includes: i) an introduction to cooling water systems, ii) an introduction to biofilms and to the exopolymeric substances produced by microorganisms within biofilms, and iii) a brief description of bovine serum albumin (BSA), its structure, conformation and physico-chemical properties, as well as the bacteria utilized for the EPS extraction. Chapter II presents the materials, electrolytes and biomolecules studied, as well as the experimental techniques used in this work: electrochemical measurements (corrosion potential (E_{corr}) vs time, polarization curves and electrochemical impedance spectroscopy (EIS)), combined to surface analysis by X-ray photoelectron spectroscopy (XPS) and time-of-flight secondary ions mass spectrometry (ToF-SIMS); their principles and instrumentation are described. Chapter III presents the study

of the corrosion behaviour of 70Cu-30Ni alloy after 1 h of immersion in marine environments (FNSW and ASW), in static conditions, under flow and stirring and in well-controlled hydrodynamic conditions. Chapter IV studies the influence of the adsorption of biomolecules on the electrochemical behaviour and surface chemical composition of 70Cu-30Ni alloy in ASW, comparing the effect of BSA and EPS extracted from *Pseudomonas NCIMB 2021*. Electrochemical measurements combined to surface analyses were performed during the very first steps of oxide layer formation (1 h immersion time). Electrochemical measurements were performed under flow and stirring and in well-controlled hydrodynamic conditions, using a rotating ring electrode. Chapter V focuses on the influence of the adsorption of biomolecules (BSA or EPS from *Pseudomonas NCIMB 2021*) on the electrochemical behaviour and surface chemical composition of passivating materials in artificial seawater (titanium) and chloride-free solutions (304L stainless steel). Finally, general conclusions of the thesis are given, together with recommendations and prospective work based on the obtained results.

The thesis also presents two annexes. A calculation sheet for converting marker concentrations (molar percentage of relevant elements, excluding hydrogen) into mass concentration (%) of model constituents in an organic phase is presented in Annex A; whereas in Annex B, the effect of *Escherichia coli K-12* adhesion on the surface chemical composition of 70Cu-30Ni, 304L stainless steel and titanium is discussed.

I. Background

I.1. Cooling water systems

I.1.1. Importance of cooling water systems

Energy requirements in industrial plants need to reject unwanted residual heat outside the process. Cooling systems are an integral part of process operation, since they enable the balance and control of temperatures and pressures drops by means of a fluid, frequently water, which takes the heat out of the system. The waste heat removed must ultimately be transferred to the contiguous environment. A typical cooling water system consists of a main condenser, a cooling tower, a coolant discharge, cooling water pump and a cooling water treatment plant [1].

Cooling water systems are used in refineries, steel mills, petrochemical plants, manufacturing facilities, food plants, large buildings, chemical processing plants, and electric utilities. The cooling water system operation can directly affect reliability, efficiency, and cost of any industrial process; when the cooling system cannot remove the heat efficiently, the entire process suffers a cost increase [1]–[3].

Water is the most used cooling agent due to its ease of handling, low cost, widely availability and useful thermal properties. The primary source for cooling water systems is the freshwater, which can be surface water (rivers, streams and reservoirs) or ground water (shallows or some deep well waters). Certain plants also use seawater and wastewater treatment plants effluents [2].

In power plants, electricity is generated when steam drives a turbine; this steam must be condensed before returning to the boiler to continue the cycle of steam and electricity generation. Electric power plants use large amounts of water to complete the steam cycle. Such volumes make uneconomical the use of treated water, thus preferred sources are streams, lakes and seawater. For this reason, power plants using seawater are strategically located in close proximity to seacoasts due to its immediate abundant availability [1], [3], [4].

I.1.2. Types of cooling water systems and heat exchangers in power supply facilities

Cooling systems can be classified using different broad criteria; however a general classification usually found in the literature distinguishes three broad categories (Figure I.1)[1]–[3].

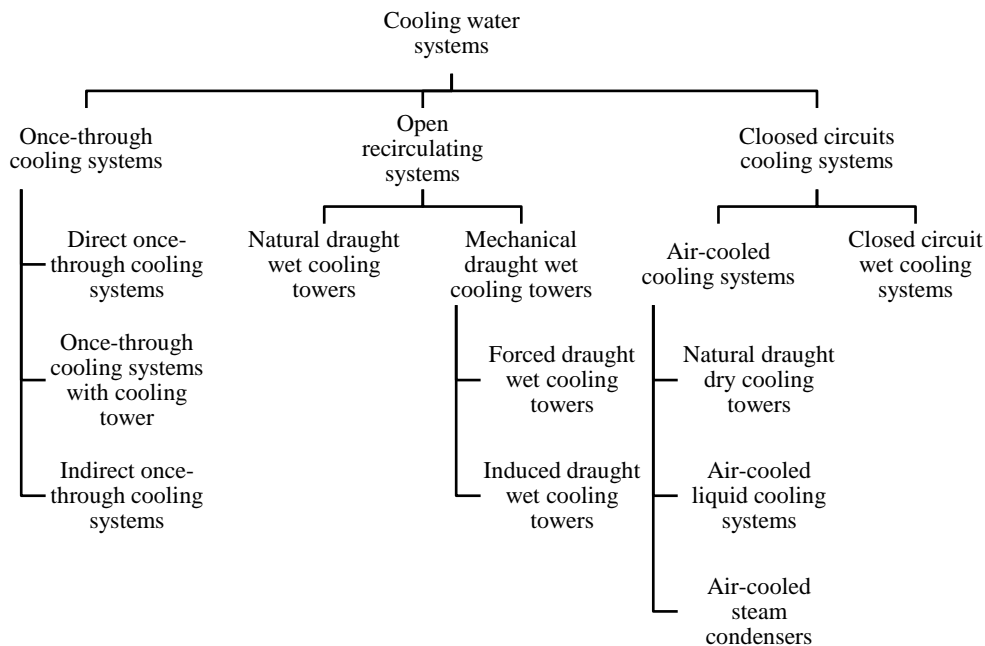


Figure I. 1: Classification of cooling water systems [1].

In once-through cooling systems (with or without cooling tower), water passes through the condenser once and returns to the water source. The mineral content of the cooling water remains practically unchanged as it passes through the system [1]–[3]. For a long time, designers found once-through cooling systems an efficient means to reject waste heat at low cost; however, because of the large volumes of cooling water are used, these systems are used less often than recirculating systems [5].

Open recirculating systems are the most widely used industrial cooling design of our days. These systems consist of pumps, heat exchangers, and a cooling tower. The pumps keep the water recirculating through heat exchangers. Water picks up heat and moves it to the cooling tower where the heat is released from the water through evaporation. Because of evaporation, the dissolved and suspended solids in the water become more concentrated [1]–[3]. Open recirculating systems are the most acceptable solution from an economical point of view, with important water savings [2].

Closed recirculating systems can be subdivided in: a) air-cooled cooling systems, and b) closed circuit wet cooling systems. In these cooling systems, the water is cycled between the condenser and a cooling tower. First, the water absorbs heat from process fluids, and then releases it into another heat exchanger. These systems are often used for critical cooling applications or when water temperature below ambient is required [1]–[3].

Generally, once-through systems and open recirculating systems are applied to power plants, and the petrochemical and chemical industries [1].

Heat exchangers are the essential heat transferring elements in cooling systems. A heat exchanger is a device used to transfer heat between two or more fluids at different temperatures and in thermal contact [6]. The fluids can be either liquids or gases, and in most heat exchangers they are ideally separated by a heat transfer surface [7].

Heat exchangers can be classified in many different ways such as according to transfer processes, number of fluids, surface compactness, flow arrangements, heat transfer mechanisms, type of fluids and industry. Figure I.2 shows a classification according to construction.

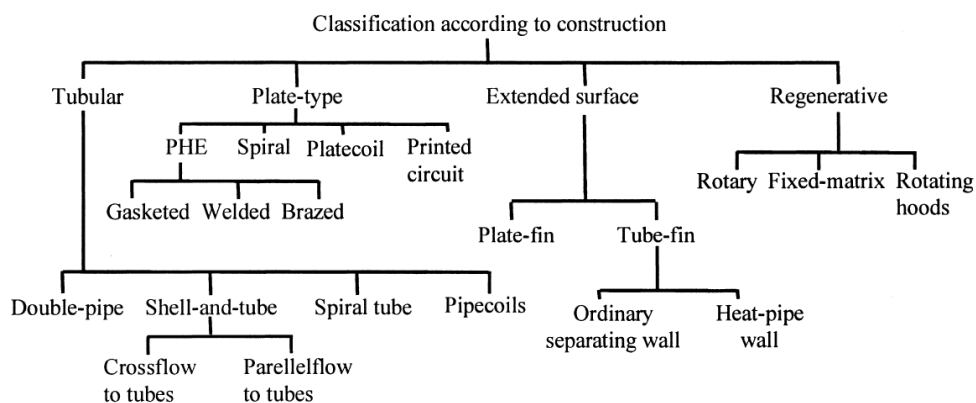


Figure I. 2: Classification of heat exchangers [7].

In power plants two types of heat exchangers are commonly used: the shell-and-tube, and the plate-and-frame heat exchangers (PHE). Shell-and-tube heat exchangers are widely used in industrial plants, and consist of a large number of tubes packed in a shell with their axes parallel to that of the shell, usually the tubes contain the cooling water and the process fluid moves around the tubes within the shell. On the other hand, plate-and-frame heat exchangers

comprise a series of plates with corrugated flat flow passages; they are economic as they can be much more compact than shell and tubes with the equivalent exchange surface area [1].

I.1.3. Materials

The selection of materials in cooling systems, and especially the selection of materials for heat exchangers, is a difficult procedure in many cases; it is a compromise between the requirements due to the chemistry of the water and the operational requirements of the system. Therefore, the parameters to consider in the materials selection process are: the type of cooler, the heat transfer properties of the material, their erosion and corrosion resistance, and the corrosiveness of the cooling water and of the fluid to be cooled [1], [8]. The use of salt or brackish water in cooling systems requires special attention to the corrosion of metallic materials [1].

Copper and copper alloys are commonly used in condensers and heat exchangers due to their high thermal and electrical conductivity, mechanical workability and good resistance to corrosion and macrofouling. Those criteria have led for a long time to the selection of copper alloys such as aluminium brass, 70Cu-30Ni (wt. %) alloy or 90Cu-10Ni (wt. %) alloy, to be used in seawater [8–11]. Alloying nickel and small amounts of iron into copper improves corrosion resistance; therefore Cu-Ni alloys are preferred in marine environments due to the formation of a thin, adherent, protective surface film which forms naturally and quickly upon exposure to clean seawater. That surface film is complex and predominantly made up of cuprous oxide (Cu_2O), often containing nickel and iron oxides, cuprous hydroxychloride ($\text{Cu}_2(\text{OH})_3\text{Cl}$) and cupric oxide (CuO) [10, 12]. Nickel passivates in acidic solutions while Cu is protective in more alkaline solutions [13]. Additionally, Cu-Ni alloys are also chosen in seawater because of their resistance to macrofouling; the reason for their antifouling behaviour is still not fully understood, but it may be the result of the action of a low level discharge of cupric ions (Cu^{+2}). Studies have shown that most of the copper present in marine environment is not present as cupric ion. In fact, the concentration of the cupric ions is at least an order of magnitude lower than the rest of the copper in the environment. Most of dissolved copper is complexed with organic and particulate material in marine and freshwater environments. This reduces or completely removes its ability to be taken up by organisms and therefore it poses toxicity to marine organisms [14]. Despite the reputation of copper alloys for toxicity, copper alloys are vulnerable to microbially induced corrosion, especially when

long periods of stagnation are involved or flow is intermittent. Differential aeration, selective leaching, underdeposit corrosion, and cathodic depolarization have been reported as mechanisms for MIC of copper alloys [9], [11], [15].

Stainless steels consist of a group of iron-based alloys which contain minimum ~ 10.5 % and maximum ~ 30 % of chromium. They are one of the most widely used materials with many different applications. They are divided into four main groups based on their microstructure: ferritic, austenitic, martensitic and austeno-ferritic (duplex). Other elements may be added to provide specific characteristics to the alloy, such as nickel, molybdenum, copper, titanium, aluminium, silicon, niobium and nitrogen contents; *e.g.* austenitic stainless steels are usually alloyed with Ni (for example, Fe-18Cr-10Ni (wt. %) (AISI 304)) [16], [17]. The corrosion resistance of stainless steels is due to the formation of a thin passive film of chromium-rich oxide which acts as a barrier against ion diffusion between the alloy and the ambient phase. This protective layer of chromium oxide develops during routine exposure to the oxygen contained in the atmosphere. The passive film on stainless steel can break down in the following environments: a) dilute and concentrated HCl, HBr, and HF, and salts that hydrolyze these acids; b) oxidizing chlorides such as FeCl₃, CuCl₂, or NaClO; c) seawater, except for brief exposures or when the stainless steel is cathodically protected; and c) some organic acids including oxalic, lactic, and formic acids [9], [17], [18]. AISI 304L and AISI 316L are the low-carbon version of the 304 and 316 stainless steels. Both stainless steels exhibit excellent corrosion resistance in a wide range of atmospheric environments and in many corrosive media. AISI 316 L is the standard molybdenum-bearing stainless steel (Fe-18Cr-10Ni-3Mo (wt. %)), which offers a better overall corrosion resistance than AISI 304L, in particular a higher resistance to pitting and crevice corrosion in chloride solutions. For this reason stainless steel 304 types are preferably to be used in freshwaters. However, both steels are susceptible to pitting and crevice corrosion in warm chloride environments, and to stress corrosion cracking above 60°C [19]. There are numerous case histories of MIC reported on stainless steels in water and aqueous systems. MIC has been reported for alloys with a relatively low content of molybdenum; pitting or crevice corrosion generally occurs at or around welds [20].

Titanium has been used in implants in the human body for many years; furthermore, over the past thirty years, the use of titanium tubes has been significantly expanded to power plants condensers, desalination plants, chemical processes and refinery heat exchangers. Titanium is

known to offer an exceptional resistance to corrosion, attributed to its surface oxide film (5-10 nm thickness) formed immediately on exposure to air. The natural titanium oxide film is dense and stable anatase (TiO_2), and protects the underlying metal from further oxidation [8], [21], [22]. Titanium shows complete resistance to general corrosion and crevice corrosion in all waters at temperatures up to 260°C for general corrosion and up to 82°C for crevice corrosion [23]. Its resistance is superior to that of stainless steels and copper alloys in most cases, especially in seawater, where titanium never corrodes and is comparable to platinum. The wall thickness of titanium tubes can be reduced, since there is no need for corrosion allowance. The tube diameter can also be reduced and the flow rate increased due to the high erosion resistance of titanium. The price of titanium has fallen dramatically in recent decades and therefore it has been cost-effectively applied. Expectations are that decreasing cost differences and increasing problems with water treatment will lead to an increased use of titanium compared to that of Cu-Ni alloys [1].

I.1.4. Operating problems in cooling water systems

The major problems associated with cooling systems are presented in Figure I.3. If these problems are not properly controlled, they can have a direct, negative impact on the cost of the entire process operation [1]:

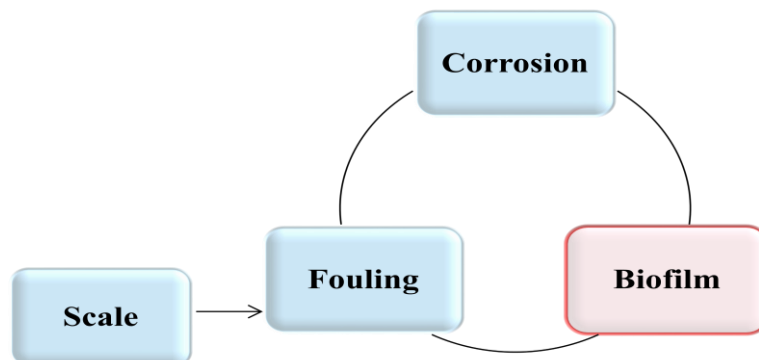


Figure I. 3: Interrelation between the different problems in cooling circuits [1].

I.1.1.1. Corrosion

Several definitions of corrosion are available. Despite different definitions, it is generally agreed that corrosion is basically the detrimental result of chemical and/or electrochemical interaction between a metal and its environment. In cooling water circuits, this result in the gradual loss of metal thickness localized sever damages or even penetration of tube wall,

which can cause leakage of process fluids into the cooling water or vice-versa. The main factors that affect corrosion are the presence of oxygen and other dissolved gases, dissolved and suspended solids, pH, fluid velocity, temperature and microbial activity [24, 25].

Corrosion cells essentially comprise anode, cathode, electrolyte (ion conductor) and metallic path (electron conductor). The anode is the area where metal is lost, typically linked to the formation of oxides and the release of metal ion into the solution, by dissolution, hydration or complex formation. It also includes precipitation of metallic ions at the metal surface. The anodic and cathodic reactions occur on the same surface, where both processes have to balance their charges. Therefore there is an increase in the valence state. In the anodic reactions, oxidation of metal takes place with releasing of electrons, leading to a higher valence state. Cathodic reactions are the reduction reactions which occur at the cathode. The electrons generated by the anodic reactions are consumed at the cathode. Common cathodic reactions are [24], [26]:



The predisposition for a given material to act as either electron donor (anode) or electron acceptor (cathode) is related to its electrochemical potential [27]. The sites hosting the cathodic and anodic reactions can be located close to each other on the metal surface or far apart depending on the circumstances. Table I.1 presents five major types of corrosion that have been identified.

Thermodynamic principles can help explaining corrosion in terms of stability of the chemical species and reactions associated to it. Nevertheless, thermodynamic calculations cannot be used to calculate corrosion rates. Therefore, principles of electrode kinetics have to be used to estimate them.

Corrosion can be directly quantified experimentally by using weight loss measurements that provide the rate at which the thickness of a material is decreasing. However, electrochemical measurements are sometimes preferred because they allow real-time monitoring and calculations of corrosion rates [26]. Corrosion rates may be expressed in two different ways: a) weight loss per area unit per time unit, usually mdd (milligrams per square decimeter per

day); or b) penetration rate, *i.e.* thickness loss per time unit. This latter may be expressed in the English system of units, mpy (mils per year, a mil being a thousandth of an inch), or in metric units, mmpy (millimeters per year).

Table I. 1: Types of corrosion [28].

Type	Characteristic	Examples
Uniform (or almost uniform)	All areas of the metal corrode at the same (or similar) rate	Oxidation and tarnishing; active dissolution in acids; anodic oxidation and passivity; chemical and electrochemical polishing; atmospheric and immersed corrosion in certain cases
Localised	Certain areas of the metal surface corrode at higher rates than others due to 'heterogeneities' in the metal, in the environment or in the geometry of the structure as a whole. Attack can range from being slightly localized to pitting	Crevice corrosion; filiform corrosion; deposit attack; galvanic coupling; intergranular corrosion
Pitting	Highly localized attack at specific areas resulting in small pits that penetrate into the metal and may lead to perforation	Pitting of passive metals such as stainless steels, aluminium alloys, etc., in the presence of specific ions, <i>e.g.</i> Cl ⁻ ions
Selective dissolution	One component of an alloy (usually the most active) is selectively removed from the alloy	Dezincification; dealuminification; graphitization
Conjoint action of corrosion and a mechanical factor	Localised attack or fracture due to the synergistic action of a mechanical factor and corrosion	Erosion-corrosion; fretting corrosion; impingement attack; cavitation damage; stress corrosion cracking; hydrogen cracking; corrosion fatigue

I.1.4.1. Scaling

Scale refers to deposits of inorganic material formed on the surface of equipment in the presence of water. Scale deposits are formed by precipitation and crystal growth at a surface, this occurs when the limit of solubility is exceeded either in the bulk water or at the surface. The common precipitates are calcium carbonate, calcium phosphate, sulphate or silicate. Such a process frequently occurs when surfaces are overheated; however, scaling is not always related to temperature [25], [29], [30].

The principal factors determining whether scale is formed are temperature, pH, water quality, concentration of scale-forming species, hydrodynamic conditions and influence of other dissolved species, which may or may not be scale-forming. In cooling systems, the most frequent type of scale is calcium carbonate deposit [29]. Scale formation reduces the heat transfer efficiency and flow velocities inside condenser tubes. Its prevention normally requires costly chemical softeners [31].

I.1.4.2. Fouling

Fouling occurs when insoluble particulates suspended in recirculating water, other than scale, form deposits on a surface. Fouling mechanisms are dominated by particle-particle interactions that lead to the formation of agglomerates. Foulants can come from external sources such as dust around a cooling tower or from internal sources such as corrosion by-products. Examples are: dirt, silt, sand, corrosion products, and natural organics. Settling occurs when the energy imparted by fluid velocity can no longer suspend the particle, due to agglomeration and growth. After the particles have settled, the nature of the deposit depends on the strength of the attractive forces between the particles themselves and between the particles and the surface they contact. The factors that influence fouling in a cooling system are the water characteristics, temperature, flow velocity, corrosion and contamination [25].

I.1.4.3. Biofouling and Microbially Influenced Corrosion (MIC)

Cooling water systems provide an ideal environment for microorganisms to grow and due to the availability of water, temperatures from 30°C to 60°C, pH of 6 to 9, good aeration, and a continuous source of bacteria and nutrients (inorganic or organic compounds) from makeup water and ambient air. The microorganisms present in cooling water circuits can be divided into planktonic and sessile cells. Planktonic cells are free-floating microorganisms whose

movements are controlled by water movement, whereas sessile cells attach to surfaces and form what is known as biofilm [25], [32]. Biofouling is hence a consequence of biofilm formation and is referred to as the undesired development of microbial layers on surfaces. The term has been adapted from heat exchanger technology, where fouling is defined generally as the undesired deposition of material on surfaces. In contrast to abiotic kinds of fouling (scale, organic and particle fouling), biofouling is a special case because the foulant (the microorganisms) are particles which can multiply and form extracellular polymeric substances (EPS). The significant negative effects of biofouling are the blockage of the free flow of water in the cooling circuit and consequent mechanical damage to pumps, and clogging of condenser tubes. Furthermore, the efficiency of the heat exchanger can be seriously decreased by biofilms, due to the formation of a gel layer that insulates the heat exchanger surface from the liquid phase. Although the heat transfer resistance of biofilms is similar to that of water, the gel allows only diffusive heat transport. Thus, heat transfer by convective transport is inhibited [20], [25], [33], [34].

Biofouling problems do not arise from microorganisms which have suddenly invaded the system, but are much more likely to be caused by an increase in nutrient concentration or an absence of inhibiting factors. In the majority of industrial systems, biofouling occurs concurrently with the abiotic fouling. Therefore, the prevention and control of biofouling should focus not only on the activity and growth of microorganisms, but also on physico-chemical conditions at the metal/solution interface. Chemical reactions in the circulating fluid should also be considered [29], [34].

Microorganisms within the biofilm are capable of maintaining an environment that is radically different from that of the bulk medium. Besides, metabolic reactions (which can be electrochemical) in living microorganisms differ fundamentally from typical reactions in metallic corrosion. Thus, the physical presence of microbial cells on the surface, in addition to their metabolic activities, modifies the more classical electrochemical processes [9], [27]. This modification of the metal/solution interface induced by the biofilm may be due to changes in the type and concentration of ions, pH values and oxidation-reduction potential [35]. As a result the intervention of microbes at the interface between metals and aqueous matrices can enhance reactions that otherwise would be thermodynamically unfavourable. The deterioration of a metallic material by processes which occur, either directly or indirectly, as a result of bacterial activity is defined as microbially induced corrosion (MIC), also called

biocorrosion [20], [32], [36]. Sessile microorganisms grow, reproduce, and form colonies that are physical anomalies on a metallic surface, resulting in local anodes and cathodes and the formation of differential aeration cells. There is a wide diversity of microorganisms that may be involved in MIC. However bacteria have been specially studied because they are the primary colonizers of metallic surfaces, which can have aerobic or anaerobic metabolism [37]. The theoretical oxygen profile and activities due to aerobic and anaerobic bacteria together in a biofilm is shown in Figure I.4. Under aerobic conditions, areas under respiring colonies become anodic and surrounding areas become cathodic. Microorganisms can simultaneously affect corrosion via several mechanisms; they have been described particularly for sulphate-reducing bacteria, and studies with other microbial types in a wide variety of conditions are still needed [20], [26]. Microbial effects that enhance corrosion are: a) the enhancement of the anodic reaction by acidic metabolites or of the cathodic reaction by microbial production of a new alternative cathodic reactant, b) the microbial breakdown of protective films, or c) the increase in conductivity of the liquid environment. Cell death or lysis within a biofilm does not necessarily mean a cessation of the influence on electrochemical processes [9], [35].

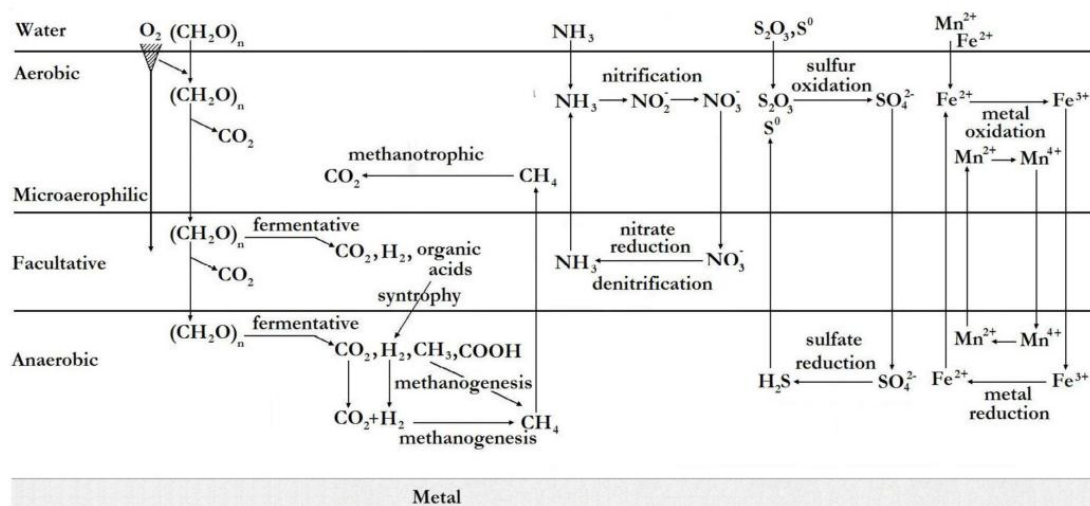


Figure I. 4: Bacterial interaction in biofilms [25], [26].

MIC and microbial inhibition of corrosion are rarely linked to one mechanism involving one species of microorganisms. Microbial corrosion inhibition is frequently due to: i) a decrease of the cathodic reaction rate by microbial consumption of a cathodic reactant, ii) a decrease of the medium aggressiveness in restricted areas at the metal/solution interface, iii) the formation

or stabilization of protective films on the metal (biofilm exopolymers with metal binding capacity) [35].

Methods used to prevent MIC should aim at either inhibiting the growth and/or metabolic activity of microorganisms, or modifying the environment in which the corrosion process takes place in order to avoid adaptation of microorganisms to the existing conditions. These methods can be divided in: a) cleaning procedures, b) biocides, c) coatings and, d) cathodic protection. The most practical and efficient method applied to prevent and control microbial activity in cooling water systems is the use of biocides. Biocides are single compounds (or a mixture of compounds) capable of killing microorganisms or inhibiting microbial growth. Chlorine is the most common oxidizing biocide and is introduced either through the electrolysis of seawater or the injection of sodium hypochlorite (NaOCl) solution. However, chlorine becomes less effective in alkaline environments (pH 6.5 to 7.5 is considered to be ideal for the action of chlorine). To improve the effectiveness of chlorine, bromine chemistry is being developed, giving a wider pH range. Bromine generation requires chlorine. However, the use of low level oxidants as antifouling agents in cooling water systems can give rise to concerns over the likely production of chlorination by-products [25], [29], [38], [39]. Therefore, the allowed chlorine concentration has been drastically reduced all over the industrialized world (0.2 mg/L) and effectively-performing treatments is now more difficult than in the past [40].

I.2. Biofilms

I.2.1. Introduction

Living organisms can be divided into three major domains: eukarya, bacteria and archaea. Eukarya domain is formed of those organisms whose cells hold a nucleus (eukaryotes), and include microorganisms (*e. g.* protozoa, algae, fungi, etc.) and macroscopic organisms (*e. g.* plants, animals, etc.). On the other hand, bacteria and archaea domains are prokaryotic, meaning that they lack of a true nucleus. In Figure I.5 is presented a classification scheme of living organisms, considering cell types, domains and kingdoms.

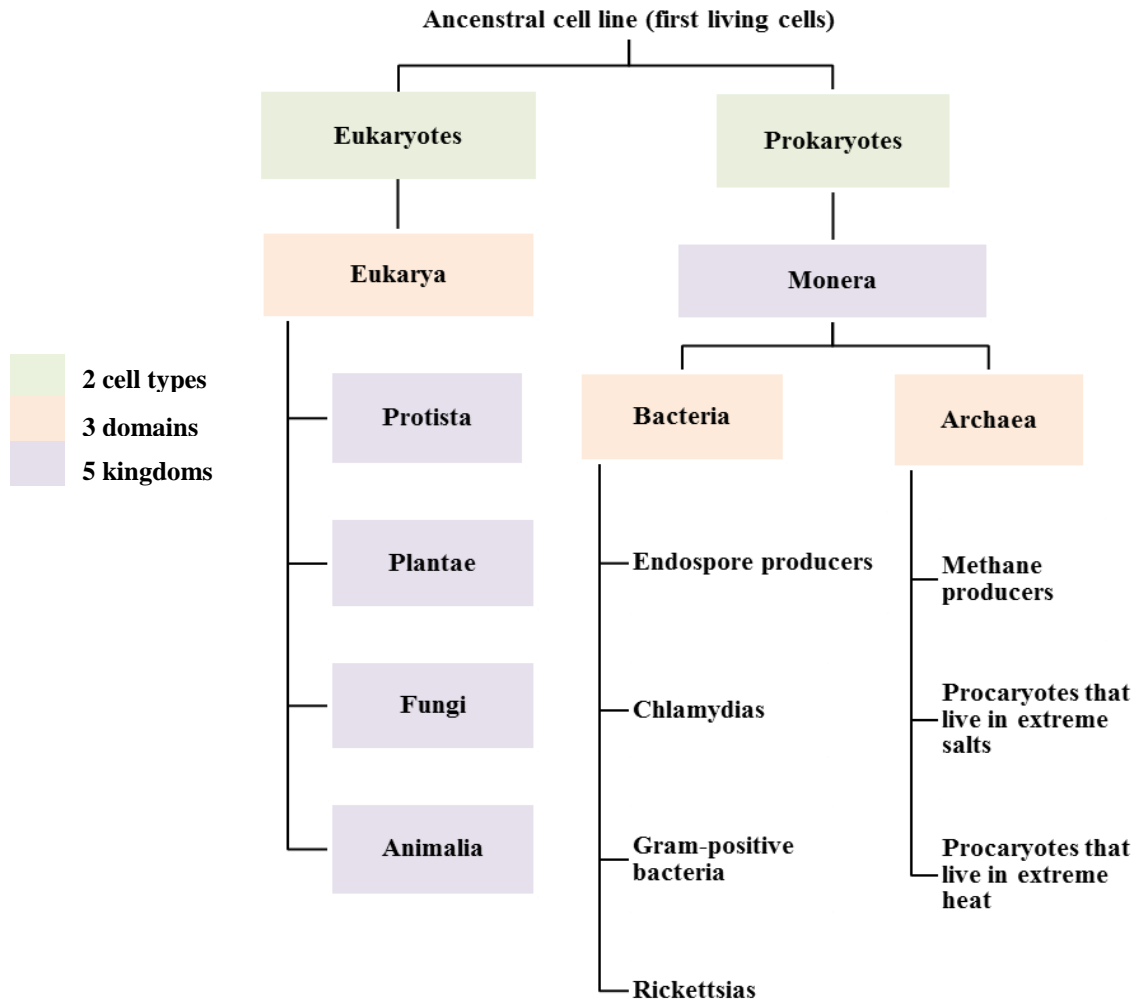


Figure I. 5: Classification scheme of living organisms.

Microorganisms can be defined as those organisms that individually are not visible to the human eye, requiring a microscope for detailed observation. Recently, the attention has been focused on bacteria due to their presence and activities within biofilms [12]. They range in size from 1 to 10 μm long and 0.5 to 1.5 μm wide; because of their size, shape (usually short rods or spheres) and coverage by biomacromolecules, the physical properties of many bacteria typically resemble those of colloids. Bacteria may be distinguished as either gram-positive or gram-negative, which reveals major differences in the cell wall structure. As shown in Figure I.6, gram positive cell wall consists of a single relatively thick layer (of peptidoglycan (made-up of a cross-linked polymer network of carbohydrates and peptides), called the sacculus, which protects the plasma membrane. Whereas gram negative cell wall has a structure which is more complex comprising a thinner layer of peptidoglycan adjacent to the plasma membrane, and an outer membrane built-up of proteins, lipopolysaccharides and

phospholipids; the gap between the peptidoglycan network and the outer membrane is known as the periplasmic space and it accomplishes various physiological roles [38].

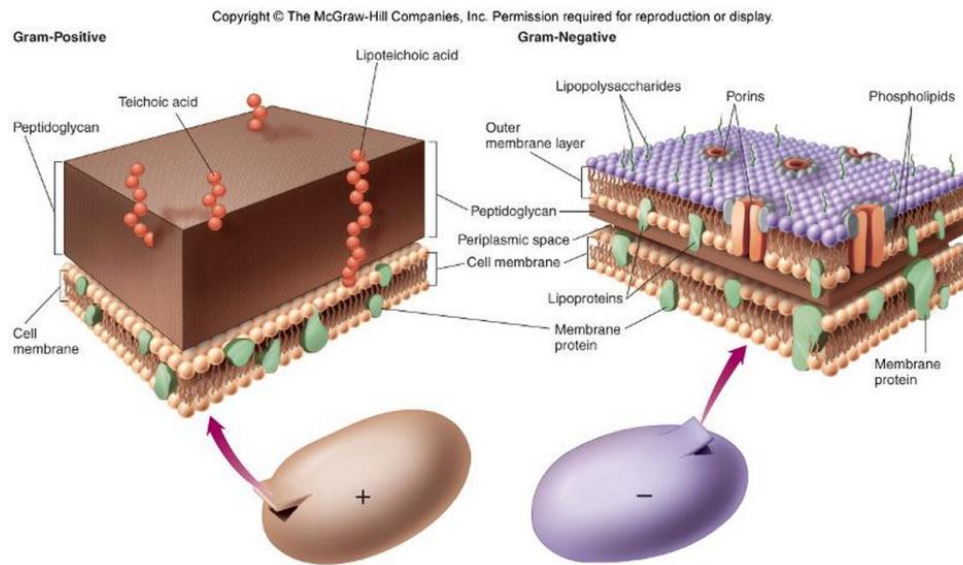


Figure I. 6: Classification of bacteria according to their cell wall structure: gram positive/gram negative.

Bacteria have a tendency to form colonies, reproducing by binary fission or cell division. Figure I.7 shows a theoretical microbial growth curve. Bacteria require a carbon source and an energy supply. The carbon source may be taken from carbon dioxide but usually additional complex organic carbon sources, such as sugars, are required; some organisms can use very complex carbon molecules, such as cellulose, lignin and tannin as carbon source. Bacteria also need an energy supply in order to accomplish the cell functions; this energy can be obtained from three possible sources: a) oxidation of inorganic compounds, b) oxidation of organic compounds, and/or c) from the light (daylight or direct sunlight). The energy is produced and subsequently stored by the cell by means of oxidation-reduction reactions, inducing an exchange of chemical compounds through the bacterial cell. Besides the energy and carbon sources, microorganisms need nitrogen, phosphorus, and trace elements [9], [20], [25], [42]. Nitrogen compounds may be inorganic ammonium and/or nitrate (sometimes nitrite) as well as organically bound nitrogen (amino acids, nucleotides, etc). Phosphorus is usually taken as inorganic phosphate or as organically bound phosphorylated compounds such as phosphorus-containing sugars and lipids. Phosphate in the form of adenosine triphosphate (ATP) serves as the main energy storage compound [20].

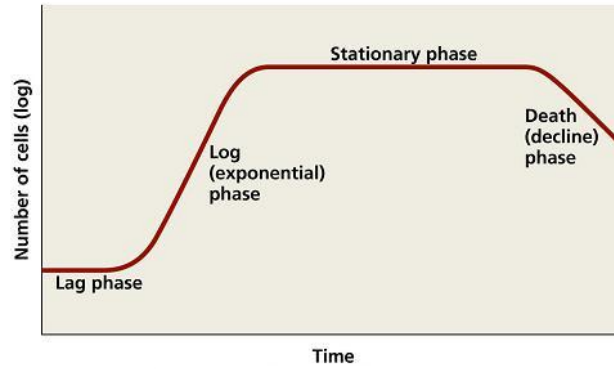


Figure I. 7: Microbial growth curves.

Biofilms have been described as sessile microbial communities that live attached to each other and to surface structures as well as microbes forming flocks and aggregates [43]. The microorganisms embedded in a biofilm can belong to one or different species, and allow bacteria to grow on surfaces in a self-produced extracellular polymeric matrix (EPS) [44]. Up to 60% of the carbon metabolized and ATP spent by microbial cells are used for the production of these extracellular secretions [45]. Biofilms provide a mechanically stable and protective environment for the bacteria, resulting in a higher resistance against extreme conditions and/or environmental stresses [46]. They can form at solid-liquid, solid-air and liquid-air interfaces [34].

Biofilm formation is a dynamic but not a random process. The development of a biofilm is considered to be a multistage process involving the following major steps (Figure I.8):

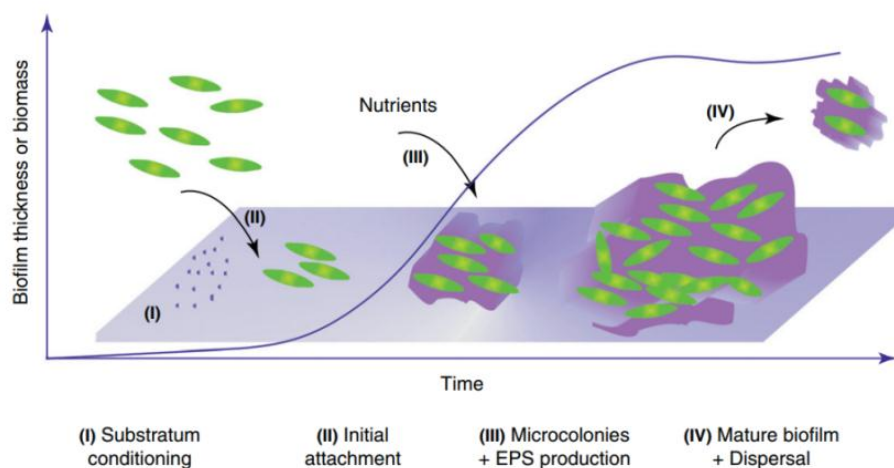


Figure I. 8: Principal steps in the biofilm formation [43].

a) formation of a conditioned film (approximately 2-8 nm) on the solid surface by adsorption of inorganic ions and biomolecules such as proteins [47];

b) transport of microorganisms from the water to the surface through and by the effects of physical forces, such as brownian motion, van der Waals attraction forces, gravitational forces, effect of surface electrostatic charge and hydrophobic interactions; making weak and transient attachments (bacteria prefer to grow on available surfaces rather than in the surrounding aqueous phase). Chemotaxis (characteristic movement or orientation of the cells along nutrients (or poisons) concentration gradients in the environment, either toward or away from the chemical stimulus) and perhaps haptotaxis (cell migration toward or along a gradient of cellular adhesion sites or surface-bound attractants) contribute to this process;

c) irreversible adhesion of microorganisms onto the surface by molecular specific interactions between bacterial surface polymeric structures (appendages such as flagella and pili as well as cell surface molecules such as lipopolysaccharides, lipoproteins, membrane proteins, adhesions; Figure I.9) and the substratum surface [48];

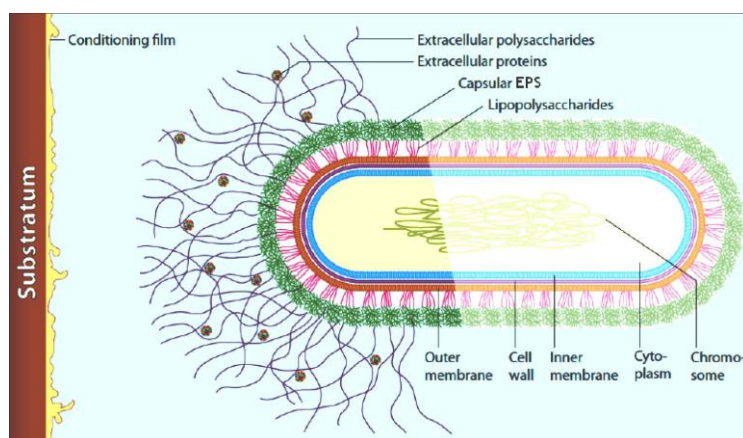


Figure I. 9: Schema of bacteria approaching to the surface [32].

d) replication of the attached cells and production of exopolymers;

e) detachment of parts of the biofilm that are swept along by the flowing water to repeat the process of biofilm formation elsewhere, stimulated by the nutrients limitation or other unfavourable environmental conditions [25], [49]. In Table I.2 the three theoretical approaches used to describe bacterial adhesion, once microorganisms reach the proximity of a surface are summarised [48], [50].

Table I. 2: Theoretical models for describing bacteria-substrate interactions

Theoretical model	Characteristics
DLVO theory (Derjaguin-Landau- Verwey-Overbeek)	Describes the interaction of a colloidal particle with a surface; according to this theory, the net interaction between a cell and a surface is the sum of their van der Waals (generally attractive) and Coulomb interactions (generally repulsive due to the negative charge of cells and substratum). This theory can account for experimentally observed low levels of bacterial attachment to negatively charged surfaces, but it cannot explain the variety of attachment behaviours observed with other types of surfaces or in solutions concentrated solutions.
Thermodynamic theory	Takes into account the various types of attractive and repulsive interactions, such as van der Waals, electrostatic or dipole interactions, but expresses them collectively in terms of free energies of the interacting surfaces. Adhesion is favoured if the free energy is negative as a result of adhesion, which means that spontaneous attachment is accompanied by a decrease in free energy of the system, as predicted by the second law of thermodynamics. However, thermodynamics principally assumes that the process is reversible, which is not often the case.
Extended DLVO theory	Neither the DLVO nor the thermodynamic approach can fully explain bacterial adhesion. For this reason the extended DLVO includes hydrophobic/hydrophilic interactions and also osmotic interactions.

I.2.2. Conditioning films

Before bacterial adhesion, the surface becomes coated with organic and inorganic components, forming what is called the conditioning film [9], [34], [51]. This formed film strongly affects the physico-chemical properties of the surfaces, having an effect on the microbial attachment and therefore the biofilm formation process. Within seconds, surfaces immersed in water become covered by macromolecules, such as humic substances, polysaccharides and proteins, which are present in water [52]. The properties of the conditioning film which is formed depend on the type of dissolved organic compounds, temperature, pH and ionic strength of the solution, as well as on the substratum surface properties (rough surfaces are more liable to microbial colonization than smooth surfaces but even on the smoothest surface, bacteria can attach), and the contact time between the substratum and the water [34], [51]. Usually, the conditioning film becomes negatively

charged in neutral conditions due to the adsorption of organic components that contribute to the charge through their carboxylic and hydroxyl groups. Humic substances and proteins are reported to be the major dissolved organic compounds in natural waters; therefore, they are expected to have a contribution in the formation of the conditioning film [53].

The adsorption of biomolecules to a bare surface is the result of a competitive adsorption; thus, the composition of the conditioning film changes with time due to the replacement of the first adsorbed molecules by higher affinity molecules [54].

The conditioning film alters the surface energy and the corrosion potential of metallic substrata [9].

I.2.3. EPS and biofilm architecture

The factors that affect biofilm are mainly the availability of nutrients (*e. g.* carbon, nitrogen, potassium, and phosphate), the bacteria motility, the intercellular communication, as well as the hydrodynamic conditions (laminar or turbulent flow influences biofilm structure, density and strength). In biofilms, the microorganisms account for less than 10% of the dry mass, whereas the matrix can account for over 90% [55]. The matrix consists of extracellular substances (known as extracellular polymeric substances, EPS) that are mainly high-molecular-weight biopolymers produced by microorganisms, and products of cellular lysis and macromolecules hydrolysis. Additionally, organic matter from the environment can also be adsorbed by electrostatic interactions, ion exchange, complexation or chelation onto the EPS matrix [56]. The abbreviation EPS is a more general and comprehensive term that represents different classes of macromolecules such as polysaccharides, proteins, nucleic acids, lipids and humic substances (mixtures of compounds that are formed by limited degradation and transformation of dead organic matter and that are resistant to complete biodegradation). Some are neutral macromolecules (*e.g.* aromatics, aliphatic), but the majority contain charged groups (*e.g.* OH⁻, COO⁻, -SH⁻, -SO₄²⁻, -H₂PO₄⁻, -NH₄⁺, -NRH₂⁺, etc) [49], [57], [58]. At neutral or slightly alkaline pH (*e. g.* seawater), EPS contains mostly negatively charged groups [59].

EPS preserve their structure with plenty of water that protects cells against dewatering and harm of toxic substances. In addition, EPS can serve as carbon or energy sources in case of nutrient deficiency, and act as a buffer against microenvironmental changes. They also

maintain symbiotic relationships, and accelerate the formation of microbial aggregates through binding cells closely. Adhesion and cohesion are based on weak physico-chemical interactions and not on covalent bonds; Figure I.10 (a) shows the major kinds of forces that may be distinguished within the matrix.

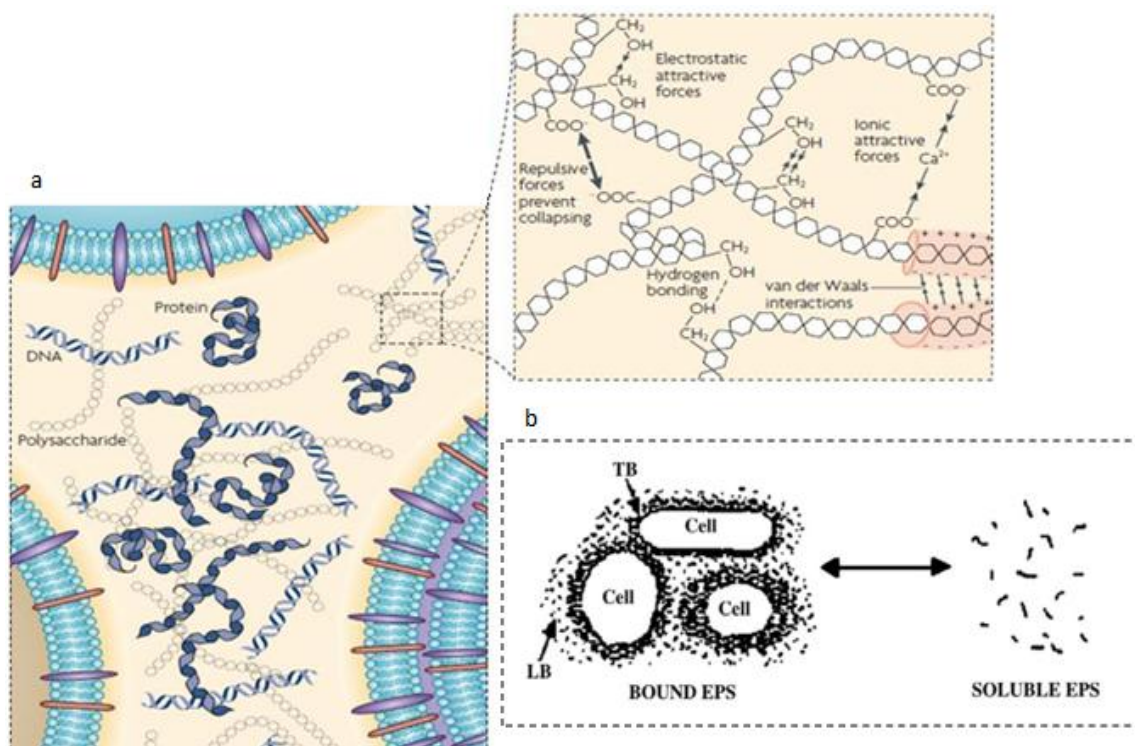


Figure I. 8: EPS matrix: a) types of physico-chemical interactions present in the EPS matrix; b) EPS categorization [55], [60].

Most bacterial strains produce exopolymers during their life cycle. However the maximal EPS production generally occurs at the end of the log phase (or exponential phase) and during the stationary phase of growth [45]. In natural environment and under laboratory conditions, microorganisms tend to produce more EPS under nitrogen-limiting conditions [61]. The EPS composition and hence their physico-chemical properties varies with the bacterial strains that are producing them. Table I.3 presents the composition of EPS from various natural and synthetic systems [60]. The variations in the composition of the extracted EPS is also attributed to many other factors, such as culture, growth phase, pH, temperature, bioreactor type, extraction method, and analytical tool used. Their physical states can be described as a continuum, ranging from gels to a fully dissolved state. These polymers exist as capsules, sheaths, looser slimes in biofilms and as dissolve organic carbon (DOC) in solution [45], [56], [61], [62].

Table I. 3: Components content in EPS.

Component	Content in EPS
Polysaccharides	40 – 95 %
Protein	< 1 – 60 %
Nucleic acids	< 1 – 10 %
Lipids	< 1 – 40 %

In gram-negative cells, the EPS are mainly composed of lipopolysaccharides, capsule polysaccharides, and other excreted polysaccharides, and proteins that are less firmly bound to the cell surface. Some EPS are neutral, whereas others are polyanionic because of the presence of uronic acids; phosphate or sulphate residues also lead to polyanionic characteristics [49], [57]. However, gram-positive cells often produce polycationic EPS, lipoteichoic acids as well as polysaccharides and proteins, which are not attached to the cell wall and contribute to the EPS [57].

Microorganisms produce EPS that can be found either in suspended cultures or in biofilms. The produced exopolymers can exist as tight capsules which are closely bound to microbial cells (tightly bound EPS), or as soluble EPS which may be weakly bound to cells or dissolved into the solution (loosely bound EPS) (Figure I.10(b)) [45], [56]. Many strains form more than one specific type of EPS, and the composition of the EPS may change during the life cycle of such organisms, due to the growth conditions and/or environmental stresses [57].

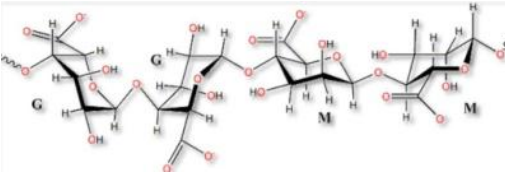
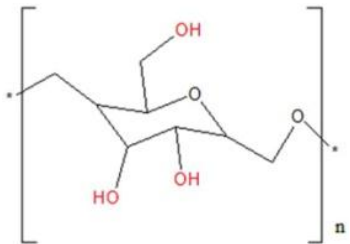
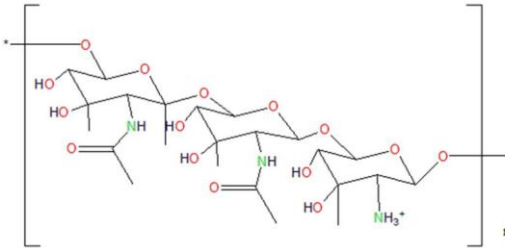
I.2.3.1. Exopolysaccharides

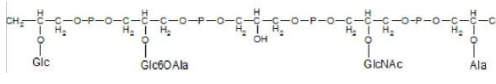
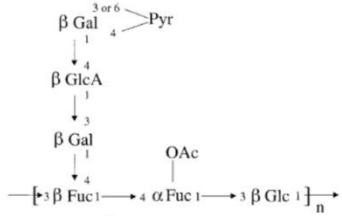
Exopolymers are primarily composed of high molecular weight polysaccharides (10 to 30 kDa) and generally have heteropolymeric composition, that consist of a mixture of neutral and charged sugar residues with organic or inorganic substituent that greatly affect their physical and biological properties. Microbial exopolysaccharides are considered to play an important role in biofilm formation, pathogen persistence, and have several applications in the food and medical industries [45], [55], [61], [63]. The most well-known exopolysaccharides present inside biofilms are presented in Table I.4 [63].

Commonly, polysaccharides are made of monosaccharides (also called monocarbohydrates), with hexoses and pentoses forming the bulk of EPS. The composition as well as conformation

of sugars monomers may modify the properties of the exopolysaccharides and thus of the biofilm matrix.

Table I. 4: Most commonly found exopolysaccharides present inside biofilms.

Polysaccharide	Description	Structure
Alginate	It is an exopolysaccharide with a relatively high molecular mass (10^4 - 10^6 g.mol ⁻¹). It consists of the uronic acid residues β -D-mannuronate (M) and its C-5-epimer, and α -L-guluronate (G). These residues can form a gel in the presence of chelating divalent cations bound to G-rich blocks and divalent cations.	
Cellulose	It is the most abundant sugar polymer found on the surface of the planet. It consists of a β -1-4-linked linear glucose. The formation of cellulose fibers is provided by hydrogen bonds between the glucose chains. Cellulose has a crystalline structure; each crystal contains numerous glycan chains in parallel orientation. The reducing ends are at one terminus while the non-reducing ends are at the opposite terminus.	
Poly-N-acetyl glucosamine (PNAG)	It is required for bacterial adhesion and biofilm formation of some bacterial species. It is a positively charged linear homoglycan composed of β -1,6-N-acetyl glucosamine residues with approximately 20% deacetylated residues. PNAG form a protective matrix around bacterial cells that is also involved in cell-to-cell interactions.	

<p>Teichoic acid</p>	<p>There are two types of teichoic acid in <i>S. epidermis</i>: teichoic acid associated with the bacterial membrane (CW TA) and extracellular teichoic acid (EC TA). EC TA is responsible for the increased viscosity of the colony; It consist in a (1-3)linked poly(glycerol pohosphate), substituted at the 2-position with a α-N-acetylglucose, D-alanine and α-glucose-6-alanine.</p>	
<p>Colanic acid</p>	<p>It is a sugar polymer composed of galactose, fructose and glucose. It is often found in the biofilm matrix of <i>E. coli</i>.</p>	

Bacterial exopolysaccharides can exist either in ordered or disordered forms, the conditions that favour the disordered forms, being favoured by elevated temperatures and extremely low ionic concentrations. One of the major components of bacterial exopolysaccharides are the uronic acids (sugars in which the terminal hydroxyl group has been oxidized to a carboxylic acid), constituting up to 20-50% of the polysaccharide fraction [61, 63].

Monocarbohydrates constituting exopolysaccharides are often D-glucose, D-galactose, D-mannose, L-fructose, L-rhamnose, L-arabinose, N-acetyl-D-glucose amine and N-acetyl-D-galactose amine as well as some uronic acids which are a class of sugar acids with both carbonyl and carboxylic acid functional groups (D-glucuronic acid, D-galacturonic acid, D-manuronic acid and L-guluroic acid). Other sugar monomers less frequently found are D-ribose, D-xylose, 3-keto-deoxy-D-mannooctulosonic acid and several hexoseamineuronic acids. The polysaccharide moieties of EPS are especially important in binding reactions because of the presence of carboxylic and hydroxyl groups, which act as binding ligands for dissolved compounds [45].

I.2.3.2. Extracellular proteins

The biofilm matrix can contain considerable amount of proteins that, in some cases, may overtake the polysaccharide content on a mass basis. The proteins in the matrix, such as the cell surface-associated and extracellular carbohydrate-binding proteins (lectins), are involved in the formation and stabilization of the polysaccharide matrix, and constitute a link between the bacterial surface and EPS. Proteins rich in acidic amino acids, including aspartic and glutamic acid, contain carboxylic groups that contribute to the anionic properties of EPS [64].

Bacteria produce a large variety of enzymes, which can be categorized as ectoenzymes (associated with the cell but expressed outside the cytoplasmic membrane) and extracellular enzymes (present in the biofilm matrix). Some extracellular enzymes have been detected in biofilms, many of which include polysaccharidases, proteases, lipases, esterases, peptidases, glycosidases, phosphatases, and oxidoreductases [64]. Extracellular enzymes can be retained in the biofilm matrix by their interactions with exopolysaccharides, enhancing the thermostability of the enzymes and their resistance to proteolysis. Furthermore, extracellular redox enzymes play a role in MIC, while other extracellular enzymes are of commercial interest and are produced on a large scale industrially. They can be, additionally, involved in the degradation of structural EPS to promote the detachment of bacteria from biofilms. The presence of such degrading enzymes makes the matrix an external digestive system that can potentially degrade EPS components in case of nutrients starvation; the resulting products can then be taken up and used as carbon and energy sources. Exopolysaccharides are degraded mainly by hydrolases and lyases, but degradation is generally slow. The chemical properties of the biofilm matrix, such as the presence of different types of binding sites within macromolecules forming this matrix, enhance close association between EPS enzymes and exogenous substrates, thus enabling enzymatic reactions [55], [64].

I.2.3.3. Extracellular nucleic acids

Although deoxyribonucleic acid (DNA) was initially considered as residual material from lysed cells, nowadays it is considered to play an important role in the formation of the biofilm structure (nucleases can be regulators of biofilm formation), and to be integral part of the matrix and of the biofilm mode of life. Lysed cells are not the only source of extracellular DNA; active excretion of DNA cannot be excluded. The localization of extracellular DNA can vary widely between biofilms; in some biofilms, it forms a grid-like structure whereas in

others, it forms a filamentous network [55], [63]. Nucleic acids are polyanionic due to the phosphate residues in the nucleotide moieties [64].

I.2.3.4. Surfactants and lipids

Lipids are also found in the matrix. Furthermore, some bacteria produce extracellular lipids with surface-active properties, referred to the ability of a molecule to alter the interface between two different phases. Substances with surface-active properties (surfactants) are amphiphilic molecules with both hydrophilic and hydrophobic or lipophilic (generally hydrocarbon) moieties able to display a variety of surface activities that allow solubilisation of hydrophobic substrates [55], [65].

Biosurfactant is a substance that is synthesized by microorganisms (mostly bacteria and yeasts) and that is surface active. It may be either extracellularly released into the environment or localized on surfaces, being associated with the cell membrane. Microorganisms produce them to increase the hydrophobicity of the cell and help them to survive in hydrophobic environment. Additionally, they can mediate the solubilisation of hydrophobic compounds in their environment, these compounds being then used as substrates. Biosurfactants can have antibacterial and antifungal properties, and are important for bacterial attachment and detachment from oil droplets. Biosurfactants generated by microorganisms at the air water interface reduce surface tension, influencing the gas exchange between oceans and the atmosphere. In addition, they stabilize emulsions, promote foam and are generally non-toxic and biodegradable [55], [65].

I.2.3.5. Interaction of EPS with metals

In order to understand the interactions between bacteria and a solid surface, all the factors that may be involved on these interactions must be considered [34]. Firstly, it has been demonstrated that the chemical composition of the substratum to which microorganisms attach is an important factor during the early stages of biofilm accumulation and may influence the biofilm formation rate and the cell distribution during the first hours of exposure [9].

Another important factor to be considered is the EPS because the EPS molecules provide the forces responsible for cohesion of the biofilm and its adhesion to the substratum [34].

Biofilm cohesion and adhesion are provided by weak interactions such as van der Waals forces, electrostatic interactions, and hydrogen bonds [57]. The cell wall is involved in the adhesion process only in the afterwards stages. Microbial adhesion can be considered mainly as an abiotic process, which can also occur when the cells are dead. This means that the cells do not need to be viable for adhesion [34].

Exopolysaccharides and other biopolymers bind a wide variety of metals such as Pb, Sr, Zn, Cd, Co, Cu, Mn, Mg, Fe, Ag, and Ni [45], [62], with various degrees of specificity and affinity [66]. The binding affinity in the complex depends principally on the ion size/charge ratio, and other factors such as EPS composition, physical gel state, pH, ionic salinity, and carbohydrate/protein ratio [62], [66].

The functional groups of microbial EPS may be either negatively or positively charged at near neutral pH values [64]. Two types of mechanisms may be involved in the EPS metal-binding capacity: a) ion exchange due to the high amount of negatively charged functional groups in EPS; and b) complexation with negatively charged functional groups, such as hydroxyl groups, amino groups, carboxylic groups, phosphoryl and sulphate groups [59], [62], [66], [67]. It has been reported that exopolymers of aquatic microorganisms act as polyanions under natural conditions by forming salt bridges with carboxylic groups of acidic polymers such as uronic acids, or by forming electrostatic bonds with hydroxyl groups on polymers containing neutral carbohydrates [66]. . Therefore, the adsorptive affinity of certain metals has been often correlated with the content of uronic acids in the exopolymers [45]. .

The influence of pH on the metal binding to exopolymer emphasizes the involvement of H^+ ions. At low pH the availability of negatively charged sites such as carboxylic groups is strongly decreased, and consequently a small number of metallic cations can be bound. Whereas at higher pH, metal binding is enhanced by a proportional increase in the number of ionized acidic groups that are free to bind ions and therefore tend to favour their chelation. The maximum binding affinities occur near the pH of seawater, generally between 8.0 and 8.2. This may vary considerably within the localized microenvironments in the biofilm due to the photosynthetic and respiratory activities of microorganisms [45], [62]. Another potential factor that may influence metal chelation is the modification of EPS by UV irradiation. Laboratory studies have shown that there is an enhancement of available carboxylic groups after exposure to UV-irradiation, which may increase their potential for binding metallic ions in EPS. [62].

The metal binding/sorption capacity of the biofilm matrix is important for MIC because EPS promoted the ionization of the metal surface, thus resulting in metal ion concentration cells and changing the electrochemical nature of the metal surface. The metal ions trapped within the biofilm matrix become concentrated, forming complex (with a range of redox potentials) that may participate in the electron-transfer processes, and affect the electrochemical characteristics of the metallic surface by increasing the corrosion rate, and providing an additional cathodic reaction [9]. Thus, metal ion chelating properties of bacterial EPS have been proposed as a key reason for MIC of metals [68].

Reports and models of EPS-metal ions interactions highlight the role of anionic polysaccharides in metal binding but rarely consider the participation of proteins, nucleic acids, or lipids [64], [69].

I.3. Bovine Serum Albumin (BSA)

In order to better understand the effects of biomolecules adsorption on the electrochemical behaviour of metallic materials, and the chemical composition, structure and thickness of the oxide layers, it is important to select, in a first step, a well-known model. Therefore, the bovine serum albumin (BSA), a model protein often used to study the protein-surface interactions due to its low cost and good knowledge of its properties was chosen [70]–[72].

I.3.1. Composition and physico-chemical properties

Serum albumin is probably one of the most studied globular proteins. It is commonly used as a model protein in several research areas such as molecular biology, food industry, medicine and environment, among others; it corresponds to the most abundant protein in blood plasma. Serum albumin function is associated with the binding and transport of several small molecules such as fatty acids, dyes, metals, and amino acids [73], [74].

Bovine serum albumin (BSA) has a molecular weight of 66.43 kDa (66430 g.mol⁻¹), and a density in aqueous solution of 1.3 g.cm⁻³, slightly varying with the pH. The isoelectric point of this protein is reported to be 4.5 and 5.6; thus in neutral solution, BSA is negatively charged as a whole molecule. The amino acid composition of BSA has been published for the first time in 1975 by J. R. Brown [75] and later by Hirayama *et al.* [76] in 1990. The amino acid composition of BSA proposed by these authors is presented in Table I.5.

Table I. 5: Amino acid composition of BSA [16].

Amino acid	Number of amino acid residues	
	Brown, J. R. (1975)	Hirayama <i>et al.</i> (1990)
Aspartic Acid	41	41
Arginine	23	26
Asparagine	13	14
Glutamic Acid	59	58
Glutamine	20	21
Histidine	17	16
Lysine	59	60
Serine	28	32
Threonine	34	34
Alanine	46	48
Isoleucine	14	15
Leucine	61	65
Methionine	04	05
Phenylalanine	27	30
Tryptophan	02	03
Tyrosine	19	21
Valine	36	38
Cysteine	35	35
Glycine	16	17
Proline	28	28
Total	582	607

Proteins can be divided into two classes, “hard” and “soft” proteins. Hard proteins have strong internal coherence and structural rearrangements that only make small contributions to the adsorption process; they adsorb onto hydrophobic surfaces but on hydrophilic surfaces, they adsorb only if they are electrostatically attracted. On the other hand, “soft” proteins, with lower structural stability, adsorb even under apparently unfavourable conditions onto hydrophilic, and electrostatically repelling surfaces [77]. BSA is a soft protein, with a large conformational adaptability. BSA has the ability to bind substances reversibly, especially negatively charged substances [74].

I.3.2. Structure/conformation

BSA presents a primary structure with the shape of a heart. Its secondary structure is constituted between 50 and 68 % of α -helix, and between 16 and 18% of β -sheets. The tertiary structure is not fully known [16].

It has been reported that BSA in solution is able to adopt different conformations that correspond to different α -helix contents, which are modified by changes in pH or ionic strength. The classification of BSA conformers according with the pH is presented in Table I.6 [73], [77].

Table I. 6: Effect of pH on the conformation of serum albumin.

pH transition		2.7	4.3	8	10				
Isomeric form	E	↔	F	↔	N	↔	B	↔	A
Name	Extended		Fast		Normal		Basic		Aged
% of α -helix	35		45		55		48		48
Global charge	+100		+99		-18		-19		-60

The normal form (N) is predominant for pH between 4.3 and 8. For pH between 4.3 and 2.7, the fast-migrating transition or fast form (F) is produced. The transition from the N form to the F one leads to the unfolding of the molecule along with an important increase of the intrinsic viscosity, and a significant decrease of the solubility and of the content of ordered (secondary) structure. At pH 2.7, the expanded (E) form appears. During the F-E transition, the molecule is again expanded and its intrinsic viscosity is significantly increased. Figure I.11 shows the different N, F and E conformations of BSA. In addition, another conformational transition takes place at pH 8.0, called and 10 called the basic form (B). The N-B transition induces a decrease of the α -helix percentage, and an increase of the β -sheet percentages. The structure of the B form is still unknown. At pH > 10, it is possible to observe the A form; for the B form, its structure is up to now unknown [16], [73].

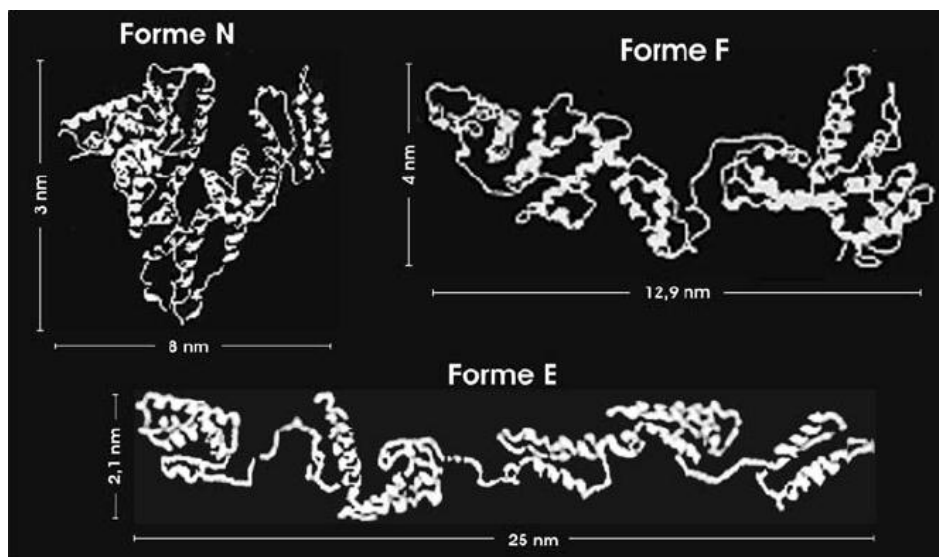


Figure I. 9: Different conformations of bovine serum albumin (BSA).

I.4. Bacterial culture (*Pseudomonas NCIMB 2021*)

Pseudomonas is considered the most prevalent species in industrial water and seawater, they have been found to be involved in the corrosion process of several metallic materials. Aerobic *Pseudomonas* strains are recognized to be the pioneer colonizer in the process of biofilm formation, and their primary role appears to create an oxygen-free environment to harbor the SRB. Furthermore, it is subsequently found that these strains are aerobic slime-formers and often grow in a patchy distribution over the metal surface and exclude oxygen via respiration; thereby creating oxygen concentration cells or ion concentration cells [68].

Pseudomonas NCIMB 2021 is a marine bacterium that has been intensively studied with the aim of solving problems related to biofouling. This strain was first isolated by Fletcher and Floodgate from the Menai Straits, Anglesey in Wales [78], [79].

The extracellular polymeric substances (EPS) of *Pseudomonas NCIMB 2021* were isolated by Fletcher in 1980, using ethanol precipitation. It was reported that the EPS consisted of 50-80% protein and a carbohydrate fraction containing mannose, glucose, glucosamine, rhamnose, galactose and ribose, but no uronic acids. However, the presence of acidic groups in the carbohydrate fraction of this marine pseudomonas was confirmed by Christensen, who also showed that this organism produces one type of polysaccharides in the exponential growth phase and a different type in the stationary phase [79].

Fletcher and Loeb compared the adhesion of the marine pseudomonas to hydrophobic and hydrophilic surfaces. Bacteria were most abundant on hydrophobic surfaces, and the number of attached cell decreased with the wettability of those surfaces. Fletcher concluded that bacteria have both active and passive attachment mechanisms [80].

I.5. Conclusions

One of the main problematic in cooling circuits of power plants is biofilm formation and subsequently biofouling of metallic materials used in heat exchangers. The significant negative effects of biofouling are the marked reduction of the heat exchange capacity, and microbially-influenced corrosion (MIC), among others.

One of the major goals for the control of biofilm formation is the prevention of microbial adhesion and growth. To reach this objective, one strategy is to modify the surface properties of the metallic material in order to control the adsorption of biomolecules and therefore the formation of the conditioning film, which is the first step in biofilm formation.

The aim of this work was to understand the role of adsorbed biomolecules on electrochemical behaviour of three metallic materials (70Cu-30Ni alloy, 304L stainless steel and Titanium) and the oxide layers developed on these materials often used in heat exchangers. As 70Cu-30Ni alloy and titanium are often used in marine environments due to their high corrosion resistance, these metallic materials were studied in artificial seawater (ASW) without and with biomolecules, and filtered natural seawater (FNSW). On the other hand, 304L stainless steel is preferred in freshwaters due to its low corrosion resistance in the presence of chlorides; for this reason, this material was studied in a chloride-free solution (without and with biomolecules), keeping the same ionic strength as for artificial seawater.

For that purpose, a model protein was selected in a first step; the chosen biomolecule was the bovine serum albumin (BSA), often used to study the protein-surface interactions due to its low cost and to a good knowledge of its properties. In a second step, loosely and tightly bound EPS were extracted from a marine strain, *Pseudomonas NCIMB 2021*, and their effect on the three metallic materials was studied.

In this work, electrochemical measurements (corrosion potential (E_{corr}) vs time, polarization curves and electrochemical impedance spectroscopy (EIS)) performed during the very first

steps of oxide layers formation (1 h immersion time) were combined to surface analyses by X-ray photoelectron spectroscopy (XPS) and time-of-flight secondary ions mass spectrometry (ToF-SIMS). In cooling circuits, the water is usually circulating but, frequently, plant outages cause provisional stagnant condition that can persist for hours or, at worst, for days. This condition is of particular concern for corrosion risk, especially at the beginning of plant operation [81]. Therefore, hydrodynamics is one of the parameters to be studied (stagnant conditions, under flow and stirring, and under well-controlled hydrodynamic conditions using a rotating ring electrode (RRE)).

II. Experimental

II.1. Materials, electrolytes, biomolecules, and bacteria

II.1.1. Metallic materials

Three metallic materials were studied: 70Cu-30Ni (wt. %) alloy, 304L stainless steel and titanium (grade 2). The chemical compositions of these metallic materials are shown in Table II.1. The samples, provided by RSE S.p.A., were disks cut from new condenser tubes practically employed in industrial environments, and then flattened at Chimie ParisTech (Figure II.1). In the case of 70Cu-30Ni alloy, the effect of different hydrodynamic conditions (static conditions, under flow and stirring, and well-controlled hydrodynamics using a rotating ring electrode) on its electrochemical behaviour was studied. As we decided to work with the industrial alloy and not to buy commercial rods, only real condenser tubes were available for the experiments using the rotating ring electrode (RRE); therefore, it was necessary to design an electrode that allows using the rotating system available at LISE. The rotating ring electrode used was built from a 1 cm long condenser tube with 2.54 and 2.28 cm external and internal diameters, respectively. The tube was protected with a process of cathodic electrodeposition (or cataphoresis), and then mounted in a non-conducting epoxy resin with a metallic contact (permitting electrical connection) welded to a part of the tube (Figure II.2).

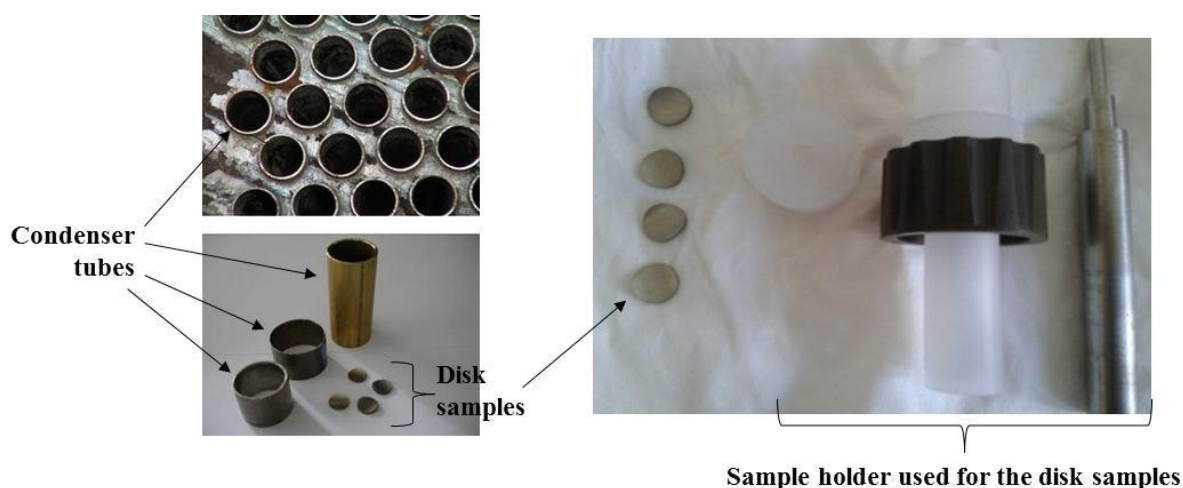


Figure II. 1: Disk electrodes, cut from real condenser tubes, and sample holder used for the measurements in static conditions, and under flow and stirring.

Table II. 1: Chemical compositions of the studied metallic materials.

Composition nominal (wt %)			
	70Cu-30Ni alloy	304L stainless steel	Titanium
Cu	Balance	-	-
Ni	29-33	8-12	-
Fe	0.80	Balance	0.30
Mn	0.80	2	-
Cr	-	18-20	-
C	-	0.03	0.10
Ti	-	-	Balance
O	-	-	0.25

For the electrochemical measurements, the geometrical surface area exposed to the solution was either 0.45 cm^2 for the experiments in static conditions and under flow and stirring, and 0.97 cm^2 for the experiments with the RRE. Before electrochemical measurements, samples were mechanically polished with SiC papers down to grade 1200, then degreased in an ultrasonic bath three times in acetone for 10 min, once in ethanol for 10 min, and once in ultra-pure water for 10 min, dried under an argon flow, and finally exposed to UV-ozone for 20 min. The disk samples (0.45 cm^2) were used for the surface analysis after polishing and after electrochemical measurements (1 h immersion at E_{corr}), and the bacterial adhesion tests. Before surface analysis, samples were mechanically polished first with SiC papers down to grade 1200, then with $6 \mu\text{m}$, $3 \mu\text{m}$, and $1 \mu\text{m}$ diamond paste. Their subsequent treatment was the same as before electrochemical measurements.

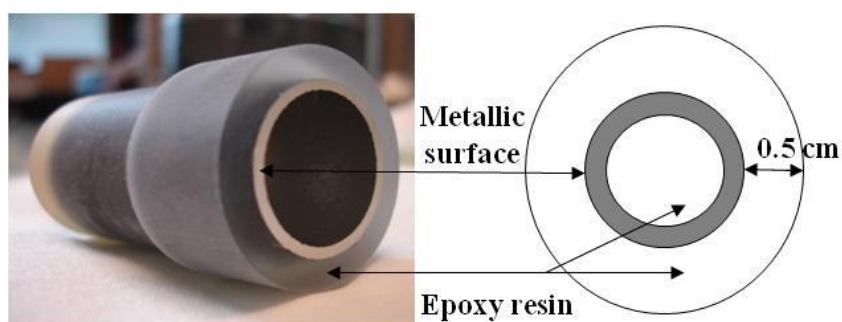


Figure II. 2: Rotating ring electrode (RRE) used for the measurements in well-controlled hydrodynamics.

II.1.2. Electrolytes

Due to the fact that the metallic materials used in this work come from real condenser tubes and that the common cooling agent used in this circuits is natural seawater, the solutions used in this work were:

- a) filtered natural seawater (FNSW) given by the industrial partner RSE S.p.A. and filtered with a pore size of 1 μ m. Although filtration removes most part of the organic matter, including bacteria, still some biomolecules may remain on the seawater;
- b) artificial seawater (ASW; composition (g.L⁻¹): NaCl (24.615), KCl (0.783), Na₂SO₄ (4.105), MgCl₂(H₂O)₆ (11.060), CaCl₂ (1.160), NaHCO₃ (0.201); pH = 8.0; ionic strength = 0.7155), without and with added biomolecules; and
- c) chloride-free solution (composition (g.L⁻¹): Na₂SO₄ (37.76) and NaHCO₃ (0.201)), without and with biomolecules, keeping the same ionic strength as ASW.

Therefore, 70Cu-30 Ni alloy and Titanium were studied in seawater alike environments; but, as 304L stainless steel is susceptible to pitting corrosion in the presence of chlorides, this material was evaluated with the chloride-free solution (see details in Chapter V). All the experiments were performed in aerated conditions at room temperature and pH 8.

II.1.3. Biomolecules

One of the main objectives of this work was to study the influence of biomolecules on the electrochemical behaviour of metallic materials often used in cooling circuits and on the surface chemical composition of oxide layers.

II.1.3.1. BSA

In a first step, the effect of bovine serum albumin (BSA), which is a model protein often used to study protein-surface interactions was studied. The concentration of BSA (~99% purity (Fraction V); Sigma Aldrich) was 20 mg.L⁻¹.

II.1.3.2. EPS extracted from *Pseudomonas NCIMB 2021*

In a second step, tightly bound (TB) and loosely bound (LB) extracellular polymeric substances (EPS) were extracted from a marine strain *Pseudomonas NCIMB 2021*. ASW

solutions were prepared with the extracted TB and LB EPS, keeping the same protein concentration in both cases (20 mg.L⁻¹).

Microorganisms are known to produce a great number of extracellular polymeric substances (EPS) with various chemical and functional properties. However, one of the problems when comparing the available data on the role of EPS in biocorrosion is the variability of methodologies used to study that effect. In addition to this lack of standard procedures for monitoring corrosion risks in the presence of EPS, the EPS isolation strategies differ significantly, resulting in a variable EPS composition.

Several extraction methods, both physical and chemical, have been proposed. Physical methods include heating, sonication, high-speed centrifugation, boiling, and use of cationic exchange resins. Among the chemical reagents, ethylenediaminetetraacetic acid (sodium edetate / EDTA), sodium hydroxide, aldehydes, phenol, sodium chloride, and crown ether (CE), have been suggested as extractants [82]–[86].

In most of the studies, only loosely bound (LB) EPS, obtained by centrifugation, have been used. However, the extraction of EPS tightly bound (TB) to the cell wall cannot be easily obtained and needs appropriate approaches [87]. Currently, the most widely used physical method for TB EPS extraction consists of employing cationic exchange resins, which results in high exopolymer yields due to the combination of two types of mechanisms: the shear forces on granules applied by the stirring, and further destabilisation of the granules structure by exchange of bivalent cations mainly with sodium ions from the resin [86], [88]. As the cells of different microorganisms might vary in resistance to physical and chemical treatments, while optimising the EPS extraction, a special attention needs to be paid to cell lysis control. This becomes especially important for a precise characterisation of EPS, since their contamination with intracellular compounds might lead to a false interpretation of results. For Gram-negative-bacteria (*Pseudomonas* case), 2-keto-3-deoxyoctonate (KDO), which is an outer membrane component, is often used as a marker for cell damage [89].

It is important to mention that a universal procedure for EPS extraction does not exist as the properties of exopolymers and, especially the susceptibility of different bacterial cells to extraction reagents can differ. Therefore, the quality of each investigation concerning EPS depends greatly on the development and use of a proper extraction procedure.

Figure II.3 illustrate the EPS extraction procedure used to extract TB and LB EPS from the chosen model bacteria (*Pseudomonas NCIMB 2021*), developed at the Biofilm Centre, University of Duisburg-Essen in Germany [87].

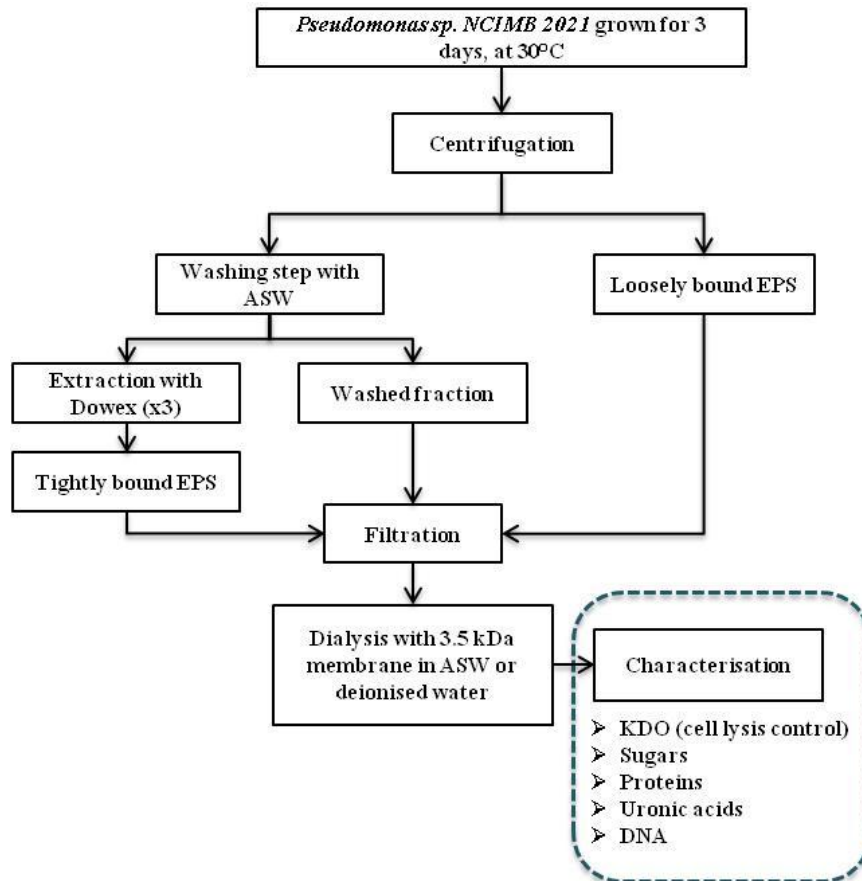


Figure II. 3: Schematic drawing of the used EPS extraction procedure [87].

Pseudomonas NCIMB 2021 bacteria were aerobically grown in 5 L sterilised fresh Marine Broth 2216 growth medium (37.4 g.L^{-1}). Medium sterilisation was achieved by autoclaving at 121°C for 30 min. The medium was inoculated with a 5% (v/v) *Pseudomonas NCIMB 2021* solution in exponential growth phase culture (initial cell number: $10^7 \text{ cells.mL}^{-1}$), and incubated for 3 days at 30°C , with gentle agitation and aeration at pH of 7.4. Once the bacteria reached the exponential growth phase, EPS extraction was performed; 1 mL of the cell suspension was taken for the positive control, and 1 mL for cell counting.

Figure II.4 (a) shows a batch *Pseudomonas NCIMB 2021* culture after 3 days of growth. This bacterial culture was centrifuged at 4°C , 7500 rpm for 12 min, to separate loosely bound EPS from tightly bound EPS (Figure II.4 (b)). After centrifugation, the supernatant was separated from the pellet and twice sterile filtered with a $0.22 \mu\text{m}$ pore size filters (Figure II.5 (a)). In

order to remove metabolites and salts of low molecular weight, filtered supernatant was dialysed overnight at 4°C using Spectra/Por 3.5 kDa dialysis tubing (45 mm width) (Figure II.5(b)). This purification was performed either in deionised water for the colorimetric assays (EPS composition analyses) or in ASW for the electrochemical measurements and the surface analysis. The membrane was activated by immersion in warm water with EDTA for 15 to 30 min. The membrane was closed with clamps and the sample was introduced into the membrane. Sterile growth medium (Marine Broth 2216) was used as a negative control and it was purified as described above. The volume of water was at least 25 times greater than the total volume of dialysed EPS. The dialysis was continued for additional 48h at 4°C, under stirring at 100 rpm. Water was changed 3 times a day. Afterwards aliquots of LB EPS were stored at -20°C for further use.

Harvested cell pellet (Figure II.6(a)) was washed with mediums mineral solution (ASW in this case) and weighted. For that, 20 mL of saline solution were added to the pellet to remove residues from the medium, avoiding pouring the solution directly to the pellet. The pellet was then transferred to the Falcon tubes (previously weighted) and centrifuged using the same conditions as for the first centrifugation. The supernatant (saline solution) was filtered and the falcon tube with the pellet weighted.

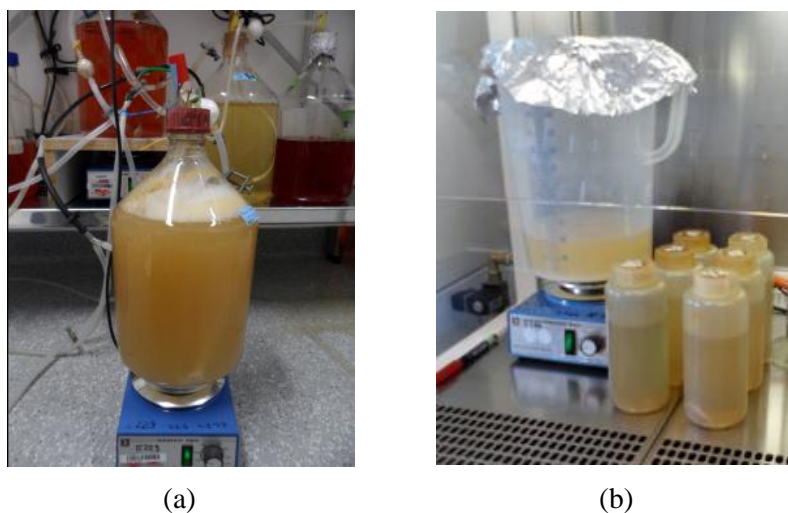


Figure II. 4: (a) *Pseudomonas* NCIMB 2021 culture after 3 days of growth and before the EPS extraction; (b) separation of loosely bound EPS from tightly bound EPS after the centrifugation step.

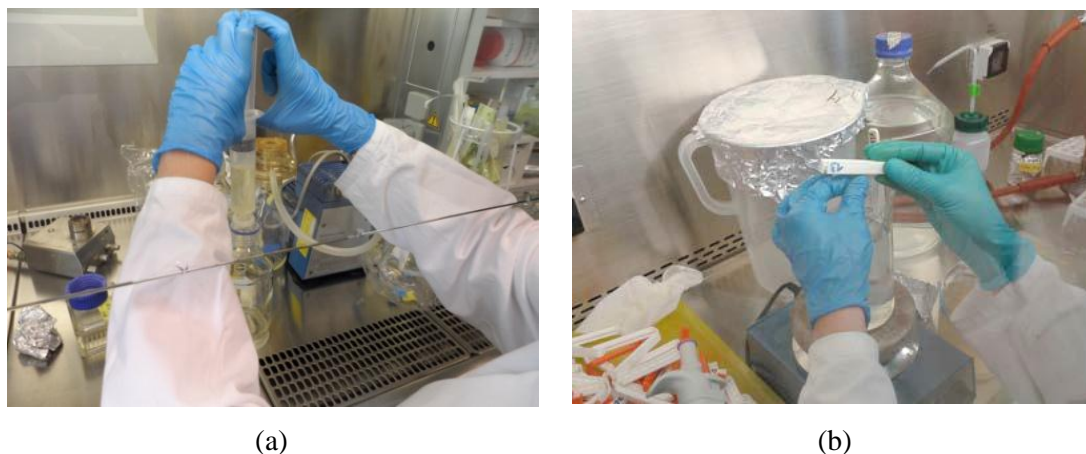


Figure II. 5: (a) Filtration of the supernatant obtained after centrifugation; (b) dialysis step using Spectra/Por 3.5 kDa dialysis tubing.

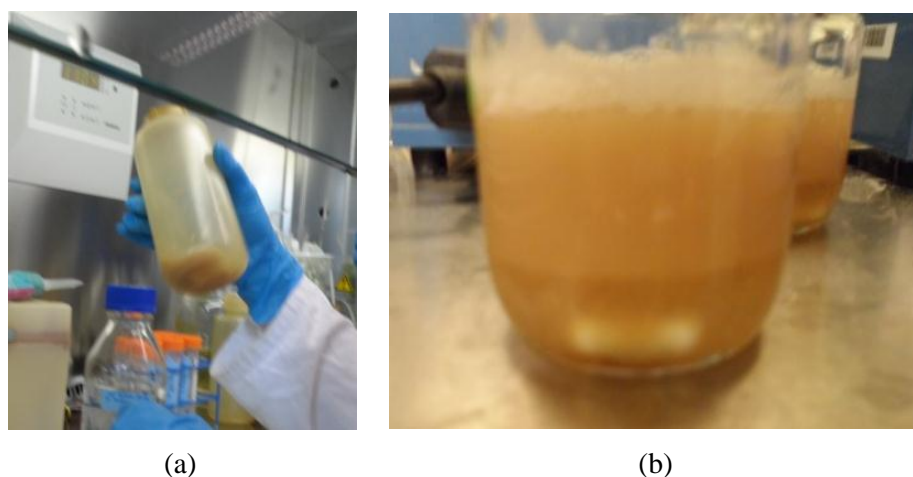


Figure II. 6: a) Cell pellet obtained after centrifugation; and b) tightly bound EPS during Dowex treatment.

The night before the extraction of TB EPS, Dowex® Marathon™ C cation exchange resin, Na⁺ form, 20–50 mesh size, was activated by addition of 20 mL of phosphate buffer solution (PBS) to 10 g of Dowex and kept agitated at 4°C overnight. Once the Dowex was activated, the PBS solution used for this purpose was discarded.. For TB EPS extraction, the pellet was resuspended in PBS, added to the activated Dowex and kept stirred for 2 h at 4°C. Figure II.6(b) shows the cell pellet twice treated with Dowex and PBS. For the negative control, 10 mL of sterile marine broth medium was added to 10 g of Dowex and 20 mL of PBS.

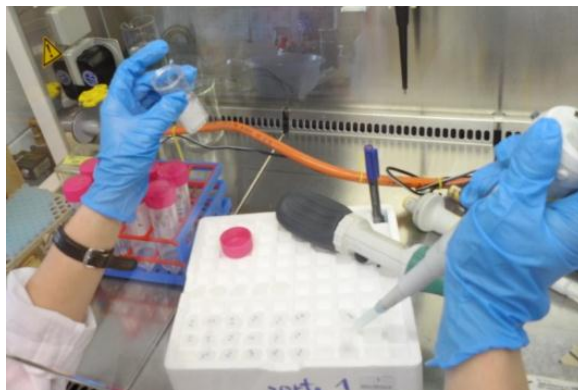


Figure II. 7: Purification and concentration of tightly bound EPS using Amicon tubes.

EPS had to be purified from the buffer and any organic compound, which could give a positive signal in any of the colorimetric determinations (EPS composition analyses). Tightly bound EPS was purified by adding 1 mL of solution to each Amicon tube (3 kDa Molecular Weight Cut Off -MWCO- dialysis membrane, Millipore) (Figure II.7)), according to the manufacturer's protocol, and completed with 11 ml of filtered deionized water (for the EPS characterisation) or ASW (for the electrochemical measurements and surface analysis). TB EPS was centrifuged for 40 min at 4200 rpm and 4°C. This procedure was repeated 3 times. The EPS was collected in Eppendorf tubes for the analysis.

All EPS aliquots were stored at -20°C and thawed prior to analysis. Pure and sterile growth medium was also investigated. All colorimetric analyses were carried out at least in triplicates for each determined parameter, using chemicals of analytical grade. For the determination of absorbance, Varian Cary 50 Bio UV/Visible spectrophotometer was used. Absorbance was measured against water, and converted to concentration by use of calibration standards for each method. Phenol-sulphuric acid method was used for the determination of polysaccharide content [90], with glucose as a standard. Uronic acids levels were determined as described by Filisetti-Cozzi and Carpita [91], with glucuronic acid as a standard. Introduction of sulfamate and diphenyl reagent in the protocol allows the measurement of analysed molecules without the interference from neutral sugars. Extracellular DNA was determined as described by Burton [92], with DNA from salmon sperm as a standard. Protein concentration was estimated as described by Bradford [93], with bovine serum albumin (BSA) as a standard.

Cell lysis might occur when EPS is extracted. An ideal EPS extraction method should result in obtaining the highest EPS yield causing minimal cell lysis [56]. However, the extent of cell lysis during extraction is difficult to evaluate. Some studies have taken the protein or nucleic

acids content in EPS as an indicator for cell lysis. As the nucleic acids content in EPS is usually low, a high level after the EPS extraction indicates severe cell disruption [56]. In order to determine the cell lysis level in extracted EPS, the 2-keto-3-deoxyoctanate (KDO) concentration was determined as described elsewhere [94]. KDO was used as a standard. In addition, a positive control with a defined amount of disrupted cells was analysed for its KDO content. Cell preparation and damage was performed as for DNA extraction. Obtained KDO values were further used to calculate the percentage of cell lysis in extracted EPS.

Table II. 2: Composition of EPS extracted from the marine strain *Pseudomonas NCIMB 2021*.

Composition [mg.L ⁻¹]	Proteins	Sugars	DNA	Uronic acids
Negative control	9.3	89.7	0.4	3.7
Tightly bound EPS	4187.6	640.1	1.0	25.0
Loosely bound EPS	20.6	50.0	0.3	4.0

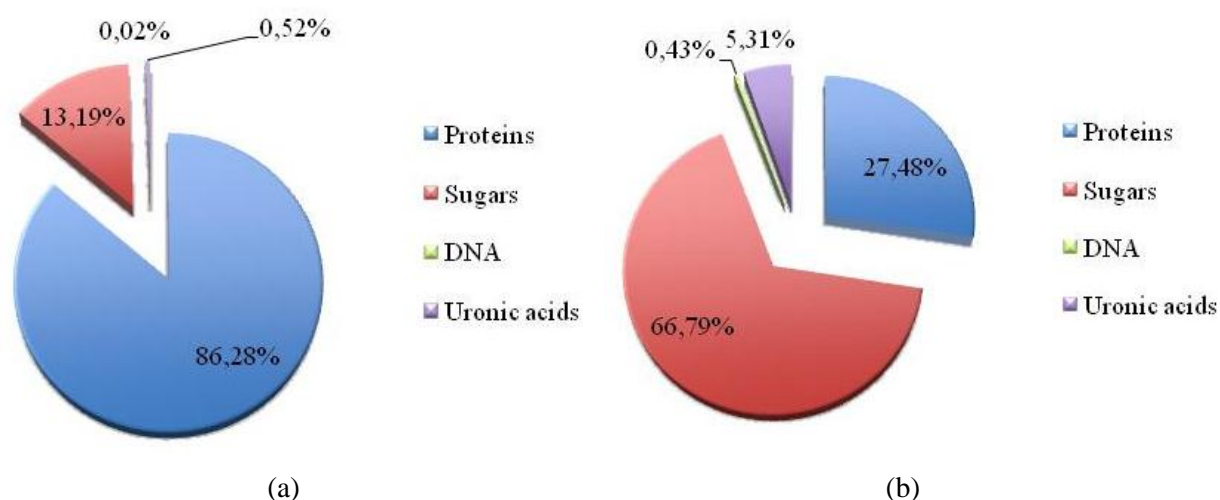


Figure II. 8: Pie chart illustrating the weight percent of biomolecules for: (a) TB EPS and (b) LB EPS.

Table II.2 presents the composition of EPS from *Pseudomonas NCIMB 2021* and the negative control. In this table, proteins appeared to be the main components of TB EPS, whereas sugars seem to be dominant in LB EPS and in the negative control. Sugars level was ten times higher than proteins level in the negative control while this ratio is about 2 in the loosely bound EPS. Figure II.8 allows better visualizing the biomolecules distribution in TB and LB EPS.

II.2. Experimental techniques

II.2.1. Electrochemical measurements

When a metallic material takes part as electronic conductor in the presence of an aqueous media, the corrosion phenomenon occurs and is usually of electrochemical nature, and therefore the use of electrochemical techniques is essential for the study of this process.

The use of electrochemical techniques for the study of corrosion has the advantage of providing results in a relatively short period of time, in comparison with the traditional weight loss measurements, and allows elucidating mechanistic information about the processes being studied [26]. The basis of electrochemical techniques consists in maintaining constant all the parameters that determine the state of the metal/solution interface (*e.g.* temperature, pressure, area), and i) applying an input potential (DC or AC), and measuring the output current (or vice versa); or ii) measuring the spontaneous potential or current fluctuations of the system without applying any perturbation [26], [95].

II.2.1.1. Electrochemical cell

The electrochemical cell is the place in which physical/chemical reactions occur with different degrees of complexity. It may consist of two, three or four electrodes immersed in an electrolyte which acts as an ionic conductor and is contained in a vessel (Figure II.9).

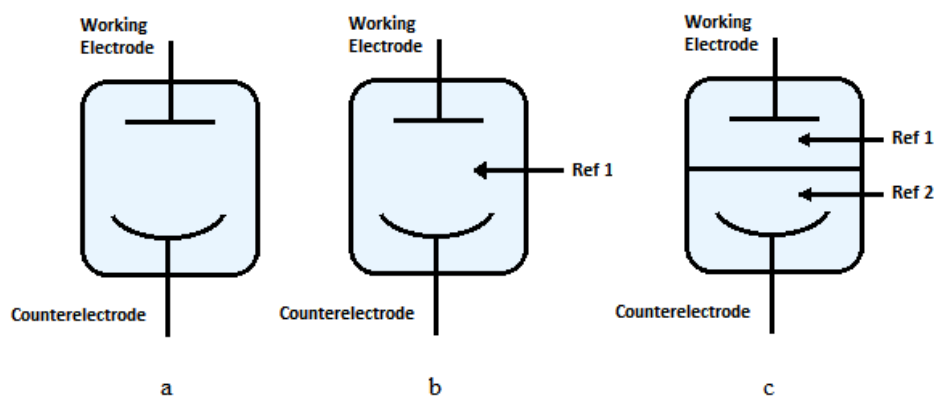
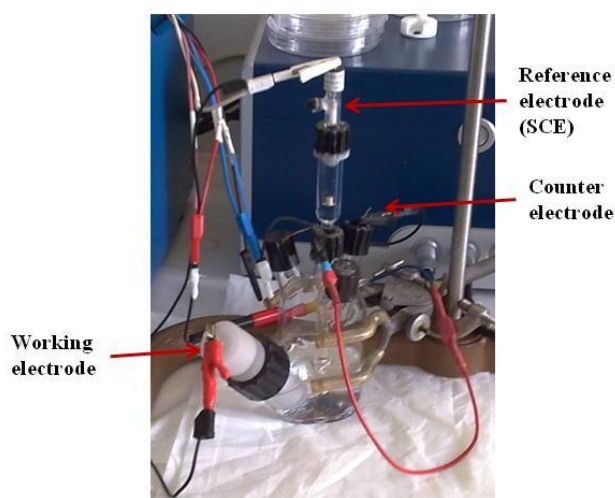


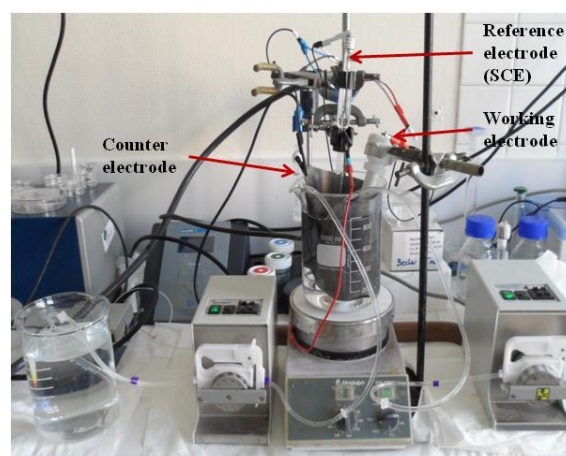
Figure II. 9: Schematic drawings of different cell configurations: a) 2-electrode; b) 3-electrode; and c) 4-electrode cell design.

Proper cell design is essential to reduce the uncertainty in data analysis. In some cases, mass transport needs to be controlled and for this purpose, rotating disk, rotating cylinder or rotating ring working electrodes can be used, allowing the control of hydrodynamics [26], [95], [96].

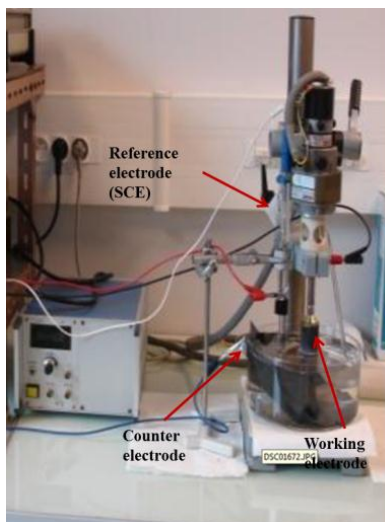
The electrochemical measurements were performed with a three-electrode cell, represented in Figure II.9(b), designed and manufactured at Chimie ParisTech. The volume of the solution was about 0.1 L for the experiments in static conditions, and about 1 L for the experiments under flow and stirring and using the rotating ring electrode. The working electrodes were the metallic materials already described (section II.1.1), the counter-electrode was either a platinum wire or a graphite sheet, and the reference electrode was a saturated calomel electrode (SCE; 0.245 V *vs* SHE). Most of the experiments were carried out in static conditions (static working electrode and solution) (Figure II.10(a)), but as mentioned before, in the case of 70Cu-30Ni alloy, some experiments were performed under flow and stirring (Figure II.10(b)), and others in well-controlled hydrodynamic conditions, using a rotating ring electrode (Figure II.10 (c)).



(a)



(b)



(c)

Figure II. 10: Different electrochemical cells used in this work: a) static conditions, b) under flow and stirring and c) using the rotating ring electrode.

II.2.1.2. Instrumentation

The DC transient response of an electrochemical system is usually measured using a potentiostat. In the case of Electrochemical Impedance Spectroscopy (EIS) an additional perturbation is added to the DC signal in order to obtain the frequency response of the system.

The impedance of the system may be measured using various techniques: a) ac bridges, b) Lissajous curves, c) phase sensitive detection (PSD), d) frequency response analysis (FRA) and e) fast Fourier transform (FFT). Frequency response analyzers (FRAs) are instruments which determine the frequency response of a studied system, and the corresponding method is a single-sine method in which a small AC wave, of 5 to 15 mV amplitude and of a given frequency, is overlaid to a desired DC bias potential applied to the working electrode; an AC current is then measured. This process is repeated by scanning the frequency and by computing the impedances from the AC voltage and current data at given frequencies (typically five to ten measurements per frequency decade). Modern FRAs carry out all the computations digitally, and offer a wide frequency range (12 decades) and a high precision [97], [98].

In this work, electrochemical measurements were performed with an EC-Lab SP-200 system from Bio-Logic (Figure II.11). This potentiostat provides 12 V compliance, ± 10 V reference

control. The current ranges available for the standard board is 10 nA to 500 mA; however the low current sensitivity can be improved using the ultra low current option (down to 1 pA current range with 76 A resolution) and for the ultra low current cable, it is from 1 pA to 500 mA. A range of nine intelligent bandwidths ensures the stability of the SP-200 series in a wide variety of experimental conditions. Electrochemical Impedance Spectroscopy (EIS) measurements can be added as an option to the SP-200 series. The built-in FRA has a frequency range of 10 μ Hz up to 7 MHz. [99].

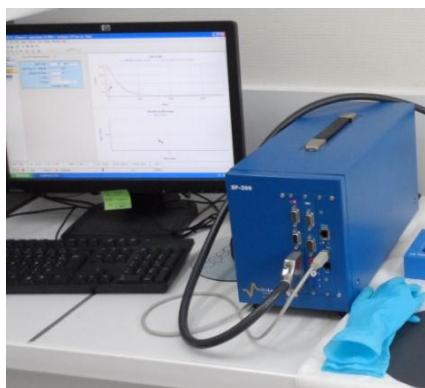


Figure II. 11: EC-Lab SP-200 system from Bio-Logic.

The instrument is driven by EC-Lab® software. The EC-Lab® software, supplied with the potentiostat, is a multifeatured software package. It provides a wide range of techniques and applications that can be sequenced and/or linked to design any experiment. A variety of analysis tools are available for electro-analytical and corrosion data, as well as equivalent circuit modeling for impedance data analysis [99].

II.2.1.3. E_{corr} vs time

The corrosion potential (E_{corr}) is also referred as free potential or open circuit potential. The E_{corr} vs time technique consists in measuring the potential difference, at zero net current, between the working electrode and the reference electrode (saturated calomel electrode, SCE) immersed in an electrolyte, as a function of time. The electrochemical response will be dependent on the nature and chemical composition of the material under study (working electrode), the electrolyte, the temperature, and the hydrodynamics. This technique does not provide mechanistic information and it is recommended to use it with other electrochemical techniques such as polarisation curves and/or electrochemical impedance spectroscopy [26], [100].

In this work, the corrosion potential was measured during the first hour of immersion before plotting a polarisation curve or an impedance diagram.

II.2.1.4. Polarisation curves

A DC polarisation scan consists in studying an electrochemical system by investigating the current-voltage relationship. The polarisation curves can be plotted either by imposing discrete and successive values of a controlled variable (current or potential), or by imposing a linear voltage ramp with a given scan rate. If the scan rate is sufficiently slow, pseudo steady-state curves are obtained. It is important to select the appropriate variable to be controlled; it depends on the current-voltage characteristics of the system and the involved reaction mechanisms, as well as on the information expected from the measurement [95], [100]. Potentiodynamic scans, also called current-potential curves or polarisation curves, provide considerable information about electrode processes. Polarisation curves provide information on the corrosion rate, pitting susceptibility, passivity, as well as on the cathodic behaviour of an electrochemical system. The working electrode is an anode if oxidation takes place and a cathode if reduction takes place [101].

As mentioned before, electrochemical processes require an anode, a cathode, and an ionic and electronic conduction path between the two, to take place. In electrochemical measurements, the ionic conduction path is provided by the electrolyte separating the working and counter electrodes, while the electrical conduction path is provided by the potentiostat [101].

The charge transfer processes induce oxidation and reduction reactions, which obeys Faraday's law. Therefore, the processes which lead to charge transfer are called Faradaic processes. The thermodynamic tendency for an electrochemical reaction to occur is determined by the free energy change associated with that reaction, and hence by the potential; therefore the potential is a thermodynamic property and a state function which means that the free energy change for a given reaction depends only on the initial and final states, and not on the path taken by the reaction. A change in the magnitude of the energy associated to the reaction provides information on whether or not a reaction can occur, and it cannot be used to predict the rate at which the reaction will take place. On the other hand, in a potentiodynamic experiment, the current represents the rate with which the anodic or the cathodic reactions take place on the working electrode. Typically, the current is expressed in terms of current per unit area [95], [101]. In addition to these Faradaic processes, non-

Faradaic processes have to be taken into account when electrochemical behaviour has to be interpreted [95]. A polarisation curve shows two different domains: the cathodic part due to reduction reactions, and the anodic part due to oxidation reactions.

In a cathodic polarisation scan, depending on the pH and dissolved oxygen concentration in the solution, the shape can illustrate the oxygen reduction reaction. This reaction is limited by how fast oxygen may diffuse in solution. A decrease of the applied potential to sufficiently cathodic values, may lead to other cathodic reactions such as the hydrogen evolution reaction (also known as water reduction reaction) or the reduction of oxides present on the electrode surface [101]. On the other hand, the shape of an anodic polarisation curve may show active metal dissolution, metal passivation, pitting corrosion, or transpassive dissolution. Additionally, when the current becomes independent of potential, this indicates either a total limitation of the reaction by mass transport, or a passivation of the electrode (visible on the anodic curve) [95].

Cathodic or anodic polarisation curves were plotted separately starting from +20 or -20 mV vs E_{corr} , respectively, and using a scan rate of $0.5 \text{ mV}\cdot\text{s}^{-1}$.

II.2.1.5. Electrochemical Impedance Spectroscopy (EIS)

II.2.1.5.1. Principle

Electrochemical Impedance Spectroscopy (EIS) consists in analyzing the frequency response of an electrochemical system to an AC signal in a transient function between an input signal (*e.g.* voltage) and an output one (*e.g.* current). Therefore, impedance experiments involve the conversion of time-domain input and output signals into a complex quantity that is a function of frequency. The input signal and the resulting output signal is processed by instrumentation to yield the frequency-dependent transfer function. Fourier analysis and phase-sensitive detection are commonly used to convert time-domain signals into the frequency domain [96].

Initially, EIS methods were applied to the determination of the double-layer capacitance and in AC polarography; nowadays, they are applied to the characterisation of electrode processes and complex interfaces. The advantages of EIS technique are, among others: it is a non intrusive technique, a big amount of mechanistic information can be obtained, it offers high precision measurements, it allows performing measurements in a wide range of frequencies,

and semi conductive, poorly-conductive, or non-conductive systems can be studied. EIS is a very sensitive technique and it must be used with great care. Besides, it is not always well understood due to the complexity of the results [26], [102].

Four conditions must be fulfilled, in order to have valid electrochemical impedance measurements [97]:

- a) **Linearity:** A system is linear when its response to a sum of individual input signals is equal to the sum of the individual responses. This also implies that the system is described by a system of linear differential equations. Electrochemical systems are usually highly nonlinear and the impedance is obtained by linearization of equations for small amplitudes. Therefore, the applied AC amplitude must be small enough so that the response of the cell can be assumed to be linear, in first approximation, but still large enough to measure a response;
- b) **Stability:** the overall state of the system must not change significantly during the acquisition of the data. A stable system remains stable unless excited by an external source and it should return to its original state once the perturbation is removed. The choice of the frequency range and measurement conditions have an influence on this condition;
- c) **Causality:** the measured AC response of the system must be entirely determined by the applied AC perturbation. The shielding of the cell from outside perturbations is important in this case; and
- d) **Finiteness:** the real and imaginary components of the impedance must be finite-values over the entire frequency range.

The application of an electrical perturbation (current, potential) to an electrochemical system induces the appearance of a response (potential, current). In the case of EIS the perturbation is a sinusoidal signal (Figure II.12).

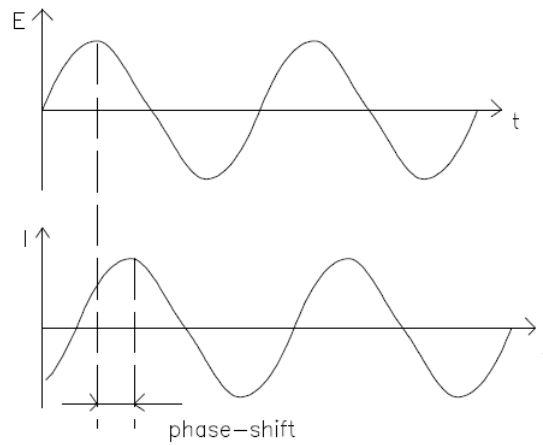


Figure II. 12: Sinusoidal AC potential with the current response phase shifted.

The optimal perturbation amplitude depends on the polarisation curve for the system under study (Figure II.13). For systems exhibiting a linear current-voltage curve, very large amplitude can be used. On the contrary, for systems exhibiting very nonlinear current-voltage curves, much smaller amplitude is needed. Therefore, the correct amplitude represents a compromise between the desire to minimize nonlinear response, and the desire to minimize noise in the impedance response [96].

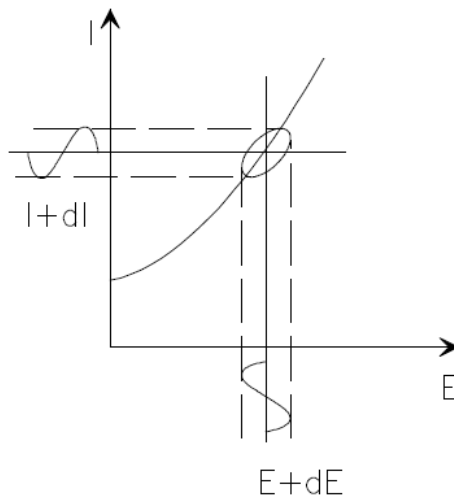


Figure II. 13: Lissajous plots for a system with potential perturbation amplitude dE .

If potential regulation is used, the potential perturbation has the form:

$$E(t) = E_0 \sin(\omega t)$$

Eq. II.1

where E_0 is the potential amplitude, $\omega = 2\pi f$ the radial frequency in rad/s, and f the frequency in Hz. The obtained response for each frequency is a sinusoidal current:

$$I(t) = I_0 \sin(\omega t + \varphi) \quad \text{Eq. II.2}$$

where φ is the phase shift and I_0 the current amplitude only if the system has a linear behaviour [26], [96], [100], [102]. Thus, the impedance, which is the inverse of the transfer function, takes the following form:

$$Z(\omega) = \frac{\tilde{E}(\omega)}{\tilde{I}(\omega)} = |Z(\omega)|e^{j\varphi} = Z'(\omega) + jZ''(\omega) = |Z|(\cos\varphi + j\sin\varphi) \quad \text{Eq. II.3}$$

where $\tilde{E}(\omega)$ and $\tilde{I}(\omega)$ are the complex potential and current, and j is the imaginary number defined as $\sqrt{-1}$.

The modulus of the impedance, $|Z|$, has units of a resistance and is equal to:

$$|Z| = \frac{E_0}{I_0} \sqrt{(Z')^2 + (Z'')^2} \quad \text{Eq. II.4}$$

and its phase shift, φ , is equal to:

$$\varphi = \tan^{-1} \frac{Z''}{Z'} \quad \text{Eq. II.5}$$

Two kinds of plots are frequently used in EIS. Figure II.14(a) presents the complex plane plots (also known as Nyquist plot), which consists in plotting the opposite of the imaginary part versus the real part of the impedance (Z'' vs Z'), plotted for various frequencies. This plot tends to give characteristic behaviours such a semi-circles or slopes, according to the phenomena taking place in the electrochemical system, and is often used in the electrochemical literature. However, it does not show all details [95].

On the other hand, Figure II.14(b) shows the Bode plots which illustrate the frequency response of the system; this plots, with the frequency as an explicit parameter, contain information complementary to that extracted from Nyquist plot. In this representation, the logarithm of the modulus and the phase-angle of the impedance are plotted versus the logarithm of the frequency [95]. In recent years, other representations have been reported, allowing visualising and extracting more information from impedance data. For example, the

imaginary part of the impedance versus the frequency has the significant advantage that the characteristic frequencies can be readily identified at the peak values. Besides, the imaginary part of the impedance is independent of electrolyte resistance, so correction for ohmic resistance is not needed [103].

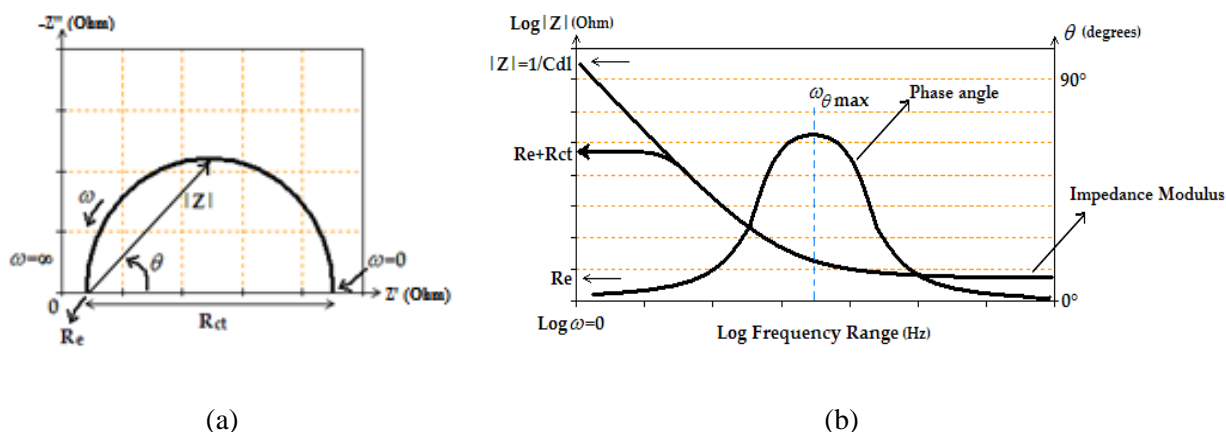


Figure II. 14: Graphical representations commonly used in EIS: a) Nyquist plot, and b) Bode plots [26].

EIS measurements should be carried out over a wide frequency range in order to identify all the phenomena involved in the electrochemical response. For example, at high frequencies the resistance of the electrolyte can be detected, while at low frequencies diffusion and adsorption/desorption phenomena can be identified [102]. Artefacts are ubiquitous to electrochemical impedance measurements at sufficiently high frequency. These artefacts, which are more intense by low conductivity solution, can arise from the measurement electronics, the reference electrode, the electrical leads, the electrochemical cell, or a combination thereof. With modern systems, frequencies up to 1 MHz can be reached. The lowest frequency typically used is 10^{-3} Hz. As the measurements at low frequencies take much longer time than at higher frequencies, the low frequency limit is connected with the possible changes in the state of the electrode during this long-period measurement [97].

In this work, electrochemical impedance diagrams were plotted at E_{corr} after 1 h of immersion, with a frequency domain ranging from 10^5 Hz down to 10^{-3} Hz, 7 points per decade, and amplitude of 10 mV peak-to-peak.

II.2.1.5.2. Impedance data analysis

The aim of the analysis of EIS data is to elucidate the electrode process. The analysis of impedance results has been usually performed using models or equivalent electrical circuits. Thus, the modelling may be classified as: a) process modelling, and b) formal or mathematical modelling. Process modelling links measured impedance with physico-chemical parameters of the process (kinetic parameters, concentrations, diffusion coefficients, sample geometry, hydrodynamic conditions, etc.). Formal or mathematical modelling explains the experimental impedances in terms of mathematical functions in order to obtain good fit between the calculated and the experimental impedances. In the latter case, the obtained parameters do not necessarily have a clear physical meaning and hence, sometimes it is difficult to justify this approach for complex systems. In general, it is possible to write the expression for the impedance for any mechanisms [96], [102].

The total electrode impedance includes the contribution of the electrolyte, and that of the electrode/electrolyte interface. An ideally polarisable electrode behaves as an ideal capacitor because there is no charge transfer across the electrode/electrolyte interface. In this case, the equivalent electrical circuit consists of the solution resistance, R_e , in series with the double-layer capacitance, C_{dl} [96], [97].

On solid electrodes, deviations from ideal behaviour are often observed; thus, the experimental impedance cannot be always represented by simple R-C-L circuits. The impedance may often be represented by an equation without simple electrical representation, through so-called distributed elements. The Warburg impedance is an example of distributed element.

In the case of an ideal ideally polarisable electrode, the impedance response is represented as a series connection with the solution resistance and the double-layer capacitance, which produces a straight line, perpendicular to the real axis, on the complex plane (Nyquist plots). However, on solid electrodes, a straight line with an angle lower than $\pi/2$ is often observed. In order to describe such behaviour, a model of distributed time constants was proposed. Such distributions can be attributed to a distribution of time constant either along the area of the electrode (surface distribution) or along the axis normal to the electrode surface (normal distribution). A surface distribution could arise from surface heterogeneities (grain boundaries, crystal faces on a polycrystalline electrode, etc.), or from geometry-induced non-

uniform current and potential distributions. A normal distribution may be attributed to changes in the conductivity of films of porosity [104]. The impedance response reflecting this distribution of time constant is commonly represented in equivalent electrical circuits as a CPE, which is a constant phase element, and its impedance is expressed in terms of model parameters α and Q as:

$$Z_{CPE}(\omega) = \frac{1}{Q(j\omega)^\alpha} \quad \text{Eq. II.6}$$

where $\omega = 2\pi f$ is the angular frequency (in s^{-1}). When $\alpha = 1$, the parameter Q has units of capacitance; otherwise, Q has units of $\Omega^{-1} \cdot \text{cm}^{-2} \cdot \text{s}^\alpha$ or $\text{F} \cdot \text{cm}^{-2} \cdot \text{s}^{(\alpha-1)}$.

The equation may represent pure capacitance for $\alpha = 1$, Warburg impedance for $\alpha = 0.5$, pure resistance for $\alpha = 0$ and pure inductance for $\alpha = -1$. Brug *et al.* presented a method for the estimation of the average double-layer capacitance [105].

EIS is a very sensitive technique but it does not provide a direct measure of the physical phenomena, or any chemical information about the electrode/electrolyte interface. Therefore, other experiments (DC, transients) should also be carried out, together with surface analysis in order to have a good knowledge of the system.

II.2.2. Surface analysis

Metallic materials were analyzed by XPS and ToF-SIMS: 1) after polishing, 2) after 1 h of immersion at E_{corr} in ASW without biomolecules, and 3) after 1 h of immersion at E_{corr} in ASW with biomolecules (BSA, TB EPS and LB EPS). After the electrochemical measurements, the samples were gently dipped in ultra-pure water three times to remove the biomolecules loosely bound to the surface, then dried with argon before introduction in the fast-entry lock chamber of the XPS spectrometer.

II.2.2.1. X-ray Photoelectron Spectroscopy (XPS)

II.2.2.1.1. Principle

Surface analysis by X-ray photoelectron spectroscopy (XPS), also known as electron spectroscopy for chemical analysis (ESCA), allows investigating thin layers formed or

adsorbed on the surface of a material. It may be applied to surface chemical analysis of minerals, catalysts, metals and polymers as well as living systems such as biofilms [87], [106].

The principle of the XPS technique is the emission of free electrons from atoms A by absorption of photons with a given energy $h\nu$ (X radiation), where h is the Plank's constant and ν the frequency of the electromagnetic radiation/wave.



In the above reaction, A^{+*} is an ion in an excited state. Photoelectron emission occurs when a photon transfers its energy to an electron, and a photoelectron can be emitted only when the photon energy is larger than the binding energy of the electron. The emitted electrons have a kinetic energy, E_k , given by:

$$E_k = h\nu - E_b - \phi_s \quad \text{Eq. II.8}$$

where E_b is the binding energy of the atomic orbital from which the electron originates and ϕ_s is the spectrometer work function, which corresponds to the required work to bring the electron from the zero attraction to the entrance of the energy analyzer; the value of ϕ_s is constant and characteristic of the spectrometer.

The sample is often irradiated with a monochromatic X-ray beam, usually Mg $K\alpha$ (1253.6 eV) or Al $K\alpha$ (1486.6 eV). XPS is similar to Auger Electron Spectroscopy (AES) in the way that it is the kinetic energy of the photoelectrons emitted from the sample surface that is analysed. The relaxation energy can dissipate either as an x-ray photon or it can be given to a second electron, an Auger electron. Since the emission of x-ray photons is low in the energy range used in XPS, photoionisation normally leads to two emitted electrons: a photoelectron and an Auger electron [106]. Figure II.15 shows an schematic illustration of the process of photoelectron ejection.

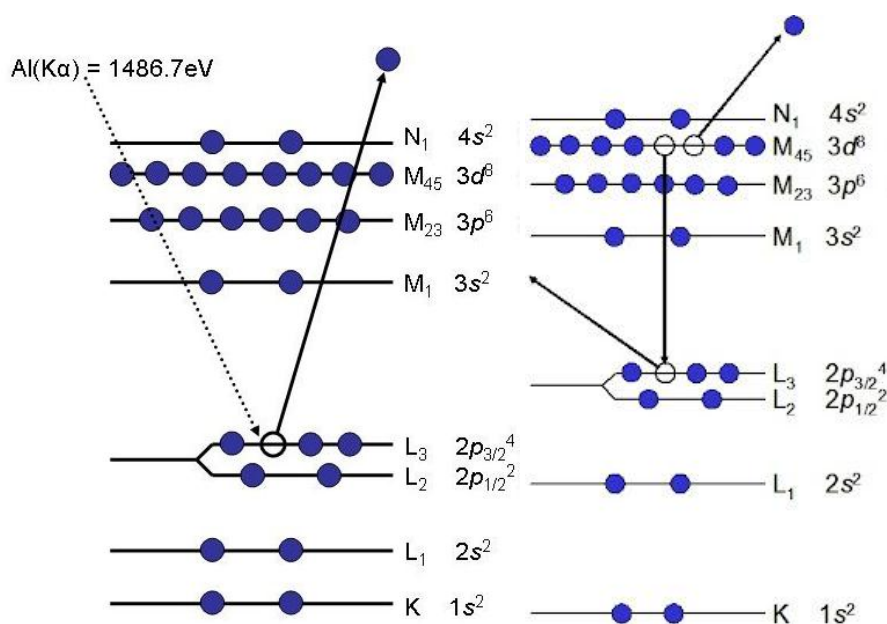


Figure II. 15: Diagrams of the photoelectric process (left) and the auger process (right).

The Fermi level corresponds to a zero binding energy (by definition), and the depth beneath the Fermi level (E_f) in Figure II.15 indicates the relative energy of the ion remaining after electron emission, or the binding energy of the electron. The binding energy may be regarded as ionization energy of the atom for the particular core level involved. The chemical state of elements can be determined due to the sensitivity of binding energies of electrons from core level to the nature of chemical bonds in which they are involved [106], [107].

For conducting samples, the positive charge developed at the sample surface by the photoemission process is immediately compensated by an electron flux. On the contrary, for insulators (as many biosystems and related materials), neutralization is only partial and a significant net positive charge accumulates at the surface (varying typically from several eV to several tens of eV); in that case, the kinetic energies of the photoelectrons are decreased by the same amount. Instability of reference charge may lead to a peak broadening, peak distortion or peak shift during the analysis. This means that the Fermi levels of the sample and the spectrometer are no longer in equilibrium, resulting in an unknown surface potential. Charge stabilization is achieved in different ways, depending on the manufacturer and on the X-ray source which used [106], [108].

II.2.2.1.2. Instrumentation

A basic scheme of an XPS spectrometer is given in Figure II.16. An XPS spectrometer is made up of at least two chambers, one to introduce samples and a second one to proceed the analysis, the later being always kept under ultra high vacuum. Chambers are made of stainless steel with a series of valves and windows. High vacuum is maintained, thanks to knife-edge flanges, which are compressed against copper gaskets. Electron trajectories are screened from earth magnetic field by using a metal with high magnetic permeability for internal walls of the analysis chamber. Additional chambers can also be added to allow sample pre-treatment or parking [106].

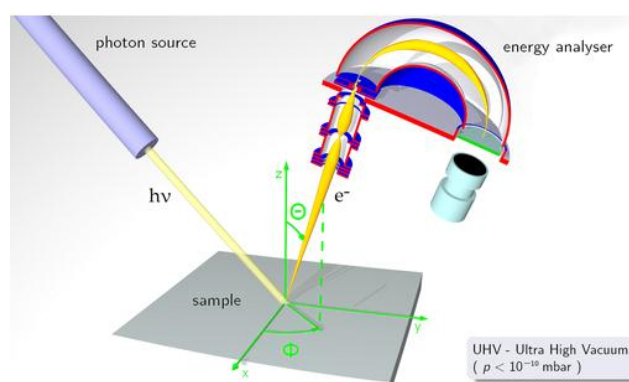


Figure II. 16: Schematic drawing of an XPS spectrometer.

XPS analyses were performed with a Thermo Electron Escalab 250 spectrometer, this equipment consist of three different chambers: a) fast entry air lock (FEAL), b) a “Preploc” chamber, and c) an analysis chamber. The FEAL chambers is the place where samples are introduced into the system and it is not a UHV chamber, due to the frequent exposure to the atmosphere, but it is capable of pumping down to 10^{-6} mbar using a proper turbo pump. The samples are transfer from the FEAL chamber to the “Preploc” chamber through a sample transfered mechanism onto which specimen holders are loaded and held by a robust spring-loaded mechanism via the gate valve. The “Preploc” chamber is a UHV chamber equipped with three sample holders, where samples can be stored; this chamber is also equipped with a sample transfer mechanism equivalent to that of the FEAL chamber, allowing moving samples to the analysis chamber via the gate valve [107].

For the XPS measurements a monochromatised Al $K\alpha$ X-ray source (1486.6 eV) was chosen. The analyser pass energy was 100 eV for survey spectra and 20 eV for high resolution

spectra. The spectrometer was calibrated using Au 4f_{7/2} at 84.1 eV. All spectra were referred to the C 1s peak for carbon involved in C-C and C-H bonds, located at 285 eV [109].

II.2.2.1.3. Data processing

Data processing was performed with the Thermo Electron software “Avantage”. The peak decomposition was performed using the recorded high resolution spectra. For that purpose, an appropriate background had to be chosen. The Avantage software offers three background subtraction methods: linear, Shirley and Tougaard. In this work, the selected method was the Shirley background subtraction, which is the most widely used method.

After the definition of the peak energy range, the following step consists in separating the peak into signal components by peak fitting. Peak fitting requires the knowledge of the energy position and the shape of individual peaks. These parameters can be obtained by comparison with spectra of standard compounds or by consulting the literature on XPS investigation. The peak shape as well as the peak position can be changed, using Avantage software, by modifying the following parameters: peak centre in eV (binding energy), peak height in counts per second (cps), Full Width Half Maximum in eV (FWHM), and Lorentzian-Gaussian (L/G) mixing ratio in %. In addition, the software offers the possibility of using asymmetric peak shape, and tailing functions. Once peak decomposition is done, the software calculates the peak intensity by integrating the area under the peak.

The integral intensity of photo-electrons emitted by an element N in a matrix M (I_N^M), depends on the specific parameters related to the spectrometer and the sample, and is given by the following equation [16], [106], [107]:

$$I_N^M = kT(E_k)\sigma_N \int D_N^M(z) \exp\left(\frac{-z}{\lambda_N^M \sin\theta}\right) dz \quad \text{Eq. II.9}$$

with:

k : spectrometer specific constant that includes the X-ray flux, the analyzed area and the yield of the detector;

$T(E_k)$: transmission function of the energy analyzer, which depends on the kinetic energy of photoelectrons emitted by the analyzed element;

σ_N : photo-ionization cross-section for an element N and for a given core level;

D_N^M : density of an element N in a matrix M;

z: depth analysed;

λ_N^M : attenuation length of photoelectrons (inelastic mean free path (IMFP)) emitted by a given core level of an element N in a matrix M;

θ : take-off angle of photoelectrons with respect to the sample surface.

Assuming homogeneous distribution of an element N, with density D_N^M , in an infinitely thick sample, Eq. II.9 simplifies to:

$$I_N^{M,\infty} = kT(E_k)\sigma_N D_N^M \int_0^\infty \exp\left(\frac{-z}{\lambda_N^M \sin\theta}\right) dz \quad \text{Eq. II.10}$$

which after integration becomes:

$$I_N^M = kT(E_k)\sigma_N D_N^M \lambda_N^M \sin\theta \quad \text{Eq. II.11}$$

The intensity can be attenuated by the formation of a thin surface layer of homogeneous composition. The following equation describes the attenuation of the signal of an element N in a substrate matrix M by a thin film F formed on top of thickness d:

$$I_N^M = kT_N(E_k)\sigma_N D_N^M \lambda_N^M \exp\left(\frac{-d}{\lambda_N^{MF} \sin\theta}\right) \quad \text{Eq. II.12}$$

M_s : Substrate matrix

M_f : Film matrix

The attenuation-coefficient is given by this equation:

$$A_i = \exp\left(\frac{-d_i}{\lambda_i \sin\theta}\right) \quad \text{Eq. II.13}$$

In this work, the inelastic mean free path values were calculated by the TPP2M formula [110], and the photoemission cross-sections were taken from Scofield [111].

II.2.2.2. Time-of-Flight Secondary Ion Mass Spectrometry (ToF-SIMS)

II.2.2.2.1. Principle

SIMS (secondary ion mass spectrometry) is a technique for analyzing the elemental and chemical composition of a surface. The principle of this technique is illustrated in Figure II.17. A focused ion beam (primary gun), which is generated by a liquid metal ion gun (LMIG), impinges upon the target surface. The energy of primary ions is transferred by atomic collisions to the target atoms, thereby setting up a collision cascade. The primary ions set atoms in motion, both by direct collision with atoms in the sample or indirectly by collision of atoms already in motion with other target atoms. Primary ion sources are typically operated in the energy range of several hundred eV to several keV. The energy is transferred back to the surface which allows surface atoms and molecules of (approximately) the top 2-3 molecular layers to overcome their surface binding energy. The ejected or sputtered atoms and molecules from the target surface are termed secondary ions. The yield of secondary ions increases with increasing energy, but higher energies results in increased sample damage. While most secondary ions come off neutrally charged, also a small portion is generated in the ionized state, which can be subsequently analyzed as positive or negative ions by their mass to charge ratio m/z [107], [112], [113].

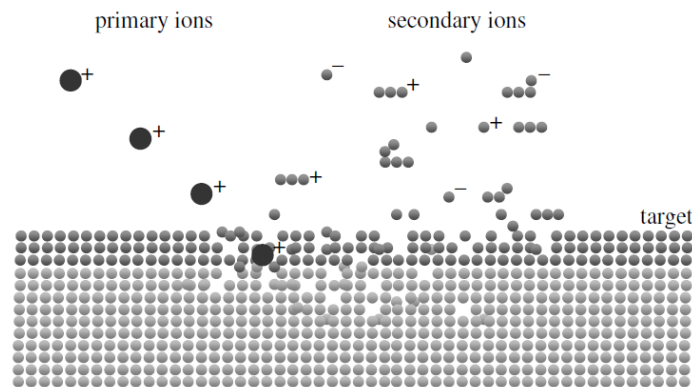


Figure II. 17: Schematic drawing of the secondary ion emission process initiated by the impact of the primary ions [113].

Depending on the ion dose, the technique can be separated into two modes: dynamic and static SIMS. In contrast to dynamic SIMS, static SIMS is performed with low primary ion doses. SIMS is destructive in nature because particles are removed from the surface. This can be used to erode the solid in a controlled manner to obtain information on the in-depth

distribution of elements. This dynamic SIMS mode is widely applied to analyse thin films, layer structures and dopant profiles. In order to receive chemical information on the original undamaged surface, the primary ion dose density must be kept low enough ($< 10^{13} \text{ cm}^{-2}$) to prevent a surface area from being hit more than once.

ToF-SIMS is an acronym for the combination of the SIMS technique with Time-of-Flight (ToF) mass analysis. The principle of ToF mass spectrometry is based on the fact that ions with different masses travel with different velocities. Basically, desorbed secondary ions from the target surface are accelerated by an electrostatic field and travel to the detector. The ToF analyzer separates secondary ions according to their m/z (mass/charge). The mass, m , of the ions is determined according to the time it takes them to travel through the length, L , of the field-free flight tube, after they have been accelerated in an extraction field to a common energy, E . The relationship between E and flight time, t , is straightforward.

$$E = \frac{m v^2}{2} = \frac{mL^2}{2zt^2} \quad \text{Eq. II.14}$$

where v is the velocity and z is the charge of a secondary ion.

The energy and angular dispersion of the secondary ions can be compensated using focusing elements such as a reflectron. Since flight time is proportional to the square root of the mass of the secondary ion, the lighter ions travel at a faster velocity and arrive at the detector earlier than the heavier ions. This mass spectrum can then be used to obtain composition, distribution and molecular information of surface constituents [113].

ToF-SIMS is a very versatile analysis technique due to its very high specific surface sensitivity, its applicability to practically all types of materials and sample forms, its ability to detect all elements including their isotopes and its ability to give direct molecular information. There are four main modes of operation of ToF-SIMS: a) large area surface analysis, b) surface imaging and microarea analysis, c) depth profiling analysis, and d) trace analysis of individual substances.

The primary aim of depth profiling analysis is to determine the elemental distribution and composition of thin films by combining a surface-analysis method with an ion gun for sample bombardment. Figure II.18 shows the sputter depth process by ToF-SIMS using two ion

beams operating in the Dual Beam Mode. While the first beam is sputtering a crater, the second beam is progressively analysing the crater bottom.

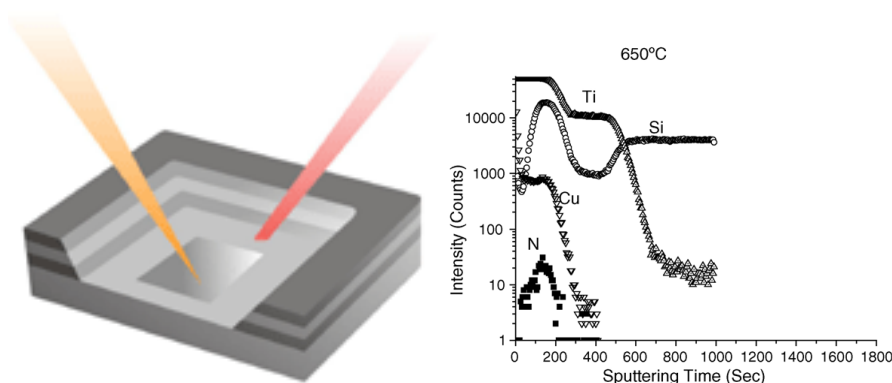


Figure II. 18: Schema illustrating the sputter-depth process.

The raw data in depth profiling consist of elemental signal intensities as a function of the sputtering time. To obtain a first-order quantification of the profile, at least one of the following three tasks should be performed: a) conversion of the measured sputtering time to sputtered depth; b) conversion of the measured signal intensities to concentrations; c) determination of the depth resolution.

The first task requires the determination of the sputtering rate (depth divided by time) by auxiliary methods like profilometry. The second task is usually performed with adequate relative elemental sensitivity factors. Supposing we have thus obtained the local concentration as a function of depth, this profile is not yet the true in-depth distribution of composition. The concentration is what the analysis method sees after the sputtering event has taken place. Sputtering creates an “altered layer” at the surface. Any deviation of the measured profile shape from the exact shape of the original in-depth distribution (errors or artefacts) introduced by ion beam-sample interactions limit the accuracy of a measured profile. Therefore, the determination of the depth resolution is an important task to be done in order estimate the accuracy of the results. Sputter-depth profiling today is characterized experimentally by high-resolution depth profiling, and theoretically by improved methods and models for quantification [114].

Most biochemical samples are electrical insulators and accumulate charges at the surface during analysis. This charge built-up can reduce or totally eliminate the secondary ion signal. Sample charging occurs during the sputtering process, from bombardment of the surface by

the positively charged primary ions and the simultaneous loss of secondary ions. Unless the sample has sufficient electrical conductivity to transport electrons to the sputtered region, this region acquires a net positive charge. To neutralize the charge build-up during ToF-SIMS analysis, the surface is flooded with pulses of low energy electrons between pulses of primary ions [113].

II.2.2.2.2. Instrumentation

ToF-SIMS analyses were done using a ToF-SIMS V spectrometer (ION-TOF GmbH); for the measurements, the analysis chamber was maintained at less than 10^{-9} Pa in operation conditions. The depth profiles were performed using the instrument in dual beam mode. A pulsed 25 keV Bi^+ primary ion source (LMIG) at a current of 1.2 pA (high mass resolution mode), rastered over a scan area of $100 \times 100 \mu\text{m}^2$, was used as the analysis beam. The sputtering was performed using a 1 keV Cs^+ ion beam at a current of 50 nA, and rastered over an area of $300 \times 300 \mu\text{m}^2$. The depth profiles were obtained in negative polarity meaning only negative ions were analysed. The distribution of the ionized fragments, all measured quasi-simultaneously, were plotted versus Cs^+ ion sputtering time.

Quantitative SIMS analysis is difficult because the secondary ions yields depend on several factors and are not directly proportional to their concentration in the sample. The yield of secondary ions M can be described in terms of secondary ion current (i_{MS}) during SIMS analysis. The important yield variables that contribute to i_{MS} include S , the yield of secondary particles per primary particle impact (sputter yield), and R^+ , the probability that a given particle will be emitted as an ion (ionization probability):

$$i_{MS} = i_p S R^+ \theta_M n \quad \text{Eq. II.15}$$

where i_p is the primary particle flux, θ_M is the fractional coverage of M , and n represents the transmission and detection efficiency of the analyzer system. The above equation indicates that the sensitivity of the technique for a particular secondary ion depends on its sputter yield and ionization probability. Often S and R^+ are grouped together in a variable referred to as the transformation probability (P).

“Matrix effects” also play a major role in SIMS quantitative analysis. The problem can be defined as the variability of ion yields with surface composition changes. The same analyte

will not have the same secondary ion yield in different chemical environments, making direct comparison among samples difficult. No method has been developed to compensate for the variation in ion yields due to matrix effects [113], [115].

The majority of depth profiles reported in the literature are only qualitative or semi-quantitative. Sometimes, in an attempt to obtain a quantitative profile, the elemental intensity signals are simply converted to atomic concentrations by means of relative elemental sensitivity factors. Likewise, sputtering time is converted to depth by estimation of a constant sputtering rate. However, these simple procedures only provide a semi-quantitative results [114].

In this work, the intensity was reported using a logarithmic scale, which gave equal emphasis to recorded signals of all intensities. The variation of the ion intensity with sputtering time reflects the variation of the in-depth concentration but is also dependent on the matrix from which the ions are emitted. Data acquisition and processing were performed using the IonSpec software.

The thickness of oxide layers was estimated from theoretical sputtering rates of corresponding pure metallic substrates (given in tables) in the same sputtering conditions; e. g. the thickness of nickel oxide was estimated from the sputtering rate of pure metallic nickel. For mixed metal oxides, the thickness was estimated from an average sputtering rate calculated by summing the sputtering rates of pure metals ponderated by the fractions of elements in the oxide.

III. Electrochemical behaviour and surface chemical composition of 70Cu-30Ni alloy after short-term immersion in artificial seawater and filtered natural seawater

This chapter is focused on the study of the corrosion behaviour of 70Cu-30Ni alloy after 1 h of immersion in aerated artificial seawater (ASW) and filtered natural seawater (FNSW). For that purpose, electrochemical measurements in static conditions, under flow and stirring, and in well-controlled hydrodynamic conditions, were combined to surface analyses. A model is proposed to analyse impedance data.

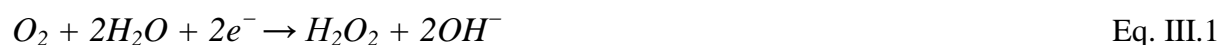
III.1. Results

III.1.1. Static conditions

III.1.1.1. Electrochemical measurements

Before each experiment, the corrosion potential was followed as a function of time (E_{corr} vs time). During the first hour of immersion, the corrosion potential E_{corr} decreases till reaching a steady-state value of -0.230 ± 0.009 V vs SCE in ASW. The E_{corr} value in FNSW is -0.231 ± 0.013 V vs SCE. Therefore, the E_{corr} values obtained in ASW are comparable to those obtained in FNSW.

Figure III.1(a) shows the cathodic polarisation curves obtained in ASW and FNSW. Two current plateaus illustrating mass transport limited reactions can be clearly observed in both cases. The short plateau at around -0.30 V vs SCE ($|j| \sim 10 \mu\text{A}\cdot\text{cm}^{-2}$) illustrates the first step of dissolved oxygen reduction with production of H_2O_2 , that can be written at $\text{pH} = 8.0$ as follows [11], [100]:



The wide plateau observed for potentials ranging from -0.40 down to -1.00 V vs SCE corresponds to the second step of dissolved oxygen reduction with transfer of 4 electrons, that can be written at $\text{pH} = 8.0$ as follows:



The ratio between the two plateau current densities is comprised between 2 and 3 (theoretical value: 2). This observation is consistent with the presence on the alloy surface of a layer composed of reducible products (oxides) in the oxygen reduction domain.

The current increase (in absolute value) observed below -1.00 V vs SCE illustrates water reduction (hydrogen evolution reaction).

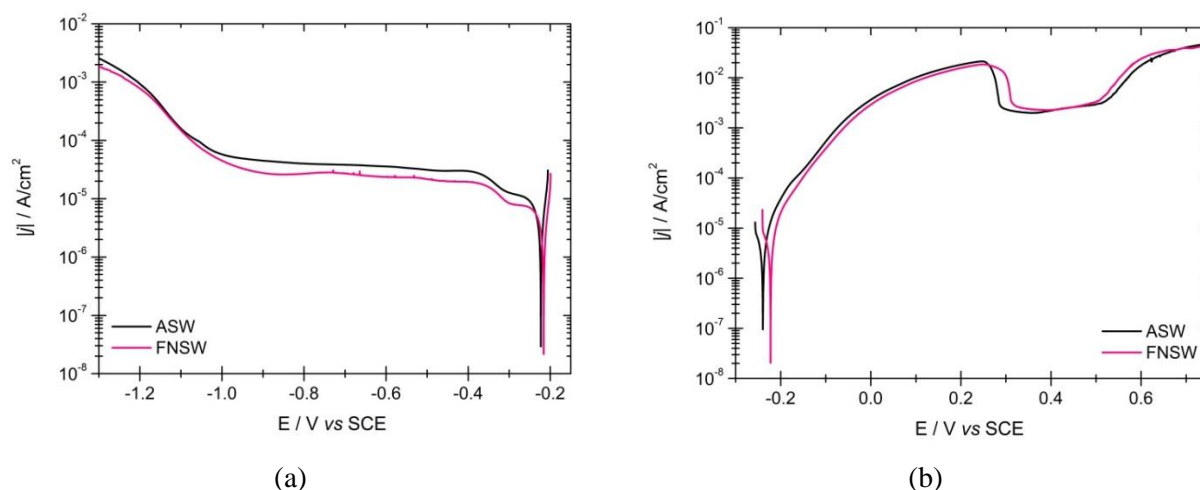


Figure III. 1: (a) Cathodic and (b) anodic polarisation curves of 70Cu-30Ni after 1 h of immersion at E_{corr} in aerated artificial seawater and filtered natural seawater. Scan rate: $0.5 \text{ mV}\cdot\text{s}^{-1}$.

The second plateau current density for the oxygen reduction reaction in FNSW ($|j| \sim 30 \mu\text{A}\cdot\text{cm}^{-2}$) is divided by 1.33 if compared to that in ASW ($|j| \sim 40 \mu\text{A}\cdot\text{cm}^{-2}$). Although the natural seawater was filtered, not all the organic matter was removed from the solution; therefore, FNSW contains some biomolecules. The lower second plateau current density may be due to the presence of these biomolecules, but may also be induced by a difference in natural convection from one experiment to another.

The anodic polarisation curves obtained in ASW and FNSW are presented in Figure III.1 (b). In ASW, the anodic polarisation curves show very high dissolution currents. In particular, a pseudo-plateau, corresponding to a current density of $\sim 2.5 \text{ mA}\cdot\text{cm}^{-2}$, can be observed at around 0.4 V vs SCE; therefore, this plateau current is not a passive current, and hence the oxide film formed on the surface is not a passive layer. Moreover, visual observation of the electrode surface after an anodic scan shows a green layer, the thickness of which increases with the end anodic potential. This green layer corresponding to high anodic currents may be formed by redeposition due to the saturation of the solution in copper ions.

On the other hand, even if the composition of the FNSW is different from that of ASW and even if some biomolecules are present in FNSW, this does not affect the anodic polarisation curve, which is similar in both media.

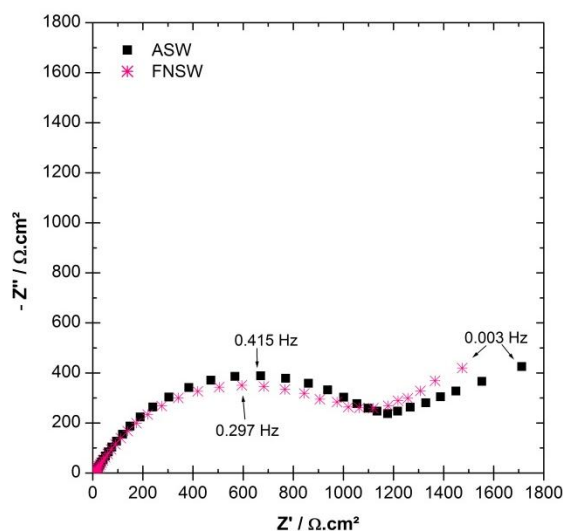


Figure III. 2: Experimental impedance diagrams in the complex plane (Nyquist diagrams) of 70Cu-30Ni plotted at E_{corr} after 1 h of immersion in artificial seawater and filtered natural seawater.

Figure III.2 shows the impedance diagrams in the complex plane (Nyquist diagrams) plotted at E_{corr} after 1 h of immersion in ASW and in FNSW. The diagrams exhibit two capacitive loops: one high frequency (HF) depressed semi-circle, and a low frequency (LF) loop. The size of the HF loop is similar in both cases.

It can be concluded that the electrochemical behaviour of the alloy in ASW is comparable to that observed in FNSW. After impedance measurement at E_{corr} in ASW and FNSW, there is no sign of pitting corrosion on the electrode surface.

III.1.1.2. Surface analysis

Scanning Electron Microscopy images (SEM, Figure III.3 (a)) and Energy Dispersive X-ray Analysis (EDS, Figure III.3 (b), (c), (d)) were performed on a $\frac{1}{4}$ 70Cu-30Ni alloy tube (1 cm length) just after polishing in order to observe the elements distribution on the surface. Results illustrate the homogeneous distribution, at the micrometer scale, of Cu and Ni along the sample surface.

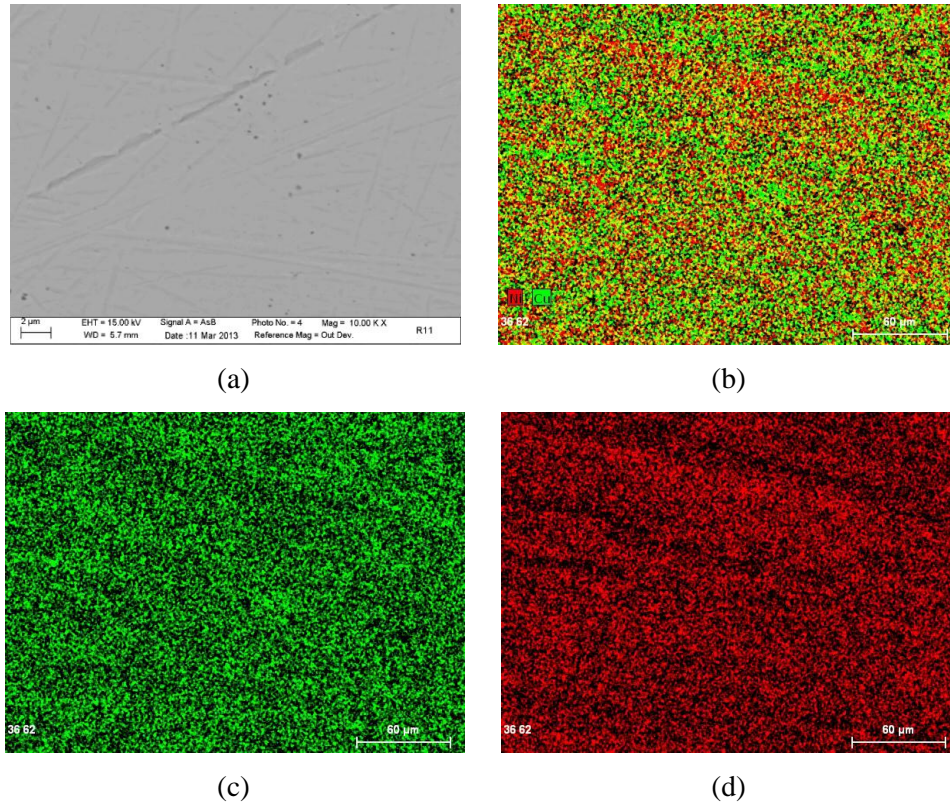


Figure III. 3: (a) SEM image; and EDS analysis of the 70Cu-30Ni tube just after polishing: (b) Cu and Ni distribution, (c) Cu distribution, and (d) Ni distribution.

If a continuous mixed oxide layer covering the metallic/alloy substrate is assumed (Figure III.4), the composition and the equivalent thickness of the oxide layer (d_{oxide}) can be calculated from XPS data using the following system of equations, in which the intensities of copper and nickel in the metallic substrate and in the oxide layer are considered:

$$I_{Cu}^{Metal} = k \cdot T_{Cu} \cdot \sigma_{Cu} \cdot D_{Cu}^{Metal} \cdot \lambda_{Cu}^{Metal} \cdot \sin\theta \cdot \exp\left(\frac{-d_{oxide}}{\lambda_{Cu}^{Oxide} \sin\theta}\right) \quad \text{Eq. III.3}$$

$$I_{Ni}^{Metal} = k \cdot T_{Ni} \cdot \sigma_{Ni} \cdot D_{Ni}^{Metal} \cdot \lambda_{Ni}^{Metal} \cdot \sin\theta \cdot \exp\left(\frac{-d_{oxide}}{\lambda_{Ni}^{Oxide} \sin\theta}\right) \quad \text{Eq. III.4}$$

$$I_{Cu}^{Oxide} = k \cdot T_{Cu} \cdot \sigma_{Cu} \cdot D_{Cu}^{Oxide} \cdot \lambda_{Cu}^{Oxide} \cdot \sin\theta \cdot \left[1 - \exp\left(\frac{-d_{oxide}}{\lambda_{Cu}^{Oxide} \sin\theta}\right)\right] \quad \text{Eq. III.5}$$

$$I_{Ni}^{Oxide} = k \cdot T_{Ni} \cdot \sigma_{Ni} \cdot D_{Ni}^{Oxide} \cdot \lambda_{Ni}^{Oxide} \cdot \sin\theta \cdot \left[1 - \exp\left(\frac{-d_{oxide}}{\lambda_{Ni}^{Oxide} \sin\theta}\right)\right] \quad \text{Eq. III.6}$$

where:

θ is the take-off angle of the photoelectrons with respect to the sample surface; in this work, $\theta = 90^\circ$;

k is the spectrometer specific constant;

σ_{Cu} , σ_{Ni} are the photo-ionisation cross-sections of Cu and Ni, respectively;

λ_{Cu}^{Metal} , λ_{Ni}^{Metal} , λ_{Cu}^{Oxide} , λ_{Ni}^{Oxide} are the inelastic mean free paths (IMFP) of the photoelectrons emitted by the Cu and Ni core levels in the metallic alloy and in the oxide, respectively;

T_{Cu} , T_{Ni} are the transmission functions for elements Cu and Ni, respectively (T_x depends on the kinetic energy, E_{kin} of the analysed element X);

D_{Cu}^{Metal} , D_{Ni}^{Metal} , D_{Cu}^{Oxide} , D_{Ni}^{Oxide} are the densities of elements Cu and Ni in the metallic alloy and in the oxide, respectively.

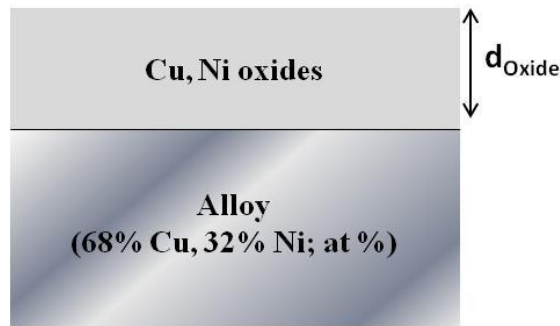


Figure III. 4: Layer model assumed for the analysis of XPS data (mixed oxide layer covering the metallic substrate).

Considering that:

$$D_{Cu}^{Metal} + D_{Ni}^{Metal} = 1 \quad \text{Eq. III.7}$$

$$D_{Cu}^{Oxide} + D_{Ni}^{Oxide} = 1 \quad \text{Eq. III.8}$$

the concentrations of copper and nickel in the oxide layer and beneath the oxide layer, as well as the oxide layer thickness can be calculated by solving the system of six equations (Eqs. III.3, III.4, III.5, III.6, III.7 and III.8) with six unknowns (D_{Cu}^{Metal} , D_{Ni}^{Metal} , D_{Cu}^{Oxide} , D_{Ni}^{Oxide} , d_{oxide} and k).

The calculated values for the transmission function T are listed in Table III.1.

Table III. 1: Transmission functions $T(E_{kin})$ of the Escalab 250 energy analyzer, provided by Thermo Electron Corporation.

$T(E_{kin})$	Cu Auger line $L_3M_{45}M_{45}$	Cu $2p_{3/2}$	Ni $2p_{3/2}$
		3492	4265

As mentioned in Chapter II, the inelastic mean free path (λ) values were taken from the QUASES-IMFP-TPP2M, a database for calculation of IMFPs by the TPP2M-formula, which is part of the QUASES-Tougaard method. These values are listed in Table III.2.

Table III. 2: Inelastic mean free paths λ in nm – Taken from the QUASES-IMFP-TPP2M.

λ (nm)						
$\lambda_{Cu2p_{3/2}}^{Cu^{+2}}$	$\lambda_{Cu2p_{3/2}}^{Cu^{+1}}$	$\lambda_{Cu2p_{3/2}}^{Metal}$	$\lambda_{Cu Auger}^{Cu^{+1}}$	$\lambda_{Cu Auger}^{Metal}$	$\lambda_{Ni2p_{3/2}}^{Ni^{+2}}$	$\lambda_{Ni2p_{3/2}}^{Metal}$
1.19	1.23	1.01	1.76	1.46	1.31	1.11

The photoionization cross-section σ_X values are presented in Table III.3.

Table III. 3: Photo-ionization cross sections σ_X at 1486.6 eV.

	Cu auger line $L_3M_{45}M_{45}^*$	Cu $2p_{3/2}$	Ni $2p_{3/2}$
σ_X	5.4	16.73	14.61

*Value calculated by: $\sigma_{Cu Auger} = \sigma_{Cu} \times \frac{I_{Cu Auger}^{metal}}{I_{Cu2p_{3/2}}^{metal}} \times \frac{\lambda_{Cu2p_{3/2}}^{metal}}{\lambda_{Cu Auger}^{metal}} \times \frac{T_{Cu2p_{3/2}}}{T_{Cu Auger}}$, using the known intensity values $I_{Cu2p_{3/2}}^{metal}$ and $I_{Cu Auger}^{metal}$ of the 70Cu-30Ni alloy after polishing, after sputtering (removal of oxides from the surface).

Although with the previous equations, it is possible to calculate the equivalent thickness and the composition of the oxide layer formed on the 70Cu-30Ni alloy, the decomposition of the Cu $2p_{3/2}$ XPS peak presents an important difficulty. Indeed, the binding energy of Cu^0 and Cu^{+1} are located at the same position as shown in Table III.4, in which the binding energy of the Cu $2p_{3/2}$ core level and the kinetic energy of the $L_3M_{45}M_{45}$ Cu Auger line are presented for the different Cu species. This difficulty was overcome by making use of the Cu Auger line

($L_3M_{45}M_{45}$), helpful to distinguish these two species. Furthermore, the Cu Auger line was used to obtain information about the relative contributions of Cu_2O , CuO and metallic Cu. For that purpose, the decomposition was performed with the software “CASA”, using the reference spectra of Cu_2O , CuO and metallic Cu. The results provide the relative proportions of these compounds at the alloy surface, considering that only these species are present. However, this is not fully correct, due to the fact that other Cu species may be part of the surface film, such as $Cu(OH)_2$, $CuSO_4$ or other Cu complexes, leading to an overestimation of the percentages of Cu^{+1} in the Auger line ($L_3M_{45}M_{45}$).

Table III. 4: Binding energy and kinetic energy of Cu $2p_{3/2}$ XPS peak and Auger line, respectively, for Cu species [12], [116]–[121].

Compound	Cu $2p_{3/2}$ (Binding energy / eV)	Cu Auger line - $L_3M_{45}M_{45}$ (Kinetic energy / eV)
Cu	932.5 ± 0.2	918.7 ± 0.3
Cu_2O	932.4 ± 0.2	917.0 ± 0.4
CuO	933.4 ± 0.2	917.9 ± 0.2
$Cu(OH)_2$	934.5 ± 0.4	916.4 ± 0.2
$CuSO_4$	935.4 ± 0.3	916.0 ± 0.1
Cu_2S	932.6 ± 0.3	917.4 ± 0.7
CuCl	932.0 ± 0.7	915.5 ± 0.3
$CuCl_2$	934.6 ± 0.6	915.5 ± 0.3

As it is not possible to know precisely what other compounds (different than Cu_2O and CuO) are involved in the formation of the oxide film and as no Auger lines ($L_3M_{45}M_{45}$) references for all the copper compound involved could be obtained, only the intensity of Cu^0 obtained from the decomposition with the available Cu Auger lines ($L_3M_{45}M_{45}$) references was taken into account. Therefore, the intensity of Cu^0 in the Auger line ($I_{Cu\ Auger}^{Cu^0}$) was calculated from the total intensity of the Auger Cu and this value was converted into $I_{Cu\ 2p_{3/2}}^{Cu^0}$ using the following equation:

$$I_{Cu\ 2p_{3/2}}^{Cu^0} = \frac{I_{Cu\ Auger}^{Cu^0} \sigma_{Cu\ 2p_{3/2}} T_{Cu\ 2p_{3/2}} \lambda_{Cu\ 2p_{3/2}}^{Metal} \exp\left(\frac{-d_{Oxide}}{\lambda_{Cu\ 2p_{3/2}}^{Oxide}}\right)}{\sigma_{Cu\ Auger} T_{Cu\ Auger} \lambda_{Cu\ Auger}^{Metal} \exp\left(\frac{-d_{Oxide}}{\lambda_{Cu\ Auger}^{Oxide}}\right)} \quad \text{Eq.}$$

III.9

The intensity of Cu^{+1} ($I_{Cu\ 2p_{3/2}}^{Cu^{+1}}$) was then calculated from $I_{Cu\ 2p_{3/2}}^{Cu^0}$ by:

$$I_{Cu\ 2p_{3/2}}^{Cu^{+1}} = I_{Cu\ 2p_{3/2}}^{932\ eV} - I_{Cu\ 2p_{3/2}}^{Cu^0} \quad \text{Eq. III.10}$$

where $I_{Cu\ 2p_{3/2}}^{932\ eV}$ corresponds to the intensity for the peak located at the position 932 eV in the Cu 2p_{3/2} core level spectra corresponding to Cu^{+1} and/or Cu^0 .

The intensities $I_{Cu\ 2p_{3/2}}^{Cu^{+1}}$ and $I_{Cu\ 2p_{3/2}}^{Cu^0}$ can be used to solve the system of equations that will allow calculate the equivalent thickness of the oxide layer and the composition of the oxide film and of the substrate beneath the oxide film.

During the XPS measurements, the following core levels were recorded: Cu 2p (and Auger line), Ni 2p, O 1s, C 1s, and N 1s. Only the Cu 2p_{3/2} and Ni 2p_{3/2} peaks were used in the decomposition and analysis of XPS data.

XPS analysis of the 70Cu-30Ni alloy sample just after polishing shows, from the Cu 2p_{3/2} core level spectrum, the presence of a first peak at 932.2 eV corresponding to Cu^{+1} and/or Cu^0 , and a second peak at 933.73 eV with a satellite at higher binding energy of 943.2 eV corresponding to Cu^{+2} (Figure III.5(a)). The position of the Auger line ($L_3M_{45}M_{45}$) at the kinetic energy of 919.1 eV indicates a major contribution of Cu^0 (Figure III.5(b)). The Ni 2p_{3/2} core level spectrum shows a peak at a binding energy of 852.2 eV characteristic of Ni^0 , and another peak at the position 855.6 eV with a satellite at the position of 860.9 eV corresponding to nickel hydroxide ($Ni(OH)_2$) (Figure III.6) [122], [123]. The thickness of the oxide layer calculated is ~1.5 nm and its atomic composition is: 27 at. % Cu_2O + 42 at. % Cu^{+2} (CuO and $Cu(OH)_2$) + 31 at. % $Ni(OH)_2$. Enrichment in copper of the alloy beneath the oxide layer is also detected (75 at. % Cu + 25 at. % Ni to be compared to 68 at. % Cu + 32 at. % Ni for the bulk alloy).

After immersion in ASW, the XPS Cu $2p_{3/2}$ core level peak with a binding energy located at 932.2 eV (Figure III.5(a)) and the Cu Auger line ($L_3M_{45}M_{45}$) at a kinetic energy of 916.8 eV (Figure III.5(b)) demonstrate, according to Table III.4, the presence of Cu^+ instead of Cu^0 observed for the sample after polishing. In the case of FNSW, the Cu $2p_{3/2}$ core level spectra exhibit a first peak at ~ 932.2 eV corresponding to Cu^{+1} and/or Cu^0 , and a second peak at higher binding energy (~ 934 eV) with a satellite at ~ 944 eV corresponding to Cu^{+2} (Figure III.5(a)). The position of the Auger line ($L_3M_{45}M_{45}$) at a kinetic energy of 916.7 eV (Figure III.5(b)) shows the presence of Cu^{+1} , similarly to what is observed in ASW.

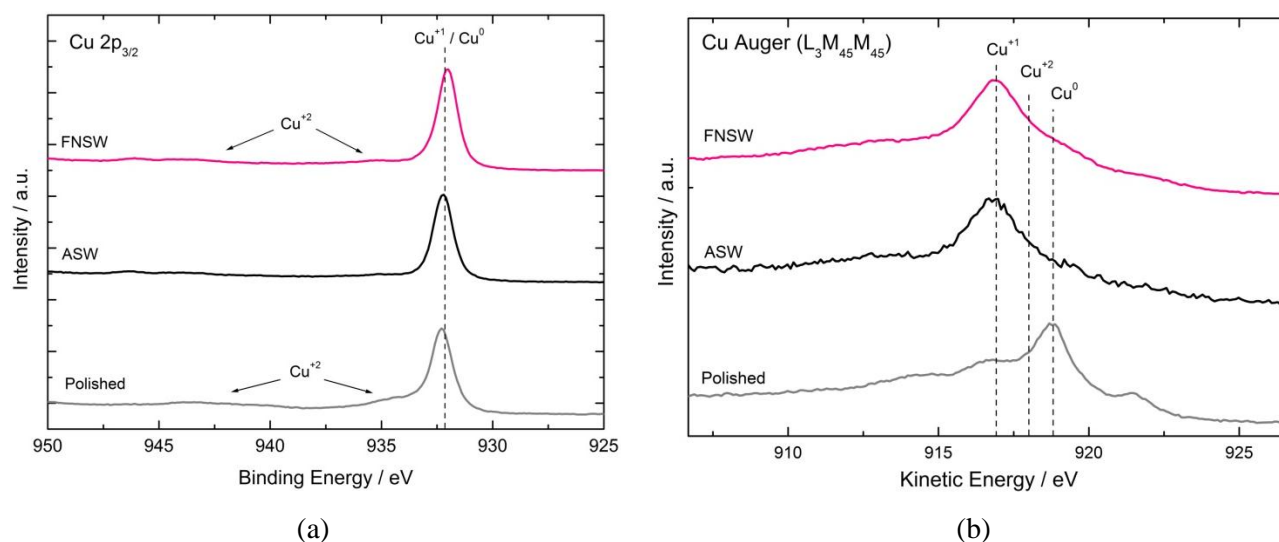


Figure III. 5: (a) X-ray photoelectron spectroscopy (XPS) Cu $2p_{3/2}$ core level spectra, and (b) Cu $L_3M_{45}M_{45}$ Auger lines of 70Cu-30Ni after polishing, after 1 h of immersion at E_{corr} in static aerated artificial seawater and in filtered natural seawater. The intensity is expressed in arbitrary unit (a.u.).

From the XPS Ni $2p_{3/2}$ core level spectrum, the presence of $Ni(OH)_2$ in the surface layer is demonstrated by a peak located at ~ 856.0 eV and the corresponding satellite at ~ 862 eV, after immersion in ASW as well as in FNSW (Figure III.6) [122], [123]. The XPS Cl 2p core level (no presented in this manuscript) shows a peak centred at 198.6 eV on the alloy exposed to ASW and FNSW. Using the intensity of the Cl 2p signal, the amount of Cl^- can be calculated; a value of $\sim 0.2\%$ is found after immersion in ASW and $\sim 0.8\%$ in FNSW.

The atomic composition of the oxide layer calculated from XPS data for 70Cu-30Ni alloy after 1h of exposure to ASW (93 at. % Cu_2O + 7 at. % $Ni(OH)_2$) indicates an enrichment in Cu_2O compared to the sample just after polishing; no Cu^{+2} compounds were detected in the oxide layer. However, after immersion in FNSW the oxide layer exhibits an enrichment in

Cu^{+1} , but also Cu^{+2} compounds were found in the oxide layer as well as $\text{Ni}(\text{OH})_2$ (55 at. % Cu^{+1} + 16 at. % Cu^{+2} + 29 at. % Ni^{+2}). The depth analyzed by XPS is about 10 nm. However, no metallic contribution was observed in the $\text{Cu } 2p_{3/2}$ or $\text{Ni } 2p_{3/2}$ core level spectrum, which means that the oxide film is thicker than 10 nm; therefore, the thickness of the oxide film cannot be calculated from XPS data.

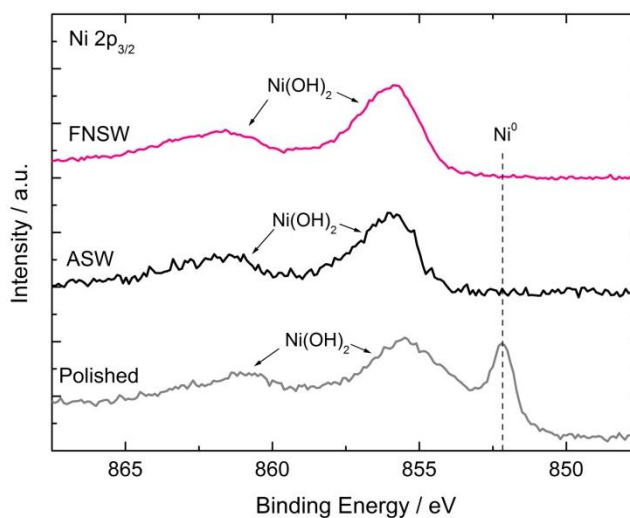


Figure III. 6: X-ray photoelectron spectroscopy (XPS) $\text{Ni } 2p_{3/2}$ core level spectra of 70Cu-30Ni alloy after polishing, after 1 h of immersion at E_{corr} in static aerated artificial seawater and in filtered natural seawater. The intensity is expressed in arbitrary unit (a.u.).

A characteristic ToF-SIMS depth profile (negative ions) obtained with 70Cu-30Ni alloy immersed during 1 h at E_{corr} in ASW is presented in Figure III.7. This profile evidences a stratification of the oxide film covering the metallic surfaces. Three regions can be observed. The first one extends from 0 to 200 s of sputtering, characterized by an intense $^{95}\text{CuO}_2^-$ signal. As one probes deeper into this first region, a progressive increase of the $^{90}\text{NiO}_2^-$ signal is observed, indicating that the outer surface layer is mainly composed of copper oxide, with the presence of some Ni oxide and/or hydroxide, in agreement with XPS data. In the second region that extends from 200 s to 290 s, a sharp decrease of the $^{95}\text{CuO}_2^-$ signal is observed, whereas $^{90}\text{NiO}_2^-$ signal reaches its maximum intensity. This second region is assigned to a nickel oxide and/or hydroxide inner layer in which the presence of oxidized copper cannot be excluded. Finally, after 290 s of sputtering, one enters the third region characterized by a sharp decrease of all oxidized signals ($^{18}\text{O}^-$, $^{95}\text{CuO}_2^-$ and $^{90}\text{NiO}_2^-$) and a constant and intense plateau for the $^{116}\text{Ni}_2^-$ signal which is characteristic of the metallic substrate. It is noticeable that Cl species (represented by the $^{35}\text{Cl}^-$ signal on the

profile) are present essentially in the outer part of the oxide layer (copper oxide). Thus, the oxide film formed on 70Cu-30Ni alloy in ASW exhibits a duplex structure with (i) a 20 nm-thick outer layer mainly composed of copper oxide and (ii) a 10 nm-thick inner layer mainly composed of oxidized nickel. The possible presence of Ni hydroxide in the inner layer can be explained by the fact that the outer layer is, in fact, redeposition of copper oxide on the surface.

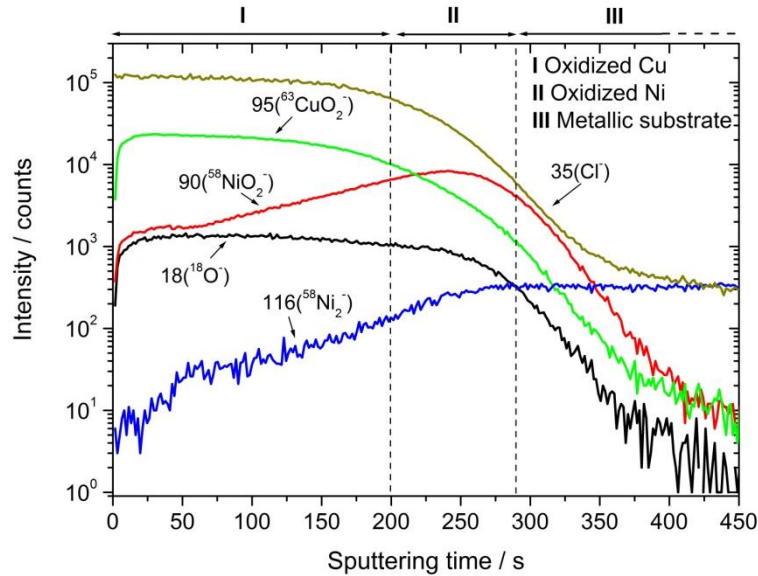


Figure III. 7: Characteristic Time-of-Flight Secondary Ions Mass Spectrometry (ToF-SIMS) depth profile (negative ions) of 70Cu-30Ni after 1 h of immersion at E_{corr} in static aerated artificial seawater (ASW).

For a layer composed of one single oxide, the thickness is estimated from the theoretical sputtering rate of the corresponding pure metal in the same sputtering conditions (given in tables). For mixed metallic oxides, the thickness was estimated from an average sputtering rate calculated from the sputtering rates of pure metals multiplied by the fraction of each element in the oxide.

Finally, Figure III.8 exhibit the negative depth profile recorded after 1 h of immersion at E_{corr} in FNSW. Three main regions can be identified. In the first region, from 0 s to 32 s of sputtering, all signals increase, particularly the 26CN^- , 32S^- , 63PO_2^- , 90^{58}NiO_2^- signals, which reach a maximum value and subsequently sharply decrease. The 95^{63}CuO_2^- , 18^{18}O^- signals start to slowly decrease at the end of this first region, whereas the 116^{58}Ni_2^- signal keeps increasing. The second region, which goes from 32 up to 187 s of sputtering, is characterized

by a new increase of the 26CN^- , 32S^- , 63PO_2^- , 90^{58}NiO_2^- signals. The 116^{58}Ni_2^- signal slightly increase until form a plateau at ~ 187 s, when all the signals representing the oxidized components sharply decrease; at this point, the interface Cu oxide/oxidized Ni has been reached. The first region can be probably due to the presence of some islands of oxidized Ni and Cu on the oxide layer, covering an oxidized Ni oxide layer, represented by region 2. The signal 35Cl^- holds its high intensity value up to 82 s of sputtering, which indicate the presence of Cl^- along the oxide layer. The 32S^- signal follows the same trend as the 90^{58}NiO_2^- signal, indicating the presence of sulphur throughout the inner layer. The global thickness estimated by ToF-SIMS was of ~ 23 nm.

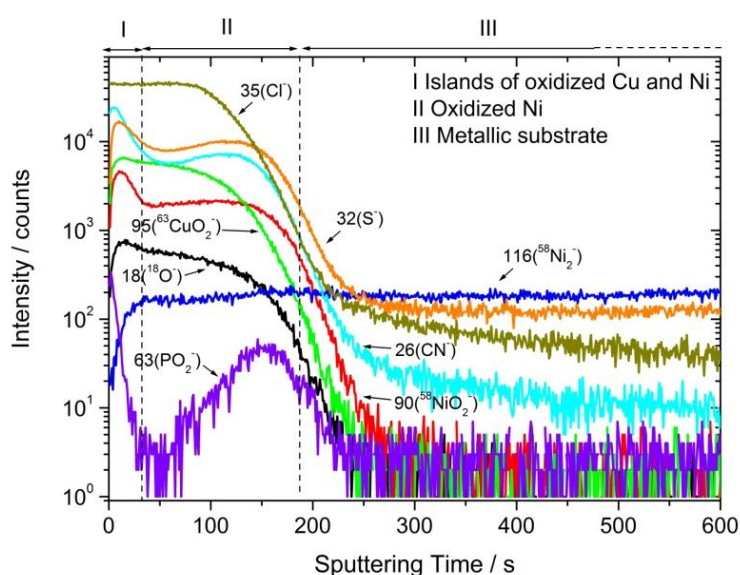


Figure III. 8: Characteristic Time-of-Flight Secondary Ions Mass Spectrometry (ToF-SIMS) depth profile (negative ions) of 70Cu-30Ni after 1 h of immersion at E_{corr} in static aerated filtered natural seawater (FNSW).

III.1.2. Effect of hydrodynamics

III.1.2.1. Comparison static conditions/under flow and stirring

As the water of cooling circuits is typically under flow and as the corrosion of copper in aerated solution is known as being controlled by mass transport processes to and from corroding surfaces [124], hydrodynamics is an important parameter to be studied. Therefore, in order to avoid the redeposition of Cu_2O and to keep the same samples as in static conditions (disc electrodes), the effect of flow and stirring on the electrochemical behaviour

and the surface chemical composition of 70Cu-30Ni alloy was first investigated. For that, a volume 10 times higher than in static conditions was used inside the electrochemical cell (1 L instead of 100 mL); the solution was continuously renewed using a peristaltic pump, with a flow rate of $\sim 0.27 \text{ mL}\cdot\text{s}^{-1}$, and the electrolyte inside the cell was stirred using a magnetic stirrer.

III.1.2.1.1. Electrochemical measurements

After 1 hour of immersion in aerated artificial seawater, the corrosion potential E_{corr} reaches a steady-state value of $-0.215 \pm 0.007 \text{ V vs SCE}$. Thus, flow and stirring induce slightly more anodic values compared to those found in static conditions ($-0.230 \pm 0.009 \text{ V vs SCE}$).

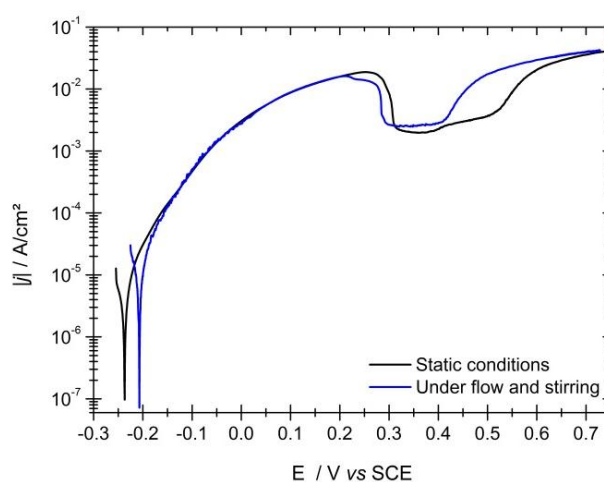


Figure III. 9: Anodic polarisation curves of 70Cu-30Ni after 1 h of immersion at E_{corr} in aerated artificial seawater, in static conditions and under flow and stirring. Scan rate: $0.5 \text{ mV}\cdot\text{s}^{-1}$.

The anodic behaviour of 70Cu-30Ni alloy after 1h of immersion time at E_{corr} in ASW under flow and stirring is compared to that obtained in static conditions in Figure III.9. The shape of the anodic polarisation curve is the same in both cases, showing very high dissolution currents, with a pseudo-plateau current density of $\sim 2.5 \text{ mA}\cdot\text{cm}^{-2}$ at around 0.4 V vs SCE . The two curves overlap at not too high anodic potentials and small differences can be observed at high anodic potentials. Therefore, the anodic behaviour does not depend strongly on hydrodynamics.

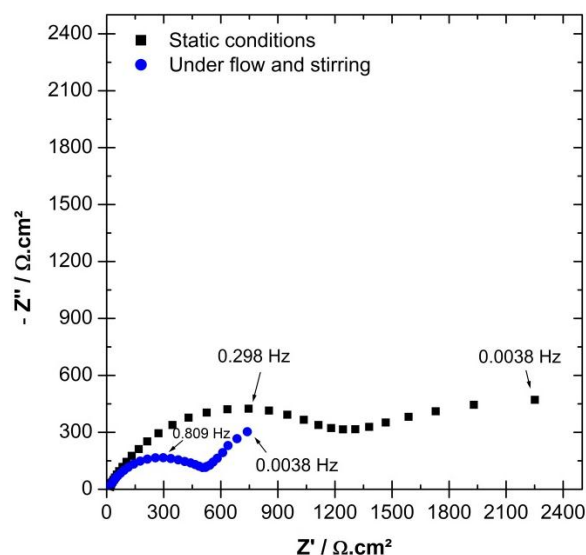


Figure III. 10: Experimental impedance diagrams in the complex plane (Nyquist diagrams) of 70Cu-30Ni plotted at E_{corr} after 1 h of immersion in aerated artificial seawater, in static conditions and under flow.

Impedance diagrams in the complex plane, plotted at E_{corr} after 1 h of immersion in aerated artificial seawater, in static conditions and under flow and stirring, are presented in Figure III.10. In both cases, the diagrams exhibit two capacitive loops: one high frequency (HF) depressed semi-circle, and a low frequency (LF) loop. The size of the HF loop is 2.5 times lower under flow and stirring. The decrease of the size of the high frequency loop when moving from static conditions to under flow (same electrode geometry) can be explained by additional mass transport effect and potential effect (details in the discussion section).

III.1.2.1.2. Surface analysis

Figure III.11(a) illustrates the Cu $2p_{3/2}$ core level spectrum for 70Cu-30Ni alloy in three different conditions: a) after polishing, b) in ASW static conditions, and c) in ASW under flow and stirring. The Cu $2p_{3/2}$ core level spectrum after immersion in ASW under flow and stirring indicates the presence of a first peak at a binding energy of 932.2 eV corresponding to Cu^0 and/or Cu^{+1} , and a second peak at a binding energy of 934.4 eV and the satellite at 943.4 eV associated to the presence of Cu^{+2} .

The Cu Auger line ($L_3M_{45}M_{45}$) of 70Cu-30Ni alloy in ASW under flow and stirring (Figure III.11(b)), located at a kinetic energy of 918.5 eV, demonstrates the presence of Cu^0 as for the sample after polishing. This result allows to conclude that the oxide layer formed on the top

of the alloy is very thin (compared with static conditions), and that its thickness can be calculated from XPS data.

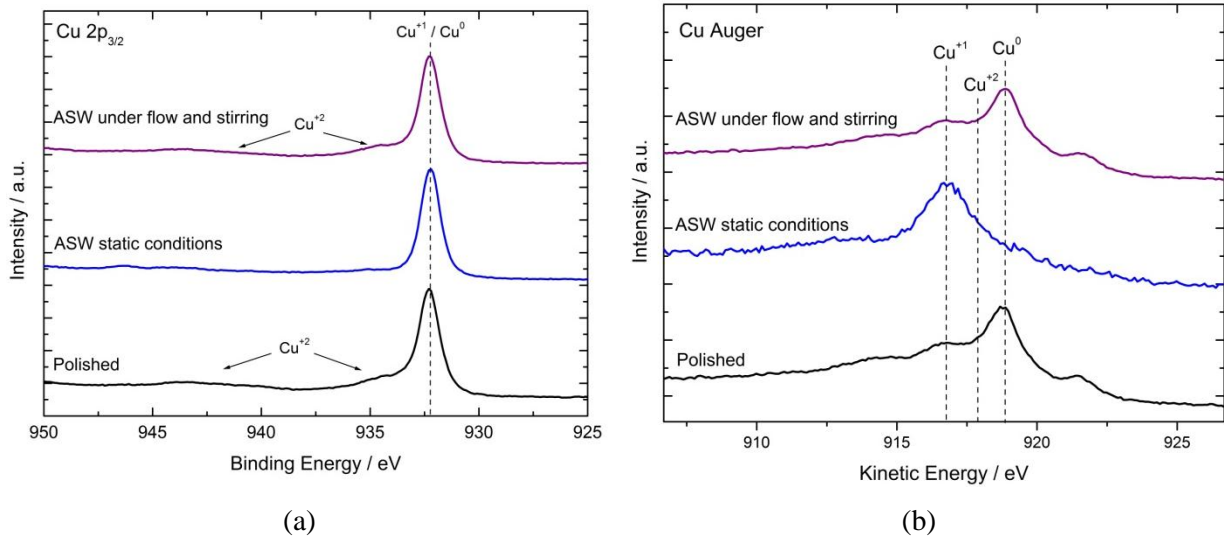


Figure III. 11: (a) X-ray photoelectron spectroscopy (XPS) $\text{Cu}2p_{3/2}$ core level spectra, and (b) $\text{Cu} L_3M_{45}M_{45}$ Auger lines of 70Cu-30Ni after polishing, after 1 h of immersion at E_{corr} in aerated artificial seawater in static conditions and under flow and stirring. The intensity is expressed in arbitrary unit (a.u.).

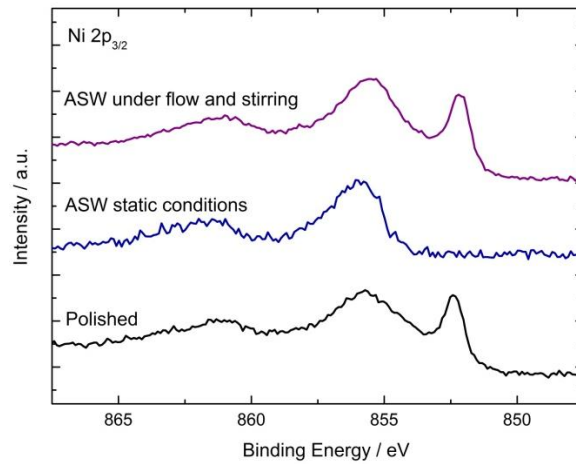


Figure III. 12: XPS $\text{Ni} 2p_{3/2}$ core level spectra of 70Cu-30Ni alloy after polishing, after 1 h of immersion at E_{corr} in aerated artificial seawater in static conditions and under flow and stirring. The intensity is expressed in arbitrary unit (a.u.).

The $\text{Ni} 2p_{3/2}$ core level spectra obtained for 70Cu-30Ni alloy under flow and stirring exhibit one peak at 852.3 eV corresponding to Ni^0 , which confirms that the oxide film formed on the surfaces is very thin. Another peak is observed at a binding energy of 855.7 eV as well as the

satellite at 861.4 eV corresponding to $\text{Ni}(\text{OH})_2$ (Figure III.12). The oxide layer is mainly composed of 42 at. % Cu^{+1} + 28 at. % Cu^{+2} + 30 at. % $\text{Ni}(\text{OH})_2$ and its thickness calculated from XPS data is of ~ 1.4 nm; the composition of the alloy beneath the oxide layer is of 67 at. % Cu + 33 at. % Ni.

Figure III.13 shows a depth profile of 70Cu-30Ni alloy (negative ions) after 1h of immersion at E_{corr} in ASW under flow and stirring. This profile was obtained in the same conditions as the ones in static conditions (same sputtering rate and analysis area). In this figure, two regions can be distinguished. The first region, from 4 to ~ 13 s, the 35Cl^- , 90^{58}NiO_2^- , 95^{63}CuO_2^- and 18^{18}O^- signals shows their maximum intensity, and the 116^{58}Ni_2^- signal continue increasing. At 13 s, the second region can be distinguished, where the 90^{58}NiO_2^- , 95^{63}CuO_2^- and 18^{18}O^- signals sharply decrease and the 116^{58}Ni_2^- signal shows an intense and constant intensity. Therefore, the first zone corresponds to the oxide covering the alloy, whereas the second region corresponds to the metallic substrate. It should be noticed that between 13 s and 62 s, the 35Cl^- , 90^{58}NiO_2^- , 95^{63}CuO_2^- and 32O_2^- signals show an inflexion point forming a shoulder and subsequently decreasing, and the 116^{58}Ni_2^- signal remains constant. This indicates that under the alloy/oxide interface, oxides are detected, which may result from the preparation of the samples (disk cut from real condenser tubes, and then flattened).

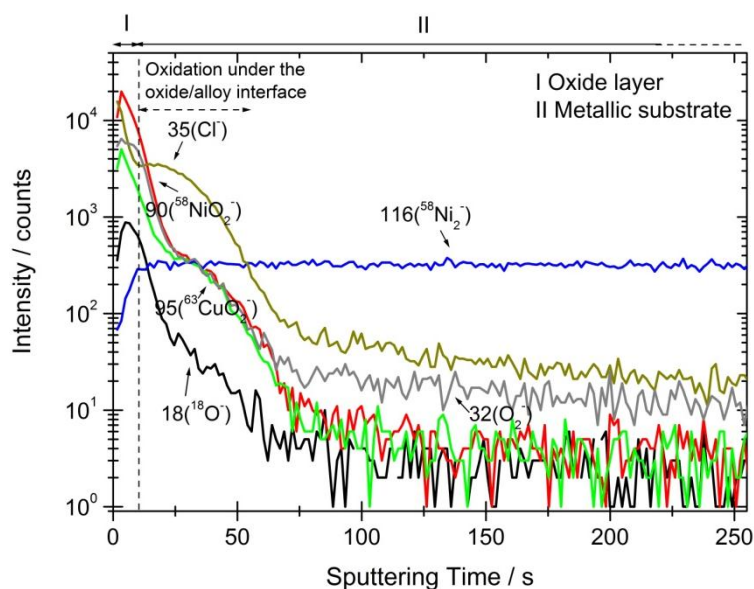


Figure III. 13: Characteristic Time-of-Flight Secondary Ions Mass Spectrometry (ToF-SIMS) depth profile (negative ions) of 70Cu-30Ni after 1 h of immersion at E_{corr} in aerated artificial seawater under flow and stirring.

If comparing the depth profiles after immersion in ASW in static conditions and under flow and stirring, both profiles are different and under flow and stirring the oxide layer is much thinner. The profile under flow and stirring is more similar to the one obtained for the sample just after polishing, which confirms that flow and stirring avoid the redeposition of Cu_2O .

III.1.2.2. Electrochemical measurements using a RRE

III.1.2.2.1. Theory for a Rotating Ring Electrode

The first mathematical treatment of convection and diffusion towards a rotating electrode was given by Levich. The general mass transport equation for the flux of species j , J_j , is given by:

$$J_j = -D_j \nabla C_j - \frac{z_j F}{RT} D_j C_j \nabla \phi + C_j \mathbf{v} \quad \text{Eq. III.11}$$

where:

D_j is the diffusion coefficient of the solution species j ($\text{cm}^2 \cdot \text{s}^{-1}$);

C_j is the molar concentration of species j ($\text{mol} \cdot \text{cm}^{-3}$);

ϕ is the electrostatic potential;

z_j is the number of transferred electrons;

\mathbf{v} is the hydrodynamic velocity vector and represents the motion of the solution; and

∇ is the vector of partial derivatives that defines the gradient operators.

The term $-D_j \nabla C_j$ represents diffusion, $-\frac{z_j F}{RT} D_j C_j \nabla \phi$ represents migration, and $C_j \mathbf{v}$ represents convection. For solutions containing an excess of supporting electrolyte the ionic migration term can be neglected.

The variation of C_j with time is given by:

$$\frac{\partial C_j}{\partial t} = -\nabla J_j \quad \text{Eq. III.12}$$

Therefore, the general convective-diffusion equation is obtained by combining Eq III.11 and III.12, assuming that migration is absent and that D_j is not a function of the position:

$$\frac{\partial C_j}{\partial t} = D_j \nabla^2 C_j - \mathbf{v} \cdot \nabla C_j \quad \text{Eq. III.13}$$

Under steady-state conditions ($\frac{\partial C_j}{\partial t} = 0$), the convective-diffusion equation written in terms of cylindrical coordinates becomes:

$$v_r \frac{\partial C_j}{\partial r} + v_y \frac{\partial C_j}{\partial y} = D_j \left\{ \frac{\partial^2 C_j}{\partial r^2} + \frac{1}{r} \frac{\partial C_j}{\partial r} + \frac{\partial^2 C_j}{\partial y^2} \right\} \quad \text{Eq. III.14}$$

where:

r is the radial flow direction;

y is the flow direction normal to the surface ;

v_r is the component of the velocity in the radial direction; and

v_y is the component of the velocity normal to the electrode surface.

Let us consider a ring electrode with an inner radius r_1 and outer radius r_2 (*surface area* = $\pi(r_2^2 - r_1^2)$). When this electrode is rotated with an angular velocity (rotation speed), Ω , then the steady-state, convective-diffusion equation that must be solved is:

$$v_r \frac{\partial C_j}{\partial r} + v_y \frac{\partial C_j}{\partial y} = D_j \frac{\partial^2 C_j}{\partial y^2} \quad \text{Eq. III.15}$$

where the mass transport by diffusion in the radial direction, represented by the terms $D_j \left\{ \frac{\partial^2 C_j}{\partial r^2} + \frac{1}{r} \frac{\partial C_j}{\partial r} \right\}$, is, at usual flow rates, small compared to convection in the radial direction ($v_r \frac{\partial C_j}{\partial r}$), so that these terms are neglected. The boundary conditions for the limiting ring current are:

$$C_j = C_j^* \quad \text{for} \quad y \rightarrow \infty \quad \text{where } C_j^* \text{ is the bulk concentration of the specie } j;$$

$$C_j = 0 \quad \text{at} \quad y = 0 \quad \text{for} \quad r_1 \leq r < r_2;$$

$$\frac{\partial c_j}{\partial y} = 0 \quad \text{at} \quad y = 0 \quad \text{for} \quad r < r_1;$$

$$C_j = C_j^* \quad \text{at} \quad y = 0 \quad \text{for} \quad r < r_1;$$

When the values of velocities of v_r and v_y are introduced, Equation III.15 becomes:

$$r \left(\frac{\partial c_j}{\partial r} \right) - y \left(\frac{\partial c_j}{\partial y} \right) = \left(\frac{D_j}{B'} \right) \left(\frac{1}{y} \right) \left(\frac{\partial^2 c_j}{\partial y^2} \right) \quad \text{Eq. III.16}$$

where $B' = 0.51\Omega^{3/2}N^{-1/2}$ and N is the kinematic viscosity ($10^{-2} \text{ cm}^2/\text{s}$).

For the reduction reaction $O + ne^- \rightarrow R$, the current at the ring electrode is given by:

$$i_0 = -zFD_0 2\pi \int_{r_1}^{r_2} \left(\frac{\partial c_O}{\partial y} \right)_{y=0} r dr \quad \text{Eq. III.17}$$

The solution to this equation yields the Levich expression for the cathodic limiting current:

$$i_{O,L} = -0.62zF\pi C_O^* D_O^{2/3} (r_2^3 - r_1^3)^{2/3} N^{-1/6} \Omega^{1/2} \quad \text{Eq. III.18}$$

where:

F is the Faraday constant (96500 C/mol);

C_O^* is the bulk concentration of the specie O to be reduced ($\text{mol}\cdot\text{cm}^{-3}$);

D_O is the diffusion coefficient of the solution specie O to be reduced ($\text{cm}^2\cdot\text{s}^{-1}$); and

Ω is the rotation speed (s^{-1}).

This equation is comparable to the Levich equation presented by Tribollet [125] for the diffusion limiting current for a Newtonian fluid considering a thin ring ($(r_2 - r_1) \ll r_1$):

$$i_{O,L} = -z \frac{F\pi}{\Gamma\left(\frac{4}{3}\right)} (3a_0)^{1/3} C_O^* D_O^{2/3} N^{-1/6} r_1^{4/3} (r_2 - r_1)^{2/3} \Omega^{1/2} \quad \text{Eq. III.19}$$

with $\Gamma\left(\frac{4}{3}\right) \sim 0.893$, and $a_0 = 0.51021599$ for a Newtonian fluid.

III.1.2.2.2. Experimental results obtained with a RRE

Electrochemical measurements in well-controlled hydrodynamic conditions were performed using a rotating ring electrode (RRE) at three different rotation speeds (40, 160, and 640 rpm).

The corrosion potential as a function of time (E_{corr} vs time) was followed for 1 h as already done in previous electrochemical measurements with the 70Cu-30Ni alloy. In Table III.5, the corrosion potential values obtained with the RRE in two different solutions (ASW and FNSW) are presented and compared with the values in static conditions using a disc electrode. When using the rotating ring electrode, the corrosion potential (E_{corr}) decreases while the rotation speed increases in the two solutions. However, in static conditions the corrosion potential values in artificial seawater and in filtered natural seawater are similar to the ones obtained at 160 rpm.

Table III. 5: Corrosion potential values for 70Cu-30Ni alloy after 1 h of immersion in artificial seawater (ASW), and filtered natural seawater (FNSW), in static conditions and using a RRE at three different rotation speeds (40, 160 and 640 rpm).

	$E_{corr} / \text{V vs SCE}$
ASW static conditions	-0.230 ± 0.009
ASW 40 rpm	-0.217 ± 0.005
ASW 160 rpm	-0.233 ± 0.006
ASW 640 rpm	-0.248 ± 0.004
FNSW static conditions	-0.231 ± 0.013
FNSW 40 rpm	-0.216 ± 0.005
FNSW 160 rpm	-0.223 ± 0.001
FNSW 640 rpm	-0.252 ± 0.005

Figure III.14 presents the cathodic polarisation curves plotted in artificial seawater with the rotating ring electrode and are compared to that obtained in static conditions. In static conditions, two cathodic plateaus can be observed, corresponding to the 2 steps of dissolved oxygen reduction, with a transfer of 2 or 4 electrons; the first plateau is observed close to E_{corr} .

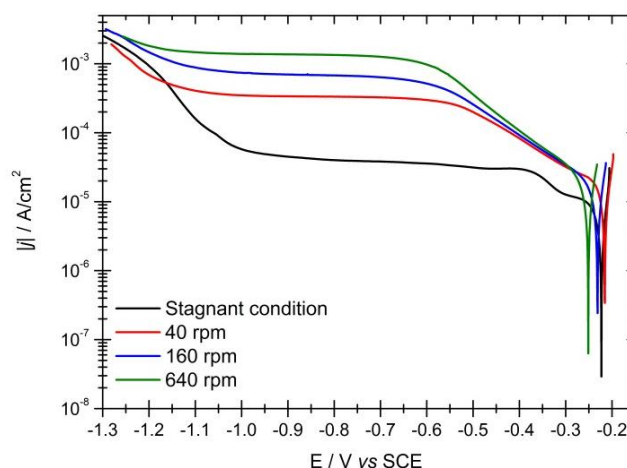


Figure III. 14: Cathodic polarisation curves of 70Cu-30Ni after 1 h of immersion at E_{corr} in aerated artificial seawater, using the rotating ring electrode at three different rotation speeds (40, 160 and 640 rpm) and in static conditions. Scan rate: $0.5 \text{ mV}\cdot\text{s}^{-1}$.

In ASW, the current densities in static conditions are lower than the current densities obtained with the rotating ring electrode. Furthermore, using the RRE, only one cathodic plateau (transfer of 4 electrons) is clearly visible and the plateau current density increases in absolute value with the rotation speed. This first current plateau observed close to E_{corr} in static conditions (first step of dissolved oxygen reduction with a transfer of 2 electrons) is replaced by an inflexion point. In Table III.6 are compared the limiting current densities values at -0.75 V vs SCE , corresponding to the second plateau for the oxygen reduction reaction, to the theoretical values calculated using Eq. III.19. For that, the oxygen concentration in the solution was considered to be 8 ppm ($2.5 \times 10^{-5} \text{ mol}\cdot\text{cm}^{-3}$) [100], and its diffusion coefficient equal to $2 \times 10^{-5} \text{ cm}^2\cdot\text{s}^{-1}$ at $25 \text{ }^\circ\text{C}$ [100][126][127].

Table III. 6: Comparison between the limiting current densities at -0.75 V vs SCE taken from Figure III.14 (corresponding to the second step of dissolved oxygen reduction reaction with transfer of 4 electrons), and the theoretical values calculated from Eq. III.19.

Limiting current densities ($\mu\text{A}/\text{cm}^2$)		
	Experimental values taken from Figure III.14 at -0.75 V vs SCE	Theoretical values calculated from Eq. III.19
Static conditions	39	-
RRE, 40 rpm	330	388
RRE, 160 rpm	662	777
RRE, 640 rpm	1314	1554

The experimental limiting current densities are in good agreement with the theoretical ones. The differences between experimental and theoretical values can be explained by an oxygen bulk concentration slightly different from 8 ppm (C_O^* depends on salts concentrations and temperature) and/or by a oxygen diffusion coefficient compromised between 1.87×10^{-5} and $2.60 \times 10^{-5} \text{ cm}^2 \cdot \text{s}^{-1}$ at 25 °C [128].

The cathodic polarisation curve plotted in FNSW at 160 rpm with a scan rate of $0.5 \text{ mV} \cdot \text{s}^{-1}$ was compared to the steady-state curve obtained at 160 rpm in ASW, and the curve plotted at 160 rpm in ASW but using a scan rate of $0.5 \text{ mV} \cdot \text{s}^{-1}$. The results, shown in Figure III.15, indicate similar shape and similar current densities in the second plateau potential domain in all cases. However, some differences can be observed close to E_{corr} : the steady-state curve in ASW exhibits higher current densities than the curve plotted at $0.5 \text{ mV} \cdot \text{s}^{-1}$ in ASW, and either a current plateau (ASW, steady-state) or an inflexion point (ASW and FNSW, 0.5) is visible. It can be conclude from these curves that the cathodic behaviour of 70Cu-30Ni alloy is the same in ASW and in FNSW.

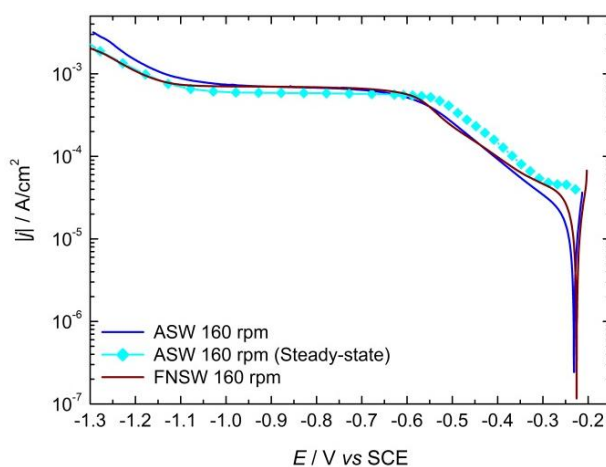


Figure III. 15: Cathodic polarisation curves of 70Cu-30Ni rotating ring electrode at 160 rpm, after 1 h of immersion time at E_{corr} in: i) aerated artificial seawater (scan rate: $0.5 \text{ mV} \cdot \text{s}^{-1}$), ii) aerated artificial seawater (steady-state curve), and iii) filtered natural seawater (scan rate: $0.5 \text{ mV} \cdot \text{s}^{-1}$).

Figure III.16 illustrates the anodic behaviour of the alloy after 1 h of immersion in ASW and in FNSW (static conditions and using the RRE, at three different rotation speeds). The anodic polarisation curves plotted in ASW using the rotating ring electrode present certain dissimilarities if compared to the curves obtained in static conditions (Figure III.16(a)). Firstly, a current peak followed by a minimum current are between -0.15 and 0.05 V vs SCE with the

rotating ring electrode; this feature, which it is not present in static conditions, becomes more evident with the increase of the rotation speed (minimum current: $400 \mu\text{A}\cdot\text{cm}^{-2}$, $300 \mu\text{A}\cdot\text{cm}^{-2}$ and $60 \mu\text{A}\cdot\text{cm}^{-2}$ at 40, 160 and 640 rpm, respectively). Secondly, the current density in static conditions is lower than using the rotating ring electrode at potentials higher than 0.05 V vs SCE . Furthermore, the wide plateau observed between 0.3 and 0.5 V vs SCE in static conditions is not well defined using the rotating ring electrode. There is an influence of the rotation speed on the anodic polarisation curves for potentials lower than 0.05 V vs SCE . However, the curves exhibit no anodic plateau at not too high anodic potential (close to E_{corr}) unlike pure copper in acidic and neutral chloride solution for which a limiting-current region can be observed around 0 V vs SCE [129][130]. These results show partial mass transport limitation (*i.e.* mixed kinetics) for the anodic reactions.

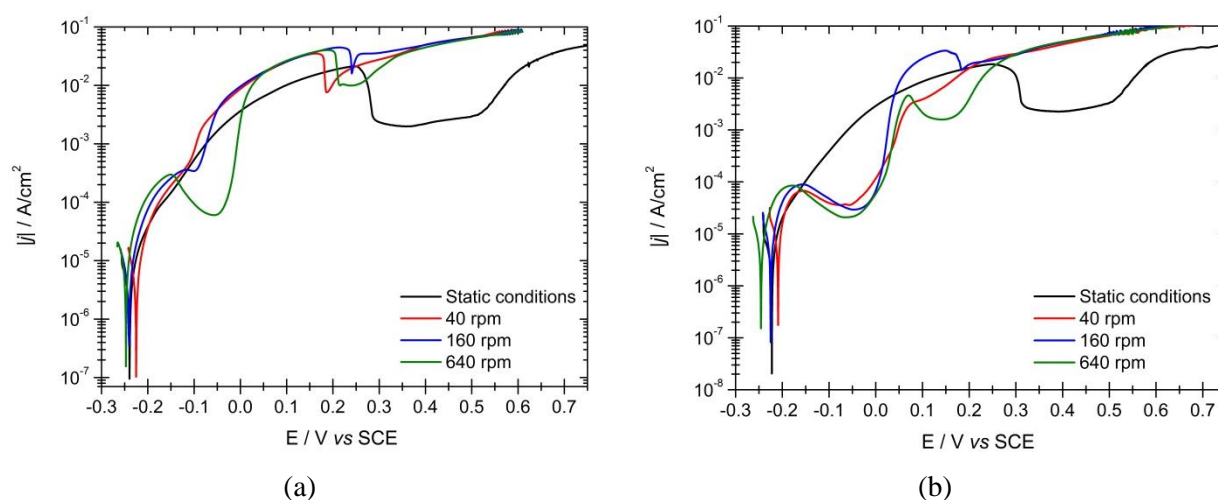


Figure III. 16: Anodic polarisation curves of 70Cu-30Ni rotating ring electrode at three different rotation speeds (40, 160 and 640 rpm), after 1 h of immersion at E_{corr} in: (a) aerated artificial seawater, and (b) aerated filtered natural seawater. Scan rate: $0.5 \text{ mV}\cdot\text{s}^{-1}$.

Figure III.16 (b) illustrates the anodic polarisation curves in FNSW. The current peak, followed by a minimum current observed with the RRE close to the corrosion potential in ASW, are also visible in FNSW; however, this feature is the same whatever the rotation speed of the RRE. Between 0.05 and 0.3 V vs SCE , there are significant changes of the current density with the rotation speed. Again the results show partial mass transport limitation (*i.e.* mixed kinetics) for the anodic reactions.

Impedance diagrams were recorded at E_{corr} using the RRE at three different rotation speeds, and the results were compared to those obtained in static conditions (disk electrode) (Figure

III.17). The shape remains similar but the magnitude of the impedance, in particular the size of the high frequency loop depends on the hydrodynamic conditions. The low frequency loop is better defined in static conditions.

In ASW (Figure III.17 (a)), the size of the high frequency loop in static conditions is considerably higher than with the RRE. Nevertheless, comparing only the impedance diagrams obtained with RRE, the magnitude of the high frequency loop increases with increasing rotation speed. Similar tendency is observed in FNSW (Figure III.17 (b)), however, the variation with the rotation speed is less pronounced. Thus, there is an effect of hydrodynamics which is more important in ASW than in FNSW.

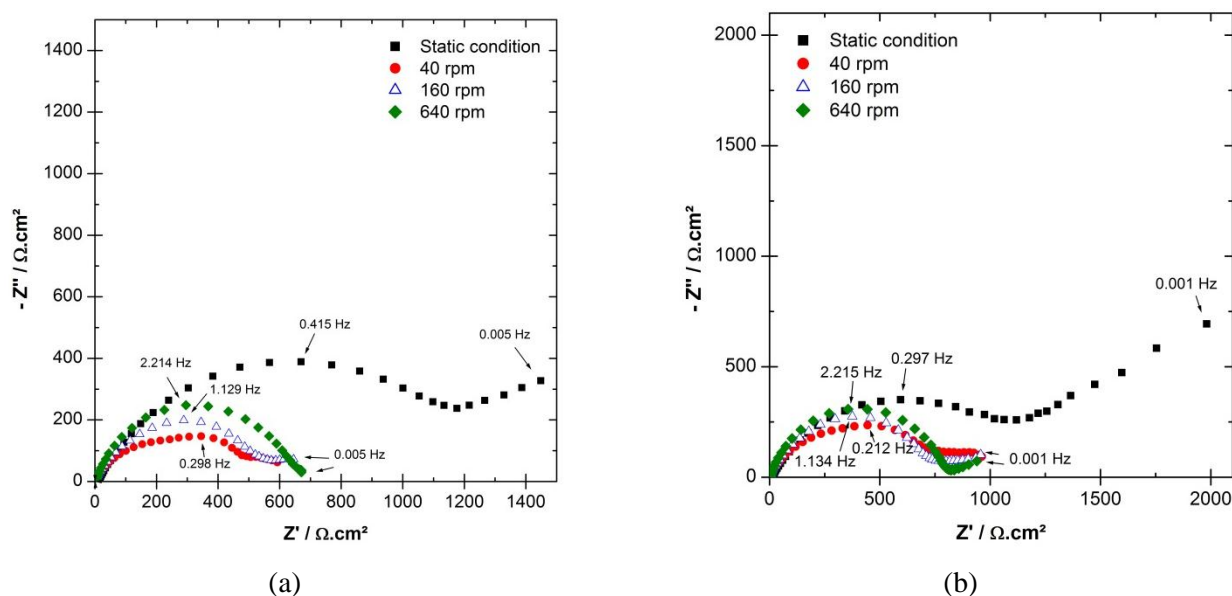


Figure III. 17: Experimental impedance diagrams in the complex plane (Nyquist diagrams) of 70Cu-30Ni rotating ring electrode at three different rotation speeds (40, 160 and 640 rpm), after 1 h of immersion at E_{corr} using the in: (a) aerated artificial seawater, and (b) aerated filtered natural seawater.

III.2. Discussion

III.2.1. Impedance model for 70Cu-30Ni

It is accepted by many authors that the corrosion of pure Cu is controlled by mass transport processes to and from corroding surfaces, involving O_2 , Cl^- , OH^- , Cu^+ and CuCl_2^- species affecting both the anodic and the cathodic partial reactions [11][124].

Four regions have been identified on the anodic polarisation curve of pure Cu in acidic and neutral chloride solution for different rotation speeds: an active dissolution region close to the corrosion potential (apparent Tafel region) followed by a limiting-current region (current plateau); then a mixed-kinetics region appears up to a second limiting current region. The first two regions (active dissolution and first plateau) are attributed to the formation of Cu^{+1} species, and the current increase beyond the first plateau accounts for copper dissolution as Cu^{+2} [129][131].

The anodic dissolution of pure copper in acidic and neutral chloride media has been extensively studied in the literature. The final model in agreement with all published experimental data is [124], [129], [131]:



In this mechanism, the soluble cuprous complex CuCl_2^- is the diffusing species and the insoluble adsorbed intermediate CuCl is the blocking species (surface coverage: γ), which is electrochemically formed in a first step (Eq. III.20) and chemically dissolved in a second step (Eq. III.21).

Deslouis *et al.* developed an expression (Eq III.22) for low anodic current densities considering that: i) the first step (Eq. III.20) is no longer at quasi-equilibrium; ii) the coverage by CuCl is small; and iii) mass transport control is only due to CuCl_2^- diffusion from the surface [124].

$$\frac{F}{i} = \frac{1}{k_1[\text{Cl}^-]_\infty \exp\left(\frac{\alpha FE}{RT}\right)} + \frac{k_{-1} \exp\left(-\frac{FE}{RT}\right)}{k_1 k_2 [\text{Cl}^-]_\infty^2} + \frac{k_{-1} k_{-2} \delta_{\text{CuCl}^-} \exp\left(-\frac{FE}{RT}\right)}{k_1 k_2 [\text{Cl}^-]_\infty^2 D_{\text{CuCl}_2^-}} \quad \text{Eq. III.22}$$

On the other hand, the cathodic behaviour of pure Cu is ascribed, in addition to O_2 reduction, to CuCl reduction and to Cu_2O reduction. It has been established that on the cathodic plateau (transfer of 4 electrons) Cu_2O does not interfere with O_2 reduction, and the interface may be considered as uniformly accessible for oxygen reduction. However, at less negative potentials

(where some CuCl is also likely to be present), the cathodic partial reaction could be controlled by diffusion through a layer (Cu₂O and/or CuCl) [124][124].

According to Pourbaix diagrams, insoluble corrosion products are expected to be formed on pure Cu surfaces at pH > 5.5. The presence of surface layers in neutral medium introduces additional complexity with respect to Cu corrosion in acidic chloride solution where corrosion products are soluble (oxide-free surface). Surface layers may partially block the metal surface and/or may influence mass transport of either oxygen or oxidized Cu species [124]. Therefore, except for the effect of a surface layer, the model for the anodic electrodisolution may also explain qualitatively the behaviour of Cu at the corrosion potential. At least, two different insoluble corrosion products are formed at E_{corr} , *i.e.* CuCl and Cu₂O. At immersion times higher than 1 h, the surface layer consists mainly of Cu₂O formed by hydrolysis of Cu⁺¹ species. This hydrolytic reaction is competitive with the complexation of CuCl by Cl⁻ and the removal of the produced CuCl₂⁻ by mass transport [124]. Cu₂O can also be formed from CuCl₂⁻ as follows [11]:



For pure Cu, only an effect of Cu₂O as an insoluble product was claimed for low anodic currents, and the effect of the Cu₂O layer on mass transport was considered. Thus, for the calculation of I_{corr} , the anodic partial reaction was considered to be partially limited by the diffusion of CuCl₂⁻ through both the Cu₂O layer and the electrolyte (mixed control), while the cathodic partial reaction (oxygen reduction) was considered to be purely kinetic.

Two difficulties arise when comparing the corrosion behaviour of Cu in acidic solution and that of 70Cu-30Ni alloy in seawater environments: a) the alloy is not pure Cu; and b) at pH 8, the alloy is covered by a corrosion product layer and, hence, there is a possible effect of the surface layers on the cathodic and the anodic mass transport.

Figure III.18 illustrates the anodic polarisation curves of two copper alloys, 70Cu-30Ni alloy and Al brass (76% Cu, 22% Zn and 2% Al), obtained after 1 h of immersion in FNSW in static conditions. The similarity of the two curves suggests that their anodic behaviour is predominated by the behaviour of copper. This observation is in agreement with what was observed by Petetin *et al.* [132], who compared the anodic polarisation curves of pure Cu, pure Ni and 70Cu-30Ni alloy after 10 min of immersion at E_{corr} in a 3% NaCl solution; they

showed that the anodic behaviour of the alloy was more similar to the one of pure Cu than to the one of pure Ni.

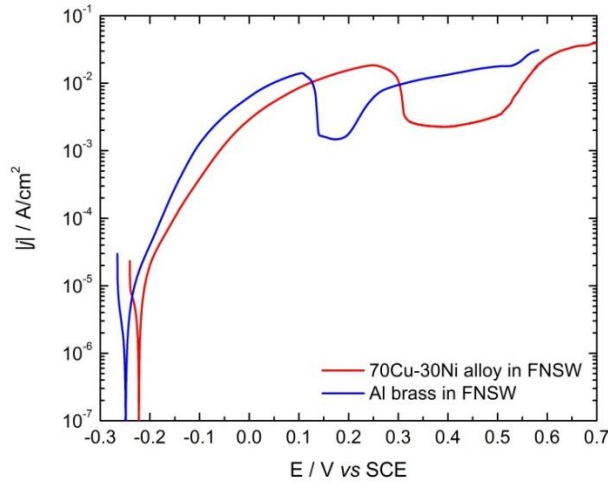
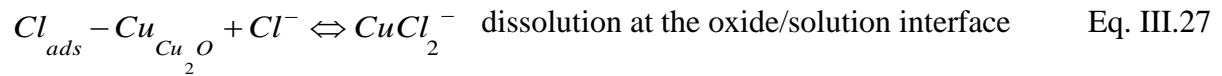
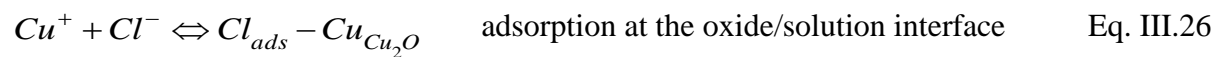
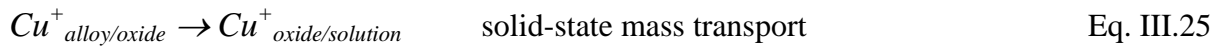
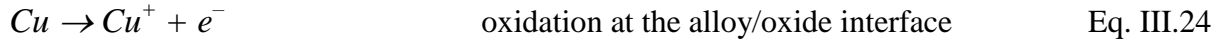


Figure III. 18: Anodic polarisation curves of 70Cu-30Ni alloy and Al brass after 1 h of immersion at E_{corr} in static aerated FNSW time. Scan rate of $0.5 \text{ mV}\cdot\text{s}^{-1}$.

From that mechanism shown for pure copper dissolution in chloride media at low anodic potential and in order to take into account the presence of an oxide layer as shown by surface analysis, a modified mechanism can be drawn for the anodic partial reaction of 70Cu-30Ni alloy at E_{corr} in ASW without and with biomolecules:



This mechanism involves four steps: 1) oxidation of Cu as Cu^+ at the alloy/oxide interface, 2) mass transport of Cu^+ by diffusion and migration in the solid phase from the alloy/oxide interface to the oxide/solution interface, 3) adsorption of chloride on a Cu^+ surface site of the Cu_2O oxide at the oxide/solution interface, and 4) dissolution of copper as CuCl_2^- at the oxide/solution interface, followed by mass transport of CuCl_2^- by diffusion in the liquid phase from the oxide/solution interface to the bulk solution.

In aerated solution, the cathodic partial reaction is the reduction of dissolved oxygen that takes place at the oxide/solution interface.

At E_{corr} , the anodic and cathodic currents have the same magnitude and the net current is equal to zero. By principles of summation of currents, the Faradaic anodic and cathodic impedances must be in parallel. The anodic polarisation curves plotted with the RRE show partial mass transport limitation *i.e.* mixed kinetics for the anodic reaction(s) and it is well-known that oxygen reduction reaction is mass transport limited (also shown by the cathodic polarisation curves plotted with the RRE). Therefore, the anodic Faradaic impedance can be depicted by a charge transfer resistance (R_t^a) in series with an impedance that illustrates Cu^+ and/or CuCl_2^- mass transport and partial blocking effect by adsorbed species, such as CuCl ($Z_{\theta,D}^a$); whereas the cathodic impedance can be depicted by a charge transfer resistance (R_t^c) in series with an impedance that illustrates O_2 mass transport (Z_D^c). A double layer capacitance C_{dl} is added in parallel with the anodic and the cathodic impedances. As the impedance response for electrochemical systems often reflects a distribution of reactivity that is commonly represented in equivalent electrical circuits as a constant-phase element (CPE), C_{dl} is replaced here by CPE_{dl} which is a constant phase element related to the double layer. The CPE impedance equation is presented in Chapter II, Eq. II.6.

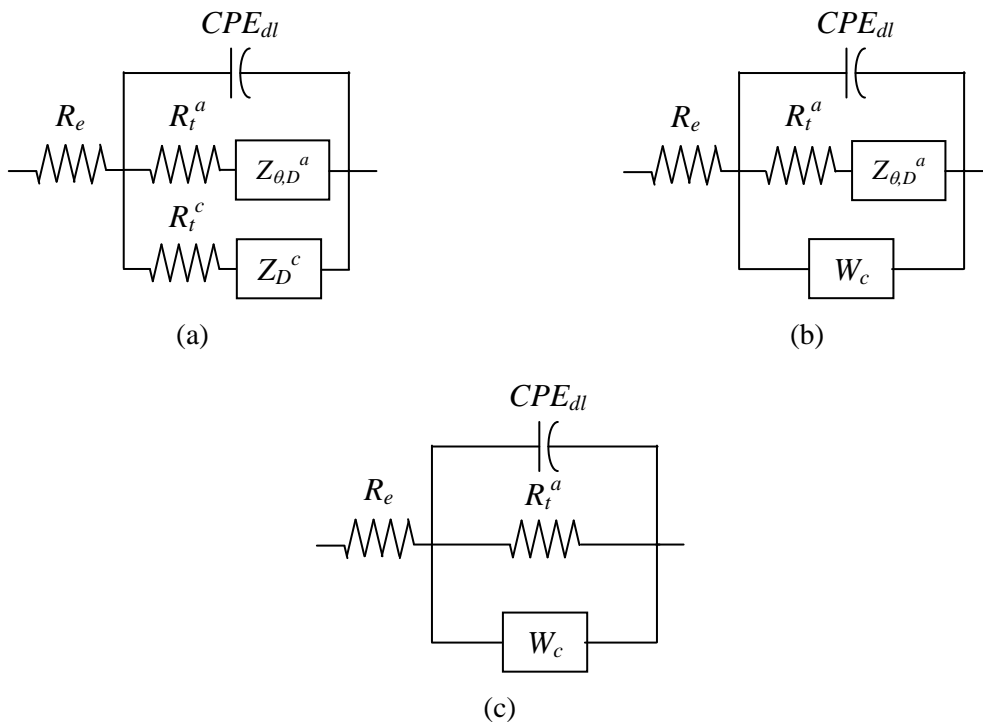


Figure III. 19: Equivalent electrical circuits to model the 70Cu-30Ni/ASW and 70Cu-30Ni/FNSW systems: (a) general circuit, (b) simplified circuit taking into account experimental cathodic polarisation curves, and (c) circuit used to analyse the HF loop of experimental impedance diagrams. R_e is the electrolyte resistance, CPE_{dl} a constant phase element related to the double layer, R_t^a the anodic charge transfer resistance, $Z_{\theta,D}^a$ an impedance that illustrates anodic mass transport and partial

blocking effect by CuCl, R_{tc} the cathodic charge transfer resistance, Z_D^c a cathodic impedance that illustrates O_2 mass transport, and W_c the cathodic Warburg impedance.

Thus, in a first approach, the 70Cu-30Ni/ASW and 70Cu-30Ni/FNSW systems can be modeled by the general equivalent electrical circuit illustrated in Figure III.19 (a), where R_e is the electrolyte resistance.

As the first current plateau for the reduction of dissolved oxygen is observed close to E_{corr} (Figure III.1 (a) and Figure III.14), one hypothesis is that this plateau can be extrapolated down to E_{corr} (pure mass transport limitation for the cathodic partial reaction); thus, R_t^c can be neglected and the cathodic mass transport impedance is a Warburg impedance (W_c) given by:

$$Z_{W_c} = 1 / (k_c \sqrt{j\omega}) \quad \text{Eq. III.28}$$

with k_c expressed in $s^{0.5} \cdot \Omega^{-1} \cdot cm^{-2}$. Taking into account experimental cathodic polarisation curves, the 70Cu-30Ni/ASW and 70Cu-30Ni/FNSW systems can be modeled by the simplified circuit presented in Figure III.19 (b).

For the same experimental impedance data as those presented in Figure III.17 in the complex plane (static conditions and RRE), the absolute value of the imaginary part of the impedance ($|Z''|$) was plotted as a function of the frequency in logarithmic coordinates (Figure III.20) [103].

In the HF range, a pseudo-straight line with a slope lower than 1 in absolute value but varying slightly with the frequency can be observed in all cases. This slope value lower than 1 suggests a CPE-like behaviour (it should be equal to 1 in case of pure capacitive behaviour). The CPE parameters α and Q can be graphically obtained in the case of a R//CPE circuit, following the method presented by Orazem *et al.* [103]. The parameter α is calculated from the slope of the $\log|Z''|$ vs $\log f$ curve in the HF range:

$$\alpha = \left| \frac{d \log |Z''(f)|}{d \log f} \right| \quad \text{at HF} \quad \text{Eq. III.29}$$

and Q is obtained from α as follows:

$$Q = -\frac{1}{Z''(f)(2\pi f)^\alpha} \times \sin\left(\frac{\alpha\pi}{2}\right) \quad \text{Eq. III.30}$$

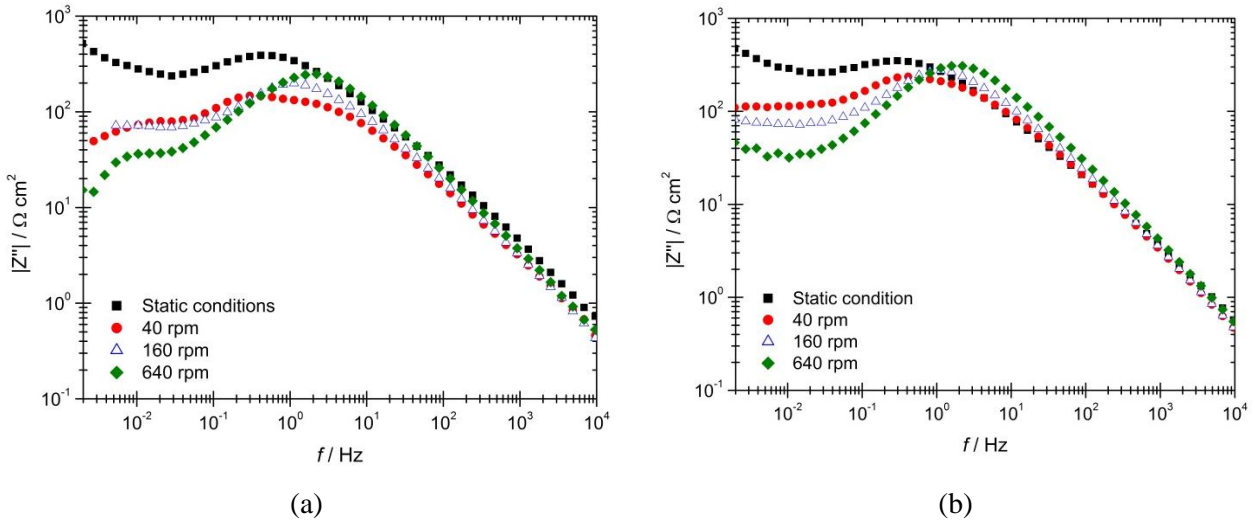


Figure III. 20: Experimental impedance data (imaginary part of the impedance as a function of frequency) of 70Cu-30Ni alloy obtained at E_{corr} after 1 h of immersion in: (a) aerated artificial seawater, and (b) aerated filtered natural seawater; in static conditions and using the rotating ring electrode at three different rotation speeds (40, 160 and 640 rpm). Same data as in Figure III.17.

However, as the slope varies with the frequency, the HF loop of impedance diagrams cannot be modelled by a R//CPE circuit, and α cannot be determined from Figure III.20. To better visualize a possible constant value of the slope in a narrow frequency range, the $d \log |Z''| / d \log f$ vs $\log f$ curves were calculated from those presented in Figure III.20 (derivative curves; Figure III.21). In the case of a R//CPE circuit, a plateau would be observed at HF corresponding to a value of $-\alpha$. In Figure III.21 (a) *i.e.* for the 70Cu-30Ni/ASW system, no plateau is visible, in particular, at very HF, and again the value of α cannot be graphically obtained. In Figure III.21 (b) *i.e.* for the 70Cu-30Ni/FNSW system, a plateau is visible at very HF, and the value of α can be graphically estimated ($\alpha = 0.87$ for the 3 rotation speeds).

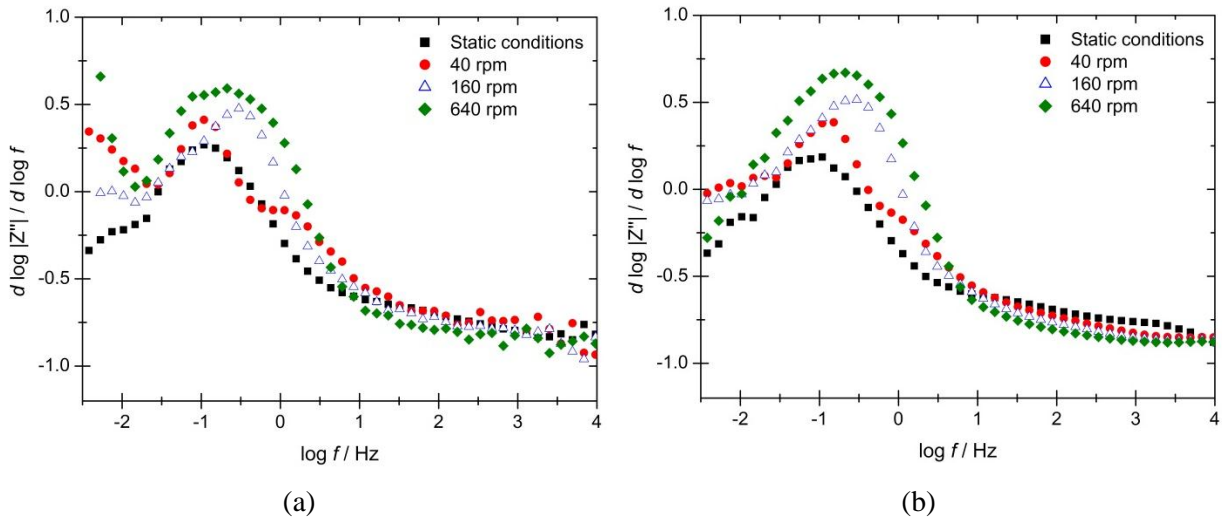


Figure III. 21: Experimental impedance data (derivative curves calculated from Figure III.20) of 70Cu-30Ni alloy obtained at E_{corr} after 1 h of immersion in: (a) aerated artificial seawater, and (b) aerated filtered natural seawater; in static conditions and using the rotating ring electrode at three different rotation speeds (40, 160 and 640 rpm). Same data as in Figure III.17.

In conclusion, the HF loop of the experimental impedance diagrams corresponds to the $CPE_{dl}/R_t^a/W_c$ equivalent circuit (Figure III.19 (c)); thus, it illustrates mainly the anodic charge transfer (diameter equal to R_t^a), and its depressed shape is partly due to the CPE and partly due to the cathodic Warburg impedance in parallel. For the 70Cu-30Ni/ASW system, since no plateau is visible at very HF in Figure III.21 (a), the effect of W_c is not negligible compared to that of CPE_{dl} even at 10^4 Hz, and there is no clear frequency domain specifically assigned to each process. For the 70Cu-30Ni/FNSW system, the effect of W_c is negligible compared to that of CPE_{dl} at very HF (plateau visible in Figure III.21(b)) and, in that case, there is clear frequency domain specifically assigned to each process (charge transfer, mass transport). The LF loop is related to the anodic mass transport and partial blocking effect by CuCl ($Z_{\theta,D}^a$).

In the case of 70Cu-30Ni alloy, the impedance data show a minor effect of anodic mass transport and blocking effect by CuCl (LF loop of impedance diagrams described only by a few points). Indeed, the amount of CuCl which is formed on the surface depends on potential and at E_{corr} this amount is low. This is in agreement with a very low amount of Cl^- compound evidenced by ToF-SIMS.

The circuits of Figures III.19 take into account the presence of an oxide layer, as shown by surface analysis, through $Z_{\theta,D}^a$ that partly illustrates Cu^+ mass transport within that layer.

As the LF loop of impedance diagrams is not well defined, the single HF loop was analysed by regression of the equivalent circuit presented in Figure III.19(c), in which CPE_{dl} , R_t^a and W_c are in parallel, using Simad® software developed at Laboratoire Interfaces et Systèmes Electrochimiques. The regression results are presented in Table III.7 and Figure III.22. The corresponding impedance equation is written as follows:

$$Z = R_e + \frac{1}{\frac{1}{R_t^a} + Q(j\omega)^\alpha + k_c \sqrt{j\omega}} \quad \text{Eq. III.31}$$

The experimental frequency range taken into account for the regression is indicated in Table III.7 for each data set, but the fitted curves in Figure III.22 are shown in the whole frequency range (0.003-10⁵ Hz), with parameters values corresponding to those given in Table III.7.

When moving from static disk to the RRE, the electrolyte resistance value changes from 12 to 3-4 $\Omega \cdot \text{cm}^2$. This variation of R_e is not linked to a change of solution conductivity but to a change of electrode geometry.

If the CPE behaviour is assumed to be associated with surface distributed time constants for charge-transfer reactions (time-constant distribution along the electrode surface), then it is possible to apply the equation derived by Brug *et al.* to calculate the effective capacitance associated with the CPE [105], [133]:

$$C_{eff} = Q^{1/\alpha} \left(R_e^{-1} + R_t^{a-1} \right)^{(\alpha-1)/\alpha} \quad \text{Eq. III.32}$$

The capacitance values calculated from the impedance diagrams shown in Figure III.22, taking for R_e and R_t^a the values extracted from the regression procedure (Table III.7), are given in Table III.7. These capacitance values are similar in all cases and are of the order of several tens of $\mu\text{F} \cdot \text{cm}^{-2}$; such values are typical of those for a double layer capacitance, which validates the equivalent electrical circuits proposed in Figure III.19. In particular, C_{eff} is independent of the rotation speed, which confirms that it is a double layer capacitance.

Hence, the HF loop illustrates mainly the anodic charge transfer and its diameter is equal to R_t^a . In order to explain the variations of R_t^a value when moving from the static disk to the RRE and when increasing the rotation speed of the RRE, theoretical considerations about R_t^a must be detailed.

The anodic polarisation curves plotted in static conditions and with the RRE show partial mass transport limitation. For mixed kinetics, the steady-state anodic current density can be written as:

$$i = Kc_0e^{bV} \quad \text{Eq. III.33}$$

$$\text{where } K = zFke^{-bV_0} \quad \text{and} \quad b = \frac{\alpha zF}{RT}$$

with c_0 the surface concentration of the diffusing species (CuCl_2^- for 70Cu-30Ni in ASW and FNSW), z the number of transferred electrons, k the rate constant for the reaction, α the symmetry factor, V the interfacial potential, and V_0 the interfacial equilibrium potential. The constant b is linked to the Tafel slope β by:

$$\beta = 2.303/b \quad \text{Eq. III.34}$$

According to first Fick's law and assuming a linear concentration gradient in the diffusion layer of thickness δ , the steady-state anodic current density can also be written as:

$$i = nFD \frac{c_\infty - c_0}{\delta} \quad \text{Eq. III.35}$$

with D the diffusion coefficient of the diffusing species (CuCl_2^-), and c_∞ the bulk concentration of the diffusing species.

By equating Eqs. III.33 and III.34, the surface concentration of the diffusing species can be obtained :

$$c_0 = \frac{c_\infty}{1 + \frac{\delta}{D} k e^{b(V-V_0)}} \quad \text{Eq. III.36}$$

On the other hand, the anodic charge-transfer resistance for a reaction dependent on potential and mass transport is defined in terms of kinetic parameters to be:

$$R_t^a = \frac{1}{Kbc_0e^{bV}} \quad \text{Eq. III.37}$$

Thus, mass transport influences charge transfer by means of the surface concentration (Eqs. III.36 and III.37).

If comparing static disk and RRE, the electrode geometry (disk/ring) as well as the hydrodynamics of the solution are changed. The diffusion layer is thinner for a ring than for a disk, and its thickness is higher in static conditions than under rotation of the electrode. Therefore, when moving from the static disk to the RRE at constant potential, the diffusion layer thickness decreases, which induces an increase of the surface concentration (Eq. III.36) and hence a decrease of the charge transfer resistance (Eq. III.37). On the other hand, a potential increase induces a decrease of R_t^a (Eq. III.37). Experimentally, when moving from the static disk to the RRE at 40 rpm in ASW as well as in FNSW, the corrosion potential increases (see Table III.5) and R_t^a decreases (see Table III.7). This decrease of R_t^a can be explained by additional mass transport (c_0) effect and potential effect.

Table III. 7: Experimental frequency range taken into account for the regression, parameters values (electrolyte resistance R_e , anodic charge transfer resistance R_t^a , constant of the cathodic Warburg impedance k_c , and CPE parameters α and Q) obtained from the regression of the equivalent circuit presented in Figure III.19(c) to experimental impedance data shown in Figure III.17, and effective capacitance C_{eff} associated with the CPE calculated from Eq. III.32.

	Frequency range / Hz	$R_e / \Omega.cm^2$	$R_t^a / \Omega.cm^2$	$k_c / s^{0.5}.\Omega^{-1}.cm^{-2}$	α	$Q / F.cm^{-2}.s^{(\alpha-1)}$	$C_{eff} / \mu F.cm^{-2}$
ASW static	$10^5-5.6 \times 10^{-2}$	12	1390	2.5×10^{-4}	0.78	1.99×10^{-4}	37
FNSW static	$10^5-7.8 \times 10^{-2}$	12	1310	3.5×10^{-4}	0.76	2.90×10^{-4}	50
ASW RRE 40 rpm	$10^5-1.52 \times 10^{-1}$	4	590	7.5×10^{-4}	0.85	1.54×10^{-4}	42
ASW RRE 160 rpm	$10^5-3.0 \times 10^{-1}$	3	650	3.1×10^{-4}	0.82	2.21×10^{-4}	45
ASW RRE 640 rpm	$10^5-1.5 \times 10^{-1}$	4	660	0.4×10^{-4}	0.83	1.92×10^{-4}	44
FNSW RRE 40 rpm	$10^5-7.8 \times 10^{-2}$	4	900	5.4×10^{-4}	0.87	1.34×10^{-4}	42
FNSW RRE 160 rpm	$10^5-1.1 \times 10^{-1}$	3	810	2.0×10^{-4}	0.84	1.78×10^{-4}	42
FNSW RRE 640 rpm	$10^5-7.8 \times 10^{-2}$	4	830	0.5×10^{-4}	0.85	1.36×10^{-4}	37

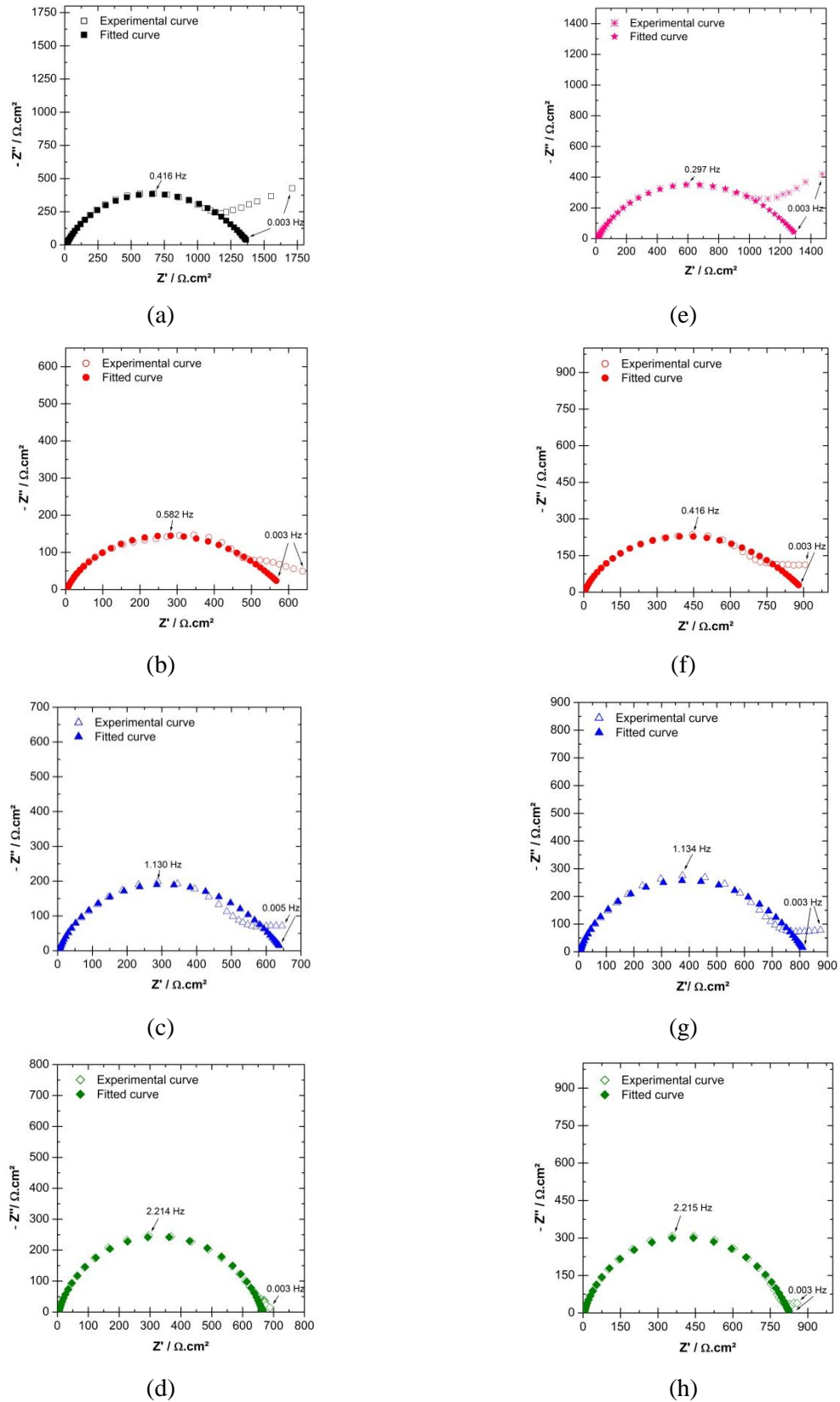


Figure III. 22: High frequency loops of Nyquist diagrams obtained for 70Cu-30Ni at E_{corr} after 1 h of immersion in aerated: (a) ASW in static conditions, (b) ASW with the RRE at 40 rpm, (c) ASW with the RRE at 160 rpm, (d) ASW with the RRE at 640 rpm, (e) FNSW in static conditions, (f) FNSW

with the RRE at 40 rpm, (g) FNSW with the RRE at 160 rpm, and (h) FNSW with the RRE at 640 rpm. Experimental curves and fit of the impedance model presented in Figure III.19(c) to the data. Same data as in Figures III.17.

Experimentally, when increasing the rotation speed of the RRE from 40 to 640 rpm, the corrosion potential decreases in ASW as well as in FNSW (see Table III.5) and R_t^a slightly increases in ASW and keeps constant in FNSW (see Figure III.17 and Table III.7). As the diffusion layer thickness is inversely proportional to the square root of the electrode rotation speed Ω ($\delta \propto \Omega^{-1/2}$), an increase of Ω would induce a decrease of δ and hence a decrease of R_t^a (Eqs. III.36 and III.37). Moreover, a decrease of the potential at constant Ω would induce an increase of R_t^a (Eq. III.37). Therefore, the increase of R_t^a in ASW can be explained by a major effect of the potential, and the constant value of R_t^a in FNSW is due to compensated potential and mass transport effects.

At the corrosion potential, E_{corr} , the overall current is equal to zero and the corrosion current density i_{corr} is given by:

$$i_{corr} = i_a = -i_c \quad \text{Eq. III.38}$$

where i_a is the anodic current density corresponding to the anodic partial reaction, and i_c is the cathodic current density corresponding to the cathodic partial reaction ($i_c < 0$).

Under assumption of Tafel kinetics (pure kinetic control) for the anodic partial reaction, i_{corr} is related to R_t^a and the anodic Tafel slope β_a by:

$$i_{corr} = \frac{\beta_a}{2.303R_t^a} \quad \text{Eq. III.39}$$

$$\text{with } \beta_a = \frac{2.303RT}{\alpha z F}$$

The assumption of minor effect of anodic mass transport is reasonable since the LF loop related to the anodic mass transport (and partial blocking effect by CuCl) is described only by a few points.

Grubitsch *et al.* calculated i_{corr} as:

$$i_{corr} = \frac{B}{R_p}, \quad \text{Eq. III.40}$$

where $B = 0.019$ V and R_p is the polarisation resistance [134]. The numerical value of the constant B was obtained by assuming a pure activation mechanism for both the anodic and the cathodic reactions (anodic and cathodic Tafel kinetics).

The anodic partial reaction of 70Cu-30Ni alloy immersed at E_{corr} in seawater involves the dissolution of Cu as Cu^+ species (modified mechanism drawn from that for pure copper dissolution in chloride media at low anodic potential; Eqs. III.24 to III.27). Then, the number of transferred electrons z in Eq. III.39 can be taken as 1. Moreover, α is comprised between 0 and 1, and is usually assumed to be equal to 0.5.

Table III.8 compares the i_{corr} values obtained (i) by application of Eq. III.39 with $z = 1$, and $\alpha = 0.5$; (ii) by application of Eq. III.36 using $R_p = R_t^a$; and (iii) graphically from the cathodic polarisation curves (i_{corr} being equal to the first plateau current density). The i_{corr} cannot be estimated graphically from the anodic polarisation curves because they do not exhibit Tafel behaviour (except in static ASW) or current plateau.

Table III. 8: Comparison of the corrosion current values obtained from R_t^a , by application of Eqs. III.39 and III.40, and from the cathodic polarisation curve (first plateau current density).

	$R_t^a / \Omega.\text{cm}^2$	$i_{corr} / \mu\text{A}.\text{cm}^{-2}$		
		Eq III.39		Cathodic polarisation curve
		$z = 1$ and $\alpha = 0.5$	Eq III.40	
ASW static	1390	36	14	12
FNSW static	1310	39	14	8
ASW RRE 40 rpm	590	86	32	26
ASW RRE 160 rpm	650	78	29	18
ASW RRE 640 rpm	660	76	29	20
FNSW RRE 40 rpm	900	56	21	-
FNSW RRE 160 rpm	810	62	23	24
FNSW RRE 640 rpm	830	61	23	-

If comparing the corrosion current densities obtained from Eq. III.39 to those deduced graphically from the cathodic polarisation curves, there is a ratio of about 3-5 between the values that may be partly explained by a value of α different from 0.5 and partly explained by the fact that polarisation curves were plotted with a scan rate of 0.5 mV.s^{-1} (non steady-state curves). Thus, for the RRE at 160 rpm in ASW, the steady-state cathodic polarisation curve yields a first plateau current density of about $50 \text{ } \mu\text{A.cm}^{-2}$ (see Figure III.15), which is much closer to the value of $78 \text{ } \mu\text{A.cm}^{-2}$ calculated from R_t^a (Eq. III.39).

Figure III.23 allows to better visualize the differences in corrosion current density calculated from Eq. III.35 (with $z = 1$ and $\alpha = 0.5$), for the two different solutions in static conditions and using the rotating ring electrode. In static conditions, the corrosion current density is similar in ASW and in FNSW.

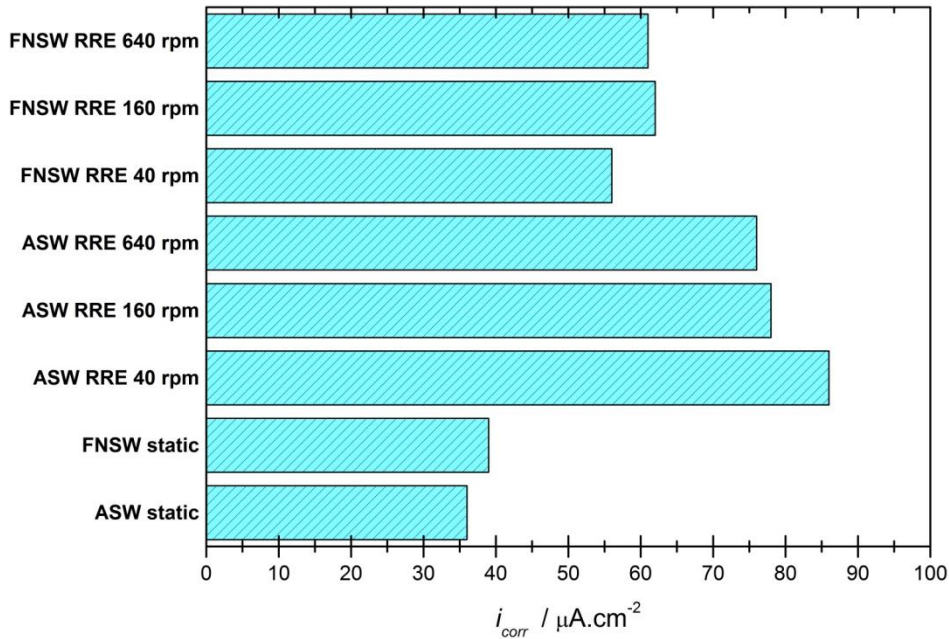


Figure III. 23: Comparison of the corrosion current density values calculated from Eq III.35 with $z = 1$ and $\alpha = 0.5$, for 70Cu-30Ni alloy after 1h of immersion in ASW or FNSW, in static condition and using the rotating ring electrode.

On the other hand, i_{corr} in ASW and FNSW using the RRE is higher than in static conditions (maximum ratio of 2). When increasing the rotation speed of the RRE, the corrosion current density slightly decreases in ASW and keeps constant in FNSW. As discussed before for R_t^a values, these results can be explained by combined potential and mass transport effect.

III.2.2. Surface layers models (combined XPS and ToF-SIMS)

Figure III.24(a) illustrates the surface layer model deduced from the surface analyses of the 70Cu-30Ni alloy just after polishing. In this model, one mixed oxide layer, made up of Cu^{+1} , Cu^{+2} and Ni^{+2} compounds covers the surface. The thickness of the oxide layer is about 1.5 nm.

The surface layer model proposed considering XPS and ToF-SIMS data for 70Cu-30Ni alloy after short-term immersion (1 h of exposure) at E_{corr} in static ASW is shown in Figure III.24(b). This model shows two oxidized layers: an outer layer mainly composed of cuprous oxide (Cu_2O) and an inner layer mainly composed of oxidized nickel; no Cu^{+2} compounds were found. A similar model with two oxidize layers is deduced for 70Cu-30Ni alloy after 1h of immersion in static FNSW (Figure III.24(c)). However, in this case, Cu^{+2} compounds were detected on the surface, and the oxidized Cu/oxidized Ni ratio in the outer oxide layer is lower than that observed in ASW.

The duplex structure observed after 1 h of immersion in static ASW and in FNSW, with a cuprous oxide-rich outer layer and a nickel oxide-rich inner layer, has already been observed by Souchet *et al.* for the early stages (1-2 h) of low temperature (100-200°C) air oxidation of CuNi alloys [135][136] but this result was not well-known for the oxidation of such alloys in aqueous solution.

Finally, Figure III.24(d) shows the surface layer model derived for the alloy after 1 h of immersion in ASW under flow and stirring. In this case, the oxide layer formed on top of the alloy is very thin and comparable to that obtained for the sample just after polishing (mixed oxide layer). Additionally, the amount of Cu_2O in the oxide layer is lower than that in static ASW and FNSW but higher than that for the sample after polishing. This could indicate that both components are rarely dissolved; nevertheless, there is a preferential dissolution of Cu^{+1} .

The Cl^- ToF-SIMS signal, visible throughout the outer layer in static ASW and FNSW, could be related to the formation of CuCl , as taken into account in the impedance models; however, by XPS it was not possible to detect the presence of chlorides after immersion in static ASW, and their amount was lower than 1% (at. %) after immersion in static FNSW. This is because ToF-SIMS is more surface sensitive than XPS. Therefore, the main Cu^{+1} compound formed on the surface layer is Cu_2O .

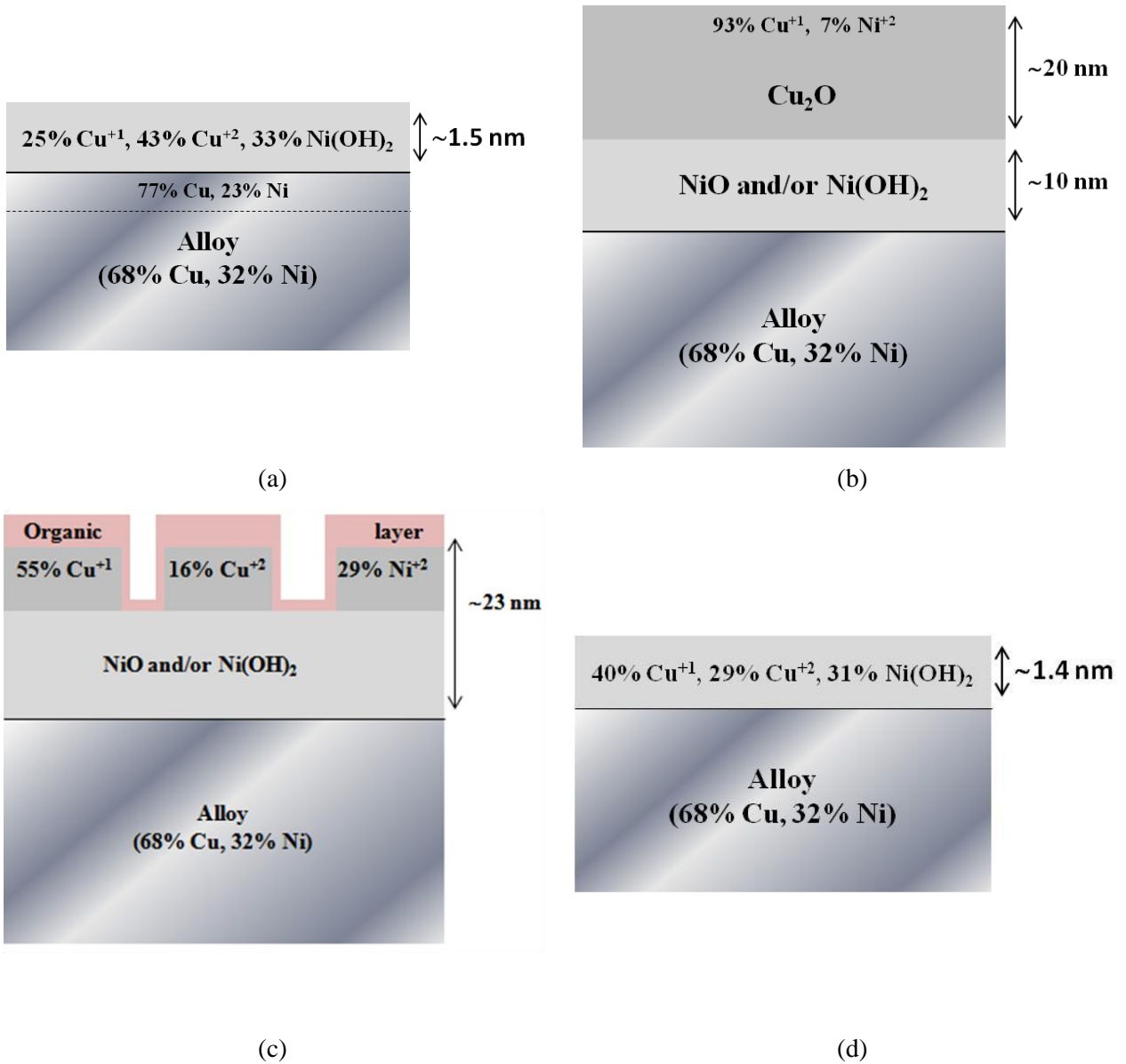


Figure III. 24: Models of the surface layers deduced from combined X-ray photoelectron spectroscopy (XPS) and Time-of-Flight Secondary Ions Mass Spectrometry (ToF-SIMS) results for 70Cu-30Ni: (a) just after polishing; (b) after 1 h of immersion at E_{corr} in static ASW; (c) after 1 h of immersion at E_{corr} in static FNSW; (d) after 1 h of immersion at E_{corr} in ASW under flow and stirring.

There are basically two mechanisms of de-alloying for binary alloys proposed in the literature [11]:

- i. simultaneous dissolution of both components of the alloy followed by redeposition of one component (usually the more noble one),
- ii. selective dissolution of one element from the alloy.

Beccaria and Crousier studied the de-alloying of Cu-Ni alloys exposed to natural seawater for 660 h and found simultaneous dissolution of both components with possible redeposition of copper for nickel contents lower than 50 %, whereas for nickel concentrations higher than 50% selective dissolution of copper took place [137]. Results obtained by Mansfeld *et al.* for long-term exposure (1-3 months) to natural seawater suggest that de-alloying of 70Cu-30Ni is initially due to simultaneous dissolution of copper and nickel and subsequent redeposition of copper in agreement with the results of Beccaria and Crousier [11].

Our results obtained for short-term exposure to ASW are in agreement with the conclusions drawn by Beccaria and Crousier, and Mansfeld *et al.*; the cuprous oxide Cu_2O detected on the surface by XPS and ToF-SIMS is formed by redeposition of dissolved copper.

III.2.3. Conclusions

In this chapter, we studied the corrosion behaviour of 70Cu-30Ni alloy after short-term immersion in artificial seawater (ASW) and filtered natural seawater (FNSW) in different hydrodynamic conditions (static, under flow and stirring, using a RRE), by combined electrochemical measurements and surface analysis. An impedance model was deduced from a general model based on the experimental observation that the electrochemical behaviour of the alloy was dominated by that of pure Cu, and that both the anodic and the cathodic partial reactions were affected by mass transport. Pure mass transport limitation was considered for the cathodic partial reaction, and mixed kinetics for the anodic partial reaction. This impedance model shows that the HF loop of experimental impedance diagrams corresponds to a $CPE_{dl}/R_t^a/W_c$ equivalent circuit, and, therefore, illustrates mainly the anodic charge transfer (diameter equal to R_t^a), with a depressed shape partly due to the CPE and partly due to the cathodic Warburg impedance in parallel. The LF loop is related to the anodic mass transport and partial blocking effect by CuCl. Electrochemical measurements, and in particular impedance data (LF loop defined only by a few points), show minor effect of mass transport for the anodic partial reaction. The R_t^a values were used to calculate the corrosion current, assuming Tafel kinetics for the anodic partial reaction. Results indicate that the dissolution current mainly corresponds to the dissolution of Cu with a transfer of 1 electron. The corrosion current density for 70Cu-30Ni alloy is similar in ASW and in FNSW, but moving from static conditions to using the RRE, the corrosion current density values increase. The values obtained for the current density in FNSW with the RRE, seems to be independent of

the rotation speed; however, the corrosion current density values are slightly lower after immersion in ASW.

Surface analysis performed for 70Cu-30Ni alloy after 1 h of immersion in static ASW showed the formation of a thick duplex oxide layer, mainly composed of Cu₂O on the outer layer. However, after 1 h of immersion in ASW under flow and stirring, this thick duplex oxide layer was no longer observed; a mixed oxide layer was obtained under flow and stirring with thickness similar to that of the sample just after polishing. This allows concluding that the layer formed in ASW in static conditions is due to the saturation and subsequently redeposition of Cu⁺¹. The thick duplex oxide layer was also observed after 1h immersion in static FNSW, nevertheless the oxidized Cu/oxidized Ni ratio was lower than in static ASW.

IV. Influence of biomolecules adsorption on the electrochemical behaviour and the surface chemical composition of 70Cu-30Ni alloy in seawater

Copper alloys often used in cooling circuits of industrial plants can be affected by biocorrosion induced by biofilm formation. The objective of this chapter is to study the influence of protein adsorption, which is the first step in biofilm formation, on the electrochemical behaviour of 70Cu-30Ni (wt. %) alloy and on the chemical composition of oxide layers. For that purpose, electrochemical measurements performed after 1 h of immersion were combined to surface analyses.

IV.1. Results

IV.1.1. Bovine Serum Albumin (BSA)

As mentioned before, bovine serum albumin (BSA) was selected as a model protein to study protein/surface interactions. The study was carried out in ASW, using different hydrodynamic conditions: static conditions, under flow and stirring, and in well-controlled hydrodynamic conditions using a rotating ring electrode.

IV.1.1.1. Static conditions

IV.1.1.1.1. Electrochemical measurements

The corrosion potential, E_{corr} , of the 70Cu-30Ni alloy was followed during 1 h of exposure to ASW in the presence of 20 mg.L⁻¹ of BSA. If comparing the corresponding E_{corr} value with the one obtained in ASW without biomolecules, it was observed that the BSA induces a more anodic E_{corr} value (-0.203 ± 0.005 V vs SCE *i.e.* a difference of ~ 30 mV with the value found without protein).

Figure IV.1 (a) shows the cathodic polarisation curves obtained with 20 mg.L⁻¹ of BSA. As for ASW without protein, two current plateaus illustrating pure mass transport limitation can be observed; these plateaus correspond to the first and second steps of dissolved oxygen reduction reaction. The second plateau current density is divided by 2 in the presence of the protein ($|j| \sim 40 \mu\text{A.cm}^{-2}$ without BSA to be compared to $|j| \sim 20 \mu\text{A.cm}^{-2}$ with BSA). This

difference in plateau current is not necessarily due to the BSA but may also be partially induced by a difference in natural convection from one experiment to another.

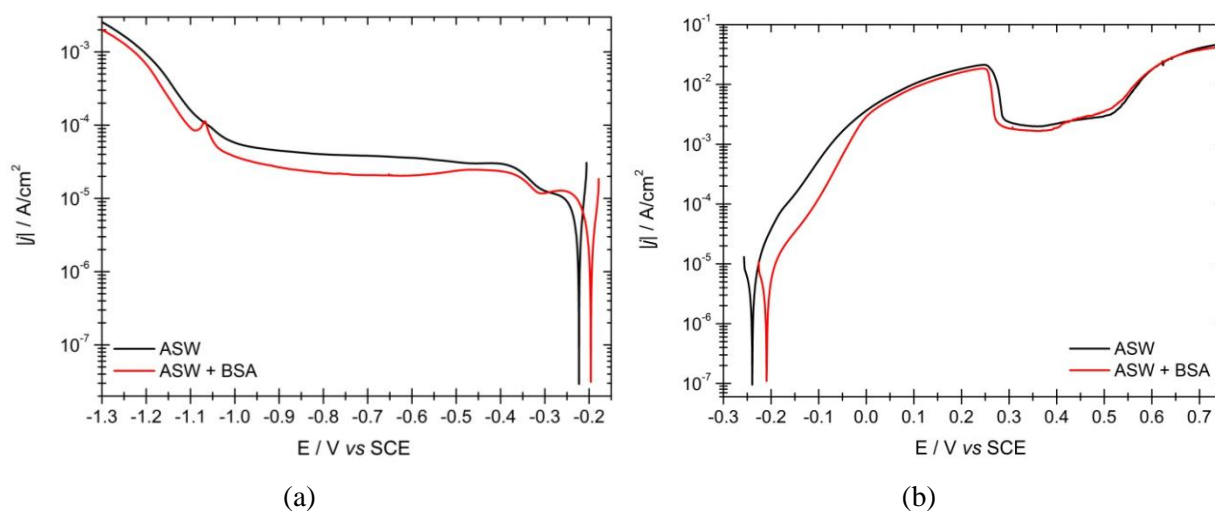


Figure IV. 1: (a) Cathodic and (b) anodic polarisation curves of 70Cu-30Ni after 1 h of immersion at E_{corr} in static aerated artificial seawater, without BSA and with 20 mg.L^{-1} of BSA. Scan rate: 0.5 mV.s^{-1} .

Figure IV.1 (b) compares the anodic polarisation curves obtained in ASW without and with BSA. In the presence of BSA, lower current densities can be observed near E_{corr} , for potentials lower than 0.0 V vs SCE ; this difference in current densities is partly due to the difference in E_{corr} values without and with BSA. Above 0.0 V vs SCE , the two anodic polarisation curves overlap. Thus, only a slight influence of the protein on the anodic electrochemical behaviour can be seen. Moreover, after the anodic polarisation curve, the green colour observed in the absence of protein (redeposited Cu_2O layer) is not visible in ASW with BSA).

Figure IV.2 shows the impedance diagrams in the complex plane plotted at E_{corr} after 1 h of immersion in ASW, without protein and with 20 mg.L^{-1} of BSA. Both diagrams exhibit two capacitive loops: one high frequency (HF) depressed semi-circle and a low frequency (LF) loop. The size of the HF loop is slightly higher in the presence of BSA.

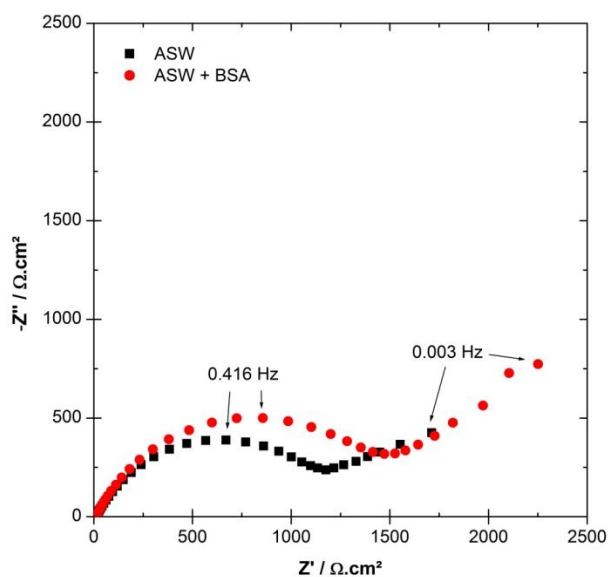


Figure IV. 2: Experimental impedance diagrams in the complex plane (Nyquist diagrams) of 70Cu-30Ni plotted at E_{corr} after 1 h of immersion in static aerated artificial seawater, without and with 20 mg.L⁻¹ of BSA.

As mentioned before, the impedance diagrams were plotted at the corrosion potential, which is not the same without and with BSA. Therefore, the analysis of data must take into account the effect of potential.

IV.1.1.1.2. Surface analysis

The composition and the equivalent thickness of the oxide layer (d_{Oxide}) formed in the presence of biomolecules were calculated from XPS data, using the system of equations presented in Chapter III (Eqs. III.3, III.4, III.5, III.6, III.7 and III.8) and considering the intensities of copper and nickel in the metallic substrate and in the mixed oxide layer formed on the alloy (the presence of biomolecules leads to mixed oxide layers, as will be shown later). Figure IV.3 illustrates the layer model used for the analysis of XPS data of a metallic material after immersion in a solution containing biomolecules (BSA in this case) that adsorb on the surface, forming an organic film on top of the oxide layer, with an equivalent thickness d_{BSA} .

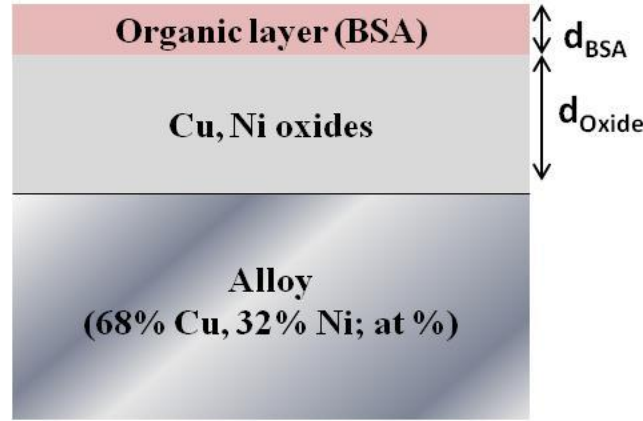


Figure IV. 3: Layer model assumed for the analysis of XPS data (organic layer -BSA- covering the mixed oxide layer formed on the metallic substrate).

The thickness d_{BSA} can be calculated from the $I_N^{BSA} / I_{Cu}^{Oxide}$ ratio. The nitrogen signal comes only from the protein and is therefore a fingerprint of the adsorbed protein. The N 1s intensity emitted by the adsorbed BSA is given by:

$$I_N^{BSA} = k \sigma_N \lambda_N^{BSA} D_N^{BSA} T_N \left[1 - \exp\left(-\frac{d_{BSA}}{\lambda_N^{BSA}}\right) \right] \quad \text{Eq. IV.1}$$

The Cu 2p_{3/2} intensity emitted by oxide layer and attenuated by the adsorbed protein is given by:

$$I_{Cu}^{Oxide} = k \sigma_{Cu} \lambda_{Cu}^{Oxide} D_{Cu}^{Oxide} T_{Cu} \exp\left(-\frac{d_{BSA}}{\lambda_{Cu}^{BSA}}\right) \left(1 - \exp\left(-\frac{d_{Oxide}}{\lambda_{Cu}^{Oxide}}\right) \right) \quad \text{Eq. IV.2}$$

Then,

$$\frac{I_N^{BSA}}{I_{Cu}^{Oxide}} \times \frac{\sigma_{Cu} \lambda_{Cu}^{Oxide} D_{Cu}^{Oxide} T_{Cu}}{\sigma_N \lambda_N^{BSA} D_N^{BSA} T_N} = \frac{1 - \exp\left(-\frac{d_{BSA}}{\lambda_N^{BSA}}\right)}{\exp\left(-\frac{d_{BSA}}{\lambda_{Cu}^{BSA}}\right) \left(1 - \exp\left(-\frac{d_{Oxide}}{\lambda_{Cu}^{Oxide}}\right) \right)} \quad \text{Eq. IV.3}$$

The calculated value for the transmission function $T(E_{kin})$ of the Escalab 250 energy analyzer for nitrogen (N 1s) is 3233.4, and the photo-ionisation cross-section of N 1s is 1.8. The values for the inelastic mean free path are presented in Table IV.1.

Table IV. 1: Inelastic mean free paths λ in nm – Taken from the QUASES-IMFP-TPP2M.

λ (nm)		
$\lambda_{Cu2p_{3/2}}^{BSA}$	$\lambda_{Ni2p_{3/2}}^{BSA}$	λ_{N1s}^{BSA}
1.94	2.13	3.39

The values of the different parameters for Cu and Ni are given in Chapter III.

During the XPS analyses, the following core levels were recorded: Cu 2p (and Auger lines), Ni 2p, O 1s, C 1s, and N 1s.

Differences in chemical composition and thickness of the oxide layers are observed without and with BSA.

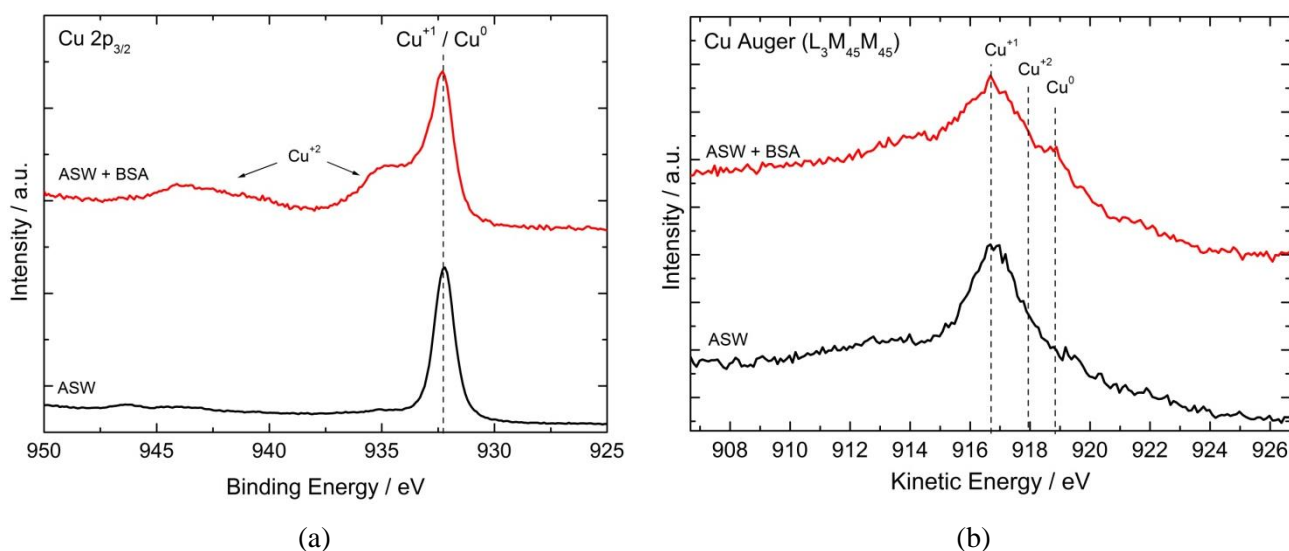


Figure IV. 4: (a) X-ray photoelectron spectroscopy (XPS) Cu 2p_{3/2} core level spectra and (b) Cu L₃M₄₅M₄₅ Auger lines of 70Cu-30Ni alloy after 1 h of immersion at E_{corr} in static aerated artificial seawater, without and with 20 mg.L⁻¹ of BSA. The intensity is expressed in arbitrary unit (a.u.).

After immersion in the BSA-containing solution, the XPS Cu 2p_{3/2} core level spectrum exhibits three peaks (Figure IV.4 (a)): one located at 932.3 eV attributed to Cu⁰ and/or Cu⁺¹, another one with a binding energy of 933.9 eV and the corresponding satellite at higher binding energy attributed to Cu⁺². Moreover, the Cu Auger line at a binding energy of 916.6 eV (Figure IV.4 (b)) shows the presence of Cu⁺¹. The XPS Ni 2p_{3/2} core level spectrum recorded in the presence of BSA exhibits the same features as without protein: a peak at a

binding energy of 856.0 eV and the corresponding satellite at 861.7 eV showing the presence of Ni(OH)₂ in the surface layer (Figure IV.5).

From these XPS data, it can be concluded that the presence of BSA leads to the presence of mixed copper oxides (Cu⁺¹ and Cu⁺²) and nickel hydroxide layer, with the following atomic composition: 16 at. % Cu⁺¹ + 33 at. % Cu⁺² + 51 at. % Ni(OH)₂. A lower amount of Cu⁺¹ and higher amounts of Cu⁺² and Ni(OH)₂ are detected compared to the results obtained in the absence of BSA (93 at. % Cu⁺¹ + 7 at. % Ni(OH)₂).

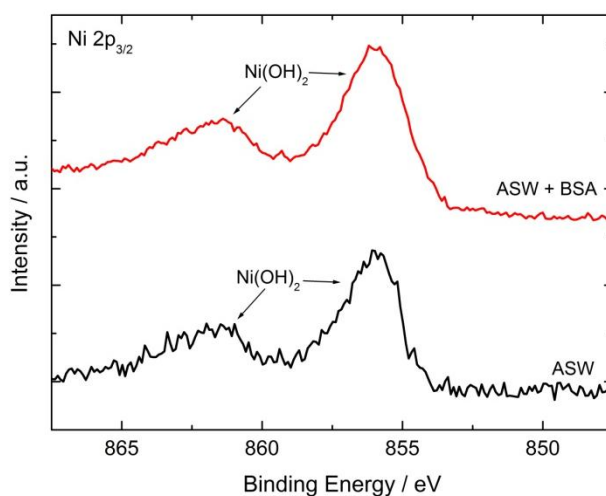


Figure IV. 5: X-ray photoelectron spectroscopy (XPS) Ni 2p_{3/2} core level spectra of 70Cu-30Ni after 1 h of immersion at E_{corr} in static aerated artificial seawater, without and with 20 mg.L⁻¹ of BSA. The intensity is expressed in arbitrary unit (a.u.).

Figure IV.6 shows the ToF-SIMS negative depth profile obtained with 70Cu-30Ni after 1 h of immersion in ASW with 20 mg.L⁻¹ of BSA. In this figure, it is possible to distinguish mainly four regions. The first region that goes from 0 to 10 s shows an increase of all the signals, and it is characterised by a maximum intensity in the 35Cl⁻ and 26CN⁻ (characteristic signal of proteins -peptidic link-) signals. From 10 s up to 25 s of sputtering the second region is observed, where the 95⁶³CuO₂⁻, 18¹⁸O⁻ and 90⁵⁸NiO₂⁻ signals reach their maximum value, and the 35Cl⁻ signal and the 26CN⁻ one sharply decrease. This region evidences an oxide layer non covered by the BSA. The third region starts from 25 up to 64 s of sputtering, when the 95⁶³CuO₂⁻, 18¹⁸O⁻, 35Cl⁻ and the 90⁵⁸NiO₂⁻ signals exhibit an inflection point, slightly increasing forming a shoulder; whereas the 26CN⁻ signals keeps sharply decreasing and the 116⁵⁸Ni₂⁻ signal gradually increases. This third region corresponds to the oxide layer beneath

the BSA layer. Finally after ~ 64 s of sputtering, oxides signal presents a sharp decrease, and the 116^{58}Ni_2^- signal form a plateau indicating that the alloy/oxide interface is reached.

By ToF-SIMS, it is not possible to identify a stratification of the different compounds on the alloy surface in the presence of the protein. Therefore, the depth profiles show one mixed oxide layer (oxidized copper and nickel) with a thickness of ~ 10 nm, being three times lower than that in the absence of the protein, and partly covered by the BSA layer.

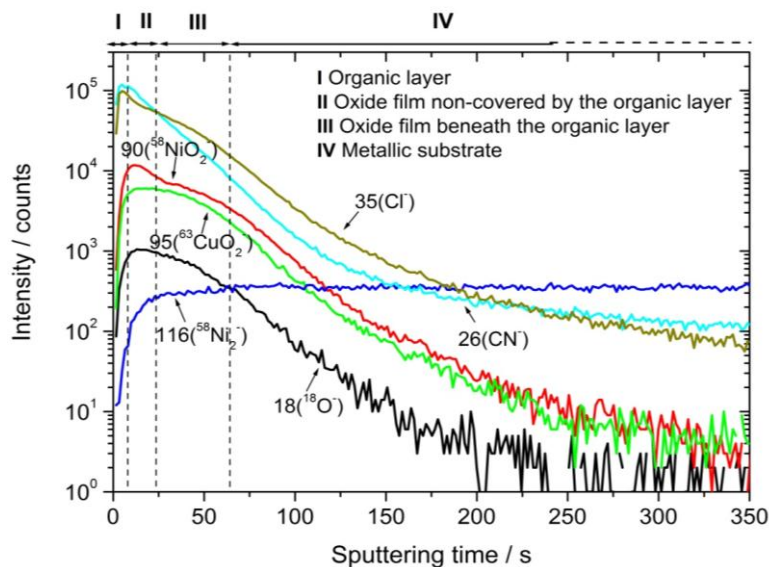


Figure IV. 6: Characteristic Time-of-Flight Secondary Ions Mass Spectrometry (ToF-SIMS) negative depth profile of 70Cu-30Ni after 1 h of immersion at E_{corr} in static aerated artificial seawater with 20 mg.L^{-1} of BSA.

The N 1s spectrum recorded after immersion in ASW with BSA (Figure IV.7 (a)) exhibits a major symmetric peak, centred at 400.2 eV, as expected for the amine or amide groups of BSA [106], [138]. The C 1s signal obtained in the same conditions is shown in Figure IV.7 (b). It can be fitted with three contributions corresponding to well identified carbon bonds present in the BSA molecule: C₁, at a binding energy of 285.0 eV, assigned to $\underline{\text{C}}\text{-C}$ and $\underline{\text{C}}\text{-H}$; C₂, at a binding energy of 286.4 eV, attributed to $\underline{\text{C}}\text{-N}$ and $\underline{\text{C}}\text{-O}$ single bonds; and C₃, at a binding energy of 288.3 eV, assigned to $\text{O}=\underline{\text{C}}\text{-O}$ and $\text{O}=\underline{\text{C}}\text{-N}$ (peptide bonds) bonds [16], [106], [138].

From the N 1s and C 1s signals, it is possible to calculate different “nitrogen/carbon” or “carbon/carbon” atomic ratios. The values of these ratios obtained for the 70Cu-30Ni alloy immersed in static ASW without and with BSA, as well as those estimated in previous studies

for the BSA powder [72][16] are presented in Table IV.2. The good agreement between the values for the sample put into contact with the BSA and the BSA powder provides a fingerprint for the protein, and allows us to conclude that the protein is present on the surface. The thickness estimated from XPS data for this adsorbed layer is ~ 3 nm which, according to the size of the BSA molecule [71], corresponds to one monolayer.

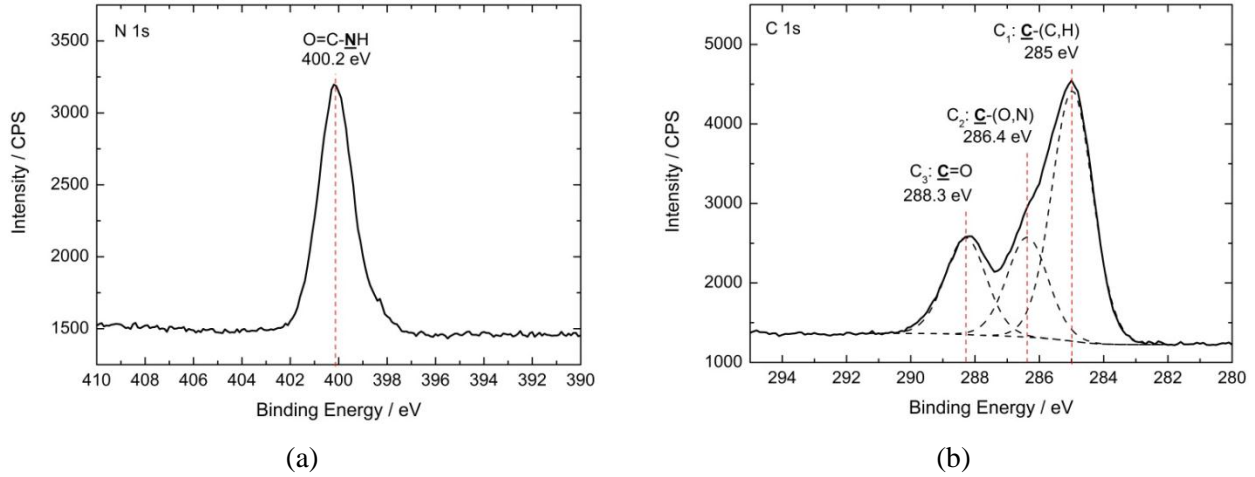


Figure IV. 7: (a) N 1s and (b) C 1s core level spectra of 70Cu-30Ni after 1 h of immersion at E_{corr} in static aerated artificial seawater with 20 mg.L⁻¹ of BSA. Solid line: experimental spectra; dashed line: peak decomposition. The intensity is expressed in counts per second (CPS).

Table IV. 2: Atomic ratios calculated from the XPS N 1s and C 1s core level spectra recorded for the BSA powder and for 70Cu-30Ni after 1 h of immersion at E_{corr} in static aerated artificial seawater, without and with 20 mg.L⁻¹ of BSA.

	N/C _{total} *	N/(C ₂ +C ₃)*	C ₁ /C _{total} *	C ₂ /C _{total} *	C ₃ /C _{total} *
BSA powder [16]	0.22	0.48	0.54	0.26	0.20
ASW	0.03	0.14	0.78	0.13	0.09
ASW+BSA	0.20	0.45	0.56	0.22	0.22

*The atomic ratio X/Y is given by:

$$X/Y = I_X \sigma_Y \lambda_Y^{BSA} T_Y / I_Y \sigma_X \lambda_X^{BSA} T_X$$

where $I_{X,Y}$ is the intensity of the peak (peak area) associated to element X or Y (X and Y equal to N or C), $\lambda_{X,Y}^{BSA}$ the attenuation length of photoelectrons emitted by the X or Y 1s core level in the BSA layer, $\sigma_{X,Y}$ the photoionization cross-section of X or Y 1s, and $T_{X,Y}$ the transmission factor of X or Y 1s. The C 1s signal is fitted with three contributions C₁, C₂ and C₃, corresponding to well identified carbon bonds present in the BSA molecule.

IV.1.1.2. Effect of hydrodynamics

IV.1.1.2.1. Effect of hydrodynamics on the surface chemical composition (comparison static conditions/under flow and stirring)

The effect of hydrodynamics on the chemical composition of the oxide layer was studied in the presence of BSA (comparison between flow and stirring/static conditions). For that purpose, a volume 10 times higher than in static conditions was used inside the electrochemical cell (1 L instead of 100 mL), the solution was continuously renewed using a peristaltic pump, with a flow rate of $\sim 0.27 \text{ mL}\cdot\text{s}^{-1}$, and the electrolyte inside the cell was stirred using a magnetic stirrer.

Figure IV.8 (a) shows the Cu $2p_{3/2}$ core level spectra of the 70Cu-30Ni alloy after 1 h of immersion at E_{corr} in ASW with $20 \text{ mg}\cdot\text{L}^{-1}$ of BSA, under flow and stirring and in static conditions. The results are compared with those obtained for the polished sample. A peak at 932.3 eV , corresponding to the presence of Cu^0 and/or Cu^{+1} , can be observed for the 3 samples. Another peak at 934.2 eV , with the corresponding satellite, are visible and show the presence of Cu^{+2} .

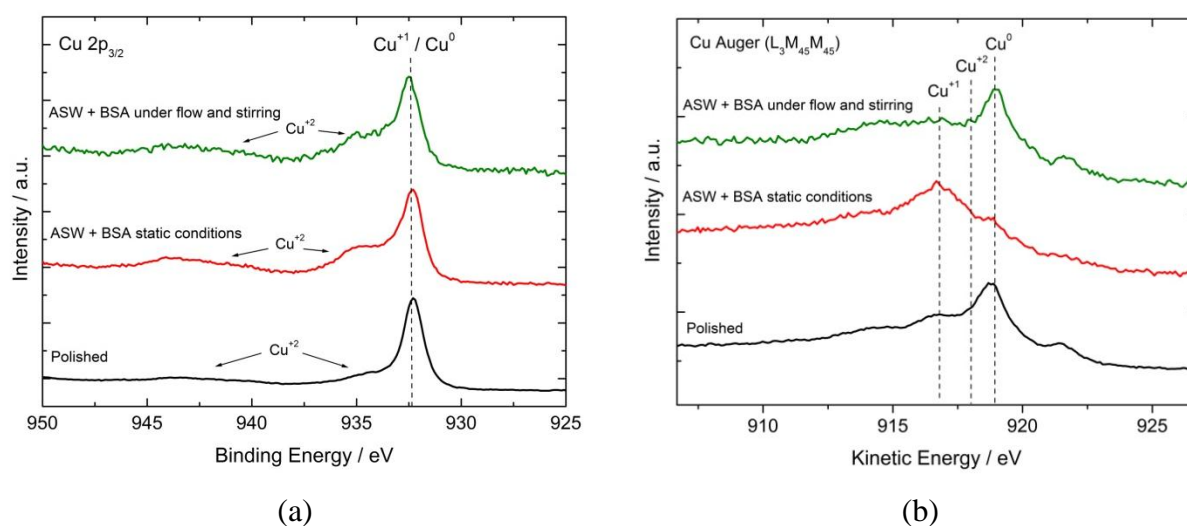


Figure IV. 8: (a) X-ray photoelectron spectroscopy (XPS) Cu $2p_{3/2}$ core level spectra, and (b) Cu $L_3M_{45}M_{45}$ Auger lines of 70Cu-30Ni after polishing and after 1 h of immersion at E_{corr} in aerated artificial seawater with $20 \text{ mg}\cdot\text{L}^{-1}$ of BSA (static and under flow and stirring). The intensity is expressed in arbitrary unit (a.u.).

The Cu Auger line ($L_3M_{45}M_{45}$) under flow and stirring, shown in Figure IV.8 (b), evidences the presence of metallic copper, Cu^0 , at a kinetic energy of 918.8 eV, as for the sample after polishing.

The Ni $2p_{3/2}$ core level spectrum under flow and stirring (Figure IV.9) shows a small peak at a binding energy of 852.3 eV, indicating the presence of metallic nickel Ni^0 and thus confirming that the surface oxide layer is very thin. The presence of $Ni(OH)_2$ is also observed at a binding energy of 855.7 eV.

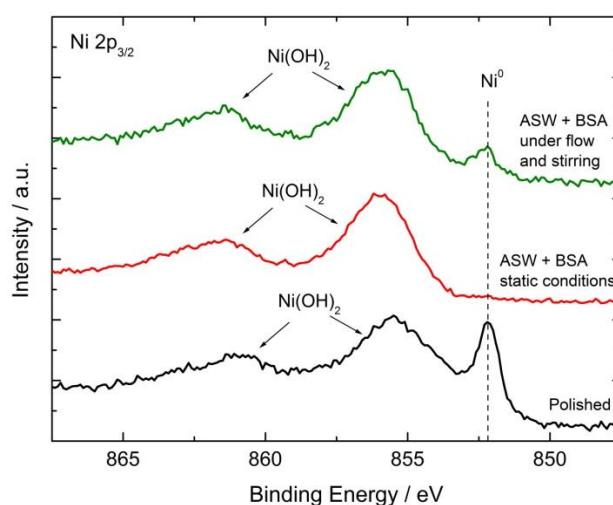


Figure IV. 9: XPS Ni $2p_{3/2}$ core level spectra of 70Cu-30Ni after polishing and after 1 h of immersion at E_{corr} in aerated artificial seawater with 20 mg.L^{-1} of BSA (static and under flow and stirring). The intensity is expressed in arbitrary unit (a.u.).

The composition of the oxide layer in ASW + BSA under flow and stirring, deduced from XPS data, is: 2 at. % Cu^{+1} + 36 at. % Cu^{+2} + 62 at. % of $Ni(OH)_2$; and its thickness is ~ 2 nm, which is close to the value obtained for the polished sample (1.5 nm) or for the sample after immersion in non-static ASW without BSA (1.4 nm).

Comparing the composition of the oxide layer in the presence of BSA, in static and non-static conditions, it is observed that flow and stirring lead to a decrease of the Cu^{+1} content in the oxide layer, and hence to a decrease of the amount of redeposited Cu_2O . A similar result was observed without BSA. There is an enrichment of Ni^{+2} in the oxide layer in the presence of the protein, in both hydrodynamic conditions.

Figure IV.10 illustrates a depth profile obtained by ToF-SIMS with a sputtering area of $700 \times 700 \mu\text{m}^2$, after 1 hour of immersion in ASW with 20 mg.L^{-1} of BSA under flow and stirring. Three main regions can be visualized. In the first region, from 0 to 27 s, all the signals increase, and the 35Cl^- , 90^{58}NiO_2^- , 95^{63}CuO_2^- , 18^{18}O^- and 26CN^- signals reach a maximum value followed by a drastical decrease. Later on, in the second region from 27 up to 124 s all the oxidized signals (35Cl^- , 90^{58}NiO_2^- , 18^{18}O^- and 26CN^-) show a shoulder, whereas the 116^{58}Ni_2^- signal continues increasing until around 124 s, forming a plateau, indicating that the metal/oxide interface is reached. The behaviour of the first region can be explained by the presence of a non uniform BSA layer adsorbed on the surface.

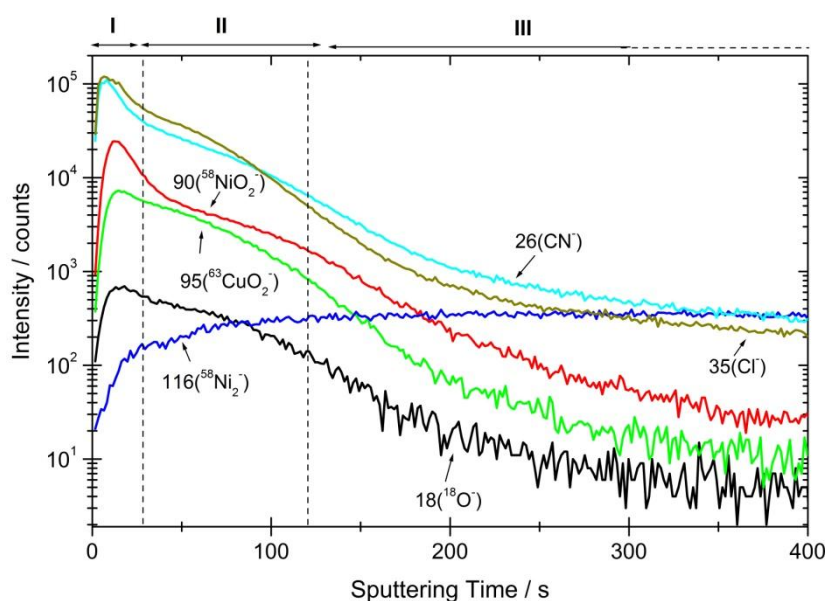


Figure IV. 10: Characteristic time-of-flight secondary ions mass spectrometry (ToF-SIMS) negative depth profiles of 70Cu-30Ni after 1 h of immersion at E_{corr} in aerated artificial seawater with 20 mg.L^{-1} of BSA, under flow and stirring. Sputtering surface area: $700 \times 700 \mu\text{m}^2$.

The oxide layer thickness in the presence of BSA, under flow and stirring, is lower compared to the one obtained in static conditions (2 nm to be compared to 10 nm). This result confirms that, with or without biomolecules, flow and stirring avoid the redeposition of Cu_2O .

The N 1s spectrum recorded after immersion in ASW with BSA under flow and stirring is presented in Figure IV.11 (a). It exhibits the same peak centred at 400.1 eV as in static ASW + BSA. The C 1s signal obtained in the same conditions is shown in Figure IV.11 (b), with

the three contributions corresponding to the different carbon bonds present in the BSA molecule.

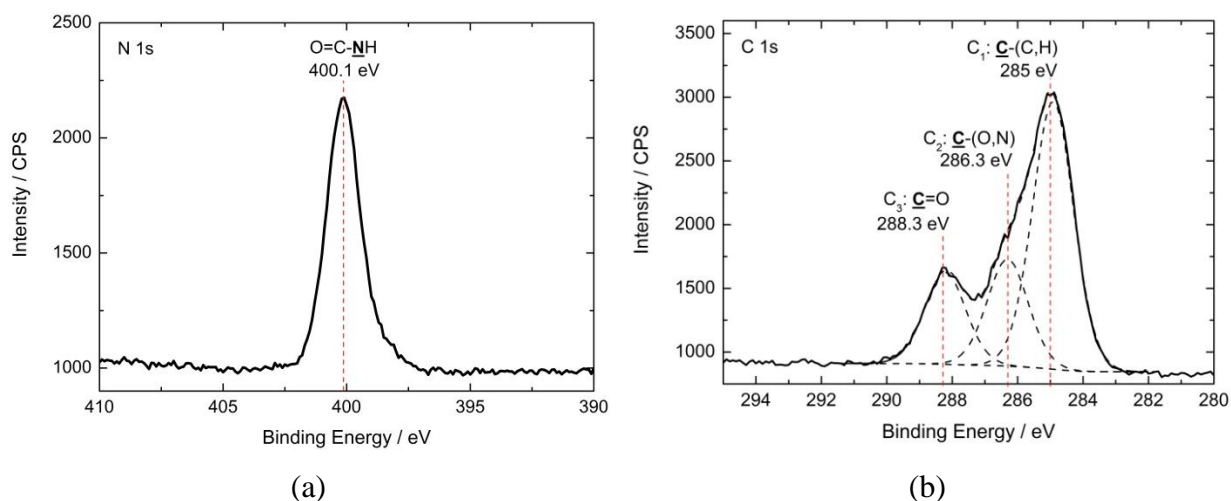


Figure IV. 11: (a) N 1s and (b) C 1s core level spectra of 70Cu-30Ni after 1 h of immersion at E_{corr} in aerated artificial seawater with 20 mg.L^{-1} of BSA under flow and stirring. Solid line: experimental spectra; dashed line: peak decomposition. The intensity is expressed in counts per second (CPS).

Using the N 1s and C 1s signals, different “nitrogen/carbon” or “carbon/carbon” atomic ratios were calculated (as done in static conditions). The values of these ratios obtained for the 70Cu-30Ni alloy immersed in ASW under flow and stirring, without and with BSA, are presented in Table IV.3. The good agreement between the values obtained for the sample put into contact with the BSA and the BSA powder allows us to conclude that the protein is adsorbed on the surface. The thickness estimated from XPS data for this organic layer formed under flow and stirring is $\sim 4 \text{ nm}$, and corresponds to one monolayer.

Table IV. 3: Atomic ratios calculated from the XPS N 1s and C 1s core level spectra recorded for the BSA powder, and for 70Cu-30Ni after 1 h of immersion at E_{corr} in aerated artificial seawater under flow and stirring, without and with 20 mg.L^{-1} of BSA.

	$\text{N}/\text{C}_{\text{total}}$	$\text{N}/(\text{C}_2+\text{C}_3)$	$\text{C}_1/\text{C}_{\text{total}}$	$\text{C}_2/\text{C}_{\text{total}}$	$\text{C}_3/\text{C}_{\text{total}}$
BSA powder	0.22	0.48	0.54	0.26	0.20
ASW under flow and stirring	0.02	0.09	0.73	0.14	0.13
ASW + BSA under flow and stirring	0.20	0.48	0.58	0.23	0.20

IV.1.1.2.2. Electrochemical measurements using a RRE

Electrochemical measurements in well-controlled hydrodynamic conditions were performed using a rotating ring electrode (RRE) at three different rotation speeds (40, 160, and 640 rpm).

The corrosion potential values after 1 h of immersion in artificial seawater with 20 mg.L⁻¹ of BSA, in static conditions using a disk electrode, and with the rotating ring electrode at three different rotation speeds, are presented in Table IV.4. Using the rotating ring electrode, E_{corr} decreases with increasing rotation speed. However, in static conditions, the corrosion potential value is more anodic compared to those obtained with the RRE. Additionally, if the values obtained in artificial seawater with BSA are compared to the values obtained without BSA, it is observed that E_{corr} becomes more anodic in static conditions and more cathodic with the RRE in the presence of the protein.

Table IV. 4: Corrosion potential values for 70Cu-30Ni alloy after 1 h of immersion in artificial seawater with 20 mg.L⁻¹ of BSA, in static conditions and using a RRE at 3 different rotation speeds.

	$E_{corr} / \text{V vs SCE}$	Difference with the value obtained in ASW without BSA
ASW + BSA stagnant conditions	-0.203 ± 0.005	~ 27 mV more anodic
ASW + BSA 40 rpm	-0.232 ± 0.003	~ 15 mV more cathodic
ASW + BSA 160 rpm	-0.249 ± 0.005	~ 16 mV more cathodic
ASW + BSA 640 rpm	-0.261 ± 0.003	~ 13 mV more cathodic

Figure IV.12 shows the cathodic polarisation curves obtained in static conditions and with the rotating ring electrode in artificial seawater with BSA. As mentioned before, two cathodic plateaus can be observed in static conditions, corresponding to the 2 steps of dissolved oxygen reduction, with a transfer of 2 or 4 electrons. The first plateau is observed close to E_{corr} . In addition, the current densities in static conditions are lower than those obtained with the rotating ring electrode. Furthermore, using the RRE, only one cathodic plateau (transfer of 4 electrons) is clearly visible and the plateau current density increases in absolute value with the rotation speed. Table IV.5 presents the current densities at -0.75 or -0.95 V vs SCE, corresponding to the second plateau for the oxygen reduction reaction in ASW without and with BSA. The presence of BSA induces lower current densities in static conditions as well as using the rotating ring electrode.

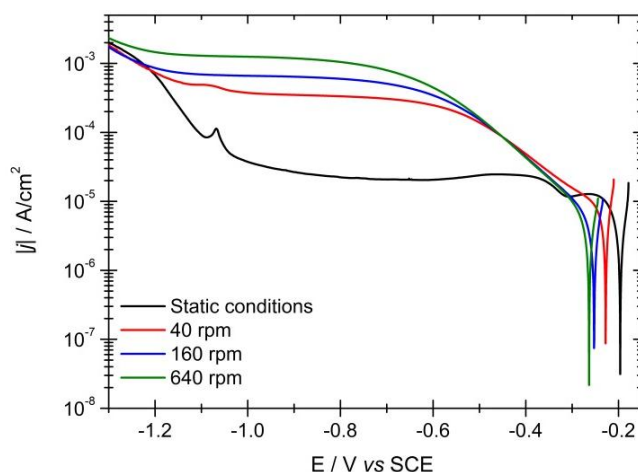


Figure IV. 12: Cathodic polarisation curves of 70Cu-30Ni after 1 h of immersion at E_{corr} , in aerated artificial seawater with 20 mg.L^{-1} of BSA using the rotating ring electrode at three different rotation speeds (40, 160 and 640 rpm) and in static conditions. Scan rate: 0.5 mV.s^{-1} .

Table IV. 5: Current densities at -0.75 or -0.95 V vs SCE , corresponding to the second step of dissolved oxygen reduction (transfer of 4 electrons), taken from Figure III.16 (a) and IV.12.

Current densities at -0.75 or -0.95 V vs SCE ($\mu\text{A/cm}^2$)		
	ASW	ASW + BSA
Static conditions	39 (-0.75 V)	21 (-0.75 V)
RRE, 40 rpm	330 (-0.75 V)	323 (-0.75 V)
RRE, 160 rpm	662 (-0.75 V)	653 (-0.95 V)
RRE, 640 rpm	1314 (-0.75 V)	1226 (-0.95 V)

The anodic polarisation curves recorded after 1 h of immersion in the presence of BSA in static conditions and with the RRE are illustrated in Figure IV.13. The current density in static conditions is lower than with the rotating ring electrode irrespective of the potential. Additionally, the current peak followed by a minimum current, observed with the RRE in ASW without biomolecules between 0.05 and -0.15 V vs SCE , is also visible with the RRE in the presence of BSA, mainly at 640 rpm. As for the experiments in ASW without BSA, the current plateau observed in static conditions between 0.3 and 0.5 V vs SCE is not well defined using the RRE. There is a slight effect of the rotation speed on the anodic behaviour for potential lower than 0.05 V vs SCE , like in ASW without biomolecules. These results show partial mass transport limitation (*i.e.* mixed kinetics) for the anodic reactions.

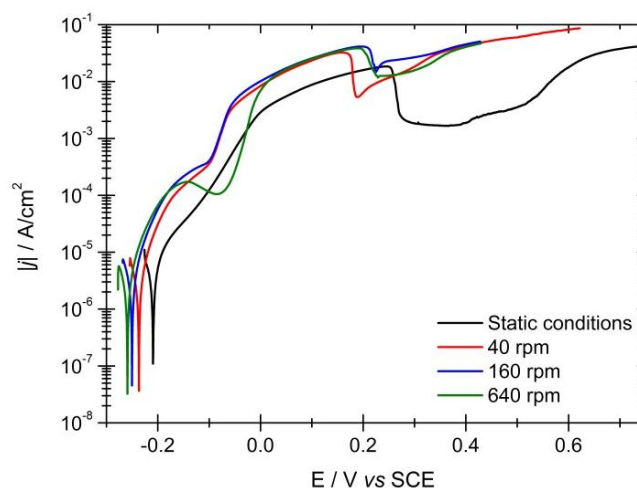


Figure IV. 13: Anodic polarisation curves of 70Cu-30Ni after 1 h of immersion at E_{corr} , in aerated artificial seawater with $20 \text{ mg}\cdot\text{L}^{-1}$ of BSA using the rotating ring electrode at three different rotation speeds (40, 160 and 640 rpm) and in static conditions. Scan rate: $0.5 \text{ mV}\cdot\text{s}^{-1}$.

Impedance diagrams were recorded at E_{corr} , in ASW with BSA using the RRE at three different rotation speeds. The results were compared to those obtained in static conditions with a disk electrode (Figure IV.14). As in ASW without biomolecules, the shape remains similar but the magnitude of the impedance, in particular the size of the high frequency loop, depends on the hydrodynamic conditions. The low frequency loop is better defined in static conditions. The magnitude of the impedance in the presence of BSA is higher than that in ASW without biomolecules and in FNSW, whatever the hydrodynamic conditions. Additionally, in ASW with BSA, the size of the high frequency loop is the same in static conditions and with the RRE at 40 rpm. Therefore, the magnitude of the impedance is lower with the RRE compared to static conditions in ASW without BSA and in FNSW, but not in ASW with BSA. Nevertheless, comparing only the impedance diagrams obtained with the RRE, the size of the HF loop increases with the rotation speed in ASW with BSA (like in ASW without BSA). These results will be discussed in details in the discussion section. (IV.2.1).

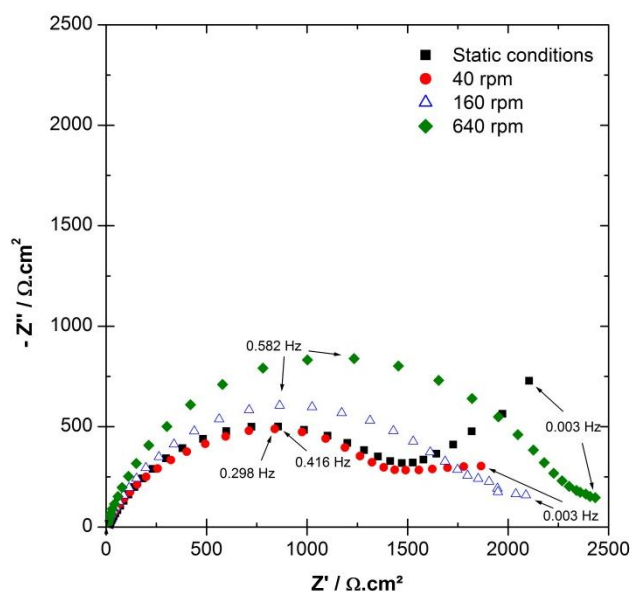


Figure IV. 14: Experimental impedance diagrams in the complex plane (Nyquist diagrams) of 70Cu-30Ni rotating ring electrode at three different rotation speeds (40, 160 and 640 rpm) after 1 h of immersion at E_{corr} in aerated artificial seawater with 20 mg.L^{-1} of BSA.

IV.1.2. EPS from *Pseudomonas NCIMB 2021*

This section is dedicated to the study of the effect of extracellular polymeric substances (EPS) on the electrochemical behaviour and the surface chemical composition of 70Cu-30Ni alloy in ASW. Results are compared with those obtained in artificial seawater with 20 mg.L^{-1} of BSA.

As mentioned in previous chapters, EPS can be found in two forms depending on their localisation and/or their role in the microbial metabolism: soluble or loosely bound EPS (LB EPS), and tightly bound EPS (TB EPS). These two kinds of EPS were extracted and their composition in proteins, sugars, DNA and uronic acids were determined. Differences in composition were detected depending on the nature of the EPS. The protein/sugar proportion is higher in TB EPS than in LB EPS. Therefore, LB EPS contain more sugars than proteins, which it is not the case for TB EPS for which the proteins concentration is considerably high.

For this study, the concentration of proteins in ASW containing TB or LB EPS was constant and equal to 20 mg.L^{-1} , in order to compare these results with those obtained in the presence of BSA (model protein). However, concentration of sugars was very different from the TB and the LB EPS solutions. (LB EPS much more concentrated in sugars than TB EPS). Experiments were performed in static conditions.

IV.1.2.1. Electrochemical measurements

Table IV.6 shows the different corrosion potential values for 70Cu-30Ni alloy after 1 h of immersion in ASW without and with biomolecules. The corrosion potential is similar for the three biomolecules and is more cathodic in the absence of biomolecules (difference of ~ 30 mV).

Table IV. 6: Corrosion potential (E_{corr}) values for 70Cu-30Ni alloy after 1 h of immersion in ASW without and with biomolecules (proteins concentration: 20 mg.L^{-1}).

	$E_{corr} / \text{V vs SCE}$
ASW	-0.230 ± 0.009
ASW + BSA	-0.203 ± 0.005
ASW + TB EPS	-0.199 ± 0.005
ASW + LB EPS	-0.203 ± 0.007

Figure IV.15 illustrates the cathodic polarisation curves recorded in the different biomolecules solutions. In all cases, except with LB EPS, the presence of two plateaus is visible. The short plateau close to the corrosion potential that illustrates the first step of dissolved oxygen reduction; and the wide plateau observed for potentials ranging from -0.40 to -1.00 V vs SCE corresponding to the second step of dissolved oxygen reduction reaction. Only the second plateau is visible in the presence of LB EPS.

The presence of biomolecules induces lower current densities in the second plateau potential domain. Compared with ASW ($|j| \sim 40 \mu\text{A.cm}^{-2}$), the plateau current density is divided by 2 in the presence of BSA ($|j| \sim 20 \mu\text{A.cm}^{-2}$), by 1.5 in the presence of TB EPS ($|j| \sim 27 \mu\text{A.cm}^{-2}$) and by 3.3 with LB EPS ($|j| \sim 12 \mu\text{A.cm}^{-2}$). Therefore, there is an effect of biomolecules on the cathodic behaviour of the 70Cu-30Ni alloy.

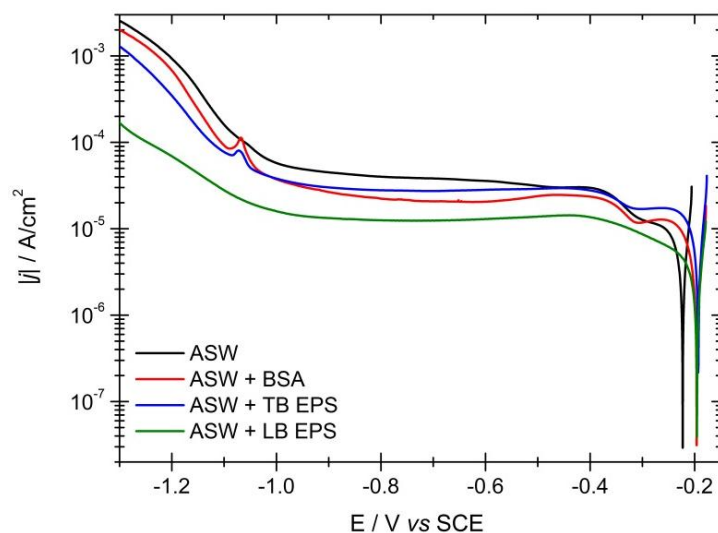


Figure IV. 15: Cathodic polarisation curves of 70Cu-30Ni after 1 h of immersion at E_{corr} in static ASW in the absence and in the presence of biomolecules (BSA, TB EPS, LB EPS) with a proteins concentration of $20 \text{ mg}\cdot\text{L}^{-1}$. Scan rate: $0.5 \text{ mV}\cdot\text{s}^{-1}$.

The anodic polarisation curves are presented in Figure IV.16. The presence of biomolecules induces lower current densities for potentials lower than 0.05 V vs SCE . Above 0.05 V vs SCE , all the curves exhibit the same shape and current densities except that with LB EPS, for which the current densities are lower up to 0.25 V vs SCE and the curve reveals some peaks between 0.25 and 0.5 V vs SCE .

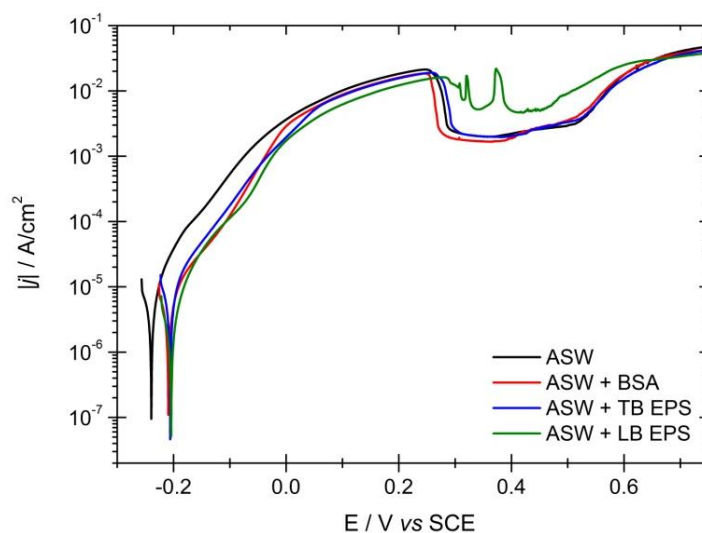


Figure IV. 16: Anodic polarisation curves of 70Cu-30Ni after 1 h of immersion at E_{corr} in ASW in the absence and in the presence of biomolecules (BSA, TB EPS, LB EPS) with a protein concentration of $20 \text{ mg}\cdot\text{L}^{-1}$. Scan rate: $0.5 \text{ mV}\cdot\text{s}^{-1}$.

Figure IV.17 shows the impedance diagrams plotted after 1 h of immersion at E_{corr} in static ASW without and with biomolecules. In all cases, two loops can be observed: one HF loop and one LF loop. The size of the high frequency loop in the presence of TB EPS is the same as that without biomolecules. However, the size of the HF loop is slightly higher in the presence of BSA, as mentioned before, and even much higher in the presence of LB EPS. The impedance diagrams were plotted at E_{corr} , which is not the same in the different solutions. Therefore, the analysis of data must take into account the effect of potential (see details in section IV.2.1).

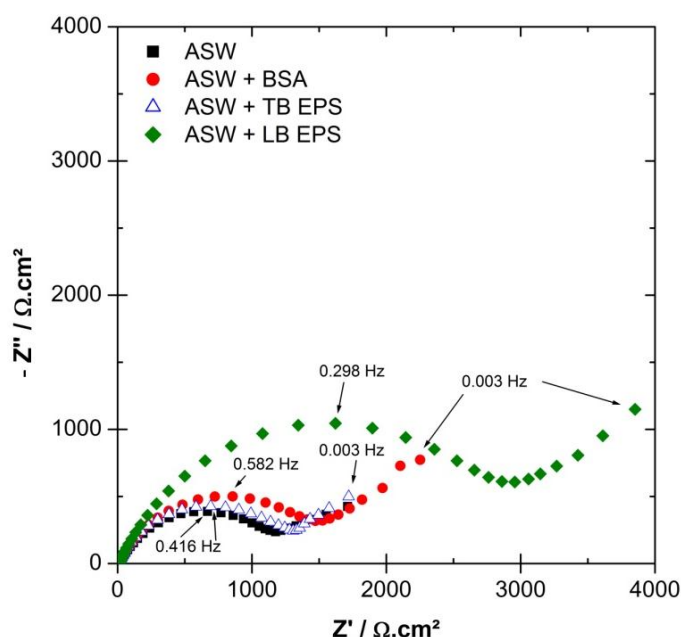


Figure IV. 17: Experimental impedance diagrams in the complex plane (Nyquist diagrams) of 70Cu-30Ni after 1 h of immersion at E_{corr} in ASW in the absence and in the presence of biomolecules (BSA, TB EPS, LB EPS) with a proteins concentration of 20 mg.L⁻¹.

IV.1.2.2. Surface analysis

The chemical composition of surface layers formed on 70Cu-30Ni alloy was investigated after 1 h of immersion in static ASW in the presence of tightly bound EPS (TB EPS) and loosely bound EPS (LB EPS) by XPS and ToF SIMS.

Figure IV.18 (a) illustrates the Cu 2p_{3/2} core level spectra for the 70Cu-30Ni alloy after 1 h of immersion in a solution containing TB EPS and LB EPS. In the two cases, a first peak at ~ 932.2 eV corresponding to Cu⁺¹ and/or Cu⁰, and a second peak at higher binding energy (~

934.0 eV) with a satellite at ~ 944.0 eV corresponding to Cu^{+2} can be observed with TB EPS. The position of the Auger line ($\text{L}_3\text{M}_{45}\text{M}_{45}$) (Figure IV.18 (b)), at 915.9 eV is probably due to a major contribution of $\text{Cu}(\text{OH})_2$ and/or $\text{Cu}_2(\text{SO})_4$ (Cu^{2+}), according to Table III.4 in Chapter III. On the other hand, with LB EPS, the Auger line at a kinetic energy of 919.2 eV indicates a major contribution of Cu^0 .

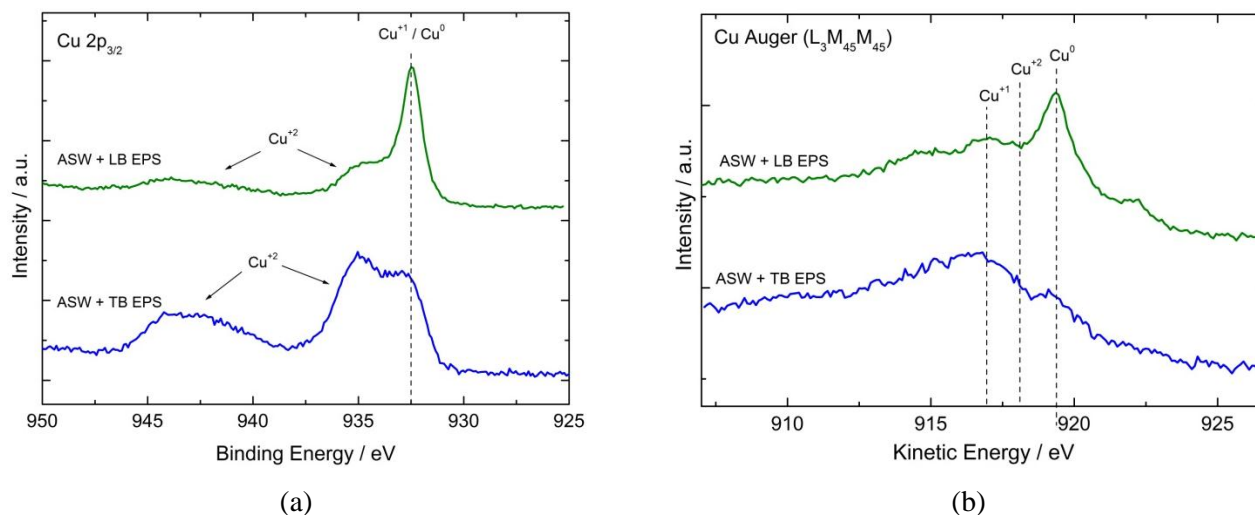


Figure IV. 18: (a) X-ray photoelectron spectroscopy (XPS) $\text{Cu } 2p_{3/2}$ core level spectra, and (b) $\text{Cu } \text{L}_3\text{M}_{45}\text{M}_{45}$ Auger lines of 70Cu-30Ni alloy after 1 h of immersion at E_{corr} in static ASW in the presence of tightly bound EPS (TB EPS) or loosely bound EPS (LB EPS), with a protein concentration of 20 mg.L^{-1} . The intensity is expressed in arbitrary unit (a.u.).

The $\text{Ni } 2p_{3/2}$ core level spectra shown in Figure IV.19 exhibit, for LB EPS, a peak at a binding energy of ~ 852.2 eV characteristic of Ni^0 , and another peak at ~ 856.0 eV with the corresponding satellite at ~ 862.0 eV corresponding to nickel hydroxide ($\text{Ni}(\text{OH})_2$). The latter two peaks characteristic of $\text{Ni}(\text{OH})_2$ are also present in ASW with TB EPS. The observation of the metallic component of Cu and Ni for the sample after immersion in ASW with LB EPS shows that the surface oxide layer is very thin compared to the one formed in static ASW, ASW with BSA, ASW with TB EPS and in static FNSW, for which the metallic components are not present in the XPS spectra.

The atomic composition of the oxide layers calculated from XPS data are: a) 11 at. % Cu^{+1} + 27 at. % Cu^{+2} + 62 at. % Ni^{+2} for ASW with TB EPS; and b) 1 at. % Cu^{+1} + 39 at. % Cu^{+2} + 60 at. % Ni^{+2} for ASW with LB EPS. The thickness of the oxide layer estimated by XPS for LB EPS is ~ 1.6 nm. The composition of the alloy beneath the oxide layer after immersion in LB EPS is 82 at. % Cu + 18 at. % Ni.

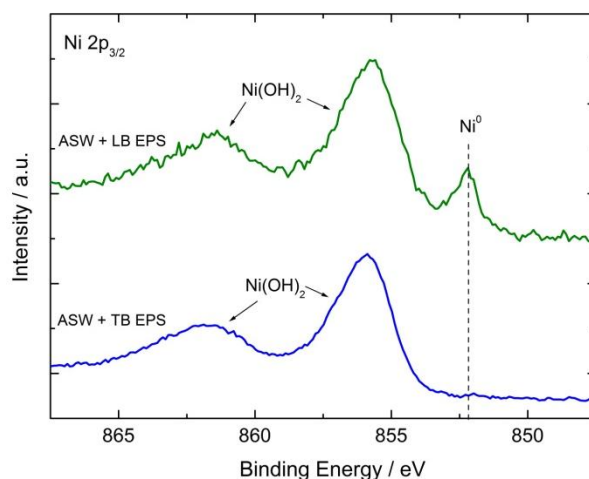
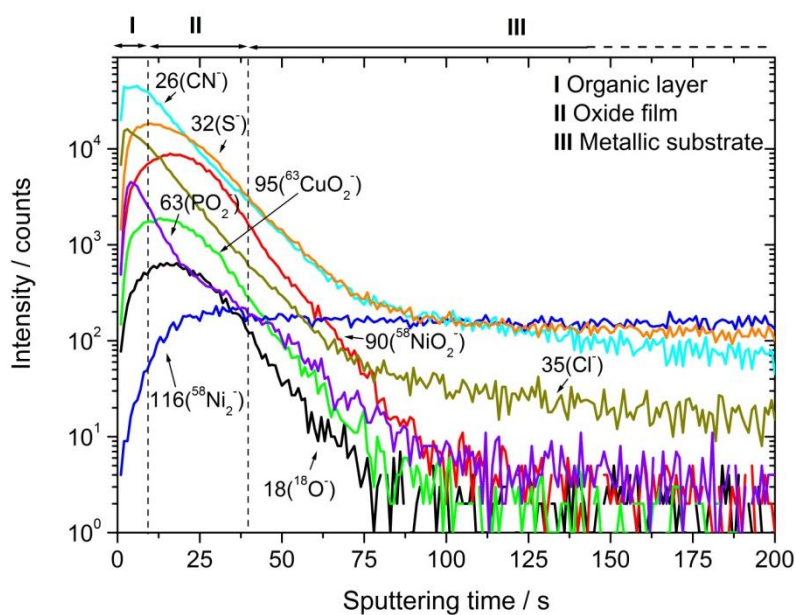
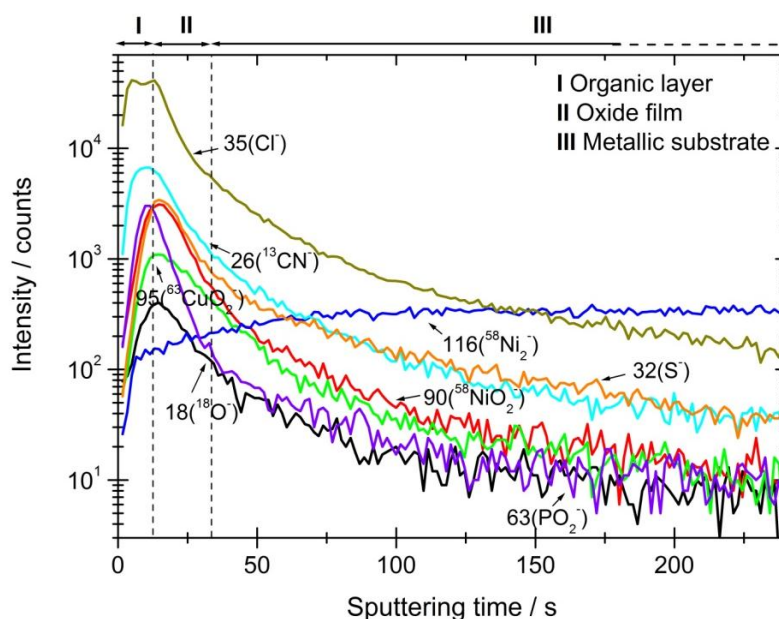


Figure IV. 19: X-ray photoelectron spectroscopy (XPS) Ni $2p_{3/2}$ core level spectra of 70Cu-30Ni alloy after 1 h of immersion at E_{corr} in static ASW in the presence of tightly bound EPS (TB EPS) or loosely bound EPS (LB EPS), with a protein concentration of $20 \text{ mg}\cdot\text{L}^{-1}$. The intensity is expressed in arbitrary unit (a.u.).

ToF-SIMS depth profiles (negative ions) were also performed on 70Cu-30Ni after 1 h of immersion in ASW in the presence of TB (Figure 20 (a)) and LB (Figure 20 (b)) EPS. The oxide layer formed on the alloy exposed to LB EPS is very thin, and the profile was performed using a higher sputtering area ($700 \times 700 \mu\text{m}^2$) (other conditions remaining unchanged) in order to have a better in-depth resolution (Figure 20(b)). Similarly to the ToF-SIMS profiles described previously, the position of the metal/oxide interface is located from the decreased intensity of the oxidized signals (95^{63}CuO_2^- , 18^{18}O^- and 90^{58}NiO_2^-) and the increase of the metallic signal (116^{58}Ni_2^-). It can be observed that whatever the kind of EPS (TB or LB), a mixed Cu and Ni oxide layer covers the metallic substrate (no oxide stratification) with a much thinner oxide film on the surface exposed to LB EPS compared to the one exposed to TB EPS. In both profiles, the oxide film is covered by an organic layer, assigned to the presence of TB or LB EPS, as indicated by the intense 26CN^- and 63PO_2^- signals that reach a maximum intensity before the signals assigned to oxide species (95^{63}CuO_2^- , 18^{18}O^- and 90^{58}NiO_2^-). Moreover, sulphur is present throughout the entire oxide layer, as indicated by the 32S^- signal that decreases around the alloy/oxide interface. The link between the TB or LB EPS and the oxide is likely made by the sulphur and the phosphorus present in the biomolecules, as indicated by the maximum intensity of the 32S^- and 63PO_2^- signals that is located in between the maximum intensity of the biomolecules signal (26CN^-) and that of the oxide signals (95^{63}CuO_2^- , 18^{18}O^- and 90^{58}NiO_2^-).



(a)



(b)

Figure IV. 20: Characteristic Time-of-Flight Secondary Ions Mass Spectrometry (ToF-SIMS) negative depth profiles of 70Cu-30Ni after 1 h of immersion at E_{corr} : (a) in static ASW with tightly bound EPS (TB EPS) with a proteins concentration of 20 mg.L⁻¹ (sputtering area: 300 x 300 μm^2); (b) in static ASW with loosely bound EPS (LB EPS) with a proteins concentration of 20 mg.L⁻¹ (sputtering area: 700 x 700 μm^2).

Figures IV.21 (a) and IV.21 (b) show the N 1s and C 1s core level spectra respectively, for the 70Cu-30Ni alloy after 1 h of immersion in ASW with the two different EPS (TB and LB).

The N 1s core level spectra exhibit for TB and LB EPS the same peak centred at 400.1 eV, also present in ASW with BSA and typical of amide groups (peptidic bond). The decomposition of the C 1s core level spectra for the two EPS solutions reveals the presence of three contributions attributed to typical carbon bonds present in biomolecules. The contribution corresponding to carbon bound only to carbon or hydrogen ($\underline{\text{C}}-(\text{C,H})$) is fixed at 285.0 eV (C_1). A second component is found at 286.4 eV (C_2) due to carbon making a single bond with nitrogen in amines or amides ($\underline{\text{C}}-\text{N}$, $\text{O}=\text{O}-\text{C}-\text{N}-\underline{\text{C}}$), or with oxygen in alcohol or ester groups ($\underline{\text{C}}-\text{O}$, $\text{O}=\text{C}-\text{O}-\underline{\text{C}}$). Finally, the third component at 288.3 eV (C_3), corresponds to carbon making two single bonds with oxygen in acetal ($\text{C}-\text{O}-\underline{\text{C}}-\text{O}-\text{C}$) or making one double bond with oxygen in amide or carboxylate ($\text{O}=\underline{\text{C}}-\text{N}-\text{C}$, $\text{O}=\underline{\text{C}}-\text{O}^-$) [87], [106][138][139][140]. The binding energies of carbon, oxygen and nitrogen in chemical functions of biochemical compounds are summarized in Table IV.7.

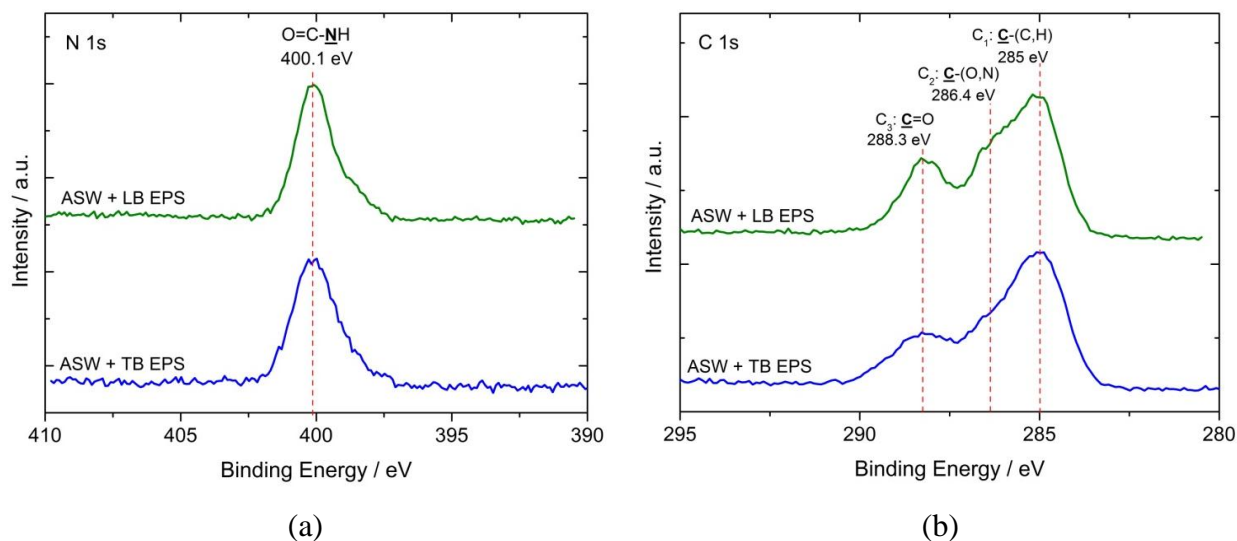


Figure IV. 21: (a) N 1s and (b) C 1s core level spectra of 70Cu-30Ni alloy after 1 h of immersion at E_{corr} in static ASW in the presence of tightly bound EPS (TB EPS) or loosely bound EPS (LB EPS), with a proteins concentration of $20 \text{ mg}\cdot\text{L}^{-1}$. The intensity is expressed in arbitrary unit (a.u.).

In a first approach, “nitrogen/carbon” and “carbon/carbon” atomic ratios were calculated from the N 1s and C 1s signals. The values of these atomic ratios obtained for the alloy in the TB and LB EPS solutions are compared in Table IV.8 to the values obtained in previous works for the model protein (BSA) [72][16]. The relatively good agreement between the values obtained for the two EPS solutions and the BSA powder shows that adsorbed proteins are the main biomolecules present on the alloy surface. However, with TB EPS, some deviations are

observed due to the presence of other biomolecules on the surface. More details will be given in the discussion section.

Table IV. 7: Binding energy of elements in chemical functions of biochemical compounds [106].

Element and function	Position (eV)	Reference compound
<i>CARBON</i>		
$\underline{\text{C}}\text{-(C,H)}$	284.8/285.0	Hydrocarbon, adventitious contamination
$\underline{\text{C}}\text{-N, O=C-N-}\underline{\text{C}}$	286.1	Amine; amide, peptide bond
$\underline{\text{C}}\text{-O}$	286.3	Alcohol
$\text{O=C-O-}\underline{\text{C}}$	286.8	Ester
$\underline{\text{C}}\text{=O, O-}\underline{\text{C}}\text{-O}$	287.8	Aldehyde, (hemi)acetal
$\text{O=}\underline{\text{C}}\text{-N-C, O=}\underline{\text{C}}\text{-O}^{\cdot}$	288.0	Amide, peptide bond; carboxylate
$\text{O=}\underline{\text{C}}\text{-O-C}$	289.0	Ester
$\text{O=}\underline{\text{C}}\text{-OH}$	289.0	Carboxylic acid
<i>OXYGEN</i>		
$\underline{\text{O}}\text{=C-}\underline{\text{O}}^{\cdot}$	531.1	Carboxylate
$\underline{\text{O}}\text{=C-N-C}$	531.3	Amide, peptide bond
$\underline{\text{O}}\text{=C-OH}$	531.8	Carboxylic acid
$\underline{\text{O}}\text{=C-O-C}$	531.9	Ester
$\text{C-}\underline{\text{O}}\text{H, C-}\underline{\text{O}}\text{-C-}\underline{\text{O}}\text{-C}$	532.6	Alcohol, (hemi)acetal
$\text{O=C-}\underline{\text{O}}\text{-C}$	533.4	Ester
$\text{O=C-}\underline{\text{O}}\text{H}$	533.4	Carboxylic acid
<i>NITROGEN</i>		
$\text{C-}\underline{\text{N}}\text{H}_2$	399.3	Amine
$\text{O=C-}\underline{\text{N}}\text{H}$	399.8	Amide, peptide bond
$\text{C-}\underline{\text{N}}\text{H}_3^+$	401.3	Protonated amine

Table IV. 8: Atomic ratios calculated from the XPS N 1s and C 1s core level spectra recorded for the BSA powder and for 70Cu-30Ni after 1 h of immersion at E_{corr} in static aerated artificial seawater in the presence of TB EPS or LB EPS, with a protein concentration of 20 mg.L⁻¹.

	N/C _{total}	N/(C ₂ +C ₃)	C ₁ /C _{total}	C ₂ /C _{total}	C ₃ /C _{total}
BSA powder	0.22	0.48	0.54	0.26	0.20
ASW + TB EPS	0.15	0.35	0.57	0.22	0.21
ASW + LB EPS	0.23	0.43	0.46	0.28	0.25

The thickness of the organic layer was estimated from XPS data, considering the same parameter values as for the model protein (BSA). That thickness is 1.3 nm for TB EPS and twice *i.e.* 2.6 nm for LB EPS. This latter value is similar to the one obtained in the BSA-containing solution (~ 3 nm corresponding to one BSA adsorbed monolayer) [106] [71].

IV.2. Discussion

IV.2.1. Analysis of impedance data

In Chapter III, an impedance model for 70Cu-30Ni alloy at E_{corr} in ASW and FNSW was developed. The bases of this model are the following:

- a) the anodic partial reaction involves the dissolution of Cu as Cu^+ species; modified mechanism drawn from that for pure copper dissolution in chloride media at low anodic potential, in order to take into account the presence of an oxide layer (Eqs. III.24 to III.27);
- b) the cathodic partial reaction is the oxygen reduction reaction (aerated solutions);
- c) the anodic and the cathodic partial reactions are affected by mass transport, with pure mass transport limitation for the cathodic partial reaction, and mixed kinetics control for the anodic partial reaction;
- d) the anodic current is mass transport-limited by the diffusion of CuCl_2^- through both the surface layer(s) and the electrolyte, as for pure Cu.

Figure IV.22 shows the absolute value of the imaginary part of the impedance ($|Z_j|$) plotted as a function of the frequency in logarithmic coordinates for the same experimental impedance data as those presented in Figures IV.14 and IV.17 in the complex plane, *i.e.* after immersion in ASW with BSA (static conditions and RRE) and in ASW with TB EPS and LB EPS (static conditions). In all cases, a pseudo-straight line with a slope lower than 1 in absolute value can be observed in the HF range. Similarly to what was observed in ASW without biomolecules and in FNSW, this slope varies with the frequency, and hence α cannot be determined graphically from Figure IV.22. Therefore, to better visualize a possible constant value of the slope in a narrow frequency range, the $d \log |Z_j| / d \log f$ vs $\log f$ curves were calculated from those presented in Figure IV.22 (derivative curves; Figure IV.23). In Figure IV.23, no plateau is clearly visible in any case, in particular at very HF, and hence, again the value of α cannot be graphically obtained. Therefore, the HF loop of the experimental impedance diagrams can

be modelled by the $CPE_{dl}/R_i^a/W_c$ equivalent circuit (Figure III.19 (c), Chapter III), and the LF loop is related to the anodic mass transport and partial blocking effect by CuCl ($Z_{\theta,D}^a$).

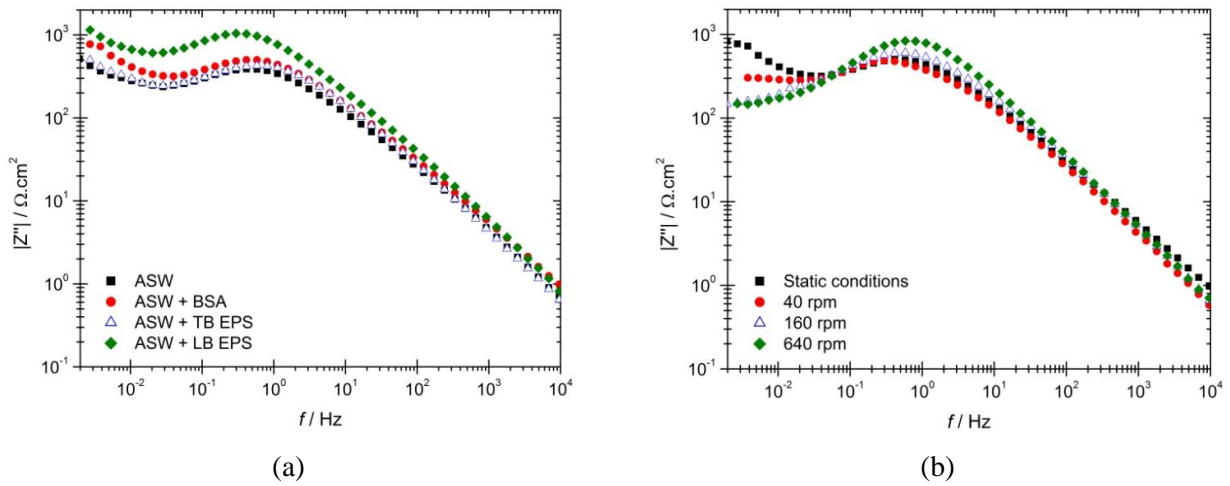


Figure IV. 22: Experimental impedance data (imaginary part of the impedance as a function of frequency) of 70Cu-30Ni obtained at E_{corr} after 1 h of immersion in aerated artificial seawater: (a) in static conditions in the absence and in the presence of biomolecules (BSA, TB EPS, LB EPS) with a protein concentration of $20 \text{ mg} \cdot \text{L}^{-1}$; and (b) with $20 \text{ mg} \cdot \text{L}^{-1}$ of BSA in static conditions and using a rotating ring electrode at three different rotation speeds (40, 160 and 640 rpm). Same data as in Figures IV.14 and IV.17.

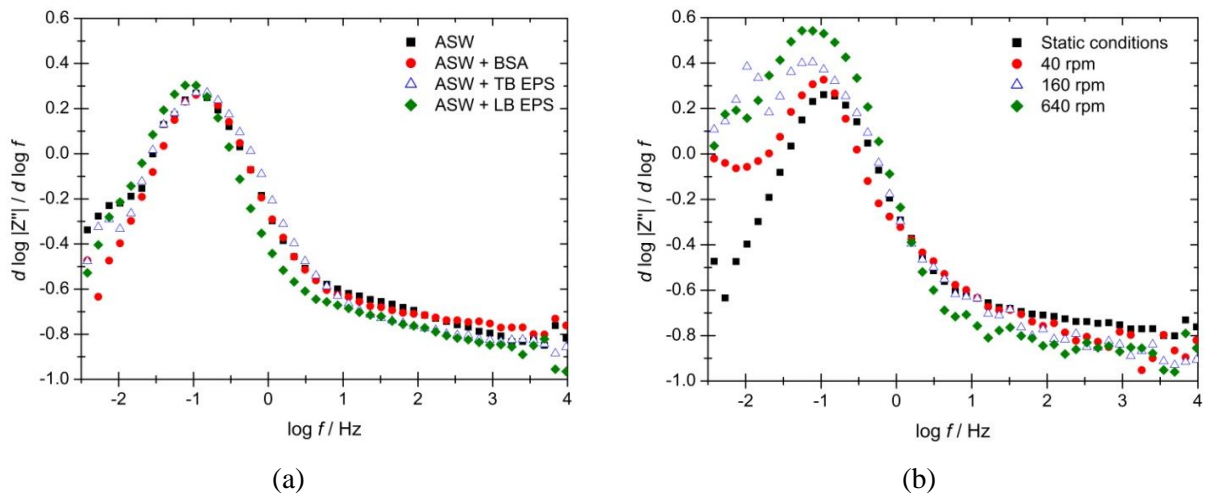


Figure IV. 23: Experimental impedance data (derivative curves calculated from Figure IV.22) of 70Cu-30Ni obtained at E_{corr} after 1 h of immersion in aerated artificial seawater: (a) in static conditions in the absence and in the presence of biomolecules (BSA, TB EPS, LB EPS) with a proteins concentration of $20 \text{ mg} \cdot \text{L}^{-1}$; and (b) with $20 \text{ mg} \cdot \text{L}^{-1}$ of BSA in static conditions and using a rotating ring electrode at three different rotation speeds (40, 160 and 640 rpm).

As only few points describe the LF loop, the single HF loop was analysed by regression of the equivalent circuit presented in Figure III.19 (c) of Chapter III, using Simad® software. The regression results are presented in Figure IV.24 and in Table IV.9.

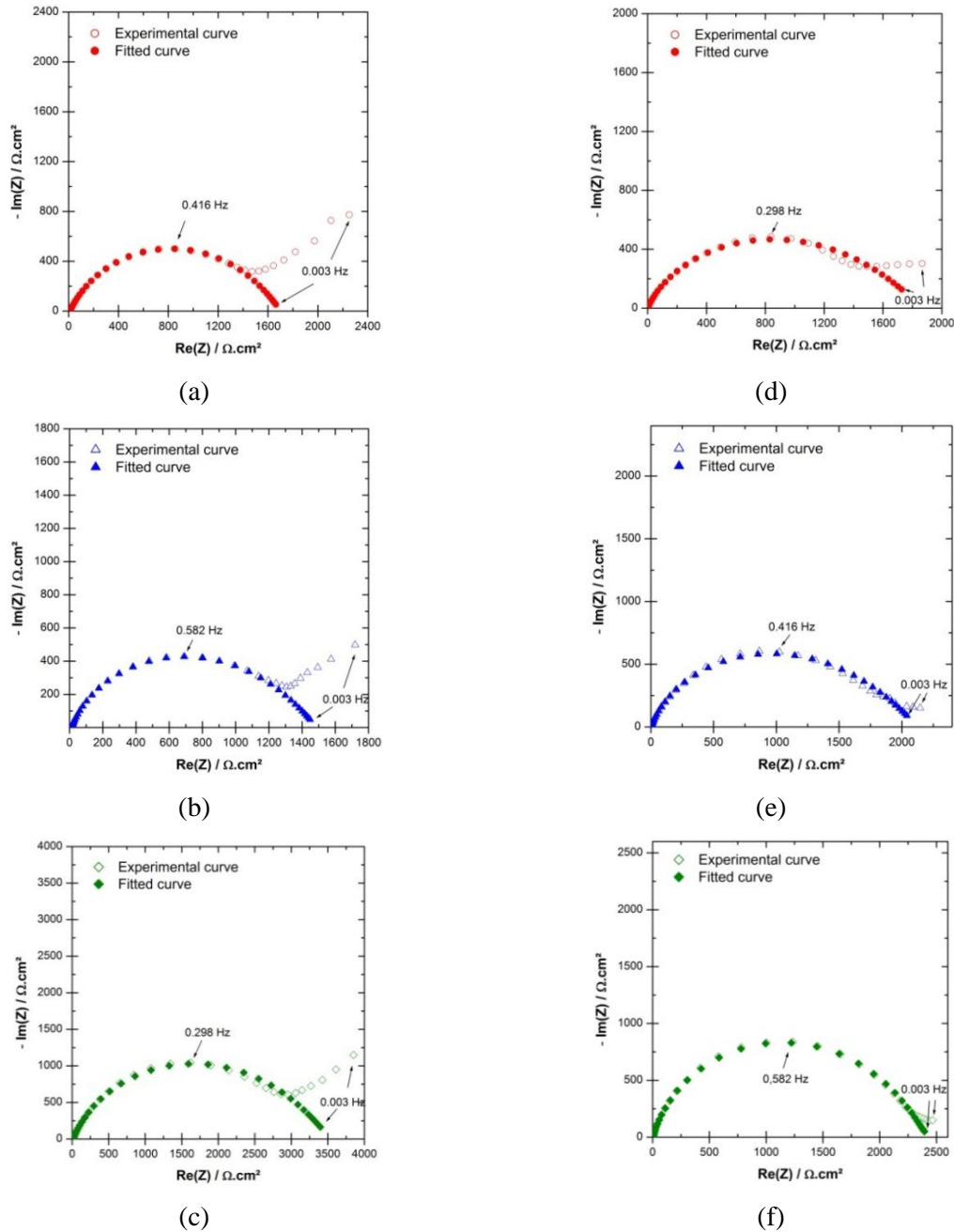


Figure IV. 24: Nyquist diagrams obtained for 70Cu-30Ni at E_{corr} after 1 h of immersion in aerated: (a) static ASW in the presence of 20 mg.L⁻¹ of BSA, (b) static ASW in the presence of TB EPS with 20 mg.L⁻¹ of proteins, (c) static ASW in the presence of LB EPS with 20 mg.L⁻¹ of proteins, and ASW with 20 mg.L⁻¹ of BSA using the RRE at (d) 40, (e) 160 and (f) 640 rpm. Experimental curves and fit of the impedance model presented in Figure III.19 (c) of Chapter III. Same data as in Figures IV.14 and IV.17.

Table IV. 9: Experimental frequency range taken into account for the regression, parameters values (electrolyte resistance R_e , anodic charge transfer resistance R_t^a , constant of the cathodic Warburg impedance k_c , and CPE parameters α and Q) obtained from the regression of the equivalent circuit presented in Figure III.19 (c) of Chapter III to experimental impedance data shown in Figures IV.14 and IV.17, and effective capacitance C_{eff} associated with the CPE calculated from Eq. III.32.

	Frequency range / Hz	$R_e / \Omega.cm^2$	$R_t^a / \Omega.cm^2$	$k_c / s^{0.5}.\Omega^{-1}.cm^{-2}$	α	$Q / F.cm^{-2}.s^{(\alpha-1)}$	$C_{eff} / \mu F.cm^{-2}$
ASW static	$10^5-5.6\times 10^{-2}$	12	1390	2.5×10^{-4}	0.78	1.99×10^{-4}	37
ASW + BSA static	$10^5-1.1\times 10^{-1}$	12	1690	1.2×10^{-4}	0.76	2.03×10^{-4}	30
ASW + TB EPS static	$10^5-1.1\times 10^{-1}$	12	1480	2.1×10^{-4}	0.84	1.33×10^{-4}	39
ASW + LB EPS static	$10^5-7.8\times 10^{-2}$	14	3530	1.1×10^{-4}	0.82	1.13×10^{-4}	27
ASW + BSA RRE 40 rpm	$10^5-5.5\times 10^{-2}$	4	1860	3.5×10^{-4}	0.87	1.04×10^{-4}	32
ASW + BSA RRE 160 rpm	$10^5-4.0\times 10^{-2}$	4	2130	2.1×10^{-4}	0.88	0.87×10^{-4}	27
ASW + BSA RRE 640 rpm	$10^5-2.0\times 10^{-2}$	4	2430	0.6×10^{-4}	0.86	0.99×10^{-4}	29

The effective capacitance values were calculated by application of the equation derived by Brug *et al* [105][133], taking for R_e and R_t^a the values extracted from the regression procedure (Table IV.9). These capacitance values are of the order of several tens of $\mu\text{F}\cdot\text{cm}^{-2}$, typical of those for a double layer capacitance, and are independent of the rotation speed. Therefore, the HF loop illustrates mainly the anodic charge transfer and its diameter is equal to R_t^a .

The C_{eff} values in the presence of $20 \text{ mg}\cdot\text{L}^{-1}$ of proteins (mean value: $31 \mu\text{F}\cdot\text{cm}^2$) are lower than those calculated without (ASW) or small amount of proteins (FNSW) (mean value: $42 \mu\text{F}\cdot\text{cm}^2$). This may be explained by a blocking effect by the adsorbed proteins which decrease the active surface area (S_{act}) where the electrons transfer occurs. Thus, the C_{eff} ratio without and with biomolecules would be equal to the active surface ratio:

$$\frac{C_{eff}^{without}}{C_{eff}^{with}} = \frac{S_{act}^{without}}{S_{act}^{with}} \quad \text{Eq. IV.4}$$

The mean value for this ratio is about 1.35.

Moreover, the C_{eff} value obtained in ASW + TB EPS seems to be higher than the values obtained in the presence of the other biomolecules. This could be linked to a lower amount of adsorbed proteins in the case of ASW + TB EPS, which is in agreement with a lower equivalent thickness of the adsorbed organic layer estimated from XPS data (see Figure IV.26); 1 nm for TB EPS to be compared to 3-4 nm for BSA and LB EPS).

Experimentally, when moving from the static disk to the RRE at 40 rpm in ASW + BSA, the corrosion potential decreases (see Table IV.4) and R_t^a slightly increases (see Table IV.9). This slight increase of R_t^a can be explained by compensated potential and mass transport effects with a higher influence of potential (see Eq. III.36 and III.37 of Chapter III). When increasing the rotation speed of the RRE from 40 to 640rpm, the corrosion potential decreases in ASW + BSA (see Table IV.4) and R_t^a greatly increases (see Table IV.9). This increase of R_t^a is due to a major effect of the potential.

Compared to the value obtained in static ASW without biomolecules, R_t^a is $\sim 22 \%$ higher in the presence of BSA, $\sim 6.5 \%$ higher in the presence of TB EPS, and $\sim 150 \%$ higher in the presence of LB EPS.

In static conditions, changes in R_t^a value can be explain by three different effects: 1) a potential effect (V in Eq. III.37 of Chapter III), 2) a kinetic effect (K in Eq. III.37 of Chapter III), and 3) a blocking or surface effect induced by the adsorbed biomolecules. If we assume constant anodic Tafel slopes *i.e.* constant b and constant surface concentration of the diffusing species c_0 without and with biomolecules, then Eq. III.37 of Chapter III, becomes:

$$\frac{R_t^a|_{with}}{R_t^a|_{without}} = \frac{K^{without}}{K^{with}} e^{b(E_{corr}^{without} - E_{corr}^{with})} \times \frac{S_{act}^{without}}{S_{act}^{with}} \quad \text{Eq. IV.5}$$

where R_t^a is expressed in Ω . Given Eq. IV.4, Eq. IV.5 can be written as:

$$\frac{K^{without}}{K^{with}} = \frac{R_t^a|_{with}}{R_t^a|_{without}} e^{b(E_{corr}^{with} - E_{corr}^{without})} \times \frac{C_{eff}^{with}}{C_{eff}^{without}} \quad \text{Eq. IV.6}$$

The anodic partial reaction of 70Cu-30Ni alloy immersed at E_{corr} in seawater involves the dissolution of Cu as Cu^+ species (modified mechanism drawn from that for pure copper dissolution in chloride media at low anodic potential; Eqs. III.24 to III.27). Then, the number of transferred electrons z can be taken as 1. Moreover, α is comprised between 0 and 1, and is usually assumed to be equal to 0.5. Therefore, $b = \frac{\alpha z F}{RT} \approx 20$ and the numeral application of Eq. IV.6 gives $\frac{K^{without}}{K^{with}} (BSA) = 1.7$, $\frac{K^{without}}{K^{with}} (TB\ EPS) = 2.1$ and $\frac{K^{without}}{K^{with}} (LB\ EPS) = 3.2$. In all cases, $K^{without} > K^{with}$ which means that the anodic reaction is slow down by the biomolecules and the effect of potential is compensated by a strong kinetic effect. Indeed, as E_{corr} is more anodic in the presence of biomolecules and almost constant for the 3 biomolecules, a single effect of the potential would induce a decrease of R_t^a (Eq. III.37 of Chapter III). This kinetic effect is the strongest in the case of LB EPS.

Corrosion currents, i_{corr} were calculated from Eqs. III.39 and III.40 of Chapter III assuming Tafel kinetics (pure kinetic control) for the anodic partial reaction, and using $z = 1$ (dissolution of Cu as Cu^{+1} species) and $\alpha = 0.5$ in Eq. III.39, and $R_p = R_t^a$ in Eq. III.40.

Table IV.10 compares the calculated i_{corr} values to those deduced graphically from the cathodic polarisation curves, taking into account the first plateau current density in some cases, or an extrapolation of the cathodic straight line in other cases. If considering static ASW, ASW + BSA and ASW + TB EPS, for which i_{corr} values can be more easily extracted from the cathodic polarisation curves (first plateau current density), there is quite a good

agreement between values obtained from Eq. III.39 and those deduced graphically, and the ratio of about 2-3 may be partly explained by a value of α different from 0.5 and partly explained by non steady-state cathodic polarisation curves (scan rate of $0.5 \text{ mV}\cdot\text{s}^{-1}$, see Chapter III).

Table IV. 10: Comparison of the corrosion current density values obtained from R_t^a , by application of Eq III.39 and III.40, and from the cathodic polarization curves.

	$R_t^a / \Omega\cdot\text{cm}^2$	$i_{corr} / \mu\text{A}\cdot\text{cm}^{-2}$		
		Eq. III.39	Eq. III.40	Cathodic polarisation curve
		$z = 1 \text{ and } \alpha = 0.5$		
ASW static	1390	36	14	12
ASW + BSA static	1690	30	11	12
ASW + TB EPS static	1480	34	13	17
ASW + LB EPS static	3530	14	5	5
ASW + BSA RRE 40 rpm	1860	27	10	13
ASW + BSA RRE 160 rpm	2130	24	9	6
ASW + BSA RRE 640 rpm	2430	21	8	7

Figure IV.25 allows to better visualize the differences in corrosion current density calculated from Eq. III.39 (with $z = 1$ and $\alpha = 0.5$), for the different solutions in static conditions and using the rotating ring electrode.

The corrosion current of 70Cu-30Ni alloy after 1 h of immersion in static ASW is slightly lower with BSA and similar with TB EPS compared to the corrosion current estimated in the absence of biomolecules. A significant decrease of the corrosion current is observed in the presence of LB EPS. Therefore, these results show a clear corrosion inhibition effect for LB EPS, a small beneficial effect for BSA and no detrimental effect for TB EPS.

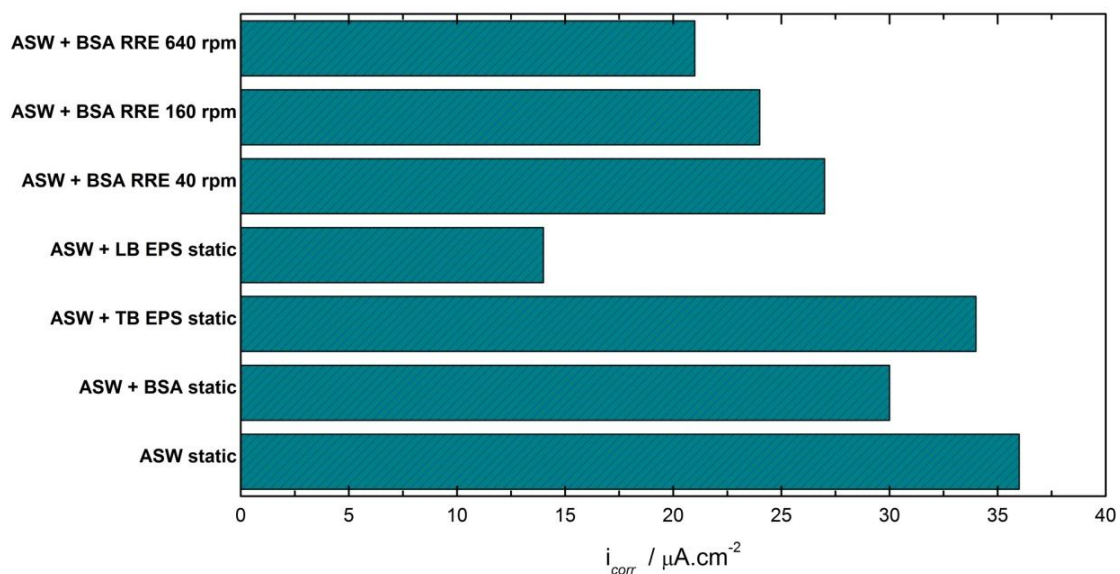


Figure IV. 25: Comparison of the corrosion current density values calculated from Eq. III.39 with $z = 1$ and $\alpha = 0.5$, for 70Cu-30Ni alloy after 1 h of immersion in ASW without and with biomolecules, in static conditions and using the rotating ring electrode.

On the other hand, the corrosion current values calculated for ASW with BSA using the RRE are lower than or equal to the value obtained in static conditions and i_{corr} decreases when the rotation speed increases.

IV.2.2. Surface layer models (combined XPS and ToF-SIMS)

In Figure IV.26 are summarized the oxide layer compositions estimated from XPS data for the 70Cu-30Ni alloy after short-term immersion (1 h of exposure) at E_{corr} in the three different solutions (ASW with BSA, TB EPS and LB EPS). The oxide layer thickness was calculated from XPS data and in the case of static ASW + BSA and ASW + TB EPS the thickness was assessed from combined XPS and ToF-SIMS data.

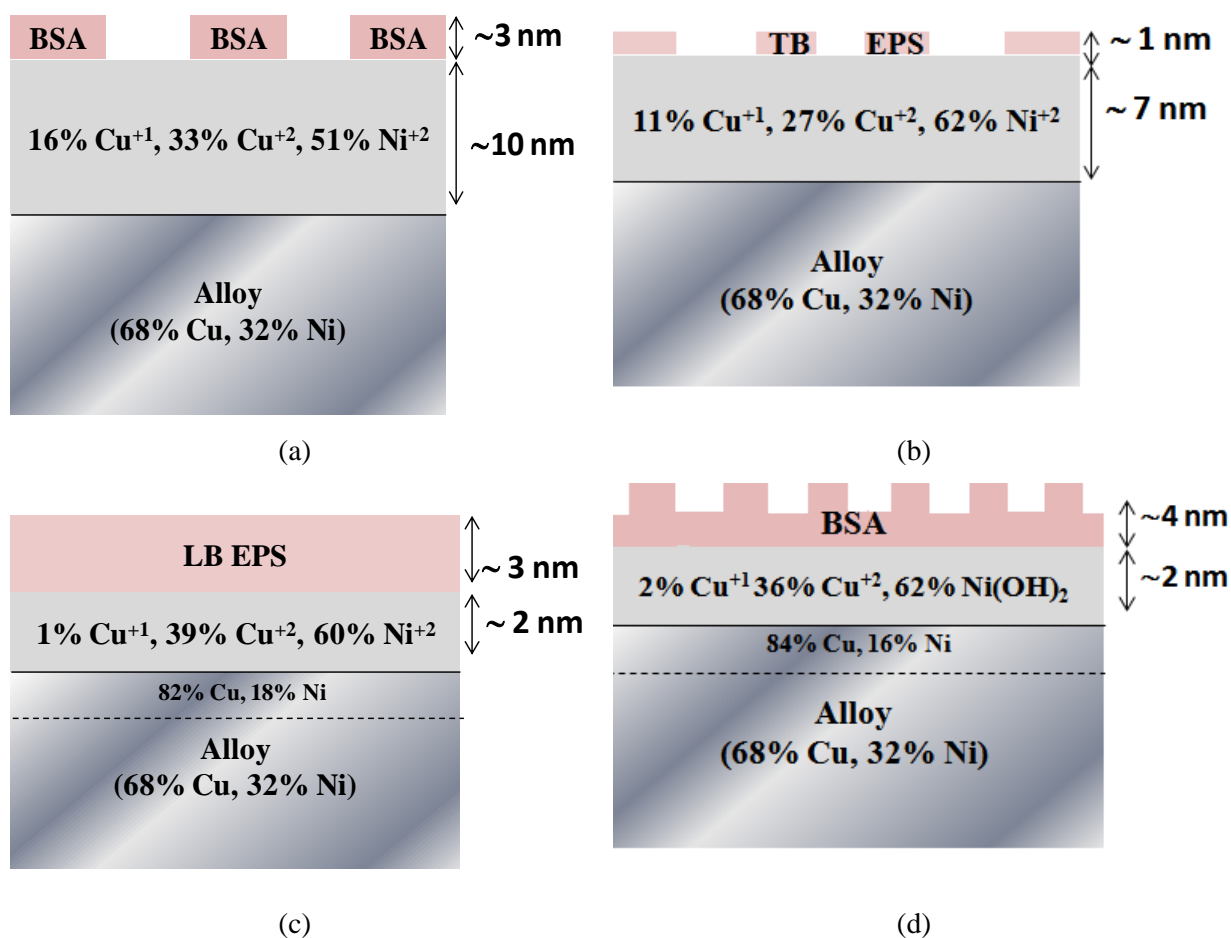


Figure IV. 26: Models of the surface layers deduced from combined X-ray photoelectron spectroscopy (XPS) and time-of-flight secondary ions mass spectrometry (ToF-SIMS) data for 70Cu-30Ni after 1 h of immersion at E_{corr} in: (a) static ASW with 20 mg.L⁻¹ of BSA; (b) static ASW in the presence of TB EPS with a proteins concentration 20 mg.L⁻¹; (c) static ASW in the presence of LB EPS with a proteins concentration of 20 mg.L⁻¹; and (d) ASW under flow and stirring with 20 mg.L⁻¹ of BSA.

Similarly to what is observed for static ASW + BSA, the presence of TB EPS induces the formation of a mixed oxide layer composed of Cu⁺¹, Cu⁺², and Ni⁺² compounds, but with a lower Cu₂O content, a higher Ni(OH)₂, as well as thinner oxide layer.

Results obtained in the presence of LB EPS show a very thin mixed oxide layer mainly composed of Cu⁺² and Ni⁺², with a thickness comparable to the one estimated for the sample just after polishing (~ 1.4 nm). Furthermore, the lowest Cu⁺¹ content was observed in the presence of LB EPS. It is important to mention that not all the Cu⁺² ions found in the oxide layer correspond to CuO but may be Cu(OH)₂ or Cu(SO₄)₂. These results for static ASW + LB EPS are very similar to the ones obtained for ASW + BSA under flow and stirring.

It has been shown from impedance data in static condition a slow-down of the anodic reaction by the biomolecules (BSA, TB EPS and LB EPS), and a corrosion inhibition effect by LB EPS and to a lesser extent by BSA.

This slow-down/inhibition of the anodic dissolution by the biomolecules can then give rise to two different cases: i) either the amount of dissolved Cu^{+1} is below the solubility limit of Cu^{+1} , and in that case, no redeposition of Cu_2O occurs, or ii) the amount of dissolved Cu^{+1} is above the solubility limit of Cu^{+1} , and in that case, adsorbed biomolecules inhibit Cu_2O redeposition by blocking the surface.

The kinetic effect and corrosion inhibition effect are the strongest in the case of LB EPS, in agreement with the lowest Cu^{+1} content in the oxide layer, and the lowest oxide layer thickness estimated from XPS data. Therefore, combined electrochemical measurements and surface analysis in static ASW show that adsorbed LB EPS inhibit the corrosion of 70Cu-30Ni alloy and suppress Cu_2O redeposition (amount of dissolved Cu^{+1} below the solubility limit), whereas adsorbed BSA and TB EPS slow-down the anodic dissolution (kinetic effect) and inhibit Cu_2O redeposition (surface blocking effect).

IV.2.3. Organic layers (XPS)

Correlations between spectral XPS data (C 1s, N 1s and O 1s) were used to generate information about the organic layer formed in the presence of BSA, TB and LB EPS [106], [139], [140].

As it was mentioned before, the C 1s peak was decomposed into three contributions. Figure IV.27 (a) presents the plot of the molar concentration of carbon responsible for the C_3 component, located at 288.3 eV ($\text{C}-\text{O}-\underline{\text{C}}-\text{O}-\text{C}$, or $\text{C}-\text{N}-\underline{\text{C}}=\text{O}$), as a function of the molar concentration of total organic nitrogen, N_{org} . A 1:1 relation is expected for the amide function ($\text{HC}-\text{NH}-(\text{C}=\text{O})$) forming the backbone of proteins (peptidic link). A deviation from this 1:1 line would indicate the presence of polysaccharides or any oxidized carbon of contaminants. As expected, the data are close to the 1:1 relation after 1 h of immersion of 70Cu-30Ni alloy in ASW with BSA in static conditions and under flow and stirring, evidencing the presence of adsorbed BSA proteins on the surface. After immersion in the LB EPS-containing solution, the data are also close to the 1:1 relation. However, the organic layers after immersion in TB EPS solution and in FNSW seem to contain other compounds than proteins.

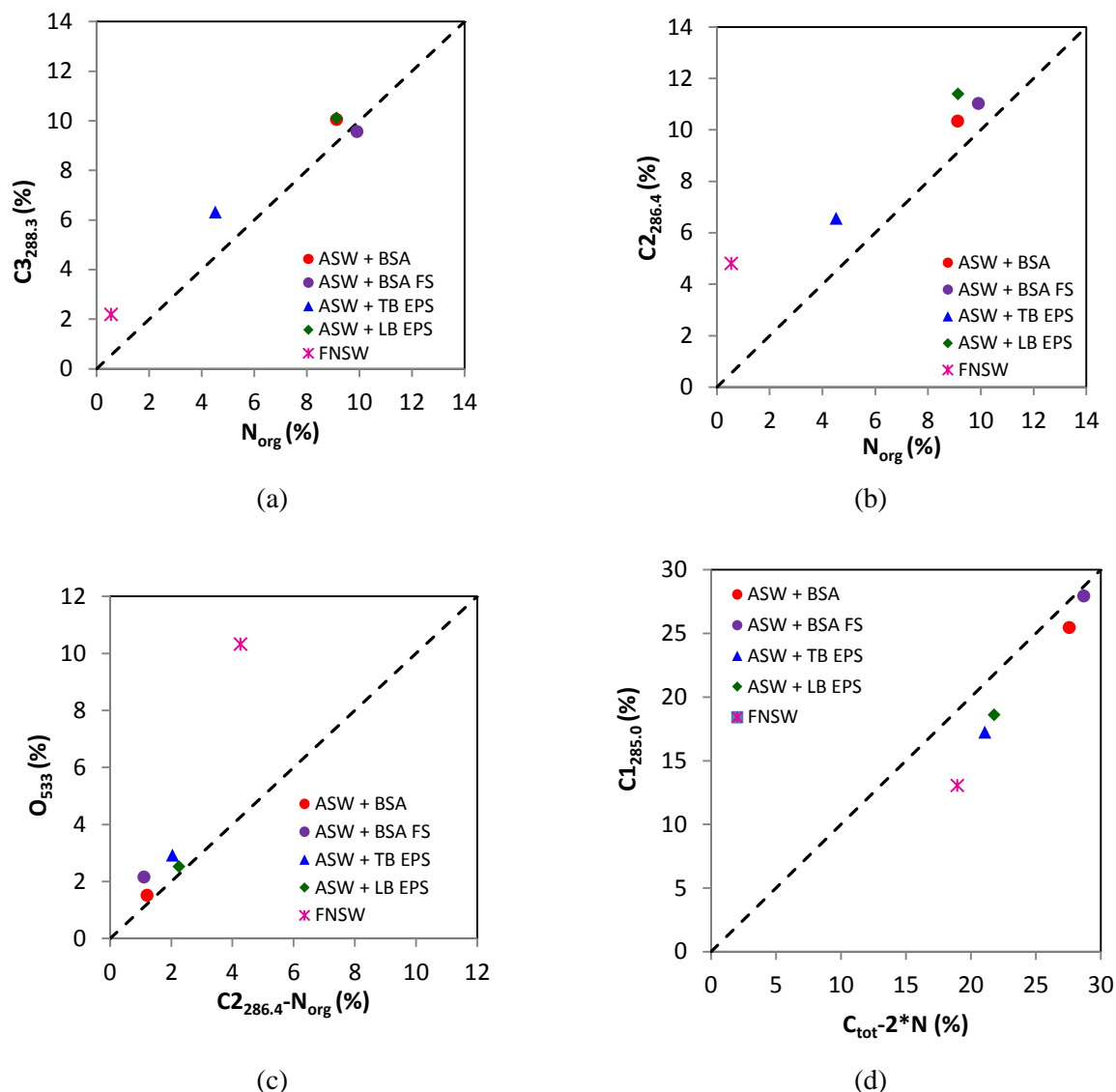


Figure IV. 27: Plot of molar concentrations determined by XPS: (a) $C_{288.3}$ vs N_{org} , (b) $C_{286.4}$ vs N_{org} , (c) O_{533} vs $C_{286.4} \cdot N_{org}$, and (d) $C_{1285.0}$ vs $C_{tot} - 2 \cdot N_{org}$. 70Cu-30Ni samples immersed 1 h at E_{corr} in ASW with $20 \text{ mg} \cdot \text{L}^{-1}$ of BSA, in static conditions (ASW + BSA) and under flow and stirring (ASW + BSA FS), in static ASW in the presence of TB EPS (ASW + TB EPS) or LB EPS (ASW + LB EPS), with a proteins concentration of $20 \text{ mg} \cdot \text{L}^{-1}$, and in static FNSW. Dashed lines: 1:1 relation.

Figure IV.27 (b) shows the molar concentration of the carbon component located at a binding energy of 286.4 eV (C_2 peak), which is due to carbon making a single bond with oxygen (in alcohol, ester or ether) or nitrogen (in amine or amide), as a function of N_{org} . In this figure, the sample after immersion in FNSW presents the highest deviation from the 1:1 relation, which may be attributed to the presence of polysaccharides or oxygen-containing organic contaminants.

Figure IV.27 (c) illustrates the O 1s at 533 eV (not shown in this manuscript), due to oxygen with one (alcohol, carboxyl) or two (ester, ether) bonds with carbon, as a function of the difference between C_2 and N_{org} ($C_2 - N_{org}$). The total organic N is subtracted from C_2 in order to remove the contribution of amide functions related to the presence of proteins. Therefore, a 1:1 relation is expected for alcohols, esters and polysaccharides. The experimental data are close to the 1:1 line except in the case of FNSW for which the observed deviation may be due to the relatively low nitrogen concentration.

Figures IV.27 (a) and IV.27 (b) allow evidencing the presence of the amide function on the surface in all cases except in FNSW. This amide function is considered as a marker of proteins. However, the presences of other functional groups that can be associated to other biomolecules, such as polysaccharides or hydrocarbons (typical of lipids) are also evidenced. Polysaccharides frequently contain N-acetylated aminosugars in which nitrogen is also in the form of amide. Considering that all the N_{org} is in the form of amide ($HC-NH-(C=O)$), the carbon which is not in the form of amide can be calculated by subtracting $2*N_{org}$ from the total carbon ($C_{tot} - 2*N_{org}$) [106], [139]–[141]. Figure IV.27 (d), shows the C_1 carbon component, due to carbon only bound to carbon and hydrogen (hydrocarbon function, typical of lipids) as a function of the total carbon which is not in the form of amide ($C_{tot} - 2*N_{org}$). The deviations from the 1:1 relation reflect the concentration of carbon which is neither in the form of hydrocarbon functions, nor in the form of amide. The samples after immersion in FNSW, TB EPS and LB EPS present significant differences with respect to this 1:1 line, with FNSW having the highest deviation.

Defining the composition of the organic adlayers is difficult due to the complexity of the biochemical compounds and the presence of organic contaminants on the surface. However, as shown in previous figures, the main biomolecules contributions can be distinguished and, therefore, the composition can be estimated in terms of these main components. In this work, the composition of the adsorbed layers was expressed in terms of 4 chemical entities: amide ($HC-NH-(C=O)$) quantified by N_{org} , CH_2 quantified by the C_1 component of the C 1s core level spectra, additional oxidized carbon quantified by $C_{add} = C_{ox} - 2*N_{org}$ and additional organic oxygen quantified by $O_{add} = O_{org} - N_{org} = C_{ox} - 2*N_{org}$ [87], [140], where C_{ox} is the oxidized carbon equal to:

$$C_{ox} = C_2 + C_3 = C_{tot} - C_1 \quad \text{Eq. IV.7}$$

and O_{org} is the organic oxygen which can be approximated by:

$$O_{org} = C_{ox} - N_{org} \quad \text{Eq. IV.8}$$

since for many organic functions (alcohol, primary amide or amine, ester, aldehyde, ketone), and mostly for those which are relevant in biosystems, $C_{ox} = O_{org} + N_{org}$ (exceptions are the cases of ether, carboxylic acid or carboxylate functions).

Thus, C_{add} is the oxidized carbon in addition to the one present in the form of amide and O_{add} the organic oxygen in addition to the one present in the form of amide.

The elemental molar concentrations, obtained from XPS spectra, were converted into weight percentages of these chemical entities (g/100 g of adlayer), as explained in Annex A. Figure IV.28 illustrates the XPS results after conversion into weight percentages in the form of a ternary composition diagram. The corners of this triangle represent 100 wt % of amide, 100 wt % of CH_2 and 100 wt % of additional carbon and oxygen ($C_{add} + O_{add}$) [140]. This figure is convenient to represent the composition of surfaces and adlayers with respect to an amide pole, shared by proteins and N-acetylated functions of polysaccharides, a hydrocarbon pole, typical of lipids, and a pole representative of oxidized organic compounds, including polysaccharide moieties.

The ternary diagram shows that after 1h of immersion in ASW + BSA in static conditions and under flow and stirring, the percentage of amide function is of 70 % and 80 %, respectively, and 20 % of hydrocarbons (CH_2); only 10% of additional carbon and oxygen ($C_{add} + O_{add}$) was observed in static conditions. The high amount of amide functions evidences the major contribution of the BSA protein present on the surface. These results are in agreement to those values obtained by Yang Yi [140].

On the other hand, ASW + TB EPS shows lower amount of amide function (50 %) than in ASW + BSA, and higher hydrocarbons and additional carbon and oxygen (30 % of CH_2 and 20 % of $C_{add} + O_{add}$). Therefore, according to the percentages, proteins remain dominant, but lipids and polysaccharides are also found on the surface. The percentages of biomolecules after immersion in ASW + LB EPS are: 80 % of amide function, 5% of hydrocarbons and 15% of additional carbon and oxygen; meaning much higher amount of proteins in this case than in the case of ASW + TB EPS.

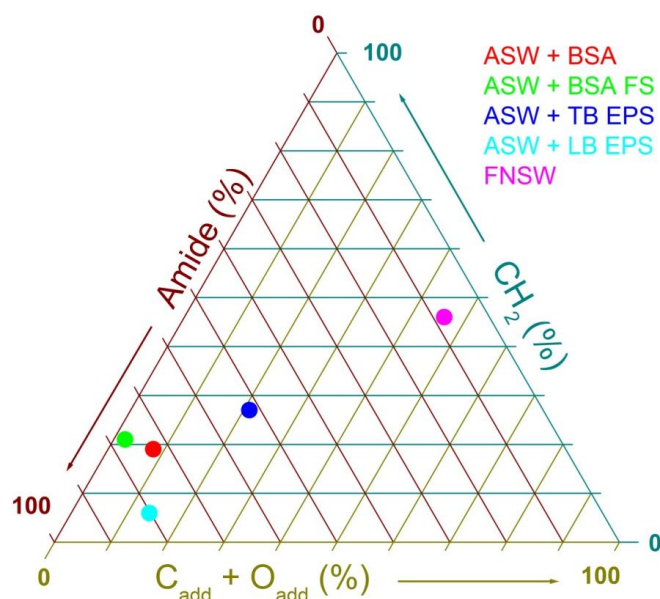


Figure IV. 28: Composition of biomolecules adsorbed on 70Cu-30Ni alloy. Relative mass concentration of amide (HC-NH-(C=O)), hydrocarbon CH₂, and other oxygen-containing molecules (C_{add} + O_{add}), including polysaccharides. 70Cu-30Ni samples immersed 1 h at E_{corr} in ASW with 20 mg.L⁻¹ of BSA, in static conditions (ASW + BSA) and under flow and stirring (ASW + BSA FS), in static ASW in the presence of TB EPS (ASW + TB EPS) or LB EPS (ASW + LB EPS), with a protein concentration of 20 mg.L⁻¹, and in static FNSW.

The ternary diagrams has probed that proteins are the main component adsorbed on the surface after immersion in TB and LB EPS. Therefore significant difference between TB and LB EPS were observed in terms of protein concentration.

Proteins dominate in surface organic layers formed on 70Cu-30Ni exposed to extracellular polymeric substances from *Pseudomonas NCIMB 2021*. Whereas in bulk solution, TB EPS are much more concentrated in proteins than LB EPS (sugars being the dominant components in LB EPS), it is the contrary in the adsorbed phase. These results are in disagreement with those found by Yang Yi [140] who showed that glass surfaces conditioned with TB EPS extracted from *Desulfovibrio Alaskensis* exhibited higher protein concentration than the same surfaces conditioned with LB EPS.

Finally, after immersion in FNSW the surface show low protein concentration (10 % amide), but equal contribution of hydrocarbon (45 % CH₂) and additional carbon and oxygen (45 % C_{add} + O_{add}).

IV.3. Conclusions

Compared to 70Cu-30Ni alloy in static ASW without biomolecules for which a thick duplex oxide layer has been evidenced, the presence of BSA, TB EPS and LB EPS leads to a mixed oxide layer (oxidized copper and nickel) with a lower thickness.

Impedance data in static conditions show a slow-down of the anodic reaction by the biomolecules (BSA, TB EPS and LB EPS), and a corrosion inhibition effect by LB EPS and to a lesser extent by BSA. These kinetic and corrosion inhibition effects are the strongest in the case of LB EPS, in agreement with the lowest Cu^{+1} content in the oxide layer and the thinner oxide layer estimated from XPS data. Therefore, combined electrochemical measurements and surface analysis in static ASW showed that adsorbed LB EPS inhibit the corrosion of 70Cu-30Ni alloy and suppress Cu_2O redeposition (amount of dissolved Cu^{+1} below the solubility limit). Whereas adsorbed BSA and TB EPS slow down the anodic dissolution (kinetic effect) and inhibit Cu_2O redeposition (blocking effect).

Proteins were found to be the major biochemical compounds in the organic adlayers formed on 70Cu-30Ni alloy after immersion in static ASW added with EPS of *Pseudomonas NCIMB 2021*. More proteins were found on the surface in the presence of LB EPS compared to TB EPS, with similar weight percentage as for BSA.

If comparing adsorbed BSA (model protein) and LB EPS, the corrosion inhibition effect induced by the biomolecules cannot be only explained by the amount of adsorbed proteins on the metallic surface but also by the nature of the proteins.

V. Influence of biomolecules adsorption on the electrochemical behaviour and the surface chemical composition of passive materials (304L stainless steel, Ti)

Several kinds of metallic materials can be affected by MIC, including copper alloys and stainless steels usually used in heaters. In some cases, using more noble materials, such as titanium (Ti) and stainless steel, can solve corrosion problems. The objective of this chapter is to study the effect of extracellular polymeric substances (EPS), extracted from *Pseudomonas NCIMB 2021*, on the electrochemical behaviour of passive materials (Ti and 304L stainless steel) and on their surface chemical composition. Results are compared with those obtained in the presence of BSA (model protein).

As mentioned in previous chapters, TB and LB EPS were extracted from *Pseudomonas NCIMB 2021*, and their compositions in proteins, sugars, DNA and uronic acids were determined. For this study, EPS solutions were prepared, and the protein concentration of ASW (for Ti) and of the chloride-free solution (for 304L stainless steel) containing TB EPS was constant and equal to 20 mg.L^{-1} , in order to compare these results with those obtained in the presence of 20 mg.L^{-1} of BSA. For LB EPS, since the dialysis was done in ASW and the concentration of proteins was already $\sim 20 \text{ mg.L}^{-1}$ (see Chapter II), the use of chloride-free solution containing LB EPS was not possible. Therefore, in order to compare the two passive materials in the same conditions, the effect of LB EPS was not studied. Experiments were performed in aerated solutions, in static conditions.

V.1. Electrochemical measurements

V.1.1. Titanium

The corrosion potential of Ti was recorded during 1 h in ASW, with and without biomolecules (Table V.1). The E_{corr} values in ASW are between -0.210 V and -0.322 V vs SCE without biomolecules, and between -0.210 V and -0.366 V vs SCE with BSA. These values do not indicate a strong influence of the protein on E_{corr} value. The mean value of the corrosion potential in the presence of TB EPS is more cathodic, compared to that observed without biomolecules.

In the case of Ti, E_{corr} values are less reproducible than for 70Cu-30Ni alloy (see Table IV.6)

Table V. 1: Corrosion potential (E_{corr}) of Ti after 1 h of immersion in static aerated ASW, without and with biomolecules (protein concentration: 20 mg.L⁻¹).

	$E_{corr} / \text{V vs SCE}$
ASW	-0.266 ± 0.056
ASW + BSA	-0.288 ± 0.078
ASW + TB EPS	-0.375 ± 0.044

Figure V.1 illustrates the cathodic polarisation curves plotted after 1 h of immersion in ASW without and with biomolecules. In all cases, an increase of the current density (in absolute value) from the corrosion potential is visible, followed by a current plateau at more cathodic potentials. This current plateau, observed between -1.1 and -1.3 V vs SCE, corresponds to the reduction of dissolved oxygen and is similar for the three solutions ($|j| \sim 13\text{-}16 \mu\text{A.cm}^{-2}$). An inflexion point around -0.6/-0.8 V vs SCE can be observed on the three curves, possibly illustrating the transition from an oxidized surface to a non oxidized one [142]. An effect on the biomolecules, mainly of BSA, is visible from E_{corr} down to the current plateau. A further analysis of this possible effect is given in the discussion section. At more cathodic potentials, the increase of the current illustrates the hydrogen evolution reaction (reduction of water with H₂ production).

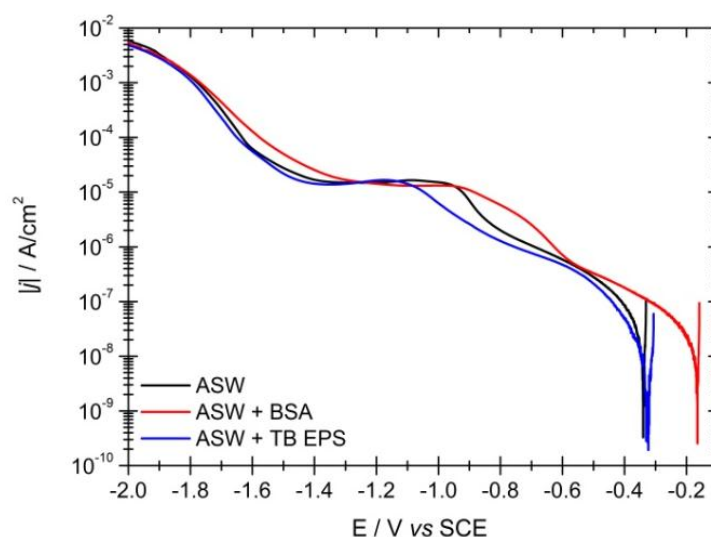


Figure V. 1: Cathodic polarisation curves of Ti after 1 h of immersion at E_{corr} in static aerated ASW, in the absence and in the presence of biomolecules (BSA, TB EPS) with a protein concentration of 20 mg.L⁻¹. Scan rate: 0.5 mV.s⁻¹.

The anodic polarization curves, presented in Figure V.2, show a Tafel-like behaviour (linear variation of the current as a function of potential), followed by a well-defined passive plateau. This Tafel-like behaviour is a measurement artefact due to the non-stationarity of the system using a scan rate of $0.5 \text{ mV}\cdot\text{s}^{-1}$ (see the discussion sections, V.3.2) [142]. The passive plateau extends over a wide range of potentials (from ~ 0.2 to 1.2 V vs SCE), and the corresponding passive plateau current density $j_{a,pl}$ is between 3 and $4 \mu\text{A}\cdot\text{cm}^{-2}$ in all cases. The peak observed around 1.6 - 1.7 V could illustrate transpassive dissolution. The shape of the anodic polarization curves and the current densities are similar in the absence and in the presence of biomolecules. Therefore, there is no great influence of the biomolecules on the anodic behaviour, except a passive current slightly lower with BSA (see more details in the discussion section).

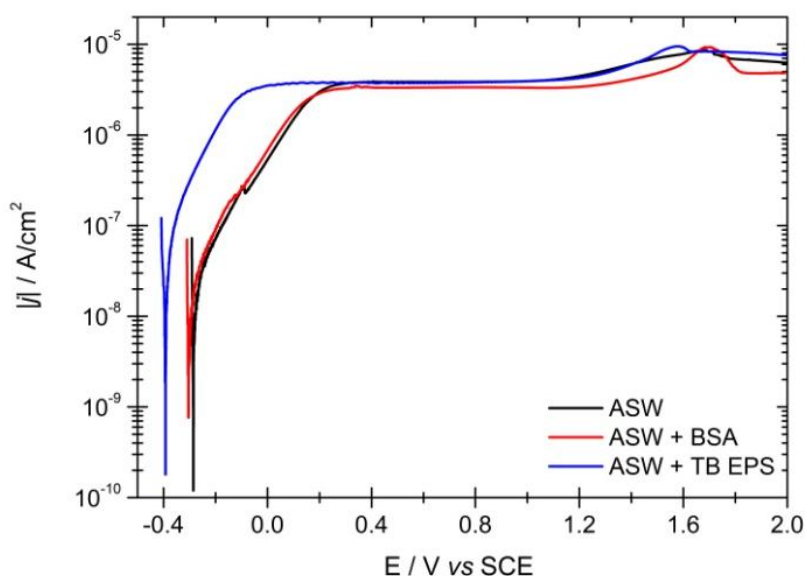


Figure V. 2: Anodic polarisation curves of Ti after 1 h of immersion at E_{corr} in static aerated ASW, in the absence and in the presence of biomolecules (BSA, TB EPS) with a protein concentration of $20 \text{ mg}\cdot\text{L}^{-1}$. Scan rate: $0.5 \text{ mV}\cdot\text{s}^{-1}$.

Figure V.3 shows the impedance diagrams of Ti plotted after 1 h of immersion in ASW, without and with biomolecules. The presence of one loop is observed for the three conditions, and the order of magnitude of the impedances (several hundreds of $\text{k}\Omega\cdot\text{cm}^2$) is in agreement with that commonly observed for passivated materials. Therefore, this loop may illustrate the presence of a passive layer on the Ti surface. The highest size of the loop corresponds to ASW + BSA, and the lowest to ASW + TB EPS. Thus, biomolecules seem to have a slight

effect on the passivation behaviour of Ti in ASW at E_{corr} : protective or beneficial effect for BSA, and minor detrimental effect for TB EPS.

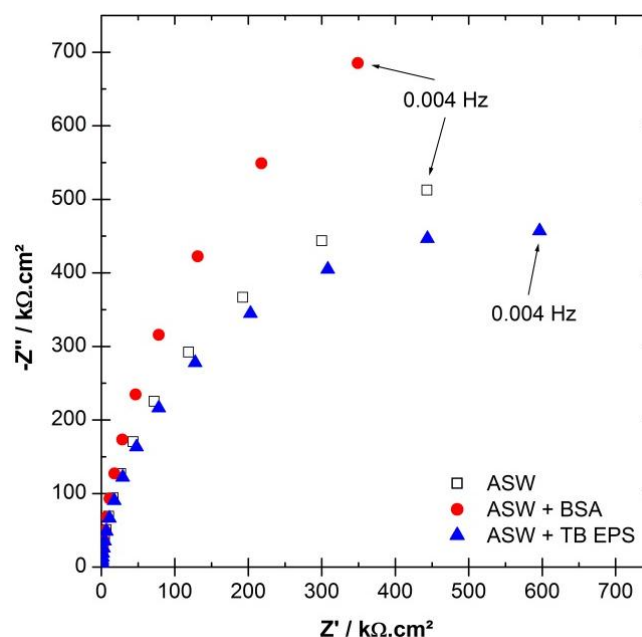


Figure V. 3: Experimental impedance diagrams in the complex plane (Nyquist diagrams) of Ti after 1 h of immersion at E_{corr} in static aerated ASW, in the absence and in the presence of biomolecules (BSA, TB EPS) with a protein concentration of 20 mg.L^{-1} .

V.1.2. 304L stainless steel

The anodic polarisation curves of 304L stainless steel after 1 h of immersion at E_{corr} in ASW are shown in Figure V.4. These curves exhibit a linear increase of the current (from 0.01 to $1 \mu\text{A/cm}^2$) in a wide potential domain, ranging from E_{corr} to the pitting potential E_p equal to $\sim 0.223 \text{ V vs SCE}$. This Tafel-like behaviour is not the usual shape observed for stainless steel; an explanation will be given in section V.3.2. (non steady-state conditions). Therefore, pitting corrosion, illustrated by the rapid current increase above E_p , is demonstrated. Furthermore, visual observation of the alloy surface after the anodic polarization curve confirms localized corrosion: pits are observed on the whole surface in contact with the solution and crevices only under the O-ring which ensures the tightness of the working electrode.

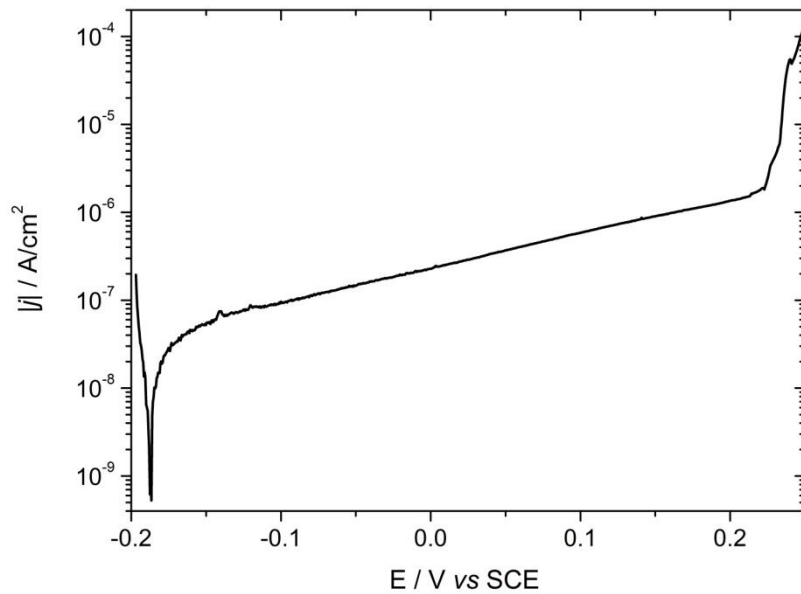


Figure V. 4: Anodic polarisation curves of 304L stainless steel after 1 h of immersion at E_{corr} in static aerated ASW. Scan rate: $0.5 \text{ mV}\cdot\text{s}^{-1}$.

It is well known that 304L stainless steel is not used for condenser tubes cooled with seawater because of the presence of chlorides which causes localized corrosion. In order to avoid pitting and crevice corrosion in the case of 304L stainless steel, it was decided to work in Cl^- -free solution ($0.24 \text{ M Na}_2\text{SO}_4 + 0.002 \text{ M NaHCO}_3$; same ionic strength and pH as artificial seawater).

The influence of biomolecules on the electrochemical behaviour of 304L stainless steel in Cl^- -free solution was investigated. For that, BSA and TB EPS were diluted in $0.24 \text{ M Na}_2\text{SO}_4 + 0.002 \text{ M NaHCO}_3$ solution, in order to have a protein concentration equal to $20 \text{ mg}\cdot\text{L}^{-1}$.

The corrosion potential of 304L stainless steel was recorded during 1 h. Reproducible values were measured. From E_{corr} vs time curves, it can be concluded that the presence of biomolecules induces more cathodic corrosion potential values (Table V.2).

Table V. 2: Corrosion potential (E_{corr}) of 304L stainless steel after 1 h of immersion in static aerated Cl^- -free solution, without and with biomolecules (protein concentration: 20 mg.L^{-1}).

	$E_{corr} / \text{V vs SCE}$
Cl^--free solution	-0.099 ± 0.004
Cl^--free solution + BSA	-0.146 ± 0.017
Cl^--free solution + TB EPS	-0.138 ± 0.008

The cathodic polarisation curves of 304L stainless steel after 1 h of immersion in Cl^- -free solution, without and with biomolecules (BSA and TB EPS), are shown in Figure V.5. In all cases, a current plateau, corresponding to the reduction of dissolved oxygen, can be observed from ~ -0.4 down to -0.9 V vs SCE . The current density of this plateau is $\sim 16 \mu\text{A.cm}^{-2}$ (in absolute value), for all the conditions, and is similar to that measured for Ti in ASW, in agreement with a non-oxidized surface in this potential range. For potentials below -0.9 V vs SCE , the increase of current (in absolute value) illustrates the hydrogen evolution reaction (reduction of water with H_2 production). No significant differences between the cathodic polarisation curves can be observed, showing that biomolecules do not affect the cathodic behaviour of 304L stainless steel in Cl^- -free solution.

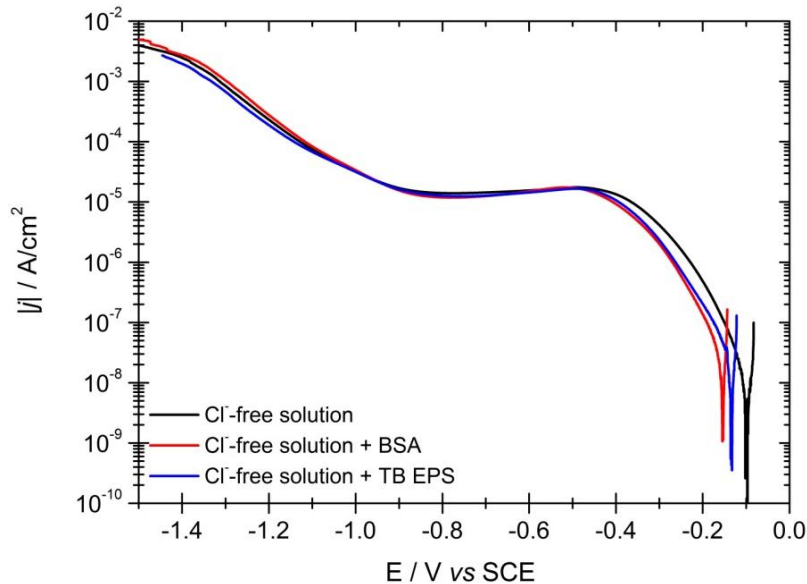


Figure V. 5: Cathodic polarisation curves of 304L stainless steel after 1 h of immersion at E_{corr} in static aerated Cl^- -free solution ($0.24 \text{ M Na}_2\text{SO}_4 + 0.002 \text{ M NaHCO}_3$), in the absence and in the presence of biomolecules (BSA, TB EPS) with a protein concentration of 20 mg.L^{-1} . Scan rate: 0.5 mV.s^{-1} .

Figure V.6 illustrates the anodic polarisation curves of 304L stainless steel after 1 h of immersion in the Cl⁻-free solution, without and with biomolecules. As for Ti in ASW, a Tafel-like behaviour followed by a pseudo-passive plateau between ~ 0.3 and 0.9 V vs SCE can be observed. The passive plateau current density $j_{a,pl}$ at 0.8 V vs SCE is equal to 4.1 , 3.4 and 2.9 $\mu\text{A}\cdot\text{cm}^{-2}$ for ASW, ASW + BSA and ASW + TB EPS, respectively. Thus, this passive current is slightly lower with biomolecules, especially with TB EPS.

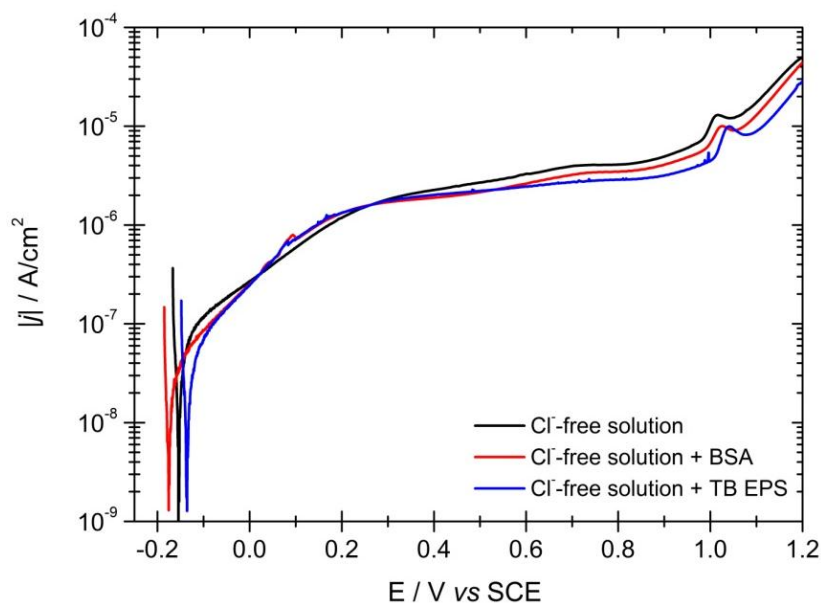


Figure V. 6: Anodic polarisation curves of 304L stainless steel after 1 h of immersion at E_{corr} in static aerated Cl⁻-free solution (0.24 M Na_2SO_4 + 0.002 M NaHCO_3), in the absence and in the presence of biomolecules (BSA, TB EPS) with a protein concentration of 20 $\text{mg}\cdot\text{L}^{-1}$. Scan rate: 0.5 $\text{mV}\cdot\text{s}^{-1}$.

Details about the possible effect of biomolecules on the cathodic behaviour are given in the discussion section.

Similarly to what is observed for Ti, the impedance diagrams plotted at E_{corr} exhibit one loop (Figure V.7). The size of the loop is lower than for Ti, but the order of magnitude of the impedance is the same (several hundreds of $\text{k}\Omega\cdot\text{cm}^2$), in agreement with the presence of a passive layer. If comparing the size of the loop, the same ranking as for Ti is obtained: BSA > without biomolecules > TB EPS. Thus, the passive layer seems to be the most protective in the presence of BSA and the less protective in the presence of TB EPS.

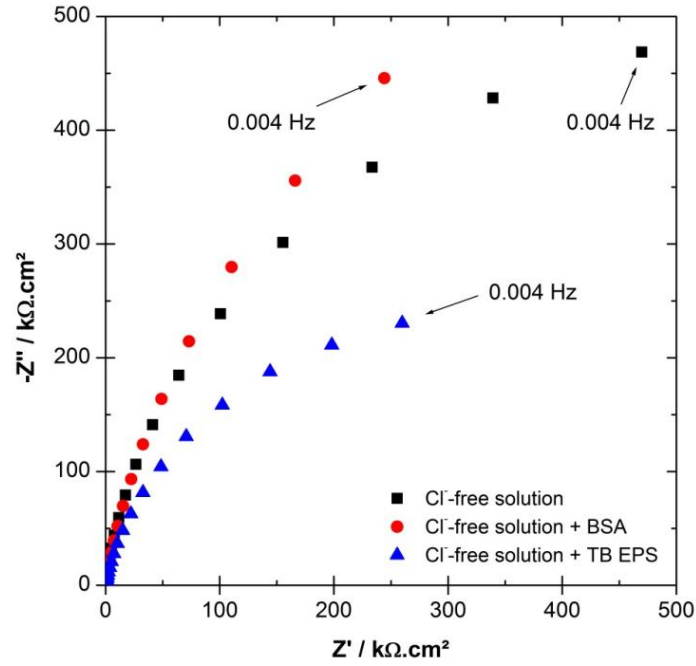


Figure V. 7: Experimental impedance diagrams in the complex plane (Nyquist diagrams) of 304L stainless steel after 1 h of immersion at E_{corr} in static aerated Cl^- -free solution (0.24 M Na_2SO_4 + 0.002 M NaHCO_3), in the absence and in the presence of biomolecules (BSA, TB EPS) with a protein concentration of $20 \text{ mg}\cdot\text{L}^{-1}$.

V.2. Surface analysis

V.2.1. Titanium

In this work, the total oxidized Ti was considered to be a single TiO_2 oxide layer in order to calculate the oxide layer thickness. Therefore, considering a continuous oxide layer covering the metallic substrate (Figure V.8 (a)), the equivalent thickness of the oxide layer (d_{oxide}) can be calculated from XPS data using the following equations, in which the intensities of Ti in the metallic substrate and in the oxide layer are considered:

$$I_{\text{Ti}}^{\text{Metal}} = k \cdot T_{\text{Ti}} \cdot \sigma_{\text{Ti}} \cdot D_{\text{Ti}}^{\text{Metal}} \cdot \lambda_{\text{Ti}}^{\text{Metal}} \cdot \sin\theta \cdot \exp\left(\frac{-d_{\text{oxide}}}{\lambda_{\text{Ti}}^{\text{Oxide}} \sin\theta}\right) \quad \text{Eq. V.1}$$

$$I_{\text{Ti}}^{\text{Oxide}} = k \cdot T_{\text{Ti}} \cdot \sigma_{\text{Ti}} \cdot D_{\text{Ti}}^{\text{Oxide}} \cdot \lambda_{\text{Ti}}^{\text{Oxide}} \cdot \sin\theta \cdot \left[1 - \exp\left(\frac{-d_{\text{oxide}}}{\lambda_{\text{Ti}}^{\text{Oxide}} \sin\theta}\right)\right] \quad \text{Eq. V.2}$$

where:

θ is the take-off angle of the photoelectrons with respect to the sample surface; in this work, $\theta = 90^\circ$;

k is a spectrometer constant;

σ_{Ti} , is the photo-ionisation cross-sections of Ti;

λ_{Ti}^{Metal} , λ_{Ti}^{Oxide} are the inelastic mean free paths (IMFP) of the photoelectrons emitted by the Ti core level in the metal and in the oxide, respectively;

T_{Ti} is the transmission function for Ti;

D_{Ti}^{Metal} , D_{Ti}^{Oxide} are the densities of Ti in the metal and in the oxide, respectively.

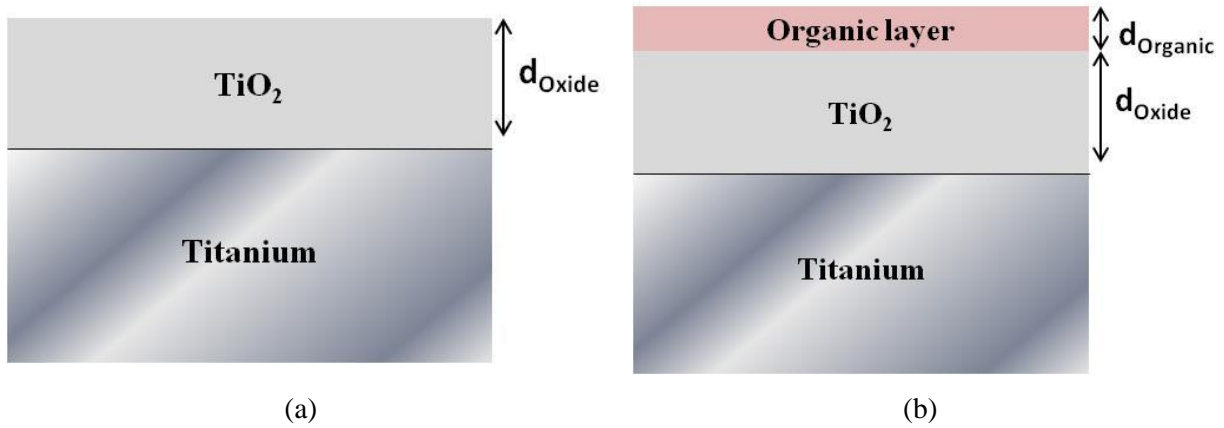


Figure V. 8: Layer model assumed for the analysis of XPS data of Ti: (a) TiO₂ oxide layer covering the metallic substrate, and (b) organic layer covering the oxide layer formed on the metal.

These equations can be rearranged, leading to the expression that allows calculating the equivalent layer thickness:

$$d_{Oxide} = \lambda_{Ti}^{Oxide} \cdot \sin\theta \cdot \ln \left(1 + \frac{D_{Ti}^{Metal} \lambda_{Ti}^{Metal} I_{Ti}^{Oxide}}{D_{Ti}^{Oxide} \lambda_{Ti}^{Oxide} I_{Ti}^{Metal}} \right) \quad \text{Eq. V.3}$$

Figure V.8 (b) illustrates the layer model used for the analysis of XPS data of Ti after immersion in a solution containing biomolecules (BSA and TB EPS) that adsorb on the surface, forming an organic film on top of the oxide layer, with an equivalent thickness $d_{Organic}$.

The thickness d_{Organic} can be calculated from the $I_N^{\text{Organic}}/I_{\text{Ti}}^{\text{Oxide}}$ ratio. The nitrogen signal comes mainly from the proteins and, hence, is considered to be a fingerprint of the adsorbed biomolecules. The N 1s intensity emitted by the adsorbed biomolecules is given by:

$$I_N^{\text{Organic}} = k\sigma_N\lambda_N^{\text{Organic}}D_N^{\text{Organic}}T_N \left[1 - \exp\left(-\frac{d_{\text{Organic}}}{\lambda_N^{\text{Organic}}}\right) \right] \quad \text{Eq. V.4}$$

The Ti 2p intensity emitted by oxide layer and attenuated by the adsorbed protein is given by:

$$I_{\text{Ti}}^{\text{Oxide}} = k\sigma_{\text{Ti}}\lambda_{\text{Ti}}^{\text{Oxide}}D_{\text{Ti}}^{\text{Oxide}}T_{\text{Ti}} \exp\left(-\frac{d_{\text{Organic}}}{\lambda_{\text{Ti}}^{\text{Organic}}}\right) \left(1 - \exp\left(-\frac{d_{\text{Oxide}}}{\lambda_{\text{Ti}}^{\text{Oxide}}}\right) \right) \quad \text{Eq. V.5}$$

Then,

$$\frac{I_N^{\text{Organic}}}{I_{\text{Ti}}^{\text{Oxide}}} \times \frac{\sigma_{\text{Ti}}\lambda_{\text{Ti}}^{\text{Oxide}}D_{\text{Ti}}^{\text{Oxide}}T_{\text{Ti}}}{\sigma_N\lambda_N^{\text{Organic}}D_N^{\text{Organic}}T_N} = \frac{1 - \exp\left(-\frac{d_{\text{Organic}}}{\lambda_N^{\text{Organic}}}\right)}{\exp\left(-\frac{d_{\text{Organic}}}{\lambda_{\text{Ti}}^{\text{Organic}}}\right) \left(1 - \exp\left(-\frac{d_{\text{Oxide}}}{\lambda_{\text{Ti}}^{\text{Oxide}}}\right) \right)} \quad \text{Eq. V.6}$$

The values for the transmission function T are listed in Table V.3.

Table V. 3: Transmission functions $T(E_{\text{kin}})$ of the Escalab 250 energy analyzer, provided by Thermo Electron Corporation.

$T(E_{\text{kin}})$	Ti 2p	N 1s
		3319

The inelastic mean free path (λ) values were taken from the QUASES-IMFP-TPP2M database (see Chapter II). These values are listed in Table V.4. For the calculation of $\lambda_N^{\text{Organic}}$, $\lambda_{\text{Ti}}^{\text{Organic}}$ and D_N^{Organic} , the organic layer was considered to be a BSA layer (model protein).

Table V. 4: Inelastic mean free paths λ in nm – Taken from the QUASES-IMFP-TPP2M.

λ (nm)			
λ_{Ti}^{Metal}	λ_{Ti}^{Oxide}	$\lambda_{Ti}^{Organic}$	$\lambda_N^{Organic}$
2.19	2.12	2.95	3.39

The photoionization cross-section σ_X values are presented in Table V.5.

Table V. 5: Photo-ionization cross sections σ_X at 1486.6 eV.

	Ti 2p	N 1s
σ_X	7.9	1.8

XPS measurements were performed for Ti after 1 h of immersion in ASW with and without biomolecules (BSA and TB EPS). No measurements were performed with LB EPS. The following core levels were recorded: Ti 2p, Ni 2p, O 1s, C 1s, and N 1s.

The Ti 2p_{3/2} core level spectra can be decomposed in 4 peaks attributed to the different oxidation states of Ti. The peak located at the binding energy of 453.6 ± 0.2 eV corresponds to Ti⁰, 455.2 ± 0.1 eV to Ti⁺², 457.2 ± 0.1 eV to Ti⁺³ and 458.9 ± 0.2 eV to Ti⁺⁴ [143]–[145]. However, due to an overlapping of the contribution of Ti⁰ in Ti 2p_{1/2} with Ti⁺⁴ in Ti 2p_{3/2} the whole Ti 2p core level was decomposed (Figure V.9 (a)).

The Ti 2p core level spectra of Ti after polishing and the Ti 2p core levels obtained after immersion in the three different solutions (ASW, ASW + BSA and ASW + TB EPS) are compared in Figure V.9 (b). In all the cases the presence of the metal component (Ti⁰ at ~ 453.6 eV) is observed indicating that the oxide layer thickness is lower than ~ 10 nm and thus it can be calculated using the XPS data. Additionally, the decomposition of the different peaks evidences the presence of the suboxides (Ti⁺² and Ti⁺³), and not only Ti⁺⁴. Nevertheless, the major contribution corresponds to Ti⁺⁴, associated with the formation of TiO₂, characteristic of the passive layer usually formed on Ti. In the literature, the oxide film on Ti is often described as a mixed oxide layer consisting of TiO₂, Ti₂O₃, TiO in which the Ti⁺³ and Ti⁺² species are described as suboxides located closer to the metal/oxide interface and the Ti⁺⁴ specie (TiO₂) is found to form the outermost layer of the oxide film [107], [146]–[149].

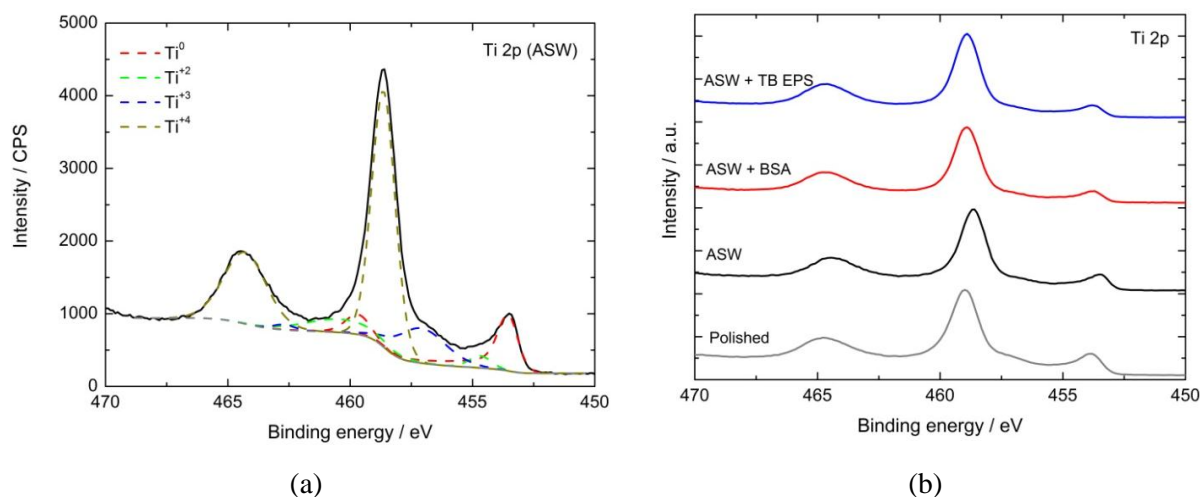


Figure V. 9: X-ray photoelectron spectroscopy (XPS): (a) decomposition of the Ti 2p core level spectra (1 h of immersion at E_{corr} in static aerated ASW), and (b) comparison of Ti 2p core level spectra of Ti after polishing and after 1 h of immersion at E_{corr} in static aerated ASW, in the absence and in the presence of biomolecules (BSA, TB EPS) with a proteins concentration of 20 mg.L^{-1} . The intensity is expressed in (a) counts per second (CPS) or (b) arbitrary unit (a.u.).

Table V.6 shows the composition of suboxides and TiO_2 forming the oxide layer, as well as the oxide layer thickness calculated considering the total oxide as TiO_2 . It is observed that the lowest Ti^{+4} and the highest Ti^{+2} content are present in the sample just after polishing. Furthermore, the presence of biomolecules induces higher Ti^{+4} and lower Ti^{+2} content than after immersion in ASW without biomolecules, and the oxide layer thickness is higher in the presence of biomolecules. The composition and the oxide layer thickness are independent of the type of biomolecules used.

Table V. 6: Oxide layer composition (oxidation state), and oxide layer thickness estimated by assuming that the total oxidized Ti (Ti^{+4} , Ti^{+3} and Ti^{+2}) corresponds to Ti^{+4} . Ti after polishing and after 1 h of immersion at E_{corr} in static aerated ASW, in the absence and in the presence of biomolecules (BSA, TB EPS) with a protein concentration of 20 mg.L^{-1} .

	Oxide layer composition / at. %			Oxide layer thickness / nm
	Ti^{+4}	Ti^{+3}	Ti^{+2}	
After polishing	69	15	16	4.1
ASW	75	15	10	3.8
ASW + BSA	79	14	7	4.6
ASW + TB EPS	78	14	8	4.6

Figure V.10 shows ToF-SIMS profiles for Ti after polishing (Figure V.10(a)) and after 1 h of immersion in aerated ASW (Figure V.10(b)), in ASW with BSA (Figure V.10(c)) and in ASW with TB EPS (Figure V.10(d)) in static conditions. The profiles were recorded with a sputtered surface area of $700 \times 700 \mu\text{m}^2$. They evidence, in all the cases, a stratification of the oxide film covering the metallic surface. Three regions are observed for the sample after polishing and after 1h of immersion in ASW. Four regions are observed in the presence of biomolecules. For the sample after polishing, the first region extends from 0 s to 92 s of sputtering, and is characterised by an intense 80TiO_2^- signal. In the case of the sample after immersion in ASW, this first area is extended from 0 to 105 s of sputtering. It is well known that the highest oxidation state of Ti is located in the outermost layer [150]; In the presence of biomolecules, this outer TiO_2 layer appears in the second region from 14 to 100 s with BSA and from 13 to 58 s with TB EPS.; and the first region illustrates the presence of the organic layer on the top of the oxide layer and is characterised by a maximum intensity of the 26CN^- signal (characteristic signal of proteins -peptidic link-). The 64TiO^- is also observed in the first region, however, this signal reach its highest intensity in the second region where the TiO_2^- signal drastically decreases, and is characteristic of the inner oxide layer composed of suboxides of Ti (Ti_2O_3 and TiO). For the sample after polishing this inner oxide layer extends from 90 to 200 s of sputtering, whereas after 1h of immersion in ASW extends form 106 to 246 s of sputtering. This inner oxide layer corresponds to the third region for the samples after immersion in ASW with biomolecules. It extends from 100 to 244 s with BSA, whereas only from 59 to 142s of sputtering for TB EPS. After the inner oxide layer, the decrease of all oxidized signals, for all types of immersion, linked with constant and intense plateau of the 96Ti_2^- signal, indicates that the metallic substrate is reached.

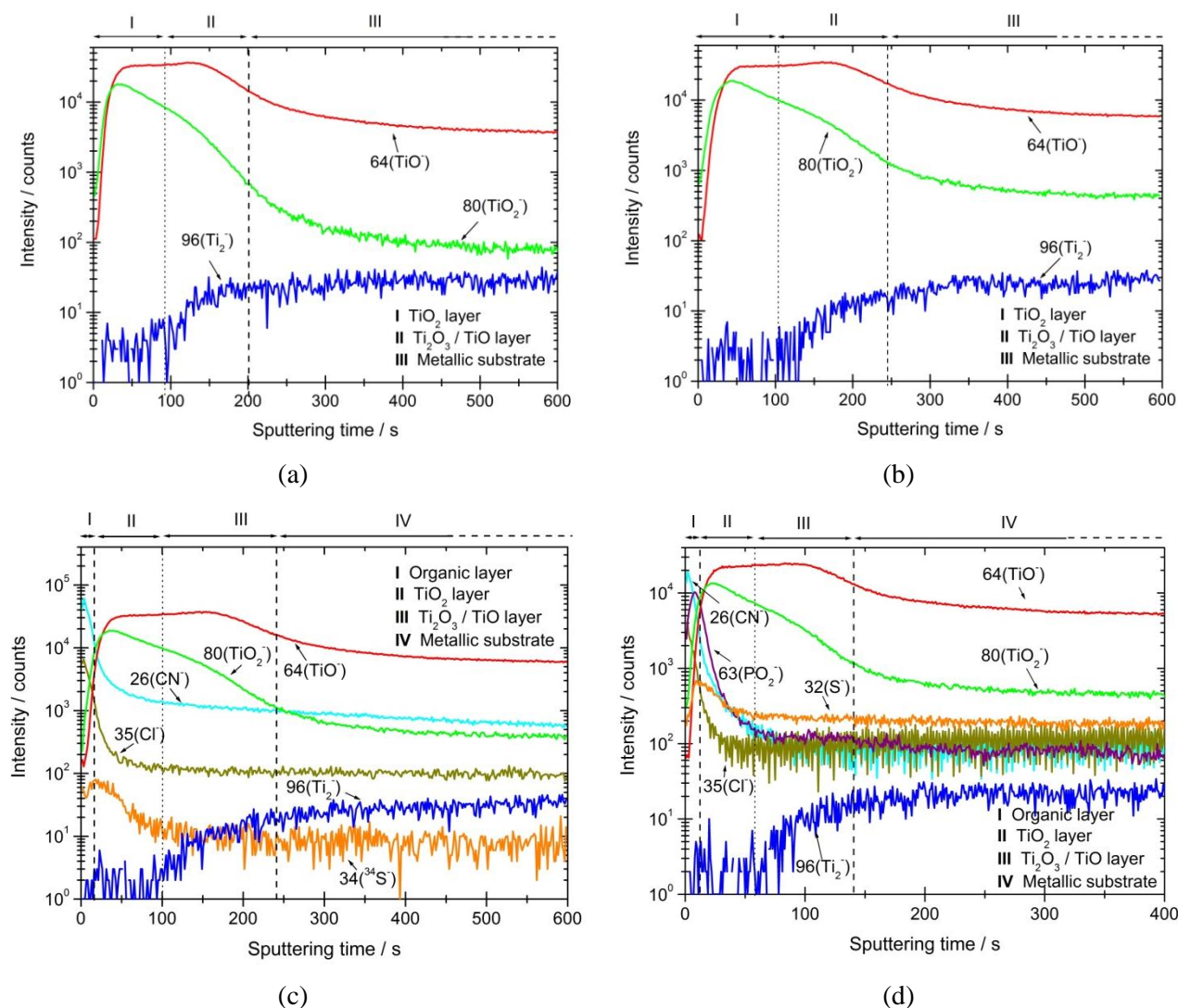


Figure V. 10: Characteristic Time-of-Flight Secondary Ions Mass spectrometry (ToF-SIMS) depth profiles (negative ions) of Ti (a) after polishing, and after 1 h of immersion at E_{corr} in static aerated: (b) ASW, (c) ASW with 20 mg.L⁻¹ of BSA, and (d) ASW with TB EPS (protein concentration: 20 mg.L⁻¹).

Figures V.11 (a) and V.11 (b) show the N 1s and C 1s core level spectra respectively, for Ti after 1 h of immersion in ASW with BSA and TB EPS. The N 1s core level spectra exhibit, for both biomolecules, the same peak centred at ~ 400.4 eV, typical of amide groups (peptidic link). The decomposition of the C 1s core level spectra for the two biomolecules solutions reveals the presence of the three typical contributions (see Chapter IV) attributed to typical carbon bonds present in biomolecules ($\underline{\text{C}}\text{-(C,H)}$, at 285.0 eV; $\underline{\text{C}}\text{-(N,O)}$ at 286.4; and $\underline{\text{C}}\text{=O}$ at 288.3 eV) [16], [72], [87], [106], [138]–[140].

Similar to what was done with 70Cu-30Ni alloy (see Chapter IV), “nitrogen/carbon” and “carbon/carbon” atomic ratios were calculated from the N 1s and C 1s signals. The values of the atomic ratios obtained for Ti after exposure to BSA and TB EPS solutions are compared in Table V.7 to the values obtained for the BSA powder [16], [72]. The good agreement between the values obtained for the ASW + BSA and the BSA powder shows the presence of the protein adsorbed on the surface. Although in ASW + TB EPS the values obtained for the atomic ratios are close to the BSA powder, some deviations are observed indicating the presence of proteins on the surface, but also other biomolecules different than proteins. However, proteins seem to be the main biomolecules present on the surface. Further details are given in the discussion section.

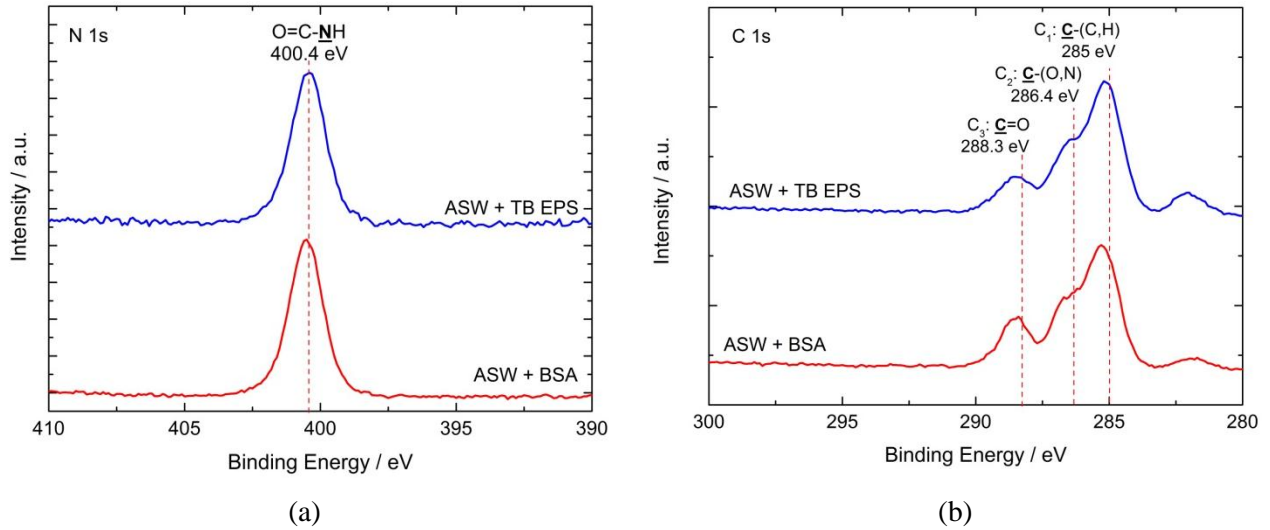


Figure V. 11: (a) N 1s and (b) C 1s XPS core level spectra of Ti after 1 h of immersion at E_{corr} in static aerated ASW, in the presence of biomolecules (BSA, TB EPS) with a protein concentration of 20 mg.L^{-1} . The intensity is expressed in arbitrary units (a.u.).

Table V. 7: Atomic ratios calculated from the XPS N 1s and C 1s core level spectra recorded for the BSA powder and for Ti after 1 h of immersion at E_{corr} in static aerated artificial seawater, in the presence of BSA or TB EPS with a protein concentration of 20 mg.L^{-1} .

	$\text{N}/\text{C}_{\text{total}}$	$\text{N}/(\text{C}_2+\text{C}_3)$	$\text{C}_1/\text{C}_{\text{total}}$	$\text{C}_2/\text{C}_{\text{total}}$	$\text{C}_3/\text{C}_{\text{total}}$
BSA powder	0.22	0.48	0.54	0.26	0.20
ASW	0.05	0.17	0.69	0.18	0.12
ASW + BSA	0.23	0.49	0.52	0.28	0.20
ASW + TB EPS	0.15	0.35	0.57	0.27	0.16

The thickness of the organic layer was estimated from XPS data, considering the same parameters values as for the model protein (BSA). The thickness is 1.9 nm for BSA and 0.9 nm for TB EPS, probably indicating the presence of a non continuous organic layer.

V.2.2. 304L stainless steel

Figure V.12 illustrates the ToF-SIMS profiles for 304L stainless steel after polishing (Figure V.12 (a)) and after 1 h of immersion in static conditions in aerated Cl⁻-free solution (Figure V.12 (b)), in Cl⁻-free solution with BSA (Figure V.12 (c)) and in Cl⁻-free solution with TB EPS (Figure V.12 (d)). The profiles were recorded with a sputtered surface area of 1000 × 1000 μm² in all the cases except with TB EPS, where the sputtered surface area was 700 × 700 μm². These profiles evidence, in all the cases, a stratification of the oxide film. Three regions are observed for the sample after polishing and after 1h of immersion in the Cl⁻-free solution; and four regions are observed in the presence of biomolecules. In the case of the sample after polishing, the first region extends from 0 s to 71 s of sputtering, and is characterised by an intense 88FeO₂⁻ signal. In the case of the sample after immersion in the Cl⁻-free solution, this first area is extended from 0 to 51 s of sputtering. This first zone corresponds to the formation of Fe₂O₃ in the outer part of the oxide layer. In the presence of biomolecules, this outer Fe₃O₂ layer (that extends from 26 to 79 s with BSA and from 11 to 27 s with TB EPS) is covered by an organic layer as shown by the maximum of intensity of the 26CN⁻ signal, characteristic signal of proteins -peptidic link. For the sample after polishing, the second region extends from 72 to 190 s of sputtering, whereas after 1h of immersion in the Cl⁻-free solution, it extends from 52 to 190 s. This region is characterised by an intense 84CrO₂⁻ signal and is assigned to the formation of an inner Cr₂O₃ layer. This second region corresponds to the third region on the samples immersed in biomolecules-containing solution. It extends from 80 to 200 s with BSA and from 28 to 63 s in presence of TB EPS. The 88FeO₂⁻ signal sharply decreases in this region. On the contrary, only the 90NiO₂⁻ signal remains at a high intensity throughout the full oxide layer and in all the conditions, indicating that Ni oxide is present throughout the entire oxide thickness. The last region, characterised by a decrease of all oxidized signals (88FeO₂⁻, 84CrO₂⁻, 18¹⁸O⁻, 90NiO₂⁻) and a constant and intense plateau for the 112Fe₂⁻ and 116Ni₂⁻ signals, characteristic of the metallic substrate, indicate that at this point the metal/oxide interface is reached.

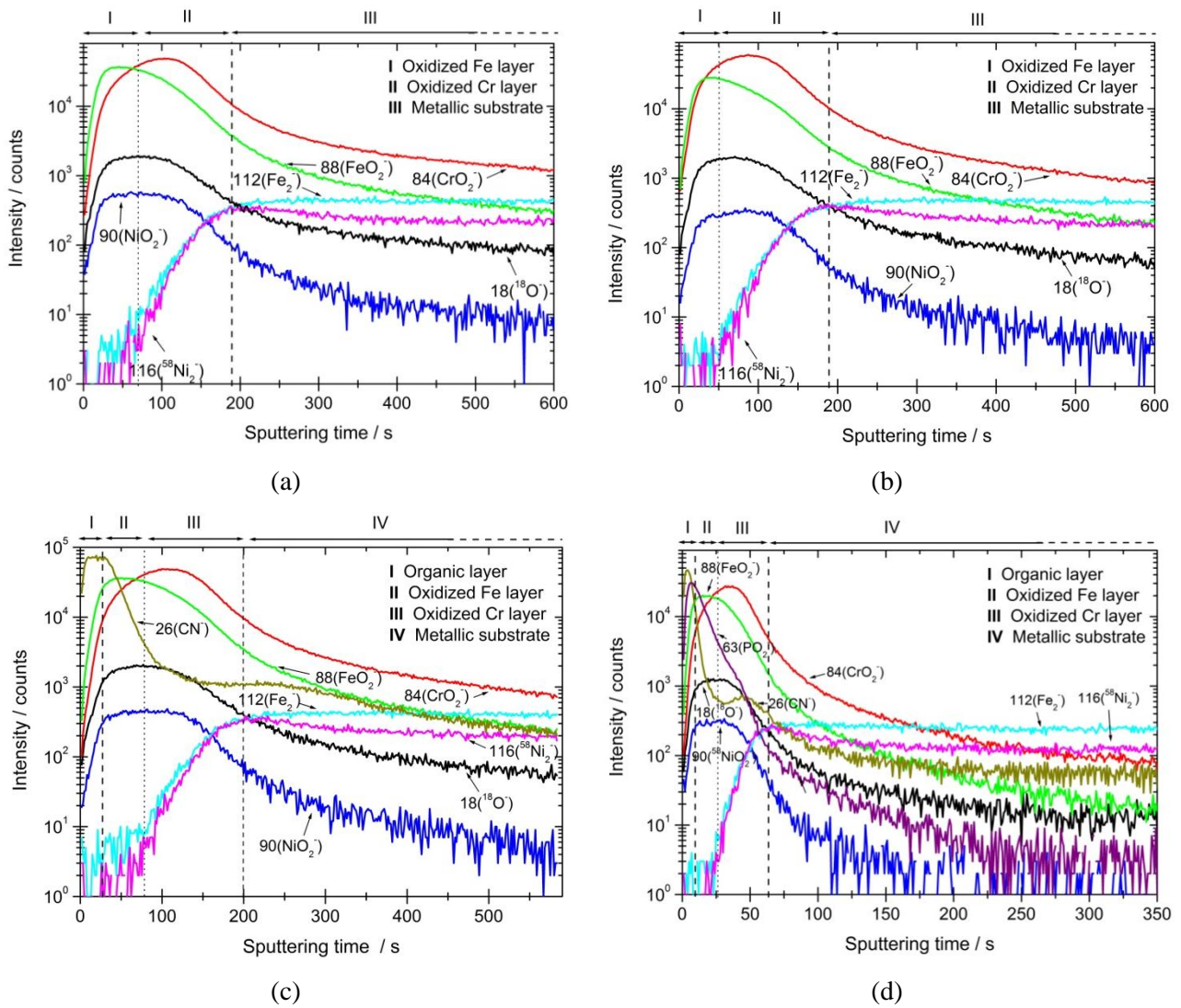


Figure V. 12: Characteristic Time-of-Flight Secondary Ions Mass spectrometry (ToF-SIMS) depth profiles (negative ions) of 304L stainless steel (a) after polishing, and after 1 h of immersion at E_{corr} in static aerated: (b) Cl⁻-free solution, (c) Cl⁻-free solution with 20 mg.L⁻¹ of BSA (sputtered surface area of $1000 \times 1000 \mu\text{m}^2$), and (d) Cl⁻-free solution with TB EPS (protein concentration of 20 mg.L⁻¹; sputtered surface area of $700 \times 700 \mu\text{m}^2$).

According to the ToF-SIMS informations, it can be concluded that, in the case of the polished sample and samples exposed to the Cl⁻-free solution with biomolecules the oxide layer formed on 304L stainless steel is duplex with oxidized Fe in the outer part and oxidized Cr in the inner part. Nevertheless, in the Cl⁻-free solution this stratification of oxides is less defined. Although ToF-SIMS depth profiles show oxidized Ni signal is visible throughout the oxide layer, by XPS no oxidized Ni was detected, and hence, this was not considered in the calculation of the oxide layer thickness.

Therefore, the equivalent thickness of each oxide layer (d_{Oxide1} and d_{Oxide2} ; Figure V.13(a)) formed on the alloy and the elemental composition beneath the oxide layer was calculated from XPS data by solving the following system of equations, considering the intensities of chromium, iron and nickel in the metallic substrate, and chromium and iron in the duplex oxide layer:

$$I_{Cr}^{Metal} = k \cdot T_{Cr} \cdot \sigma_{Cr} \cdot D_{Cr}^{Metal} \cdot \lambda_{Cr}^{Metal} \cdot \exp\left(\frac{-d_{Oxide2}}{\lambda_{Cr}^{Oxide2}}\right) \cdot \exp\left(\frac{-d_{Oxide1}}{\lambda_{Cr}^{Oxide1}}\right) \quad \text{Eq. V.7}$$

$$I_{Ni}^{Metal} = k \cdot T_{Ni} \cdot \sigma_{Ni} \cdot D_{Ni}^{Metal} \cdot \lambda_{Ni}^{Metal} \cdot \exp\left(\frac{-d_{Oxide2}}{\lambda_{Ni}^{Oxide2}}\right) \cdot \exp\left(\frac{-d_{Oxide1}}{\lambda_{Ni}^{Oxide1}}\right) \quad \text{Eq. V.8}$$

$$I_{Fe}^{Metal} = k \cdot T_{Fe} \cdot \sigma_{Fe} \cdot D_{Fe}^{Metal} \cdot \lambda_{Fe}^{Metal} \cdot \exp\left(\frac{-d_{Oxide2}}{\lambda_{Fe}^{Oxide2}}\right) \cdot \exp\left(\frac{-d_{Oxide1}}{\lambda_{Fe}^{Oxide1}}\right) \quad \text{Eq. V.9}$$

$$I_{Cr}^{Oxide} = k \cdot T_{Cr} \cdot \sigma_{Cr} \cdot D_{Cr}^{Oxide} \cdot \lambda_{Cr}^{Oxide} \cdot \left[1 - \exp\left(\frac{-d_{Oxide2}}{\lambda_{Cr}^{Oxide2}}\right)\right] \cdot \exp\left(\frac{-d_{Oxide1}}{\lambda_{Cr}^{Oxide1}}\right) \quad \text{Eq. V.10}$$

$$I_{Fe}^{Oxide} = k \cdot T_{Fe} \cdot \sigma_{Fe} \cdot D_{Fe}^{Oxide} \cdot \lambda_{Fe}^{Oxide} \cdot \left[1 - \exp\left(\frac{-d_{Oxide1}}{\lambda_{Fe}^{Oxide1}}\right)\right] \quad \text{Eq. V.11}$$

and considering that:

$$D_{Cr}^{Metal} + D_{Ni}^{Metal} + D_{Fe}^{Metal} = 1 \quad \text{Eq. V.12}$$

On the other hand, Figure V.13 (b) illustrates the layer model used for the analysis of XPS data of 304L stainless steel after immersion in a solution containing biomolecules (BSA and TB EPS) that adsorb on the surface. The thickness $d_{Organic}$ can be calculated from the $I_N^{Organic} / I_{Cr}^{Oxide}$ ratio. The N 1s intensity emitted by the adsorbed biomolecules is given by Eq V.4. The Cr 2p_{3/2} intensity emitted by the oxide layer and attenuated by the adsorbed protein is given by Eq. 13:

$$I_{Cr}^{Oxide} = k \sigma_{Cr} \lambda_{Cr}^{Oxide} D_{Cr}^{Oxide} T_{Cr} \exp\left(-\frac{d_{Organic}}{\lambda_{Cr}^{Organic}}\right) \left(1 - \exp\left(-\frac{d_{Oxide}}{\lambda_{Cr}^{Oxide}}\right)\right) \quad \text{Eq. V.13}$$

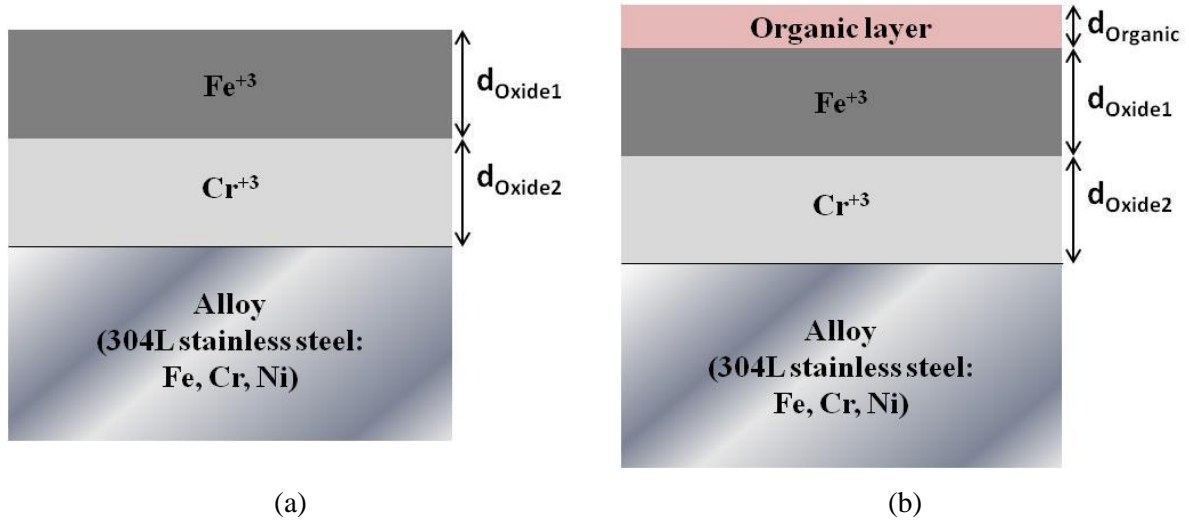


Figure V. 13: Layer model assumed for the analysis of XPS data of 304L stainless steel considering: (a) a duplex oxide layer formed on the metallic substrate, with an outer Fe_2O_3 layer and an inner Cr_2O_3 layer, and (b) organic layer covering the duplex oxide layer formed on the metallic substrate.

The values for the transmission function T for Cr, Ni and Fe are listed in Table V.8.

Table V. 8: Transmission functions $T(E_{kin})$ of the Escalab 250 energy analyzer, provided by Thermo Electron Corporation.

$T(E_{kin})$	Cr 2p _{3/2}	Fe 2p _{3/2}	Ni 2p _{3/2}
	3502	3753	4062

The inelastic mean free path (λ) values are listed in Table V.9.

Table V. 9: Inelastic mean free paths λ in nm – Taken from the QUASES-IMFP-TPP2M.

λ (nm)						
λ_{Cr}^{Metal}	λ_{Fe}^{Metal}	λ_{Ni}^{Metal}	λ_{Cr}^{Oxide}	λ_{Fe}^{Oxide}	λ_{Ni}^{Oxide}	$\lambda_{Cr}^{Organic}$
1.52	1.35	1.17	1.83	1.63	1.40	2.95

The photoionization cross-section σ_X values are presented in Table V.10.

Table V. 10: Photo-ionization cross sections σ_X at 1486.6 eV.

	Cr 2p _{3/2}	Fe 2p _{3/2}	Ni 2p _{3/2}
σ_X	7.69	10.82	14.61

XPS measurements were performed for 304L stainless steel after polishing and after 1 h of immersion in Cl^- -free solution with and without biomolecules (BSA and TB EPS). The following core levels were recorded: Cr $2p_{3/2}$, Fe $2p_{3/2}$, Ni $2p_{3/2}$, O 1s, C 1s, and N 1s.

Figure V.14 (a) illustrates the Cr $2p_{3/2}$ core level spectra of 304L stainless steel. In all the cases, the presence of the metal contribution Cr^0 at the binding energy of ~ 573.8 eV is observed. Additionally, another peak located at the binding energy of ~ 576.2 eV is also visible, and corresponds to the formation of Cr^{+3} [107], [144], [151], [152].

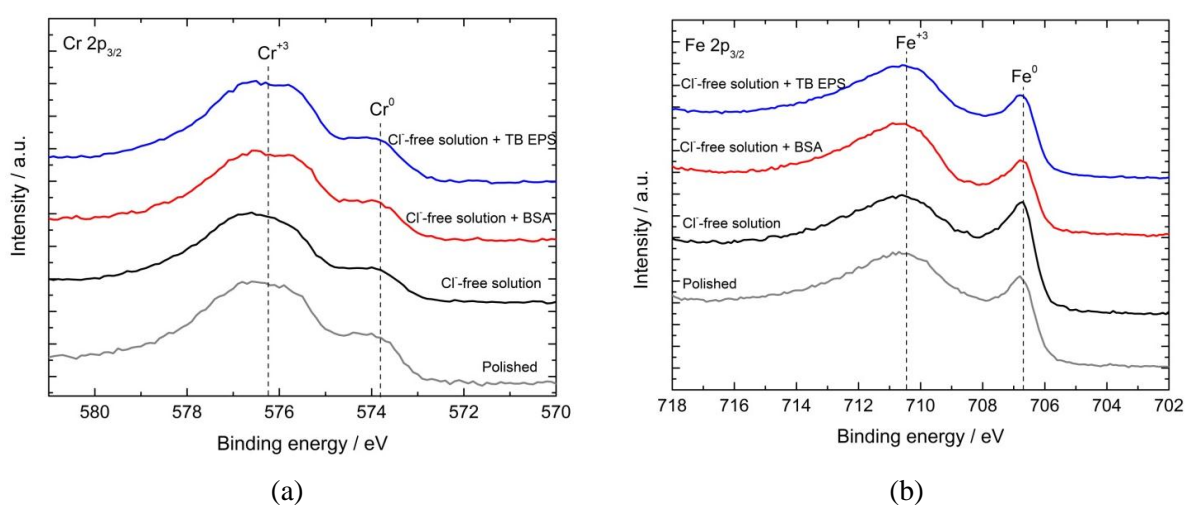


Figure V. 14: X-ray photoelectron spectroscopy (XPS) (a) Cr $2p_{3/2}$ and (b) Fe $2p_{3/2}$ core level spectra of 304L stainless steel after polishing and after 1 h of immersion at E_{corr} in static aerated Cl^- -free solution, in the absence and in the presence of biomolecules (BSA, TB EPS) with a protein concentration of $20 \text{ mg}\cdot\text{L}^{-1}$. The intensity is expressed in arbitrary unit (a.u.).

The Fe $2p_{3/2}$ core level spectra, shown in Figure V.14 (b), illustrate in all the cases the presence of the characteristic metal peak Fe^0 located at the binding energy of ~ 706.7 eV. This confirms the oxide layer formed on the alloy surface is very thin and it can be calculated using the XPS data. The Fe $2p_{3/2}$ core level spectra also show another peak at ~ 710.5 eV, indicating the presence of Fe^{+3} [16], [107], [152]. The Ni $2p_{3/2}$ core level spectra shows only the presence of the metallic component Ni^0 , and not any oxidation state of nickel. Therefore, if there is oxidized nickel forming the oxide layer, the amount of this is too small to be detected by XPS.

Table V.11 summarizes the thickness of the oxidized Fe and Cr layers, as well as the elemental composition beneath the oxide layer. It is observed that the thickness of the Cr⁺³ layer is higher than the one of the Fe⁺³ layer in all the conditions, and that the lowest oxide layer thickness for the Fe⁺³ layer is observed after 1 h of immersion in the Cl⁻-free solution. Furthermore, comparing the composition beneath the oxide layer with the composition of the bulk alloy, it is observed that the alloy is depleted in Cr in all cases and enriched in Ni only in the presence of TB EPS. On the other hand, the variation of the total oxide layer thickness between the four cases is very small to consider an effect of solutions on these.

Table V. 11: Oxide layer thickness and elemental composition beneath the oxide layer estimated by considering a duplex oxide layer: 304L stainless steel after polishing and after 1 h of immersion at E_{corr} in static aerated Cl⁻-free solution, in the absence and in the presence of biomolecules (BSA, TB EPS) with a protein concentration of 20 mg.L⁻¹.

	Oxide layer thickness / nm			Elemental composition beneath the oxide layer / at. %		
	Fe ⁺³	Cr ⁺³	Total	Cr	Fe	Ni
After polishing	1.0	1.2	2.2	7	81	12
Cl⁻-free solution	0.6	1.7	2.3	10	77	13
Cl⁻-free solution + BSA	1.0	1.3	2.3	6	81	13
Cl⁻-free solution + TB EPS	0.9	1.3	2.2	6	77	17

The N 1s and C 1s core level spectra are shown in Figure V.15 (a) and V.15 (b) respectively, for 304L stainless steel after 1 h of immersion in Cl⁻-free solution with BSA and TB EPS. The N 1s core level spectra exhibit, for both biomolecules, the same peak centred at ~ 400 eV, typical of amide groups (peptidic link); and the decomposition of the C 1s core level spectra for the two biomolecules solutions reveals the presence of the three typical contributions attributed to carbon bonds present in biomolecules.

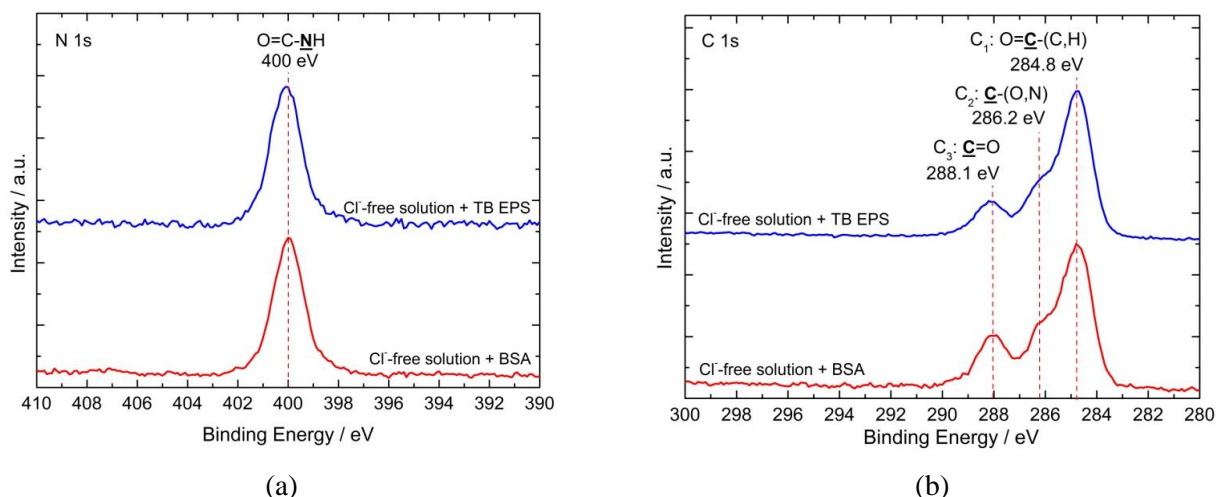


Figure V. 15: (a) N 1s and (b) C 1s core level spectra of 304L stainless steel after 1 h of immersion at E_{corr} in static aerated Cl^- -free solution in the presence BSA and TB EPS, with a protein concentration of $20 \text{ mg}\cdot\text{L}^{-1}$. The intensity is expressed in arbitrary unit (a.u.).

The “nitrogen/carbon” and “carbon/carbon” atomic ratios were calculated from the N 1s and C 1s signals. The values of the atomic ratios obtained in the BSA and TB EPS solutions are compared in Table V.12 to the values obtained for the BSA powder [72][16]. The values obtained with BSA are close to the one obtained for the BSA powder; showing that the protein is adsorbed on the surface. Although in ASW + TB EPS the values obtained for the atomic ratios are close to those measured for the BSA powder, deviations are observed indicating the presence of other biomolecules in addition to proteins, but also contamination. Further details are given in the discussion section.

Table V. 12: Atomic ratios calculated from the XPS N 1s and C 1s core level spectra recorded for the BSA powder and for 304L stainless steel after 1 h of immersion at E_{corr} in static aerated Cl^- -free solution, in the presence of BSA or TB EPS with a protein concentration of $20 \text{ mg}\cdot\text{L}^{-1}$.

	$\text{N}/\text{C}_{\text{total}}$	$\text{N}/(\text{C}_2+\text{C}_3)$	$\text{C}_1/\text{C}_{\text{total}}$	$\text{C}_2/\text{C}_{\text{total}}$	$\text{C}_3/\text{C}_{\text{total}}$
BSA powder	0.22	0.48	0.54	0.26	0.20
Cl^--free solution	0.01	0.07	0.77	0.12	0.11
Cl^--free solution + BSA	0.17	0.38	0.56	0.23	0.21
Cl^--free solution + TB EPS	0.11	0.30	0.63	0.22	0.15

Similarly to what was done in the case of Ti, the thickness of the organic layer was estimated from XPS data, considering the same parameters values as for the model protein (BSA). That thickness is 2.7 nm for BSA and 2.6 nm for TB EPS.

V.3.Discussion

V.3.1. Surface layers models (combined XPS and ToF-SIMS)

The oxide layer compositions estimated from XPS data for Ti after polishing and after short-term immersion (1 h of exposure) at E_{corr} in the three different solutions (ASW, ASW + BSA and ASW + TB EPS) are summarized in Figure V.16. The oxide layer thickness was calculated from XPS data and the elemental distribution throughout the oxide layer was determined from ToF-SIMS data.

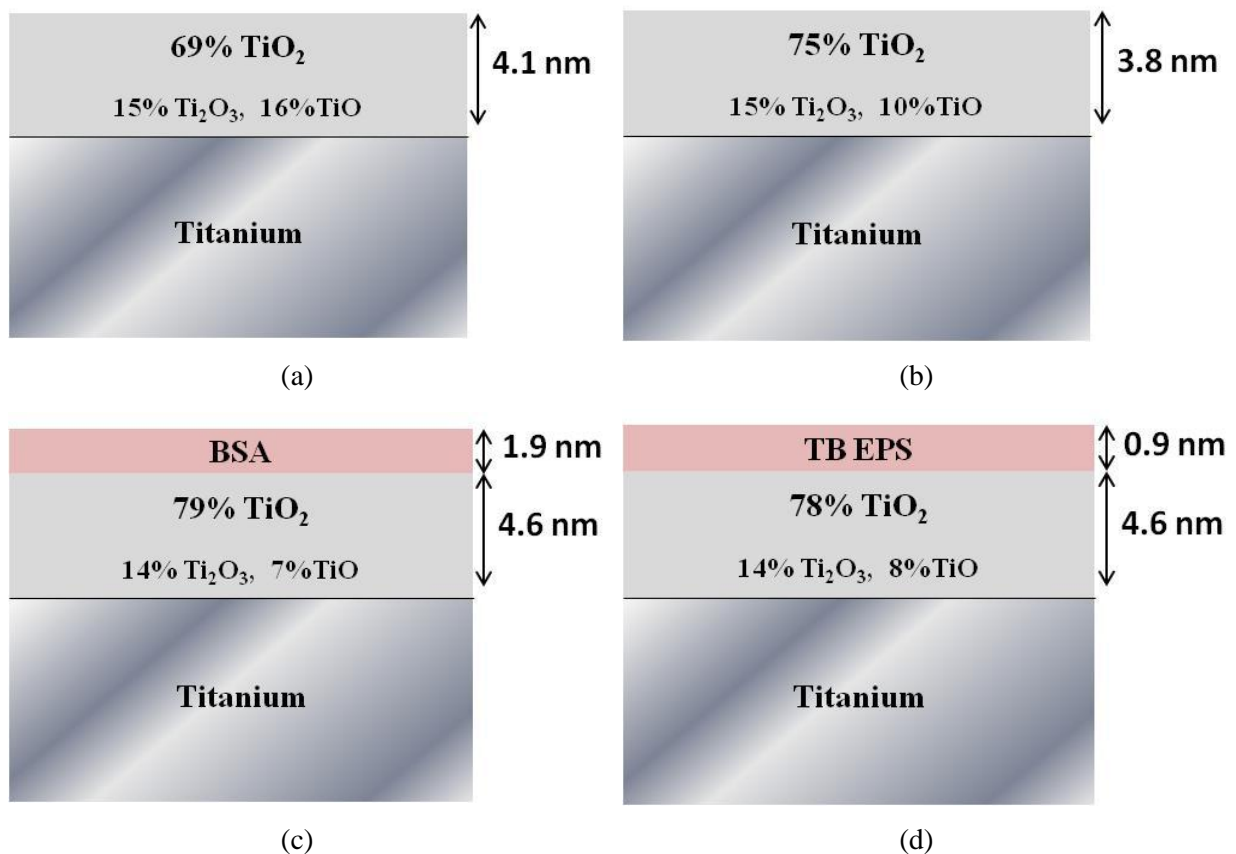


Figure V. 16: Models of the surface layers deduced from combined X-ray photoelectron spectroscopy (XPS) and time-of-flight secondary ions mass spectrometry (ToF-SIMS) results for Ti (a) just after polishing, and after 1 h of immersion at E_{corr} in static aerated (b) ASW, (c) ASW with 20 mg.L⁻¹ of BSA, and (d) ASW in the presence of TB EPS with a protein concentration of 20 mg.L⁻¹.

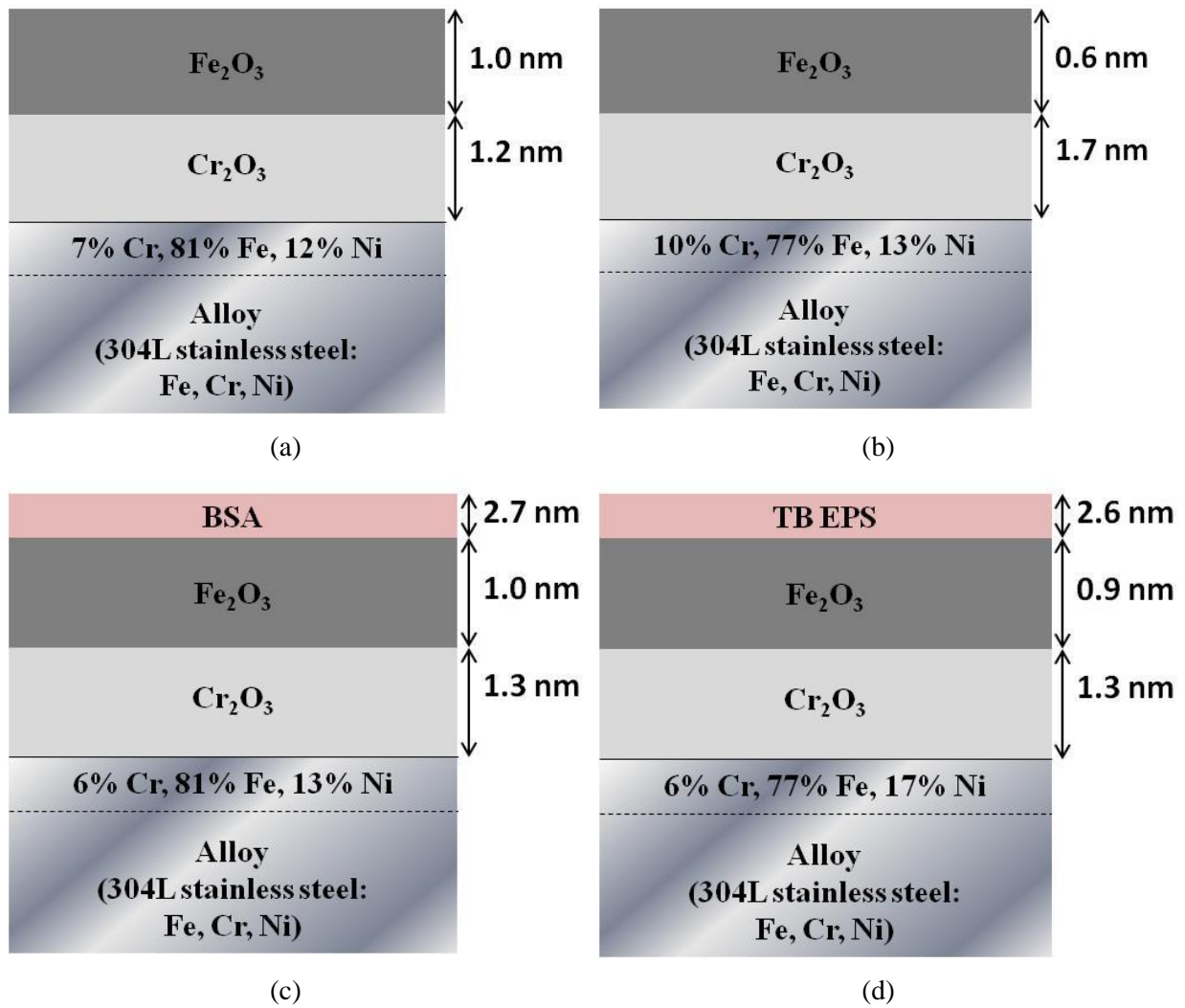


Figure V. 17: Models of the surface layers deduced from combined X-ray photoelectron spectroscopy (XPS) and time-of-flight secondary ions mass spectrometry (ToF-SIMS) results for 304L stainless steel (a) just after polishing, and after 1 h of immersion at E_{corr} in static aerated (b) Cl^- -free solution, (c) Cl^- -free solution with $20 \text{ mg}\cdot\text{L}^{-1}$ of BSA, and (d) Cl^- -free solution in the presence of TB EPS with a protein concentration of $20 \text{ mg}\cdot\text{L}^{-1}$.

The data show that the lowest oxide layer thickness is obtained after immersion in ASW without biomolecules, followed by the sample just after polishing and then by the sample after immersion in ASW with biomolecules. The relative amount of Ti^{+4} is the lowest, compared to the percentages of Ti^{+3} , and Ti^{+2} , in the sample after polishing and slightly increased after immersion in ASW. The presence of biomolecules induced the highest percentage of Ti^{+4} , which is independent of the kind of biomolecules here investigated. The organic layer thickness is considerably lower with TB EPS (0.9 nm) compared to that with BSA (1.9 nm). As for 70Cu-30Ni alloy (see Chapter IV), the calculated value of the

equivalent thickness is low for TB EPS, meaning that the surface is probably not totally covered by biomolecules.

The surface layers models obtained for 304L stainless steel after 1 h of immersion at E_{corr} in the Cl⁻-free solution are presented in Figure V.17. ToF-SIMS data evidenced a duplex structure with an outer layer mainly composed of iron oxide (Fe₂O₃) and a Cr₂O₃ inner layer. The presence of oxidized Ni was detected throughout the full oxide layer by ToF-SIMS but not by XPS. Therefore, the corresponding concentration was very low and it was not considered in the calculation of oxide layer thicknesses. In all cases, the thickness of the Cr₂O₃ inner layer was higher than that of the Fe₂O₃ outer layer, and this was especially evident after immersion in the Cl⁻-free solution without biomolecules. The organic layer thickness formed on top of the oxide layer is similar in both biomolecules-containing solutions, and it is higher in the case of stainless steel compared to Ti.

V.3.2. Analysis of impedance data

The anodic polarisation curves of Ti and 304L stainless steel without and with biomolecules exhibit a Tafel-like behaviour close to E_{corr} , followed by a current plateau which can be interpreted as a passive plateau (Figure V.2 and V.6). However, these curves have been plotted with a scan rate of 0.5 mV.s⁻¹ and, hence, they are not steady-state curves. This means that the current measured using a scan rate of 0.5 mV.s⁻¹ is not a current corresponding to stationary conditions. It has been shown in recent works that, for carbon steel in pH 13 solution, the steady-state passive current is two decades lower than the passive current corresponding to 0.5 mV.s⁻¹, and that the Tafel-like behaviour between E_{corr} and the passive plateau is not observed anymore on the steady-state curves plotted point by point [142].

Impedance diagrams were plotted in the passive domain for Ti and 304L stainless steel (Figures V.18 (a) and (b), respectively). In both cases, the size of the loop is smaller at anodic potentials than at the corrosion potential. This can be explained by the fact that the diagrams at anodic potentials were not plotted after the one at E_{corr} *i.e.* different diagrams correspond to different experiments. Moreover, the diagrams were not plotted in real steady-state conditions (after 1 h of immersion at E_{corr} or after 1 h of immersion at E_{corr} followed by 30 min of polarisation in the passive domain). Such conditions could have been obtained after several tens of hours of immersion or polarisation as in the case of carbon steel in pH 13 solution (passivating conditions) [142]. However, the shape of the diagrams and the order of

magnitude of the impedance are the same whatever the potential. Therefore, the impedance at the corrosion potential corresponds to the single anodic impedance which illustrates the presence of the passive layer. The cathodic impedance in parallel is very high and then, the cathodic branch can be neglected. This assumes that the passive current plateau observed on the anodic polarisation curves can be extrapolated down to E_{corr} .

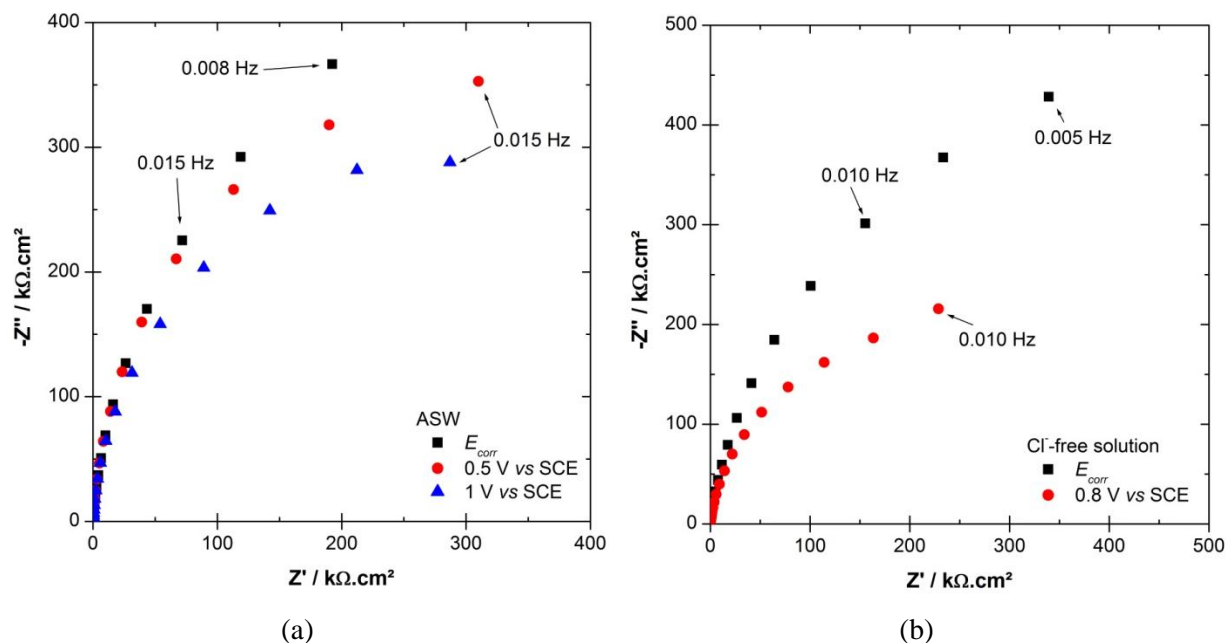


Figure V. 18: Experimental impedance diagrams in the complex plane (Nyquist diagrams) of (a) Ti after in ASW and (b) 304L stainless steel in Cl-free solution, plotted at E_{corr} after 1 h of immersion and in the passive domain after 1 h of immersion at E_{corr} followed by 30 min of polarisation.

Figures V.19 (a) and V.19 (b) illustrate the cathodic polarisation curves corrected for the anodic contribution, for Ti and 304L stainless steel, respectively. In these figures, the absolute value of the cathodic current $|j_c|$, which is equal to $|j - j_{a,pl}|$ with j the measured global current (< 0) and $j_{a,pl}$ the passive plateau current (> 0), is plotted against the potential, in the whole cathodic domain. The values of $j_{a,pl}$ were taken from Figure V.2 for Ti ($j_{a,pl} \sim 3-4 \mu\text{A.cm}^{-2}$) and from Figure V.6 for 304L stainless steel ($j_{a,pl} \sim 3-4 \mu\text{A.cm}^{-2}$). As the passive current densities are much higher than the global cathodic current densities close to the corrosion potential (a few 10^{-8} to a few $10^{-7} \text{ A.cm}^{-2}$, in absolute value), no cathodic Tafel behaviour can be evidenced. This can be explained by a possible overestimation of the anodic passive current using a scan rate of 0.5 mV.s^{-1} . If the anodic curves would have been plotted in steady-state conditions, the measured passive currents would have been much lower than the ones at 0.5 mV.s^{-1} [142]. Thus, from the cathodic curves corrected from the steady-state

passive currents, a possible Tafel behaviour could have been evidenced and a possible effect of biomolecules on the cathodic reaction kinetics could have been discussed.

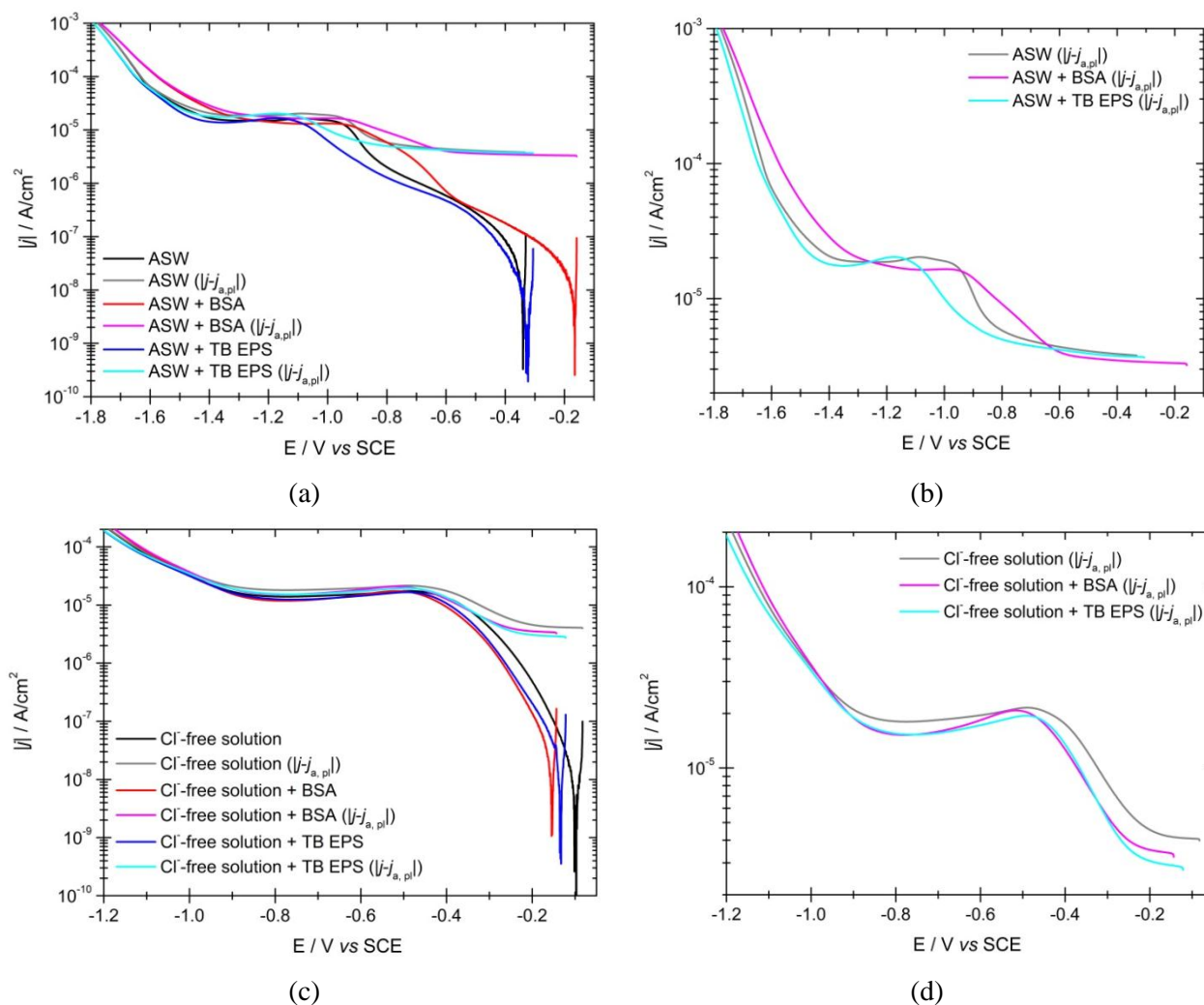


Figure V. 19: Cathodic polarisation curves without ($|j|$) and with correction for the anodic contribution ($j - j_{a, pl}$) of (a) Ti and (c) 304L stainless steel; and zooms of the corrected curves for (b) Ti and (d) 304L stainless steel. Experiments performed after 1 h of immersion at E_{corr} in static aerated ASW (Ti) or Cl⁻ free solution (304L stainless steel), in the absence and in the presence of biomolecules (BSA, TB EPS) with a protein concentration of 20 mg.L⁻¹. Scan rate: 0.5 mV.s⁻¹.

Figure V.20 shows the absolute value of the imaginary part of the impedance ($|Z_j|$) plotted as a function of the frequency in logarithmic coordinates, for the same experimental impedance data as those presented in Figures V.3 and V.7. In all cases, a straight line with a slope lower than 1 in absolute value can be observed in the HF range, showing CPE behaviour.

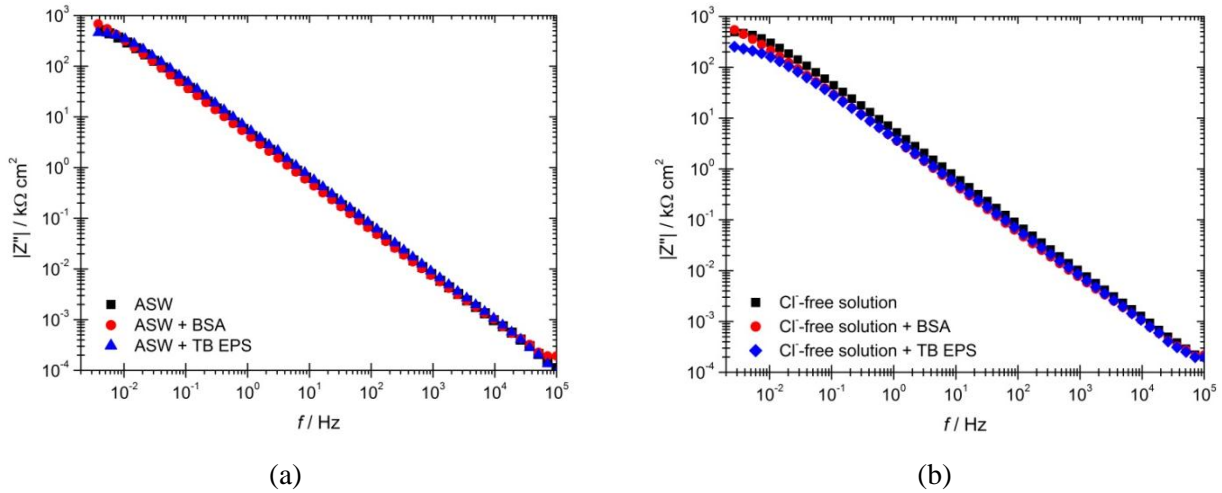


Figure V. 20: Experimental impedance data (imaginary part of the impedance as a function of frequency) of (a) Ti in ASW and (b) 304L stainless steel in Cl⁻-free solution, plotted at E_{corr} after 1 h of immersion in static conditions, in the absence and in the presence of biomolecules (BSA, TB EPS) with a protein concentration of 20 mg.L⁻¹. Same data as in Figures V.3 and V.7.

The values of the CPE parameters, α and Q , estimated graphically from Eqs. III.29 and III.30, are presented in Table V.13. The order of magnitude of Q is a few 10^{-5} F.cm⁻².s^($\alpha-1$). These values are typical of those found for passive systems [153], indicating that the HF CPE can be related to the passive layer formed on Ti or 304L stainless steel.

Table V. 13: α and Q CPE parameters estimated graphically from Eqs. III.25 and III.26. Same data as in Figures V.3 and V.7.

Material	Solution	α	$Q / F.cm^{-2}.s^{(\alpha-1)}$
Ti	ASW	0.93	3.9×10^{-5}
	ASW + BSA	0.93	2.6×10^{-5}
	ASW + TB EPS	0.94	3.1×10^{-5}
304L stainless steel	Cl ⁻ -free solution	0.91	3.2×10^{-5}
	Cl ⁻ -free solution + BSA	0.90	4.8×10^{-5}
	Cl ⁻ -free solution + TB EPS	0.89	4.7×10^{-5}

It is recalled that the impedance of Ti and 304L stainless steel at E_{corr} corresponds to the single anodic impedance illustrating the presence of the passive layer. A CPE behaviour may be attributed to the distribution of physical properties in films, such as oxide films, in the

direction normal to the electrode surface [153]. In the case of normal time constant distribution, Hirschorn *et al.* identified a relationship between CPE parameters and physical properties by regressing a measurement model to synthetic CPE data [104], [153]. The concept was to identify the distribution of resistivity along a film thickness that, under the assumption that the dielectric constant ϵ is independent of position, would result in CPE behaviour. The resistivity was found to follow a power-law profile:

$$\frac{\rho}{\rho_{\delta}} = \xi^{-\gamma} \quad \text{Eq. V.14}$$

where ξ is the dimensionless position $\xi = y/\delta$, y represents the position through the depth of the film, and δ is the film thickness. The parameter ρ_{δ} is the resistivity at $\xi = 1$, and γ is a constant indicating how sharply the resistivity varies. A distribution of resistivity that provides a bounded value for resistivity was proposed to be:

$$\frac{\rho}{\rho_{\delta}} = \left(\frac{\rho_{\delta}}{\rho_0} + \left(1 - \frac{\rho_{\delta}}{\rho_0} \right) \xi^{\gamma} \right)^{-1} \quad \text{Eq. V.15}$$

where ρ_0 and ρ_{δ} are the boundary values of resistivity at the interfaces. The impedance of the film can be written for an arbitrary resistivity distribution $\rho(y)$ as:

$$Z_f(f) = \int_0^{\delta} \frac{\rho(y)}{1 + j2\pi f \epsilon \epsilon_0 \rho(y)} dy \quad \text{Eq. V.16}$$

Under the conditions that $\rho_0 \gg \rho_{\delta}$ and $f < (2\pi\rho_{\delta}\epsilon\epsilon_0)^{-1}$, a semi-analytic solution to Eq. V.16 could be found for the resistivity profile given in Eq. V.15:

$$Z_f(f) = g \frac{\delta \rho_{\delta}^{1/\gamma}}{(\rho_0^{-1} + j2\pi f \epsilon \epsilon_0)^{(\gamma-1)/\gamma}} \quad \text{Eq. V.17}$$

where g is a function of γ . Numerical integration was used to develop the interpolation formula:

$$g = 1 + 2.88\gamma^{-2.375} \quad \text{Eq. V.18}$$

Eq. V.23 is in the form of a CPE for $f > (2\pi\rho_0\epsilon\epsilon_0)^{-1}$, *i.e.*:

$$Z_f(f) = g \frac{\delta \rho_\delta^{1/\gamma}}{(j2\pi f \epsilon \epsilon_0)^{(\gamma-1)/\gamma}} = \frac{1}{(j2\pi f)^\alpha Q} \quad \text{Eq. V.19}$$

Inspection of Eq. V.19 suggests that:

$$\alpha = \frac{\gamma-1}{\gamma} \quad \text{Eq. V.20}$$

and:

$$Q = \frac{(\epsilon \epsilon_0)^\alpha}{g \delta \rho_\delta^{1-\alpha}} \quad \text{Eq. V.21}$$

Thus, a relationship between the CPE parameters Q and α and the physical properties of the film ($\rho_\delta, \epsilon, \delta$) is given by Eq. V.21.

The experimental impedance data presented in Figures V.3 and V.7 were analysed by regression of the equivalent circuit presented in Figure V.21, where R_s is the electrolyte resistance, and PLM is the power-law model expressed as Eq. V.17. In this circuit, the anodic impedance is replaced by the power-law model that illustrates a distribution of resistivity within the passive film. Such a circuit can be used at E_{corr} as well as at anodic potential. The regression procedure was performed keeping only δ as a fixed parameter (corresponding to the oxide layer thickness calculated from XPS data. In the case of 304 L stainless steel, the total thickness was considered equal to the sum of Fe_2O_3 and Cr_2O_3 thicknesses. Other parameters in Figure V.21 were free.

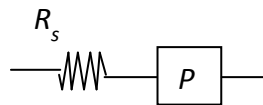


Figure V. 21: Equivalent circuit to model the Ti/ASW and 304L stainless steel/ Cl^- -free solution systems at E_{corr} , with R_s the electrolyte resistance, and PLM the power-law model accounting for the passive layer.

The regression results are presented in Table V.14 for Ti and in Table V.15 for 304L stainless steel. Lower ρ_δ values are obtained for Ti compared to 304 L stainless steel. However, in both cases, ρ_δ values are typical values for a semi-conductor, which is in agreement with the semi-conductive properties of oxide films grown on stainless steel [19] and on Ti [154]. On the

other hand, the obtained ρ_0 values are similar for both materials, and are typical values for an insulator [19]. The resulting ε values for Ti ($\varepsilon = 22$) and 304 L ($\varepsilon = 12$) stainless steel are in agreement with those found in the literature [153], [155]–[157]. Thus, the analysis of impedance data yields parameters (ρ_δ and ε) which are in agreement with XPS results (oxide layer composition).

The ranking of ρ_0 values in the case of Ti is: ASW + TB EPS < ASW < ASW + BSA; and same ranking is obtained in the case of 304L stainless steel: Cl⁻-free solution + TB EPS < Cl⁻-free solution < Cl⁻-free solution + BSA.

The low-frequency limit of the impedance $Z_f(0)$ can be deduced from Eq. V.17:

$$Z_f(0) = g\delta\rho_\delta^{1-\alpha}\rho_0^\alpha \quad \text{Eq. V.22}$$

Thus, an increase of ρ_0 induces an increase of $Z_f(0)$. In Figure V.3 for Ti, it can be observed that the size of the capacitive loop increases in the following order: ASW + TB EPS < ASW < ASW + BSA; and the same tendency is obtained in Figure V.7 for 304 L stainless steel in the Cl⁻-free solution. This observation is in agreement with the ranking of ρ_0 values. Therefore, different diameters of impedance diagrams correspond to different ρ_0 values and, hence, to different oxide layer properties.

As for ρ_0 , the highest value of ρ_δ is obtained in the presence of BSA for both materials.

Table V. 14: Parameters values for Ti obtained from the regression of the equivalent circuit presented in Figure V.22 to experimental impedance data shown in Figure V.3.

	α	δ / nm	$\rho_\delta / \Omega.\text{cm}$	$\rho_0 / \Omega.\text{cm}$	ε	$R_s / \Omega.\text{cm}^2$
ASW	0.94	3.8	950	1.08×10^{13}	22	11
ASW + BSA	0.94	4.6	2750	1.51×10^{13}	22	13
ASW + TB EPS	0.95	4.6	70	0.73×10^{13}	22	14

Table V. 15: Parameters values of 304L stainless steel obtained from the regression of the equivalent circuit presented in Figure V.22 to experimental impedance data shown in Figure V.7.

	α	δ / nm	$\rho_{\delta} / \Omega.\text{cm}$	$\rho_0 / \Omega.\text{cm}$	ε	$R_s / \Omega.\text{cm}^2$
Cl⁻-free solution	0.92	2.3	0.23×10^6	1.69×10^{13}	12	19
Cl⁻-free solution + BSA	0.91	2.3	4.40×10^6	1.73×10^{13}	12	20
Cl⁻-free solution + TB EPS	0.89	2.2	0.51×10^6	1.38×10^{13}	12	22

The resistivity profiles calculated from the parameters values by application of Eq. V.15 are shown in Figure V.22. It is assumed that ρ_0 is located at the metal/oxide interface ($\xi = 0$) and ρ_{δ} at the oxide/solution interface ($\xi = 1$) since the outer part of the oxide layer is hydrated and hence would correspond to the lower value of resistivity. These curves illustrate the power-law nature of the distribution. The maximum amplitude of resistivity variation within the passive layer can be observed for titanium.

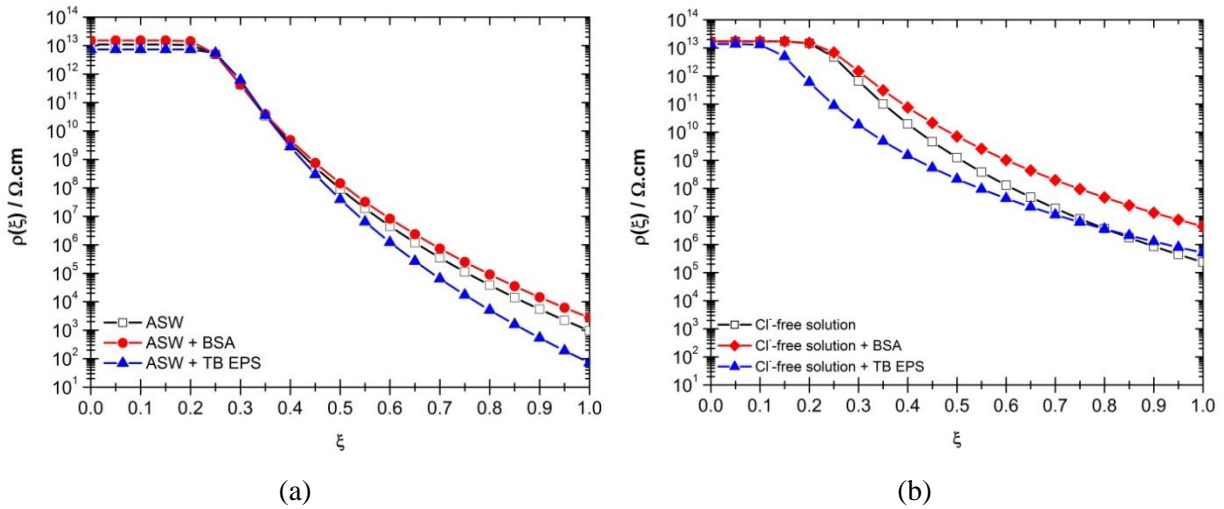


Figure V. 22: Resistivity profiles of (a) Ti and (b) 304L stainless steel, calculated from the parameters values by application of Eq. V.15.

V.3.3. Organic layer

Figures V.23 and V.24 illustrate different correlations between spectral XPS data (C 1s, N 1s and O 1s) obtained for Ti and 304L stainless steel, respectively, after immersion in the two different solutions with biomolecules. These correlations were used to generate information about the organic layer formed in the presence of BSA, and TB EPS [106], [139], [140]. Figures V.23 (a) and V.24 (a) present the plot of the molar concentration of carbon

responsible for the C_3 component, located at 288.3 eV ($C-O-C-O-C$, or $C-N-C=O$), as a function of the molar concentration of total organic nitrogen, N_{org} . A 1:1 relation is expected for the amide function ($HC-NH-(C=O)$) forming the backbone of proteins (peptidic link). As expected, the data are close to the 1:1 relation after 1 h of immersion of Ti in ASW with BSA and with TB EPS, evidencing the presence of adsorbed proteins on the surface. However, in the case of 304L stainless steel, the organic layers seem to contain other compounds than proteins, probably due to the presence of polysaccharides or any oxidized carbon in contaminants.

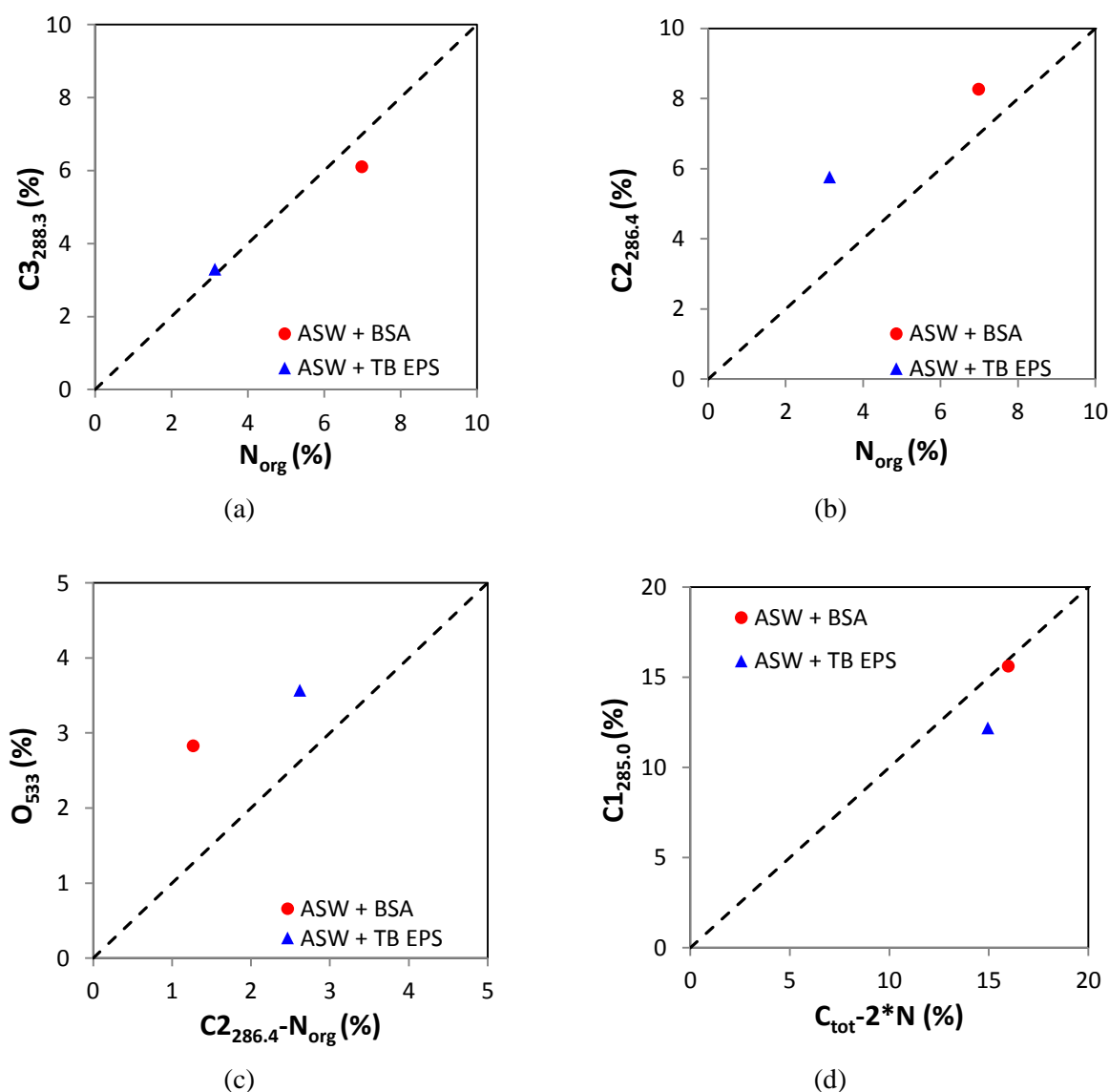


Figure V. 23: Plot of molar concentrations determined by XPS: (a) $C3_{288.3}$ vs N_{org} , (b) $C2_{286.4}$ vs N_{org} , (c) O_{533} vs $C2_{286.4} - N_{org}$, and (d) $C1_{285.0}$ vs $C_{tot} - 2*N_{org}$. Ti samples immersed 1 h at E_{corr} in static aerated ASW with 20 mg.L^{-1} of BSA (ASW + BSA), and in the presence of TB EPS (ASW + TB EPS) with a protein concentration of 20 mg.L^{-1} . Dashed lines: 1:1 relation.

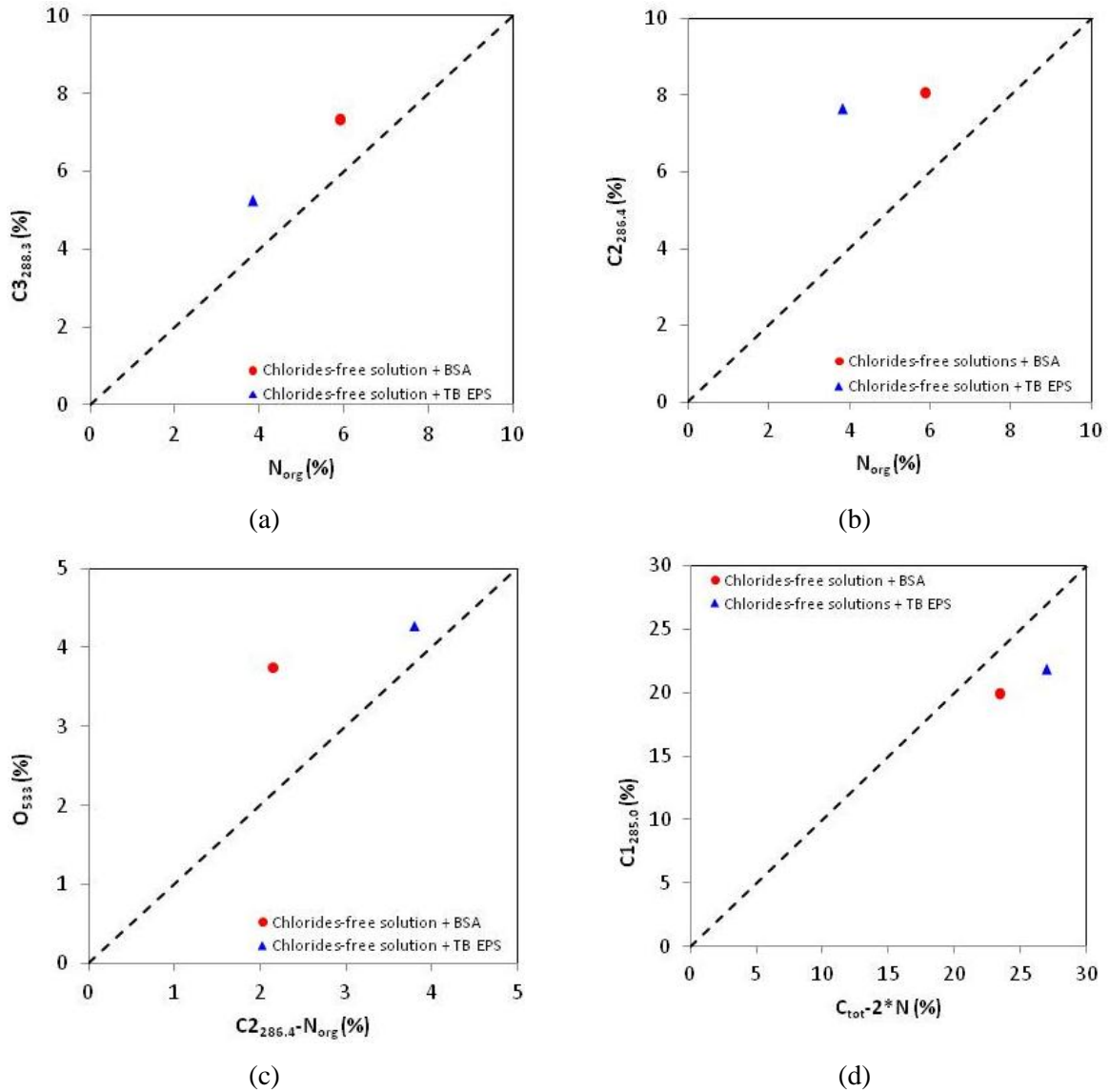


Figure V. 24: Plot of molar concentrations determined by XPS: (a) $C_{3_{288.3}}$ vs N_{org} , (b) $C_{2_{286.4}}$ vs N_{org} , (c) O_{533} vs $C_{2_{286.4}} - N_{org}$, and (d) $C_{1_{285.0}}$ vs $C_{tot} - 2 * N_{org}$. 304L stainless steel samples immersed 1 h at E_{corr} in static aerated Cl^- -free solution with 20 mg.L^{-1} of BSA (Cl^- -free solution + BSA), and in the presence of TB EPS (Cl^- -free solution + TB EPS) with a protein concentration of 20 mg.L^{-1} . Dashed lines: 1:1 relation.

In Figures V.23 (b) and V.24 (b), the molar concentration of the carbon component located at a binding energy of 286.4 eV (C_2 peak), which is due to carbon making a single bond with oxygen (in alcohol, ester or ether) or nitrogen (in amine or amide), is plotted as a function of N_{org} for Ti and 304 L stainless steel, respectively. Deviations from the 1:1 relation are observed in both cases. Furthermore, the highest deviations from the 1:1 relation are observed in the presence of TB EPS, which may be attributed to the presence of polysaccharides or oxygen-containing organic contaminants.

Figures V.23 (c) and V.24 (c) illustrate the O 1s at or near 533 eV, due to oxygen making one (alcohol, carboxyl) or two (ester, ether) single bonds with carbon, as a function of the difference between C_2 and N_{org} ($C_2 - N_{org}$) for Ti and 304L stainless steel, respectively. The total organic N is subtracted from C_2 in order to remove the contribution of amide functions related to the presence of proteins. Therefore, a 1:1 relation is expected for alcohol, ester and polysaccharides. Only in the case of stainless steel after immersion in the TB EPS solution, the correlation is significantly close to the 1:1 relation.

In Figures V.23 (d) and V.24 (d), the C_1 carbon component, due to carbon only bounded to carbon and hydrogen (hydrocarbon function, typical of lipids), is plotted as a function of the total carbon which is not in the form of amide ($C_{tot} - 2 * N_{org}$), for Ti and 304L stainless steel, respectively. The deviation from the 1:1 relation reflects the concentration of carbon which is neither in the form of hydrocarbon functions, nor in the form of amide. Results obtained with Ti show lower deviation from the 1:1 line than those obtained with 304L stainless steel, especially in the presence of BSA.

The main biomolecules contributions can be distinguished and, therefore, the composition can be estimated in terms of proteins, polysaccharides and lipids. In this work, the composition of the adsorbed organic layers was expressed in terms of 4 chemical entities: amide (HC-NH-(C=O)) quantified by N_{org} , CH_2 quantified by the C_1 component of the C 1s core level spectra, additional oxidized carbon quantified by $C_{add} = C_{ox} - 2 * N_{org}$ and additional organic oxygen quantified by $O_{add} = O_{org} - N_{org} = C_{ox} - 2 * N_{org}$ (see details in Chapter IV and Annex A) [87], [140]. Thus, C_{add} is the oxidized carbon in addition to the one present in the form of amide and O_{add} the organic oxygen in addition to the one present in the form of amide.

The elemental molar concentrations, obtained from XPS spectra, were converted into weight percentages of these chemical entities (g/100 g of adlayer), as explained in Annex A. Figure V.25 illustrates the XPS results after conversion into weight percentages in the form of a ternary composition diagram. The corners of this triangle represent 100 wt % of amide, 100 wt % of CH_2 and 100 wt % of additional carbon and oxygen ($C_{add} + O_{add}$) [140]. This figure is convenient to represent the composition of surfaces and adlayers with respect to an amide pole, shared by proteins and N-acetylated functions of polysaccharides, an hydrocarbon pole, typical of lipids, and a pole representative of oxidized organic compounds, including polysaccharide moieties.

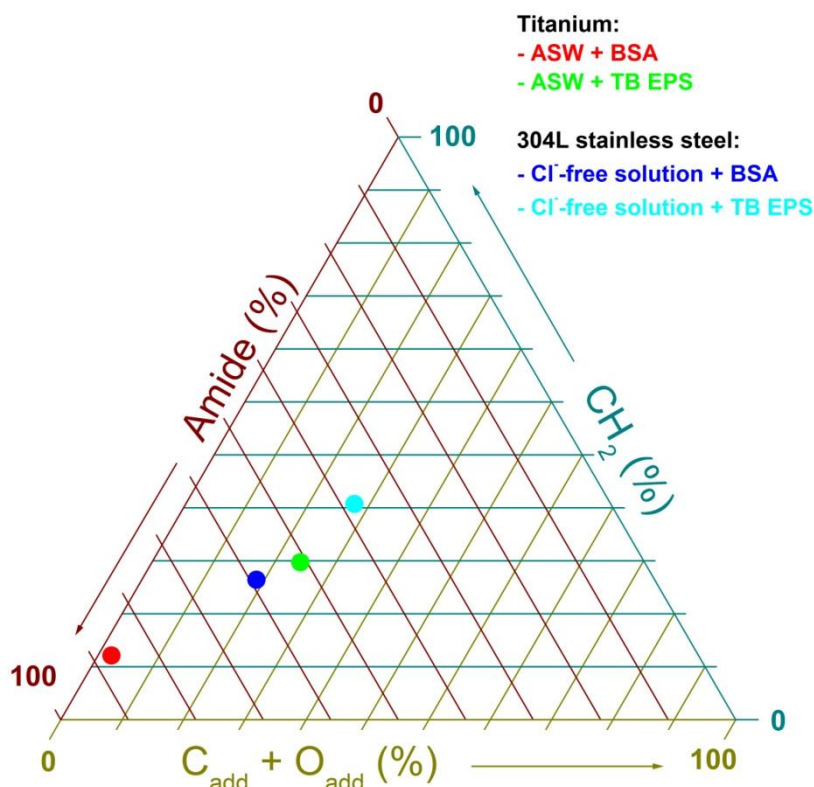


Figure V. 25: Biomolecules composition of the surfaces. Relative mass concentration of amide (HC-NH-(C=O)), hydrocarbon CH₂, and other oxygen-containing molecules (C_{add} + O_{add}), including polysaccharides. Ti samples immersed 1 h at E_{corr} in static aerated ASW with 20 mg.L⁻¹ of BSA (ASW + BSA), and in the presence of TB EPS (ASW + TB EPS) with a protein concentration of 20 mg.L⁻¹; and 304L stainless steel samples immersed 1 h at E_{corr} in static aerated Cl⁻-free solution with 20 mg.L⁻¹ of BSA (Cl⁻-free solution + BSA), and in the presence of TB EPS (Cl⁻-free solution + TB EPS) with a protein concentration of 20 mg.L⁻¹.

The ternary diagram shows that, for Ti in the presence of BSA, the organic adlayer is mainly composed of proteins (87 % amide), with the presence of hydrocarbons (11 % CH₂) and additional carbon and oxygen (2 % C_{add} + O_{add}). In the case of Ti in the presence of TB EPS, proteins are also dominant in the adlayer (51 % amide), but in lower amount than with BSA; the contributions of hydrocarbons (27 % CH₂) and additional carbon and oxygen (22 % C_{add} + O_{add}) are similar.

The biomolecules composition of the organic adlayer is similar for Ti and 70Cu-30Ni alloy in the presence of TB EPS; whereas with BSA, the adlayer on Ti contains more proteins than that on 70Cu-30Ni alloy.

On the other hand, in the case of 304L stainless steel in the presence of BSA, the percentage of proteins found on the surface is much lower than in the case of Ti (59 % amide); the contribution of hydrocarbons is 24 % and that of additional carbon and oxygen 17 %. For 304L stainless steel in the presence of TB EPS, similar percentages of proteins and hydrocarbons (38 % amide and 37% CH₂) are estimated, along with a higher additional carbon and oxygen concentration than with BSA (25 %).

In general, proteins dominate in surface organic layers formed on Ti and 304L stainless steel exposed to BSA or to TB EPS from *Pseudomonas NCIMB 2021*.

V.4. Conclusions

The effect of biomolecules (BSA and TB EPS from *Pseudomonas NCIMB 2021*) on the passivation behaviour of Ti in ASW and 304L stainless steel in Cl⁻-free solution was studied by electrochemical measurements and surface analysis. Polarisation curves were plotted using a scan rate of 0.5 mV.s⁻¹. The passive currents obtained from the anodic curves were quite high (a few μA.cm⁻²), and can be explained by the use of non steady-state conditions. The latter could not be subtracted from the cathodic polarisation curves close to the corrosion potential, in order to study the effect of biomolecules on the cathodic reaction. The importance of plotting polarisation curves and EIS diagrams in stationary conditions was pointed out.

High frequency CPE behaviour was evidenced for both materials and the electrochemical impedance results were fitted with the power-law model (PLM), commonly used in case of normal distributions of time constants induced by resistivity distributions within passive films. Resistivity profiles were plotted. For Ti and 304L stainless steel, the low-frequency limit of impedance diagrams, which is related to the highest boundary value of resistivity at the metal/oxide interface, is higher with BSA and lower with TB EPS compared to the solution without biomolecules; therefore, the oxide layer is more protective in the presence of BSA and less protective in the presence of TB EPS.

On the other hand, surface analysis evidenced the presence of a duplex oxide layer in the case of 304L stainless steel, with an outer Fe₂O₃ layer and an inner Cr₂O₃ layer. The oxide layer thickness was estimated for both passive materials (Ti and 304L stainless steel), and a global thickness of ~ 2.3 nm similar without and with biomolecules (BSA, TB EPS). In the case of

Ti, the oxide layer is mainly composed of TiO_2 and its thickness is ~ 3.8 nm without biomolecules and ~ 4.6 nm with BSA or TB EPS. With BSA or TB EPS, XPS results also show the presence of an adsorbed organic layer on top of the oxide layer, with an equivalent thickness of ~ 3 nm for 304L stainless steel and of $\sim 1-2$ nm for Ti.

From XPS results, the biomolecules composition in terms of proteins, polysaccharides and lipids of the organic layer adsorbed on the metallic surfaces, was estimated. Proteins were found to be the major biochemical compounds in the adlayers.

VI. General conclusions and future work

Cooling circuits of power plants are ideal incubators for microorganisms and they can be divided into planktonic and sessile cells. Planktonic cells are free-floating microorganisms whose movements are controlled by water movement, whereas sessile cells attach to surfaces and form what is known as biofilm. The development of a biofilm is considered to be a multistage process. Biofouling is a consequence of biofilm formation and is able to change the electrochemical properties of the metal/water interface, both in aerobic and anaerobic environments. The significant negative effects of biofouling are the blockage of water free flow in the cooling circuit and consequent mechanical damage to pumps, clogging of condenser tubes, reduction of the heat transfer efficiency (having a direct effect on the efficiency of the thermal cycle of power plants), and microbially induced corrosion (MIC) also called biocorrosion.

Controlling the adsorption of biomolecules, which is the first step in biofilm formation, by modifying the surface properties of the material may represent a good strategy for inhibiting microbial growth. Thus, the objective of this work was to study the effect of biomolecules adsorption on the electrochemical behaviour of three metallic materials often used in heat exchangers (70Cu-30Ni (wt. %) alloy; 304L stainless steel; titanium), and the chemical composition of oxide layers in seawater environment. The first part of the work was focused on the study of the corrosion behaviour of 70Cu-30Ni alloy after short-term immersion (1 h) in aerated artificial seawater (ASW) and filtered natural seawater (FNSW). Electrochemical measurements in static conditions, under flow and stirring, and in well-controlled hydrodynamic conditions using a rotating ring electrode, were combined to surface analysis. An impedance model is proposed to analyse the impedance data. This model is deduced from a general model based on the experimental observation that the electrochemical behaviour of the alloy is dominated by that of pure copper, and that both the anodic and the cathodic partial reactions are affected by mass transport. Pure mass transport limitation is considered for the cathodic partial reaction, and mixed kinetics for the anodic partial reaction. This impedance model shows that the HF loop of experimental impedance diagrams corresponds to a $CPE_{dl} // R_t^a // W_c$ equivalent circuit, with CPE_{dl} the constant phase element related to the double layer, R_t^a the anodic charge transfer resistance and W_c the cathodic Warburg impedance. Therefore, the HF loop illustrates mainly the anodic charge transfer (diameter equal to R_t^a), and its depressed shape is partly due to the CPE and partly due to the cathodic Warburg impedance in parallel. The LF loop of experimental diagrams is related to the anodic mass

transport and partial blocking effect by adsorbed species, such as CuCl. However, impedance data show minor effect of mass transport on the anodic partial reaction (LF loop defined only by a few points). Additionally, corrosion currents were calculated, using the R_t^a values and assuming Tafel kinetics for the anodic partial reaction. In static conditions, the corrosion current density i_{corr} of 70Cu-30Ni alloy is similar in ASW and in FNSW ($i_{corr} \sim 10 \mu\text{A}\cdot\text{cm}^{-2}$). In both solutions, i_{corr} is higher with the RRE compared to static conditions (maximum ratio of 2). When increasing the rotation speed of the RRE, i_{corr} slightly decreases in ASW and keeps constant in FNSW. On the other hand, surface analysis of 70Cu-30Ni alloy after 1 h of immersion in static ASW shows the formation of a thick duplex oxide layer (~ 30 nm), with an outer layer mainly composed of cuprous oxide (Cu_2O) and an inner layer mainly composed of oxidized nickel. However, this duplex structure is no longer observed under flow and stirring; in that case, a mixed Cu and Ni oxide layer is obtained, with a thickness similar to that for the sample just after polishing (~ 1.5 nm). In static FNSW, the thick duplex oxide layer is also observed; nevertheless, the oxidized Cu/oxidized Ni ratio is lower than in static ASW. This cuprous oxide-rich outer layer evidenced in static conditions is formed by redeposition due to the saturation of the solution in copper ions.

As protein adsorption is the first step in biofilm formation and extracellular polymeric substances (EPS) produced by bacteria play a fundamental role in the different stages of biofilm formation, the second part of this work was to study the influence of loosely bound (LB) and tightly bound (TB) EPS, extracted from a marine strain of *Pseudomonas* (*Pseudomonas* NCIMB 2021), on the electrochemical behaviour of 70Cu-30Ni alloy in static ASW and on the chemical composition of oxide layers was studied by combined electrochemical measurements and surface analysis. Results were compared with those obtained in the presence of bovine serum albumin (BSA), a model protein. Compared to 70Cu-30Ni alloy in static ASW without biomolecules for which a thick duplex oxide layer has been shown, the presence of BSA, TB EPS and LB EPS leads to a mixed oxide layer (oxidized copper and nickel) with a lower thickness. Impedance data show a slow-down of the anodic reaction by the biomolecules (BSA, TB EPS and LB EPS), and a corrosion inhibition effect by LB EPS and to a lesser extent by BSA. These kinetic effect and corrosion inhibition effect are the strongest in the case of LB EPS, in agreement with the lowest Cu^+ content in the oxide layer and the lowest oxide layer thickness (~ 1.6 nm) estimated from XPS data. Therefore, combined electrochemical measurements and surface analysis show that adsorbed LB EPS inhibit the corrosion of 70Cu-30Ni alloy in static ASW and suppress Cu_2O

redeposition (amount of dissolved Cu^{+1} below the solubility limit); whereas adsorbed BSA and TB EPS slow down the anodic dissolution (kinetic effect) and inhibit Cu_2O redeposition (blocking effect). On the other hand, XPS results show the presence of an adsorbed organic layer, with an equivalent thickness of $\sim 1\text{-}3$ nm, covering the oxide layer formed on 70Cu-30Ni alloy exposed to BSA or EPS of *Pseudomonas NCIMB 2021*. From XPS data, the biomolecules composition in terms of proteins, polysaccharides and lipids, of the organic adlayer was estimated. Proteins are found to be the major biochemical compounds in these adlayers. However, proteins are more concentrated on the surface in the presence of LB EPS compared to TB EPS, with a weight percentage similar to that obtained for adsorbed BSA. This result is contrary to what is observed in bulk solution (TB EPS are much more concentrated in proteins than LB EPS). If comparing BSA and LB EPS, the corrosion inhibition effect induced by the biomolecules cannot be only explained by the amount of adsorbed proteins on the metallic surface but also by the nature of the adsorbed biomolecules.

Finally, the effect of TB EPS extracted from *Pseudomonas NCIMB 2021* on the passivation behaviour of Ti in ASW and of 304L stainless steel in chloride-free solution was studied, and results were compared with those obtained in the presence of BSA (model protein). We focused only on the influence of TB EPS since for LB EPS, the dialysis was done in ASW, and chlorides should be avoided in the case of 304L stainless steel. Polarisation curves were plotted using a scan rate of $0.5 \text{ mV}\cdot\text{s}^{-1}$. The passive currents obtained from the anodic curves are quite high (a few $\mu\text{A}\cdot\text{cm}^{-2}$), due to non steady-state conditions, and they cannot be subtracted from the cathodic polarisation curves close to the corrosion potential, in order to study the effect of biomolecules on the cathodic reaction. Therefore, the importance of plotting polarisation curves and EIS diagrams in real stationary conditions is pointed out. High-frequency CPE behaviour is evidenced for both materials and the electrochemical impedance results can be fitted with the power-law model (PLM), commonly used in the case of normal distributions of time constants induced by resistivity distributions within passive films. Resistivity profiles were plotted. For Ti and 304L stainless steel, the low-frequency limit of impedance diagrams, which is related to the highest boundary value of resistivity at the metal/oxide interface, is higher with BSA and lower with TB EPS compared to the solution without biomolecules; therefore, the oxide layer is more protective in the presence of BSA and less protective in the presence of TB EPS. On the other hand, surface analysis evidences the presence of a duplex oxide layer in the case of 304L stainless steel, with an outer layer of Fe_2O_3 and an inner layer of Cr_2O_3 , and a global thickness of ~ 2.3 nm similar

without and with biomolecules (BSA, TB EPS). In the case of Ti, the oxide layer is mainly composed of TiO_2 and its thickness is ~ 3.8 nm without biomolecules and ~ 4.6 nm with BSA or TB EPS. With BSA or TB EPS, XPS results also show the presence of an adsorbed organic layer on top of the oxide layer, with an equivalent thickness of ~ 3 nm for 304L stainless steel and of $\sim 1-2$ nm for Ti. As for 70Cu-30Ni alloy, proteins were found to be the major biochemical compounds in the organic adlayers. Table VI.1 summarizes the main conclusions obtained from this PhD work.

Table VI. 16: Summary of main conclusions of this work.

		70Cu-30Ni alloy	304L stainless steel	Titanium
Corrosion behaviour	BSA	<ul style="list-style-type: none"> • Slow-down of the anodic reaction • Small corrosion inhibition effect 	Oxide layer more protective	Oxide layer more protective
	TB EPS	<ul style="list-style-type: none"> • Slow-down of the anodic reaction • No detrimental effect 	Oxide layer less protective	Oxide layer less protective
	LB EPS	<ul style="list-style-type: none"> • Slow-down of the anodic reaction • Strong corrosion inhibition effect 	-	-
Oxide layer thickness		Decrease of the thickness in the presence of biomolecules specially with LB EPS	No significant effect	No significant effect
Chemical composition		Reduction or suppression of Cu_2O redeposition in the presence of biomolecules	No significant effect of biomolecules	No significant effect of biomolecules

In the case of 70Cu-30Ni in seawater, our results show a corrosion inhibition effect by LB EPS of *Pseudomonas NCIMB 2021*, and no detrimental effect by TB EPS. Analyses of the

nature of the EPS are required, in order to better understand the behaviours observed with the different kinds of EPS. Additionally, transmission electron microscopy can be performed to determine how EPS components can organise themselves on the surfaces. On the other hand, EPS were dialysed in artificial seawater (ASW), however, in the case of 304L stainless steel, EPS need to be dialysed in a chloride-free solution. Finally, for passive materials, it is necessary perform polarisation curves and EIS diagrams in real stationary conditions

One main result of this work is that the EPS of *Pseudomonas NCIMB 2021* are suitable candidate compounds to be potentially used as green corrosion inhibitors of 70Cu-30Ni in seawater.

References

- [1] E. Commission, “Integrated Pollution Prevention and Control (IPPC) Reference Document on the application of Best Available Techniques to Industrial Cooling Systems December 2001,” no. December, 2001.
- [2] L. F. S. de Almeida, V. de Matos Beleza, and I. M. Brás Pereira, “Contribution of air pollution to the fouling of heat exchangers in cooling water circuits,” *Exp. Therm. Fluid Sci.*, vol. 14, no. 4, pp. 438–441, May 1997.
- [3] M. J. Fernandez-Torres and F. Ruiz-Bevia, “Chlorine use reduction in nuclear or conventional power plants: a combined cooling-and-stripping tower for coastal power plants,” *J Clean Prod*, vol. 26, pp. 1–8, May 2012.
- [4] E. H. Poornima, M. Rajadurai, V. N. R. Rao, S. V. Narasimhan, and V. P. Venugopalan, “Use of coastal waters as condenser coolant in electric power plants: Impact on phytoplankton and primary productivity,” *J. Therm. Biol.*, vol. 31, no. 7, pp. 556–564, Oct. 2006.
- [5] A. E. Conradie and D. G. Kröger, “Performance evaluation of dry-cooling systems for power plant applications,” *Appl. Therm. Eng.*, vol. 16, no. 3, pp. 219–232, 1996.
- [6] H. A. Jenner, J. W. Whitehouse, C. J. L. Taylor, and M. Khalanski, *Cooling water management in European power stations, biology and control of fouling*. Chatou: Electricité de France, 1998, pp. 1–225.
- [7] R. K. Shah, B. Thonon, and D. M. Benforado, “Opportunities for heat exchanger applications in environmental systems,” *Appl. Therm. Eng.*, vol. 20, no. 7, pp. 631–650, 2000.
- [8] H. Richaud-Minier, P. Gerard, and H. Marchebois, “Titanium and super stainless steel welded tubing solutions for seawater cooled heat exchangers.”
- [9] B. Little and P. Wagner, “Microbiologically influenced corrosion of metals and alloys,” *Int. Mater. Rev.*, vol. 36, no. 6, 1991.
- [10] C. A. Powell and H. T. Michels, “Copper-Nickel alloys for seawater corrosion resistance and antifouling-A state of the art review,” *NACE Corros. 2000*, 2000.
- [11] F. Mansfeld, G. Liu, H. Xiao, C. H. Tsai, B. J. Littler, , “The corrosion behavior of copper alloys, stainless steels and titanium in seawater,” *Corros. Sci.*, vol. 36, no. 12, pp. 2063–2095, 1994.
- [12] Y. Z. Wang, A. M. Beccaria, and G. Poggi, “The effect of temperature on the corrosion behaviour of a 70/30 Cu-Ni commercial alloy in seawater,” *Corros. Sci.*, vol. 36, no. 8, pp. 1277–1288, 1994.

- [13] H. H. Strehblow, V. Maurice, and P. Marcus, "Passivity of Metals," in *Corrosion Mechanisms in Theory and Practice*, Third Edit., P. Marcus, Ed. CRC Press, 2011, pp. 235–326.
- [14] A. M. Alfantazi, T. M. Ahmed, and D. Tromans, "Corrosion behavior of copper alloys in chloride media," *Mater. Des.*, vol. 30, no. 7, pp. 2425–2430, Aug. 2009.
- [15] G. J. Licina, "MIC in the Power Industry," in *Microbiologically Influenced Corrosion, NACE International*, J. G. Stoecker, Ed. 1993.
- [16] L. Lartundo-Rojas, "Influence de l'adsorption de protéine (BSA) sur le comportement électrochimique et la composition de surface d'un alliage Fe-17Cr en solution aqueuse," University of Paris 6, 2007.
- [17] C.-O. . Olsson and D. Landolt, "Passive films on stainless steels—chemistry, structure and growth," *Electrochim. Acta*, vol. 48, no. 9, pp. 1093–1104, 2003.
- [18] Č. Donik, A. Kocijan, J. T. Grant, M. Jenko, A. Drenik, and B. Pihlar, "{XPS} study of duplex stainless steel oxidized by oxygen atoms," *Corros. Sci.*, vol. 51, no. 4, pp. 827–832, 2009.
- [19] A. Kocijan, Č. Donik, and M. Jenko, "Electrochemical and {XPS} studies of the passive film formed on stainless steels in borate buffer and chloride solutions," *Corros. Sci.*, vol. 49, no. 5, pp. 2083–2098, 2007.
- [20] D. Thierry and W. Sand, "Microbially Influenced Corrosion," in *Corrosion Mechanisms in Theory and Practice*, Third Edit., P. Marcus, Ed. 2011, pp. 737–776.
- [21] B. Feng, J. Weng, B. C. Yang, J. Y. Chen, J. Z. Zhao, L. He, S. K. Qi, and X. D. Zhang, "Surface characterization of titanium and adsorption of bovine serum albumin," *Mater. Charact.*, vol. 49, no. 2, pp. 129–137, 2002.
- [22] Y. Bao, W. Wang, B. He, M. Wang, Y. Yin, L. Liang, L. Xu, and G. Xu, "EIS analysis of hydrophobic and hydrophilicTiO₂ film," *Electrochim. Acta*, vol. 54, no. 2, pp. 611–615, Dec. 2008.
- [23] J. A. Mountford, "Titanium-properties, advantages and applications solving the corrosion problems in marine service," in *NACE International*, 2002.
- [24] Z. Ahmad, *Principles of corrosion Engineering and Corrosion Control*, First edit. Elsevier Ltd, 2006, p. 656.
- [25] S. G. Choudhary, "Emerging microbial control issues in cooling water systems," *Hydrocarb. Process.*, vol. 77, no. 5, pp. 91–102.
- [26] X. Dominguez-Benetton, "Biocomplexity and Bioelectrochemical Influence of Biofilms in Carbon Steel Deterioration A Transmission Line Approach for Electrochemical Impedance Analysis," Mexican Petroleum Institute, 2007.

- [27] W. A. Hamilton, "Microbially Influenced Corrosion as a Model System for the Study of Metal Microbe Interactions: A Unifying Electron Transfer Hypothesis," *Biofouling*, vol. 19, no. 1, pp. 65–76, Feb. 2003.
- [28] L. L. Shreir, R. A. Jarman, and G. T. Burstein, Eds., "Principles of Corrosion and Oxidation," in *Corrosion: Metal/Environment Reactions*, Third edit., Butterworth Heinemann, 1994.
- [29] H. Videla, "Prevention and control of biocorrosion," *Int. Biodeterior. Biodegradation*, vol. 49, no. 4, pp. 259–270, Jun. 2002.
- [30] G. V. Chilingar, R. Mourhatch, and G. D. Al-Qahtani, *The Fundamentals of Corrosion and Scaling for Petroleum and Environmental Engineers*. Gulf Publishing Company, 2008.
- [31] T. Y. Soror, "Scale and Corrosion Prevention in Cooling Water Systems Part I: Calcium Carbonate," *Open Corros. J.*, vol. 2, pp. 45–50, 2009.
- [32] H.-C. Flemming, "Microbial Biofouling: Unsolved Problems, Insufficient Approaches, and Possible Solutions," in *Biofilm Highlights*, H.-C. Flemming, J. Wingender, and U. Szewzyk, Eds. Springer Berlin Heidelberg, 2011, pp. 81–109.
- [33] S. Rajagopal, K. V. K. Nair, G. Azariah, G. van der Velde, and H. A. Jenner, "Chlorination and Mussel Control in the Cooling Conduits of a Tropical Coastal Power Station," *Mar. Environ. Res.*, vol. 41, no. 2, pp. 201–221, 1996.
- [34] C. Flemming, "Biofouling in water systems – cases , causes and countermeasures," *Appl. Microbiol. Biotechnol.*, vol. 59, pp. 629–640, 2002.
- [35] H. A. Videla and L. K. Herrera, "Biocorrosion," *Stud. Surf. Sci. Catal.*, vol. 151, pp. 193–218, 2004.
- [36] S. E. Coetser and T. E. Cloete, "Biofouling and biocorrosion in industrial water systems.," *Crit. Rev. Microbiol.*, vol. 31, no. 4, pp. 213–32, Jan. 2005.
- [37] I. B. Beech and J. Sunner, "Biocorrosion: towards understanding interactions between biofilms and metals.," *Curr. Opin. Biotechnol.*, vol. 15, no. 3, pp. 181–6, Jun. 2004.
- [38] C. J. L. Taylor, "The effects of biological fouling control at coastal and estuarine power stations.," *Mar. Pollut. Bull.*, vol. 53, no. 1–4, pp. 30–48, Jan. 2006.
- [39] M. Khalanski, "Organic by-products generated by the chlorination of cooling water at marine power stations," *La Trib. l'eau*, vol. 55–56, no. 619–21, pp. 24–39.
- [40] P. Cristiani, "Electrochemical technologies for antifouling treatments" *Biofouling*, vol. 7, pp. 1–24, 2010.
- [41] J. Ubbink and P. Scharzammaretti, "Colloidal properties and specific interactions of bacterial surfaces," *Curr. Opin. Colloid Interface Sci.*, vol. 12, no. 4–5, pp. 263–270, Oct. 2007.

- [42] M. Magot, "Micro-organismes et métabolisme," in *Biodétérioration des matériaux: Action des micro-organismes, de l'échelle nanométrique à l'échelle macroscopique*, F. Fritz-Feugeas, A. Cornet, and B. Tribollet, Eds. Paris: Ellipses, 2008, pp. 45–58.
- [43] B. Halan, K. Buehler, and A. Schmid, "Biofilms as living catalysts in continuous chemical syntheses," *Trends Biotechnol.*, vol. 30, no. 9, pp. 453–465, 2012.
- [44] J. Harrison, R. Turner, L. Marques, and H. Ceri, "Biofilms: A new understanding of these microbial communities is driving a revolution that may transform the science of microbiology," *Am. Sci.*, vol. 93, p. 508, 2005.
- [45] A. W. Decho, "Microbial exopolymer secretions in ocean environments: their role(s) in food webs and marine processes," *Oceanogr. Mar. Biol. an Annu. Rev.*, vol. 28, pp. 73–153, 1990.
- [46] J. S. Dickschat, "Quorum sensing and bacterial biofilms.," *Nat. Prod. Rep.*, vol. 27, no. 3, pp. 343–69, Mar. 2010.
- [47] G. T. Taylor, P. J. Troy, and S. K. Sharma, "Protein adsorption from seawater onto solid substrata , I. Influences of substratum surface properties and protein concentration," *Methods*, vol. 45, pp. 15–30, 1994.
- [48] M. Katsikogianni and Y. F. Missirlis, "Concise review of mechanisms of bacterial adhesion to biomaterials and of techniques used in estimating bacteria-material interactions," *Eur. Cells Mater.*, vol. 8, pp. 37–57, 2004.
- [49] K. Kierek-Pearson and E. Karatan, "Biofilm Development in Bacteria," vol. 57, no. 05, pp. 79–111, 2005.
- [50] K. Hori and S. Matsumoto, "Bacterial adhesion : From mechanism to control," *Biochem. Eng. J.*, vol. 48, pp. 424–434, 2010.
- [51] R. P. Schneider and K. C. Marshall, "Retention of the Gramnegative marine bacterium {SW8} on surfaces — effects of microbial physiology, substratum nature and conditioning films," *Colloids Surfaces B Biointerfaces*, vol. 2, no. 4, pp. 387–396, 1994.
- [52] G. I. Loeb, Neihof, and R. E. X. A., "Marine Conditioning Films," in *Applied Chemistry at Protein Interfaces*, 1975, pp. 319–335.
- [53] A. Lee, R. N. Lamb, B. Gong, and R. P. Schneider, "Evidence for the contribution of humic substances to conditioning films from natural waters," *Biofouling*, vol. 15, no. 1–3, pp. 207–220, 2000.
- [54] R. P. Schneider, "Bacterial adhesion to solid substrata coated with conditioning films derived from chemical fractions of natural waters," *J. Adhes. Sci. Technol.*, vol. 11, no. 7, pp. 979–994, 1997.
- [55] H.-C. Flemming and J. Wingender, "The biofilm matrix," *Nat. Rev. Microbiol.*, vol. 8, no. 9, pp. 623–633, 2010.

- [56] G.-P. Sheng, H.-Q. Yu, and X.-Y. Li, "Extracellular polymeric substances (EPS) of microbial aggregates in biological wastewater treatment systems: A review," *Biotechnol. Adv.*, vol. 28, no. 6, pp. 882–894, 2010.
- [57] H. C. Flemming and A. Leis, "Sorption Properties of Biofilms," in *Encyclopedia of Environmental Microbiology*, 2003, pp. 2958–2967.
- [58] I. W. Sutherland, "Biofilm exopolysaccharides: a strong and sticky framework," *Microbiology*, vol. 147, pp. 3–9, 2001.
- [59] C. Xu, S. Zhang, C. Chuang, E. J. Miller, K. A. Schwehr, and P. H. Santschi, "Chemical composition and relative hydrophobicity of microbial exopolymeric substances (EPS) isolated by anion exchange chromatography and their actinide-binding affinities," *Mar. Chem.*, vol. 126, no. 1–4, pp. 27–36, 2011.
- [60] H.-C. C. Flemming and J. Wingender, "Relevance of microbial extracellular polymeric substances (EPSs) - Part I: Structural and ecological aspects," *Water Sci. Technol.*, vol. 43, no. 6, pp. 1–8, Jan. 2001.
- [61] P. V. Bhaskar and N. B. Bhosle, "Microbial extracellular polymeric substances in marine biogeochemical processes," *Curr. Sci.*, vol. 88, no. 1, pp. 45–53, 2005.
- [62] A. W. Decho, "Microbial biofilms in intertidal systems: an overview," *Cont. Shelf Res.*, vol. 20, no. 10–11, pp. 1257–1273, 2000.
- [63] P. Lembre, C. Lorentz, P. Di Martino, and P. Di Martino, "Exopolysaccharides of the Biofilm Matrix: A Complex Biophysical World," in *Biochemistry, Genetics and Molecular Biology: "The complex World of Polysaccharides,"* D. Nedra-Karunaratne, Ed. 2012, pp. 371–392.
- [64] I. B. Beech, J. a Sunner, and K. Hiraoka, "Microbe-surface interactions in biofouling and biocorrosion processes.," *Int. Microbiol.*, vol. 8, no. 3, pp. 157–68, Sep. 2005.
- [65] S. K. Satpute, I. M. Banat, P. K. Dhakephalkar, A. G. Banpurkar, and B. A. Chopade, "Biosurfactants, bioemulsifiers and exopolysaccharides from marine microorganisms," *Biotechnol. Adv.*, vol. 28, no. 4, pp. 436–450, 2010.
- [66] A. Pal and A. K. Paul, "Microbial extracellular polymeric substances: central elements in heavy metal bioremediation," *Indian J. Microbiol.*, vol. 48, no. 1, pp. 49–64, 2008.
- [67] Y. Tian, L. Zheng, and D. Sun, "Functions and behaviors of activated sludge extracellular polymeric substances (EPS): a promising environmental interest," *J. Environ. Sci.*, vol. 18, no. 2, pp. 420–427, 2006.
- [68] S. J. Yuan, A. M. F. Choong, and S. O. Pehkonen, "The influence of the marine aerobic *Pseudomonas* strain on the corrosion of 70/30 Cu–Ni alloy," *Corros. Sci.*, vol. 49, no. 12, pp. 4352–4385, 2007.
- [69] H. H. P. Fang, L.-C. Xu, and K.-Y. Chan, "Effects of toxic metals and chemicals on biofilm and biocorrosion.," *Water Res.*, vol. 36, no. 19, pp. 4709–16, Nov. 2002.

- [70] T. J. Peters, "Serum albumin," *Adv. Protein Chem.*, vol. 37, pp. 161–245, 1985.
- [71] D. C. Carter and J. X. Ho, "Structure of serum albumin," *Adv. Protein Chem.*, vol. 45, pp. 153–203, 1994.
- [72] A. Ithurbide, I. Frateur, A. Galtayries, and P. Marcus, "XPS and flow-cell EQCM study of albumin adsorption on passivated chromium surfaces: Influence of potential and pH," *Electrochim. Acta*, vol. 53, no. 3, pp. 1336–1345, Dec. 2007.
- [73] L. R. S. Barbosa, M. G. Ortore, F. Spinozzi, P. Mariani, S. Bernstorff, and R. Itri, "The Importance of Protein-Protein Interactions on the pH-Induced Conformational Changes of Bovine Serum Albumin: A Small-Angle X-Ray Scattering Study," *Biophys. J.*, vol. 98, no. 1, pp. 147–157, Jan. 2010.
- [74] T. Kopac, K. Bozgeyik, and J. Yener, "Effect of pH and temperature on the adsorption of bovine serum albumin onto titanium dioxide," *Colloids Surfaces A Physicochem. Eng. Asp.*, vol. 322, no. 1–3, pp. 19–28, Jun. 2008.
- [75] J. R. Brown, "Structural origins of mammalian albumin," *Fed. Proc.*, vol. 35, no. 10, p. 2141, 1976.
- [76] K. Hirayama, S. Akashi, M. Furuya, and K. Fukuhara, "Rapid confirmation and revision of the primary structure of bovine serum albumin by ESIMS and Frit-FAB LC/MS," *Biochem. Biophys. Res. Commun.*, vol. 173, no. 2, pp. 639–646, 1990.
- [77] B. Jachimska and a Pajor, "Physico-chemical characterization of bovine serum albumin in solution and as deposited on surfaces," *Bioelectrochemistry*, vol. 87, no. 0, pp. 138–146, Oct. 2012.
- [78] M. Fletcher and G. D. Floodgate, "An Electron-microscopic Demonstration of an Acidic Polysaccharide Involved in the Adhesion of a Marine Bacterium to Solid Surfaces," *J. Gen. Microbiol.*, vol. 74, pp. 325–334, 1973.
- [79] K. Rasmussen and K. Østgaard, "Adhesion of the marine bacterium *Pseudomonas* sp. {NCIMB} 2021 to different hydrogel surfaces," *Water Res.*, vol. 37, no. 3, pp. 519–524, 2003.
- [80] M. Fletcher and G. I. Loeb, "Influence of Substratum Characteristics on the Attachment of a Marine *Pseudomonas* to Solid Surfaces," *Appl. Environ. Microbiol.*, vol. 37, no. 1, pp. 67–72, 1979.
- [81] P. Cristiani, G. Perboni, and a Debenedetti, "Effect of chlorination on the corrosion of Cu/Ni 70/30 condenser tubing," *Electrochim. Acta*, vol. 54, no. 1, pp. 100–107, Dec. 2008.
- [82] M. J. Brown and N. J. Lester, "Comparison of Bacterial Extracellular Polymer Extraction Methods," *Appl. Environ. Microbiol.*, vol. 40, no. 2, pp. 179–185, 1980.

- [83] R. M. Platt, G. G. Geesey, J. D. Davis, and D. C. White, "Isolation and partial chemical analysis of firmly bound exopolysaccharide from adherent cells of a freshwater sediment bacterium," *Can. J. Microbiol.*, vol. 31, no. 8, pp. 675–680, 1985.
- [84] N. K. Karapanagiotis, T. Rudd, R. M. Sterritt, and J. N. Lester, "Extraction and characterisation of extracellular polymers in digested sewage sludge," *J. Chem. Technol. Biotechnol.*, vol. 44, no. 2, pp. 107–120, 1989.
- [85] J. Azeredo, V. Lazarova, and R. Oliveira, "Methods to extract the exopolymeric matrix from biofilms: A comparative study," *Water Sci. Technol.*, vol. 39, no. 7, pp. 243–250, 1999.
- [86] A. Aguilera, V. Souza-Egipsy, P. S. Martín-Úriz, and R. Amils, "Extracellular matrix assembly in extreme acidic eukaryotic biofilms and their possible implications in heavy metal adsorption," *Aquat. Toxicol.*, vol. 88, no. 4, pp. 257–266, 2008.
- [87] A. J. Wikiel, "Role of extracellular polymeric substances on biocorrosion initiation or inhibition," Universität Duisburg-Essen, 2013.
- [88] P. d'Abzac, F. Bordas, E. van Hullebusch, P. N. L. Lens, and G. Guibaud, "Effects of extraction procedures on metal binding properties of extracellular polymeric substances (EPS) from anaerobic granular sludges," *Colloids Surfaces B Biointerfaces*, vol. 80, no. 2, pp. 161–168, 2010.
- [89] S. S. Adav, D.-J. Lee, and J.-H. Tay, "Extracellular polymeric substances and structural stability of aerobic granule," *Water Res.*, vol. 42, no. 6–7, pp. 1644–1650, 2008.
- [90] M. DuBois, K. A. Gilles, J. K. Hamilton, P. A. Rebers, and F. Smith, "Colorimetric Method for Determination of Sugars and Related Substances," *Anal. Chem.*, vol. 28, no. 3, pp. 350–356, 1956.
- [91] T. M. C. C. Filisetti-Cozzi and N. C. Carpita, "Measurement of uronic acids without interference from neutral sugars," *Anal. Biochem.*, vol. 197, no. 1, pp. 157–162, 1991.
- [92] K. Burton, "A study of the conditions and mechanism of the diphenylamine reaction for the colorimetric estimation of deoxyribonucleic acid," *Biochem. J.*, vol. 62, no. 2, pp. 315–323, 1956.
- [93] M. M. Bradford, "A rapid and sensitive method for the quantitation of microgram quantities of protein utilizing the principle of protein-dye binding," *Anal. Biochem.*, vol. 72, no. 1–2, pp. 248–254, 1976.
- [94] Y. D. Karkhanis, J. Y. Zeltner, J. J. Jackson, and D. J. Carlo, "A new and improved microassay to determine 2-keto-3-deoxy-octonate in lipopolysaccharide of gram-negative bacteria," *Anal. Biochem.*, vol. 85, no. 2, pp. 595–601, 1978.
- [95] C. Gabrielli, *Use and applications of electrochemical impedance techniques: technical report*. Farnborough, Hampshire, England: Schlumberger Technologies, Instruments Division, 1990, p. 102.

- [96] M. E. Orazem and B. Tribollet, *Electrochemical Impedance Spectroscopy*. Wiley, 2008, p. 523.
- [97] A. Lasia, "Electrochemical Impedance Spectroscopy and its Applications," vol. 32, pp. 143–248, 1999.
- [98] B.-Y. Chang and S.-M. Park, "Electrochemical impedance spectroscopy.," *Annu. Rev. Anal. Chem. (Palo Alto. Calif.)*, vol. 3, pp. 207–29, Jan. 2010.
- [99] Bio-Logic, "SP300-based installation and configuration manual," 2012. [Online]. Available: <http://www.bio-logic.info/electrochemistry-ec-lab/downloads/manuals/>.
- [100] I. Frateur, "Incidence de la corrosion des matériaux ferreux sur la demande en chlore libre en réseaux de distribution d'eau potable," Université Pierre et Marie Curie, Paris 6, 1997.
- [101] D. G. Enos and L. L. Scribner, "The potentiodynamic Polarization Scan," 1997.
- [102] C. Gabrielli, "Identification of electrochemical processes by frequency response analysis, Solartron, Technical report number 004/83," 1998.
- [103] M. E. Orazem, N. Pébère, and B. Tribollet, "Enhanced Graphical Representation of Electrochemical Impedance Data," *J. Electrochem. Soc.*, vol. 153, no. 4, pp. B129–B136, Apr. 2006.
- [104] M. E. Orazem, I. Frateur, B. Tribollet, V. Vivier, S. Marcelin, N. Pébère, A. L. Bunge, E. A. White, D. P. Riemer, and M. Musiani, "Dielectric Properties of Materials Showing Constant-Phase-Element (CPE) Impedance Response," *J. Electrochem. Soc.*, vol. 160, no. 6, pp. C215–C225, Jan. 2013.
- [105] G. J. Brug, A. L. G. van den Eeden, M. Sluyters-Rehbach, and J. H. Sluyters, "The analysis of electrode impedances complicated by the presence of a constant phase element," *J. Electroanal. Chem. Interfacial Electrochem.*, vol. 176, no. 1–2, pp. 275–295, 1984.
- [106] M. Genet, C. C. Dupont-Gillain, and P. Rouxhet, "XPS analysis of biosystems and biomaterials," in *Medical Applications of Colloids*, E. Matijevic, Ed. Springer (New York), 2008, pp. 177–307.
- [107] S. Brunner, "Surface analytical and electrochemical characterization of biomaterial surfaces," Friedrich-Alexander University, 2006.
- [108] A. Cros, "Charging effects in X-ray photoelectron spectroscopy," *J. Electron Spectros. Relat. Phenomena*, vol. 59, pp. 1–14, 1992.
- [109] I. Frateur, J. Lecoœur, S. Zanna, C.-O. A. Olsson, D. Landolt, and P. Marcus, "Adsorption of BSA on passivated chromium studied by a flow-cell EQCM and XPS," *Electrochim. Acta*, vol. 52, no. 27, pp. 7660–7669, Oct. 2007.

- [110] S. Tanuma, C. J. Powell, and D. R. Penn, "Calculations of electron inelastic mean free paths (IMFPs). IV. Evaluation of calculated IMFPs and of the predictive IMFP formula TPP-2 for electron energies between 50 and 2000 eV," *Surf. Interface Anal.*, vol. 20, no. 1, pp. 77–89, 1993.
- [111] J. H. Scofield, "Hartree-Slater subshell photoionization cross-sections at 1254 and 1487 eV," *J. Electron Spectros. Relat. Phenomena*, vol. 8, no. 2, pp. 129–137, 1976.
- [112] K. Richter, "Application of imaging ToF-SIMS in cell and tissue research," Göteborg University, 2007.
- [113] A. M. Belu, D. J. Graham, and D. G. Castner, "Time-of-flight secondary ion mass spectrometry: techniques and applications for the characterization of biomaterial surfaces," *Biomaterials*, vol. 24, no. 21, pp. 3635–3653, 2003.
- [114] S. Hofmann, "Sputter depth profile analysis of interfaces," *Reports Prog. Phys.*, vol. 61, no. 7, p. 827, 1998.
- [115] S. Hofmann, "Ultimate Depth Resolution and Profile Reconstruction in Sputter Profiling with AES and SIMS," Feb. 2000.
- [116] C. D. Wagner, W. M. Riggs, L. E. Davis, and J. F. Moulder, *Handbook of X-ray Photoelectron Spectroscopy*. Perkin-Elmer Corporation, 1979, p. 192.
- [117] S. K. Chawla, N. Sankarraman, and J. H. Payer, "Diagnostic spectra for XPS analysis of Cu-O-S-H compounds," *J. Electron Spectros. Relat. Phenomena*, vol. 61, no. 1, pp. 1–18.
- [118] M. C. Biesinger, L. W. M. Lau, A. R. Gerson, and R. S. C. Smart, "Resolving surface chemical states in {XPS} analysis of first row transition metals, oxides and hydroxides: Sc, Ti, V, Cu and Zn," *Appl. Surf. Sci.*, vol. 257, no. 3, pp. 887–898, 2010.
- [119] G. Deroubaix and P. Marcus, "X-ray photoelectron spectroscopy analysis of copper and zinc oxides and sulphides," *Surf. Interface Anal.*, vol. 18, no. 1, pp. 39–46, 1992.
- [120] A. Galtayries, J. Grimblot, and J.-P. Bonnelle, "Interaction of SO₂ with different polycrystalline Cu, Cu₂O and CuO surfaces," *Surf. interface Anal.*, vol. 24, no. 5, pp. 345–354.
- [121] A. Galtayries and J. P. Bonnelle, "XPS and ISS studies on the interaction of H₂S with polycrystalline Cu, Cu₂O and CuO surfaces," *Surf. Interface Anal.*, vol. 23, pp. 171–179, 1995.
- [122] P. Marcus and J.-M. Herbelin, "The entry of chloride ions into passive films on nickel studied by spectroscopic (ESCA) and nuclear (³⁶Cl radiotracer) methods," *Corros. Sci.*, vol. 34, no. 7, pp. 1123–1145, Jul. 1993.
- [123] H. Ayoub, V. Lair, S. Griveau, A. Galtayries, P. Brunswick, F. Bedioui, and M. Cassir, "Ageing of nickel used as sensitive material for early detection of sudomotor dysfunction," *Appl. Surf. Sci.*, vol. 258, pp. 2724–2731, 2012.

- [124] C. Deslouis, B. Tribollet, G. Mengoli, and M. M. Musiani, "Electrochemical behavior of copper in neutral aerated chloride solution. 2. Impedance investigation", *J. Appl. Electrochem.*, vol. 18, no. 3, pp. 384–393, 1988.
- [125] B. Tribollet, "Applications des methodes electrochimiques a l'etude des solutions de polymere en ecoulement," Université Pierre et Marie Curie, Paris 6, 1978.
- [126] P. Han and D. M. Bartels., "Temperature dependence of oxygen diffusion in H₂O and D₂O," *J. Phys. Chem.*, vol. 100, no. 13, pp. 5597–5602, 1996.
- [127] E. L. Cussier, *Diffusion, mass transfer in fluid systems*, 2nd editio. New york: New York: Cambridge University Press, 1997, p. 580.
- [128] F. C. Tse and O. C. Sandall, "Diffusion coefficients for oxygen and carbon dioxide in water at 25°C by unsteady state desorption from quiescent liquid," *Chem. Eng. Commun.*, vol. 3, no. 3, pp. 147–153, 1979.
- [129] E. D'Elia, O. E. Barcia, O. R. Mattos, N. Pébère, and B. Tribollet, "High-Rate Copper Dissolution in Hydrochloric Acid Solution," *J. Electrochem. Soc.* , vol. 143 , no. 3 , pp. 961–967, Mar. 1996.
- [130] O. E. Barcia, O. R. Mattos, N. Pebere, and B. Tribollet, "Mass-Transport Study for the Electrodeposition of Copper in 1M Hydrochloric Acid Solution by Impedance," *J. Electrochem. Soc.* , vol. 140 , no. 10 , pp. 2825–2832, Oct. 1993.
- [131] C. Deslouis, O. R. Mattos, M. M. Musiani, and B. Tribollet, "Comments on mechanisms of copper electrodeposition in chloride media," *Electrochim. Acta*, vol. 38, no. 18, pp. 2781–2783, 1993.
- [132] S. Petetin, J. Crousier, and J.-P. Crousier, "Comportement de l'alliage Cuivre-Nickel 7030 dans une solution de NaCl A 3%," *Mater. Chem. Phys.*, vol. 10, no. 4, pp. 317–329, 1984.
- [133] B. Hirschorn, M. E. Orazem, B. Tribollet, V. Vivier, I. Frateur, and M. Musiani, "Determination of effective capacitance and film thickness from constant-phase-element parameters," *Electrochim. Acta*, vol. 55, no. 21, pp. 6218–6227, 2010.
- [134] H. Grubitsch, F. Hilbert, and R. Sammer, "Auswertung von potentiokinetischen Strom-Spannungsmessungen an Cu-Ni-Legierungen, Kupfer und Messung in Meerwasser," *Mater. Corros.*, vol. 17, no. 9, pp. 760–765, 1966.
- [135] R. Souchet, F. Danoix, A. D'huysser, and L. M., "APFIM and XPS study of the first stages of low temperature air oxidation of industrial CuNi alloys," *Appl. Surf. Sci.*, vol. 87–88, pp. 271–278.
- [136] R. Souchet, M. Lenglet, P. Miche, S. Weber, and S. Scherrer, "Study of copper-nickel alloy oxidation by FTIR and SIMS," *Analisis*, vol. 21, no. 3, pp. 173–176.
- [137] A.-M. Beccaria and J. Crousier, "Dealloying of Cu-Ni alloys in natural sea water," *Br. Corros. J.*, vol. 24, no. 1, pp. 49–52.

- [138] Y. F. Dufr, P. G. Rouxhet, and Y. F. Dufrêne, "X-ray photoelectron spectroscopy analysis of the surface composition of *Azospirillum brasilense* in relation to growth conditions," *Colloids Surfaces B Biointerfaces*, vol. 7, no. 5–6, pp. 271–279, Nov. 1996.
- [139] P. G. Rouxhet, N. Mozes, P. B. Dengis, Y. F. Dufrêne, P. A. Gerin, and M. J. Genet, "Application of X-ray photoelectron spectroscopy to microorganisms," *Colloids Surfaces B Biointerfaces*, vol. 2, no. 1–3, pp. 347–369, 1994.
- [140] Y. Yang, "Biofouling of metal surfaces: study of adsorbed biomolecules and prevention strategy based on a renewable copolymer layer," Université catholique de Louvain, 2013.
- [141] F. Ahimou, C. J. P. Boonaert, Y. Adriaensen, P. Jacques, P. Thonart, M. Paquot, and P. G. Rouxhet, "{XPS} analysis of chemical functions at the surface of *Bacillus subtilis*," *J. Colloid Interface Sci.*, vol. 309, no. 1, pp. 49–55, 2007.
- [142] S. Chakri, I. Frateur, E. Sutter, B. Tribollet, and V. Vivier, "Comportement électrochimique des armatures métalliques des bétons en solution NaOH 0.1M: Intérêt des mesures stationnaires," in *Actes du 25ème Forum sur les Impédance électrochimiques*, 2014.
- [143] B. W. Callen, R. N. S. Sodhi, and K. Griffiths, "Examination of clinical surface preparations on titanium and Ti6Al4V by X-ray photoelectron spectroscopy and nuclear reaction analysis," *Prog. Surf. Sci.*, vol. 50, no. 1–4, pp. 269–279.
- [144] V. Payet, S. Brunner, A. Galtayries, I. Frateur, and P. Marcus, "Cleaning of albumin-contaminated Ti and Cr surfaces: an XPS and QCM study," *Surf. Interface Anal.*, vol. 40, no. 3–4, pp. 215–219, 2008.
- [145] V. Payet, "Bioadhésion sur surfaces métalliques modèles de biomatériaux à usage médical: influence de protéine sur le comportement de cellules du tissu osseux," Université Pierre et Marie Curie, 2009.
- [146] J. Kunze, A. Ghicov, H. Hildebrand, J. M. Macak, L. Traveira, and P. Schmuki, "Challenges in the surface analytical characterisation of anodic TiO₂ films : a review," *Zeitschrift für Phys. Chemie*, vol. 219, no. 11, pp. 1561–1582.
- [147] T. Mertens and H. Kollek, "On the stability and composition of oxide layers on pre-treated titanium," *Int. J. Adhes. Adhes.*, vol. 30, no. 6, pp. 466–477, Sep. 2010.
- [148] C. Gadois, "Traitement de surface sur le titane et caractérisation physico-chimique des interfaces adhésif-titane pour la réalisation d'un réservoir de gaz haute pression destiné à l'aérospatiale.," Université Pierre et Marie Curie, 2013.
- [149] K. Hafidi, M. Azizan, Y. Ijdiyaou, and E. L. Ameziane, "La spectroscopie XPS et les effets du bombardement ionique : Réduction des couches minces de dioxyde de titane élaborées par pulvérisation cathodique radio fréquence," *Silic. Ind.*, no. 9–10, pp. 173–180.

-
- [150] E. McCafferty and J. . Wightman, "An X-ray photoelectron spectroscopy sputter profile study of the native air-formed oxide film on titanium," *Appl. Surf. Sci.*, vol. 143, no. 1–4, pp. 92–100, Apr. 1999.
- [151] V. Maurice, S. Cadot, and P. Marcus, "XPS, LEED and STM study of thin oxide films formed on Cr(110)," *Surf. Sci.*, vol. 458, no. 1–3, pp. 195–215, Jun. 2000.
- [152] K. Zumsande, A. Weddeling, E. Hryha, S. Huth, L. Nyborg, S. Weber, N. Krasokha, and W. Theisen, "Characterization of the surface of Fe–19Mn–18Cr–C–N during heat treatment in a high vacuum — An XPS study," *Mater. Charact.*, vol. 71, pp. 66–76, Sep. 2012.
- [153] B. Hirschorn, M. E. Orazem, B. Tribollet, V. Vivier, I. Frateur, and M. Musiani, "Constant-Phase-Element Behavior Caused by Resistivity Distributions in Films. Applications," *J. Electrochem. Soc.*, vol. 157, no. 12, p. C458, 2010.
- [154] R. Memming, "Solar energy conversion by photoelectrochemical processes," *Electrochim. Acta*, vol. 25, no. 3, pp. 77–88, 1980.
- [155] T. Shibata, "The effect of temperature on the growth anodic oxide film on titanium" vol. 37, no. 1, pp. 133–144, 1995.
- [156] B. Kang, S. Lee, and J. B. U, "Growth of TiO₂ thin films on Si (100) substrates using single molecular precursors by metal organic chemical vapor deposition," pp. 88–92, 2000.
- [157] I. Oja, a. Mere, M. Krunk, R. Nisumaa, C.-H. Solterbeck, and M. Es-Souni, "Structural and electrical characterization of TiO₂ films grown by spray pyrolysis," *Thin Solid Films*, vol. 515, no. 2, pp. 674–677, Oct. 2006.

Annex A

Table A. 1 : Calculation sheet for converting marker concentrations (molar percentage of relevant element, excluding hydrogen) into mass concentration (%) of model constituents in an organic phase.

Model constituent		Marker	$W = X * MM^{(c)}$	$W * 100 / Tot$ Constituent concentration [mass %]
Nature	$MM^{(a)}$	Name and concentration $X^{(b)}$		
Protein	56.08	N_{org}	●●●	●●●
CH_2	14.01	$C_{285/284.8}$	●●●	●●●
Extra C	12.01	$C_{284.8} - 2 * N_{org}$	●●●	●●●
Extra O_{org}	16.00	$C_{ox} - 2 * N_{org}$	●●●	●●●
Total	–	– -	Tot = ●●●	100

(a) Molar mass of constituent

(b) Name of marker, concentration X deduced from XPS spectra (mole/100 moles excluding hydrogen)

(c) In gram of constituent / 100 moles of elements other than hydrogen

●●● From measurement

Annex B

Effect of *Escherichia coli* K12 adhesion on the surface chemical composition of 70Cu-30Ni alloy, 304L stainless steel and titanium

Escherichia coli are the most-studied prokaryotic cells. *E. coli* is a usually harmless inhabitant of the human intestinal tract. Most *E. coli* serotypes are benign and may even contribute to normal function and nutrition in the gastrointestinal tract, just few *E. coli* serotypes are pathogens. The *E. coli* cell is about 1 μm long and a little less than 0.5 μm in diameter. It has a protective outer membrane and an inner plasma membrane that encloses the cytoplasm and the nucleoid. Between the inner and outer membranes is a thin but strong layer of polymers called peptidoglycans, which gives the cell its shape and rigidity. *E. coli* is a facultative anaerobe which has both a respiratory and a fermentative type of metabolism. *E. coli* is used as a model organism in research in microbial genetics and physiology, and it is used in industrial applications. It was originally isolated from a convalescent diphtheria patient in 1922. *E. coli* K-12 strains in use today are from standard culture collections, such as the American Type Culture-Collection.

In this Annex, XPS and ToF-SIMS measurements were performed in order to determine the effect of *Escherichia coli* K-12 adhesion on the surface chemical composition of 70Cu-30Ni, 304L stainless steel and titanium. For that, the *E. coli* K12 bacteria were pre-cultivated by addition of 1 mL of bacteria stock solution (cryotube) into 40 mL of Luria-Bertani Broth (LBB) medium and stored up to 5 h at 37°C under stirring, in order to reactivate the frozen cells. Then, 15 mL of pre-culture was added into 85 mL of LBB medium and kept overnight at 37°C under stirring before each experiment.

70Cu-30Ni alloy, 304L stainless steel and titanium coupons were prepared (polishing with diamond spray down to 1 micron, and degreasing in an ultrasonic bath 3 times in acetone during 5 min, once in ethanol during 10 min, and once in ultrapure water during 1-2min) for the bacterial adhesion experiments with *Escherichia coli* K12. Three kinds of experiments were performed: a) biofilm growth, b) 1 hour of exposure to the bacteria, and c) negative control.

For the biofilm growth and the 1 hour bacterial exposure experiments, the cells were washed, placing 50 ml of culture in two falcon tubes, and centrifuged at 7000 rpm for 10 min; the supernatant was removed. Then, the pellet was resuspended in 9 ml of 9 g.L⁻¹ NaCl solution, and both falcon tubes were combined. The cells were washed with the NaCl solution three times following the same procedure. After washing the cells, the remaining pellet was resuspended in 20 ml of 9 g.L⁻¹ NaCl solution, and the resulting bacterial suspension was diluted until having an optical density (OD_{400nm}) = 0.6-0.7 (108 cfu/ml).

For the biofilm growth tests, each sample was introduced in a petri dish, 20 ml of the diluted bacterial suspension was added, and the petri dishes were stored during 1 h at 20°C. Subsequently, the samples were rinsed by removing the bacterial suspension with a pipette and introducing fresh sterile 9 g.L⁻¹ NaCl solutions, in order to remove the cells loosely bound to the surface. Finally, 10 ml of fresh sterile LBB medium were added to the petri dishes and maintained at 20°C during 24 h. Then, the coupons were rinsed in the same way as before.

For the 1 hour bacterial exposure experiments, the coupons were introduced in petri dishes, 20 ml of the diluted bacterial suspension (OD_{400nm} = 0.6-0.7) was added, then the petri dishes were stored during 1 h at 20°C. After 1 h, the samples were rinsed in the same mode as for the biofilm growth tests. The negative controls were prepared following the same procedure as for the 1 h bacterial exposure tests, but using sterile 9 g.L⁻¹ NaCl solution instead of the diluted bacterial suspension.

Once the samples were ready, they were subjected to a fixation and dehydration procedure before XPS and ToF-SIMS analysis. The fixation procedure consists in immersing the samples in a 3% glutaraldehyde solution prepared in 0.1 M cacodylate buffer solution (pH 7.2), during 1h at 4°C. After 1 h, new solution was added to each coupon which was stored during 10 min; this step was repeated twice.

After the fixation procedure, the deposits were dried by treating the coupons with ethanol at different concentration (10%, 20%, 30%, 40%, 50%, 60%, 70%, 80%, 90%, and 96%). For that, the ethanol solution was changed every 10 min starting from the lowest to the highest ethanol concentration.

The negative control was repeated one more time for the 3 materials (70Cu-30Ni alloy, 304L stainless steel, Ti), at different time and place. The samples were analyzed without performing the dehydration and fixation procedure.

The samples that constitute the negative control after dehydration and fixation procedure were compared to the negative control without any treatment. A large carbon contribution related to carbon bound to carbon and/or hydrogen, as well as a nitrogen peak were observed by XPS for the negative control after dehydration and fixation procedure. This carbon and nitrogen contributions were even higher than those present in the samples with biofilm and those after 1 h of exposure to *E. coli*. A possible explanation for this event is that the water used for the experiments was sterile but containing organic compounds (*e. g.* dead microorganisms) that the dehydration and fixation procedure fixed on the surface layer. Although the same water was used for the 1 h exposure to *E. coli* test and the biofilm growth test, it is possible that these organic compounds present in the water were used by the bacteria as carbon source, reducing the carbon component observed in the negative control. In the case of the repeated negative controls without the dehydration and fixation procedure, as these samples were prepared at different time and place and, thus, the water used for these experiments was different (sterile ultrapure water), no large contribution of carbon and nitrogen were observed.

Due to the difficulty of interpreting the results for the negative control after dehydration and fixation procedure and considering that the carbon and nitrogen compounds present in the water were consumed by the bacteria, results for the negative control after dehydration and fixation procedure were omitted in this annex with the consideration that experiments need to be repeated.

Therefore, in all the materials, three sets of measurements were obtained:

- a) negative control without treatment (without dehydration and fixation procedure);
- b) *E. coli* biofilm;
- c) *E. coli* 1 h of exposure.

B.1. 70Cu-30Ni

During the XPS analyses, the following core levels were recorded: Cu 2p (and Auger lines), Ni 2p, O 1s, C 1s, and N 1s. The composition and the thickness of the oxide layer was calculated from XPS data considering a continuous mixed oxide layer covering the

metallic/alloy substrate, in which the intensities of copper and nickel in the metallic substrate and in the oxide layer were considered. The XPS spectra of Cu 2p_{3/2}, Cu Auger, Ni 2p_{3/2} C 1s and N 1s are shown in Figure B.1.

As mentioned in Chapter III, the decomposition of the Cu 2p_{3/2} XPS peak presents an important difficulty. Indeed, the binding energy of Cu⁰ and Cu⁺¹ are located at the same binding energy. This difficulty is overcome by making use of the Cu Auger line (L₃M₄₅M₄₅), helpful for distinguishing these two species. For the negative control, the XPS Cu 2p_{3/2} core level peak with a binding energy located at 932.7 eV (Figure B.1 (a)) and the Cu Auger line (L₃M₄₅M₄₅) at a kinetic energy of 916.6 eV (Figure B.1 (b)) demonstrate the presence of Cu⁺¹. Another peak is visible in the Cu Auger line, corresponding to the metallic substrate, indicating that the film is thin enough to calculate the thickness by XPS. In the case of the samples after 1 h of exposure to *E. coli* and the biofilm growth test, the first peak at 932.7 eV corresponding to Cu⁺¹ and/or Cu⁰ is visible. Additionally, a second peak at higher binding energy is visible (934.0 eV with a satellite at 944.0 eV) corresponding to Cu⁺². As in the case of the negative control, the Cu⁰ and the Cu⁺¹ components are evidenced in the Cu Auger line (L₃M₄₅M₄₅). The position of the Auger line (L₃M₄₅M₄₅) (Figure B.1 (b)) at 917.4 eV for the sample after the biofilm growth test is probably due to a major contribution of Cu (OH)₂ and/or Cu₂(SO)₄ (Cu²⁺).

The XPS Ni 2p_{3/2} core level spectra exhibits the same features in all cases: a peak at a binding energy of 856.0 eV and the corresponding satellite at 861.7 eV, showing the presence of Ni(OH)₂ in the surface layer (Figure B.1 (c)). A peak at a binding energy of 852.2 eV characteristic of Ni⁰ is also observed in the negative control and the sample after 1h of exposure to *E. coli*.

The N 1s spectrum recorded after 1 h of exposure to *E. coli* and to the biofilm growth test (Figure B.1 (d)) exhibits a major symmetric peak, centred at ~ 400 eV, as expected for non-protonated nitrogen like in the amine or amide groups of proteins. Besides, after 1h of exposure to *E. coli*, another component is observed at higher binding energy probably due to protonated nitrogen, e.g. ammonium ion. The C 1s signal obtained in the same conditions is shown in Figure B.1 (e). It can be fitted with three contributions: C₁, at a binding energy of 285.0 eV, assigned to C-C and C-H; C₂, at a binding energy of 286.4 eV, attributed to C-N and C-O single bonds; and C₃, at a binding energy of 288.3 eV, assigned to O=C-O and O=C-N (peptide bonds) bonds.

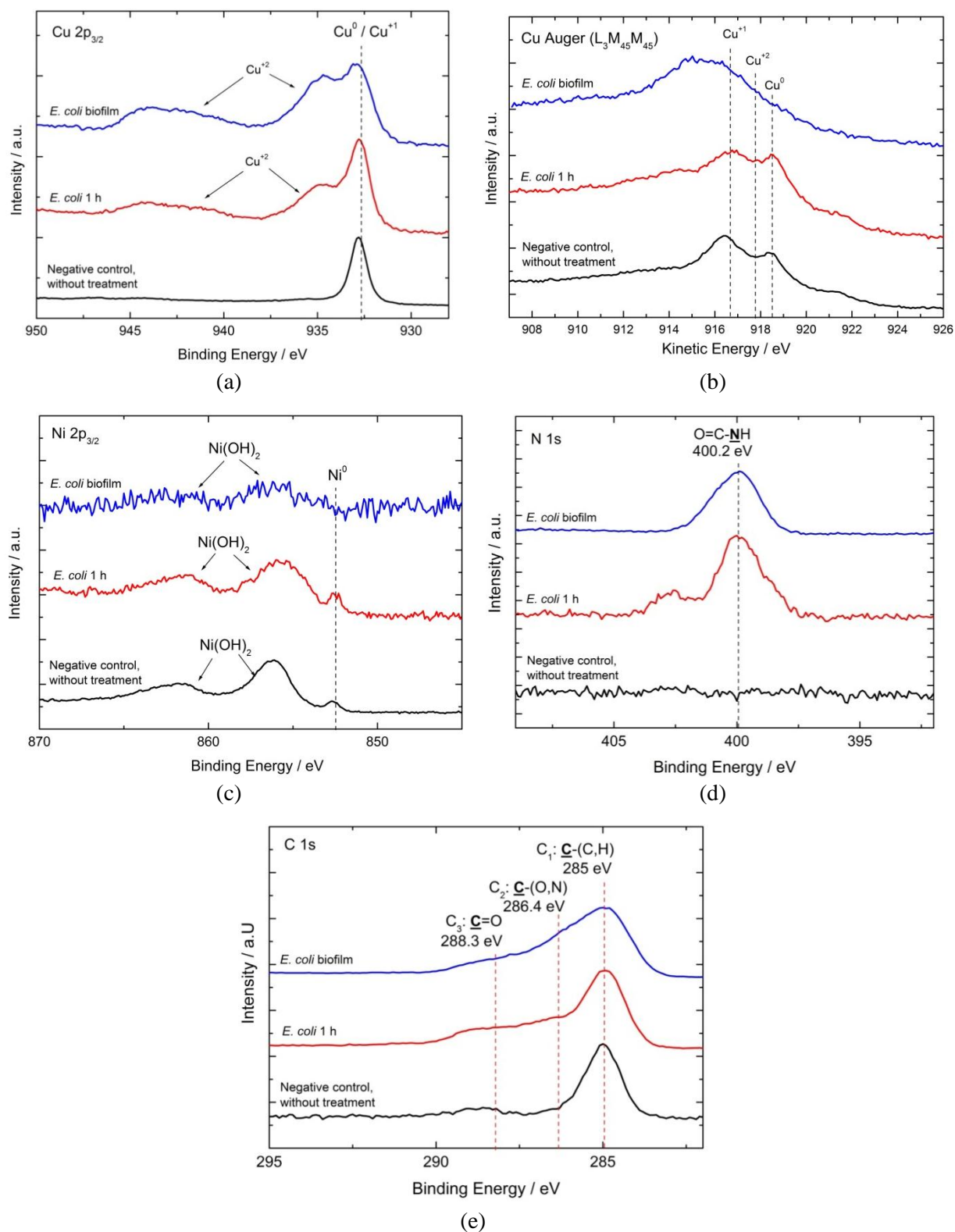


Figure B. 1: X-ray photoelectron spectroscopy (XPS) (a) Cu 2p_{3/2} core level spectra (b) Cu L₃M₄₅M₄₅ Auger lines (c) Ni 2p_{3/2} core level spectra (d) N 1s core level spectra and (e) C 1s core level spectra of 70Cu-30Ni alloy: negative control without treatment (without dehydration fixation procedure), 1 h of exposure to *E. coli* and *E. coli* biofilm. The intensity is expressed in arbitrary unit (a.u.).

Table B.1 compares the atomic compositions and oxide layer thickness of 70Cu-30Ni alloy obtained for the three conditions. It is observed that only in the case of the negative control without treatment (without dehydration and fixation procedure) and after 1 h of exposure to *E. coli*, the oxide layer thickness could be calculated, being of the same order in both cases (2.4 and 2.6 nm respectively) whereas in the case of the samples exposed to the biofilm growth test, the oxide layer could not be estimated by XPS. The content of oxidized nickel is decreased in the presence of bacteria. The lowest amount of oxidized Ni is observed after the biofilm growth test. The amount of Cu^{+2} compounds is high in the presence of the bacteria whereas no Cu^{+2} compounds are found in the negative control.

Table B. 1: Chemical composition and thickness of the surface oxide layer calculated from XPS data recorded for 70Cu-30Ni after experiments.

	Composition (at %)			Oxide layer thickness / nm
	% Cu^{+1}	% Cu^{+2}	% Ni^{+2}	
Negative control without treatment	58	0	42	2.4
<i>E. coli</i> 1 h	23	47	30	2.6
<i>E. coli</i> biofilm	35	61	4	Not measured by XPS

Carbon/nitrogen atomic ratios were calculated from the C 1s and N 1s XPS core level spectra and results were compared in Table B.2 to experimental atomic ratios values previously published for *E. coli* K-12¹. It is observed that the values obtained after 1 h of exposure to *E. coli* are more similar to the reference values, and the values obtained for the sample after biofilm growth test are different. This could indicate that after 1 h the bacteria is present on the surface, whereas in the case of the sample after biofilm growth test, a big amount of organic compounds (essentially nitrogen containing compound) is present. This difference may be explained by exopolymers generated by bacteria on the surfaces or decomposition of dead *E.coli* cells due to the biocide effect of Cu compounds.

¹ H. Latrache, N. Mozes, C. pelletier, P. Bourlioux. Chemical and physicochemical properties of Escherichia coli : variations among three strains and influence of culture conditions. Colloids and Surface B : Biointerfaces, vol. 2, 1994, pp. 47–56.

Table B. 2 : Atomic ratios calculated from the XPS N 1s and C 1s core level spectra recorded for the 70Cu-30Ni alloy after 1 h of exposure to *E. coli* and the biofilm growth test.

	C_1/N_{total}	C_2/N_{total}	C_3/N_{total}
Reference values for <i>E. coli</i> K-12^l	6.10	3.08	1.30
<i>E. coli</i> 1h	8.13	2.51	1.40
<i>E. coli</i> biofilm	3.21	1.43	0.67

Figure B.2 shows the ToF-SIMS depth profiles (negative ions) obtained for the 70Cu-30Ni alloy after three different conditions; the profiles obtained for the negative control without treatment were recorded with a sputtered area of $300 \times 300 \mu\text{m}^2$; whereas the others were recorded on an area of $700 \times 700 \mu\text{m}^2$. Figure B.2 (a) illustrates the profiles obtained for the negative control. These profiles are similar to the one obtained in FNSW (see Chapter III) and evidence the presence of an oxidized Ni layer covered by islands of oxidized Cu and Ni. Figure B.2 (b) shows the depth profiles of the sample after 1 h of exposure to *E. coli*. In this profile, a first region extended from 0 to 70s of sputtering and characterized by very intense oxidized signal (CuO_2^- , O^- , NiO_2^-) is assigned to a mixed Cu and Ni oxide layer, covering the metallic substrate. In addition, intense signals for the organic species are observed in this first region, indicating that a fraction of the surface is covered by an organic layer (EPS + bacteria). Then, the drastic decrease of the oxidized signals, in the second region, concomitantly with the increase of the metallic signal, indicates that the metal/oxide interface is reached (~ 70 s of sputtering). Nevertheless, the oxidized signals do not reach their minimum, indicating that an oxide film remains under the organic layer that partially covers the metallic substrate identified in the first region of the profile. The oxide film identified in this second region is assigned to the oxide covered by EPS that partially covers the metallic substrate after 1 h of exposure to *E. coli*. After ~ 300 s, one enters a third region that is characterized by a decrease of the oxidized signal without reaching their minimum intensity; an increase of the S^- , Cl^- , PO_2^- signals is also observed. This region corresponds to a third type of area on the substrate, which is assigned to the oxide film remaining under the bacteria fixed on the surface of the 70Cu-30Ni alloy. The slight increase of the oxidized signals, indicates that the bacteria are fixed on the oxide layer covering the metallic substrate. The increase of the S^- , Cl^- , PO_2^- signals at the bacteria/oxide interface would indicate that these species are involved in the adhesion of the bacteria on the oxide covering the metallic substrate. Finally, one enters the fourth region that is fully related to the metallic substrate.

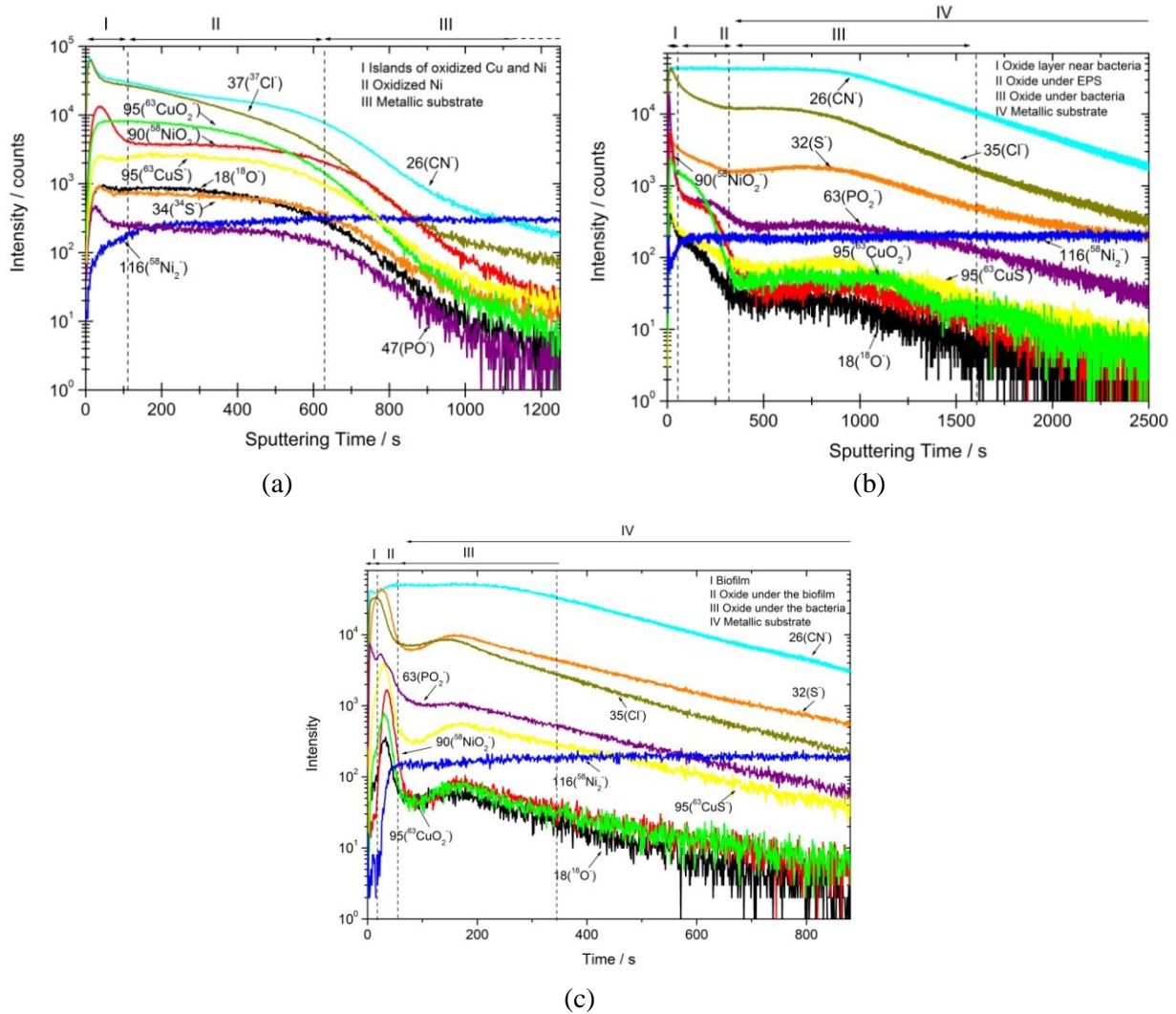


Figure B. 2: Characteristic Time-of-Flight Secondary Ions Mass Spectrometry (ToF-SIMS) depth profiles (negative ions) for 70Cu-30Ni alloy (a) negative control without treatment (dehydration and fixation procedure; sputtered surface area of $300 \times 300 \mu\text{m}^2$), (b) *E. coli* 1 h exposure, and (c) *E. coli* biofilm (sputtered surface area of $700 \times 700 \mu\text{m}^2$).

A similar distribution can be observed in Figure B.2 (c) for the sample after the biofilm growth test except that the substrate is fully covered by the biofilm that corresponds to the first region on the profile. Thus, the second region corresponds to the oxide film covered by the EPS that forms the biofilm, the increase of the oxidized signals in the third region corresponds to the oxide film covered by the bacteria and the fourth region corresponds to the metallic substrate.

Ratios between the maximum intensity of the oxidized Cu and Ni signals (CuO_2^- and NiO_2^-) were calculated in the different regions detected on the ToF-SIMS depth profile,

corresponding to the oxide non-covered by the bacteria and the oxide under the bacteria, in order to detect changes of Cu and Ni in the oxide layer. The results indicate that after 1 h of exposure to *E. coli*, the content of Cu in the oxide layer is higher with respect to the content of Ni, compared to the oxide non-covered (Table B.3). Therefore, the presence of bacteria induces higher amount of oxidized Cu and lower oxidized Ni.

Table B. 3: Ratios between the maximum intensity of the CuO_2^- and NiO_2^- signals obtained from the ToF-SIMS experiments of 70Cu-30Ni alloy after 1 h of exposure to *E. coli* and the biofilm growth test.

	Oxidized Cu/Oxidized Ni	
	Oxide non-covered	Oxide under bacteria
<i>E. coli</i> 1h	0.43	1.22
<i>E. coli</i> biofilm	-	1

In this study, it is interesting to observe that the 70Cu-30Ni substrate is still covered by an oxide film even after exposure to *E. coli* bacteria during 1 h. According to the ToF-SIMS $\text{CuO}_2^-/\text{NiO}_2^-$ intensity ratio, the oxide film is modified under the bacteria and seems to be enriched in Cu.

B.2. 304L stainless steel

The XPS spectra of Fe $2p_{3/2}$, Cr $2p_{3/2}$, Ni $2p_{3/2}$ C 1s and N 1s are shown in Figure B.3.

The Fe $2p_{3/2}$ core level spectra, shown in Figure B.3 (a), illustrate in all the cases the presence of the characteristic metal peak Fe^0 located at the binding energy of ~ 706.7 eV. Additionally, another peak at higher binding energy (~ 710.5 eV) indicates the presence of Fe^{+3} [16], [107], [152][16], [107], [152][16], [107], [152][16], [107], [152][16], [107], [152][16], [107], [154].

Figure B.3 (b) illustrates the Cr $2p_{3/2}$ core level spectra of 304L stainless steel. In the cases, the presence of the metal contribution Cr^0 at the binding energy of ~ 573.8 eV is observed. Additionally, another peak located at the binding energy of ~ 576.2 eV is also visible, and corresponds to the formation of Cr^{+3} related to the presence of Cr_2O_3 , but also to $\text{Cr}(\text{OH})_3$, this is more evident for the sample after 1h of exposure to *E. coli* and in the presence of the biofilm growth. The Ni $2p_{3/2}$ core level spectra shows only the presence of the metallic component Ni^0 , and not any oxidation state of nickel.

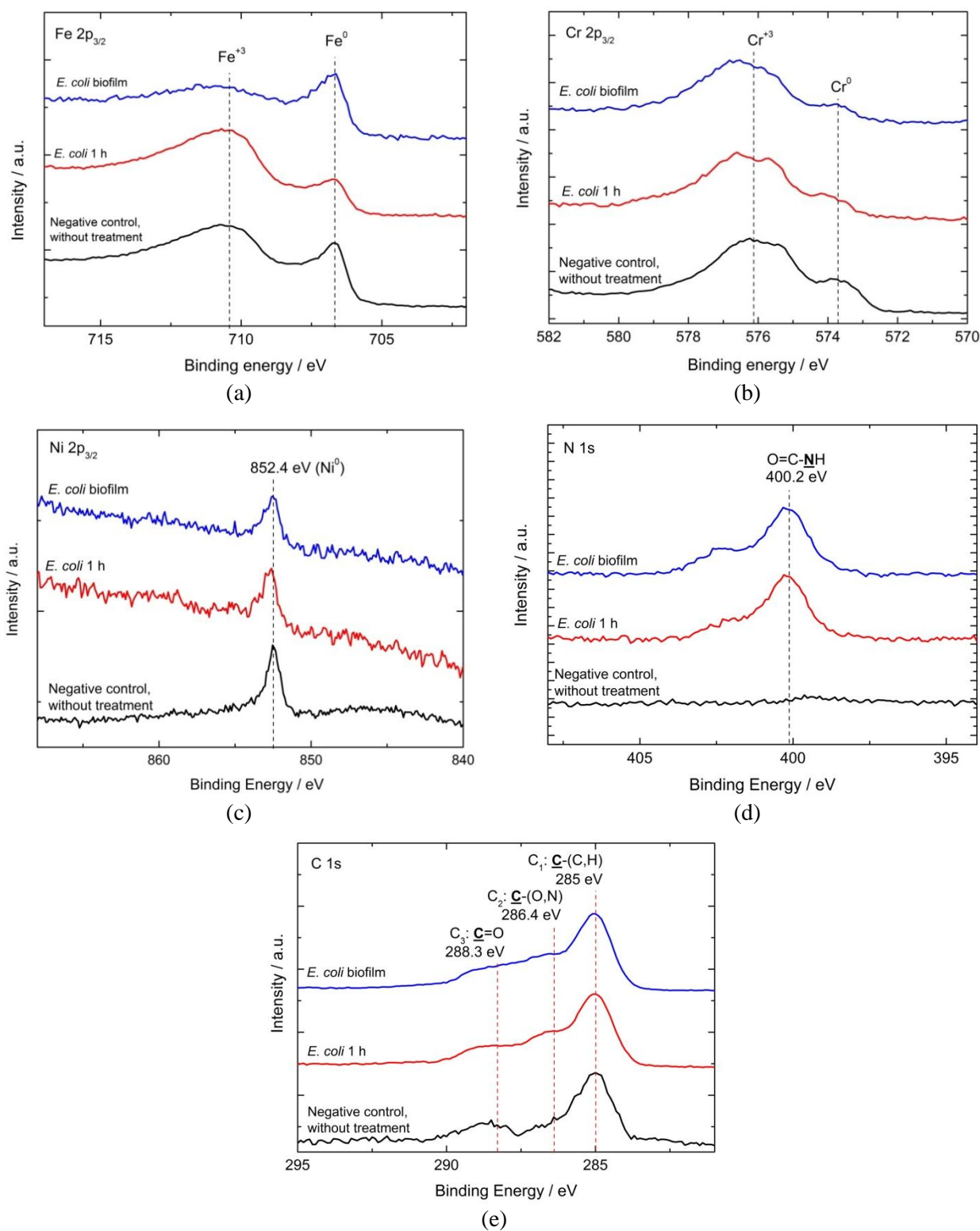


Figure B. 3: X-ray photoelectron spectroscopy (XPS) (a) Fe $2p_{3/2}$ core level spectra (b) Cr $2p_{3/2}$ core level spectra (c) Ni $2p_{3/2}$ core level spectra (d) N 1s core level spectra and (e) C 1s core level spectra of 304L stainless steel: negative control without treatment (without dehydration fixation procedure), 1 h of exposure to *E. coli* and *E. coli* biofilm. The intensity is expressed in arbitrary unit (a.u.).

Similarly to what is observed with 70Cu-30Ni alloy, the N 1s spectrum recorded after 1 h of exposure to *E. coli* and to the biofilm growth test (Figure B.3 (d)) exhibits a major symmetric peak, centred at ~ 400 eV, as expected for non-protonated nitrogen like in the amine or amide groups of proteins. Furthermore, the second component observed at higher binding energy is present in both cases probably due to protonated nitrogen, *e.g.* ammonium ion. The C 1s signal obtained in the same conditions is shown in Figure B.3 (e). It can be fitted with the three characteristic contributions: C₁, at a binding energy of 285.0 eV, C₂, at a binding energy of 286.4 eV, and C₃, at a binding energy of 288.3 eV.

According to the ToF-SIMS information, presented in Chapter V, the oxide layer formed on 304L stainless steel is a duplex film enriched in oxidized Fe in the outer part and in oxidized Cr in the inner part at the oxide/metal interface. Besides, no oxidized Ni was detected by XPS, and, thus, it was not considered in the calculation of the oxide layer thickness. The equivalent thickness of the duplex oxide layer formed on the alloy and the elemental composition beneath the oxide layer was calculated from XPS data, considering the intensities of Cr, Fe and Ni in the metallic substrate, and it was considered only the intensity of Cr for the inner part and Fe in the outer part of the duplex oxide layer (the contribution of Fe and Cr forming the inner and outer layer, respectively, was neglected). The results are presented in Table B.4.

Table B. 4: Chemical composition of the surface film calculated from XPS data recorded for 304L stainless steel after experiments.

	Oxide layer thickness / nm			Atomic composition beneath the oxide layer		
	Fe ⁺³ enriched outer layer	Cr ⁺³ enriched inner layer	Total	Fe	Cr	Ni
Negative control without treatment	0.9	1.1	2.0	77	6	17
<i>E. coli</i> 1 h	1.0	1.3	2.3	81	6	13
<i>E. coli</i> biofilm	0.9	1.3	2.2	77	6	17

The total thickness is similar in all cases, and thus, apparently no significant effect of bacteria and biofilm on this is observed. Nevertheless, observing the XPS spectra of Fe, the peak corresponding to oxidized Fe is more depressed in the case of the sample with biofilm than

the negative control and the sample after 1 h of immersion. Therefore, the oxide layer thickness is not the same and, thus, the model considered for the calculations is not a good representation of the system, particularly in the presence of bacteria.

Similarly to what is done with 70Cu-30Ni alloy, carbon/nitrogen atomic ratios were calculated from the C 1s and N 1s XPS core level spectra. The results are presented in Table B.5.

Table B. 5: Atomic ratios calculated from the XPS N 1s and C 1s core level spectra recorded for 304L stainless steel after 1 h of exposure to *E. coli* and the biofilm growth test.

	C_1/N_{total}	C_2/N_{total}	C_3/N_{total}
Reference values for <i>E. coli</i> K-12¹	6.10	3.08	1.30
<i>E. coli</i> 1h	8.97	3.77	2.52
<i>E. coli</i> biofilm	7.79	3.39	2.26

Table B.5 compares these values to the atomic ratios obtained experimentally in previous works for *E. coli* K-12. In this material, the values obtained after 1 h of exposure and after the biofilm growth test are close to the reference values obtained for *E. coli* K-12, indicating in both cases the presence of bacteria on the surface. Slight difference may be explained by exopolymers generated by the bacteria on the surface.

Figure B.4 shows the ToF-SIMS depth profiles (negative ions) obtained for the 304L stainless steel samples under the three different conditions (negative control, 1h of exposure to *E. coli* and biofilm). As in the case of 70Cu-30Ni alloy, the profiles obtained for the negative control without treatment were recorded on a sputtered area of 300 x 300 μm^2 ; the others were recorded on a sputtered area of 700 x 700 μm^2 . Figure B.4 (a) illustrate the profiles obtained for the negative control without treatment. This profile illustrates the presence of two main regions that correspond to the oxide layer, which is a duplex oxide film with an outer Fe-rich oxide layer and an inner Cr-rich oxide layer (see Chapter V) and the metallic substrate. Figure B.4 (b) and (c) show the depth profiles (negative ions) of the sample after 1 h of exposure to *E. coli* and the *E. coli* biofilm growth test, respectively. Whatever the conditions, three main regions are distinguished in the profiles. The first region evidences the area that is not covered by the EPS and/or bacteria. The maximum intensity of all oxidized signals (FeO_3^- , CrO_3^- , NiO_2^- , O^-) indicate that an oxide film remains in the free from bacteria. As one probes deeper into the substrate, the entrance into a second region is evidenced by the decrease of all oxidized signals concomitantly with the increase of the metallic substrate signal (Ni_2^- , Fe_2^- ,

Cr_2^-). It is important to notice that in the second region, one observes a wave in the oxidized signals. This wave is assigned to the oxide film that remains under the bacteria initially attached to the surface and that have been sputtered away. Thus, as observed on 70Cu-30Ni samples, the bacteria adhere to an oxide layer and not directly to the metallic substrate. The increase of the S^- , PO_4^{2-} and Cl^- signals just before the wave observed on the oxidized signals allow us to conclude, as for the 70Cu-30Ni substrate, that these species are involved in the bacteria adhesion, which leave the oxide film on the metallic substrate.

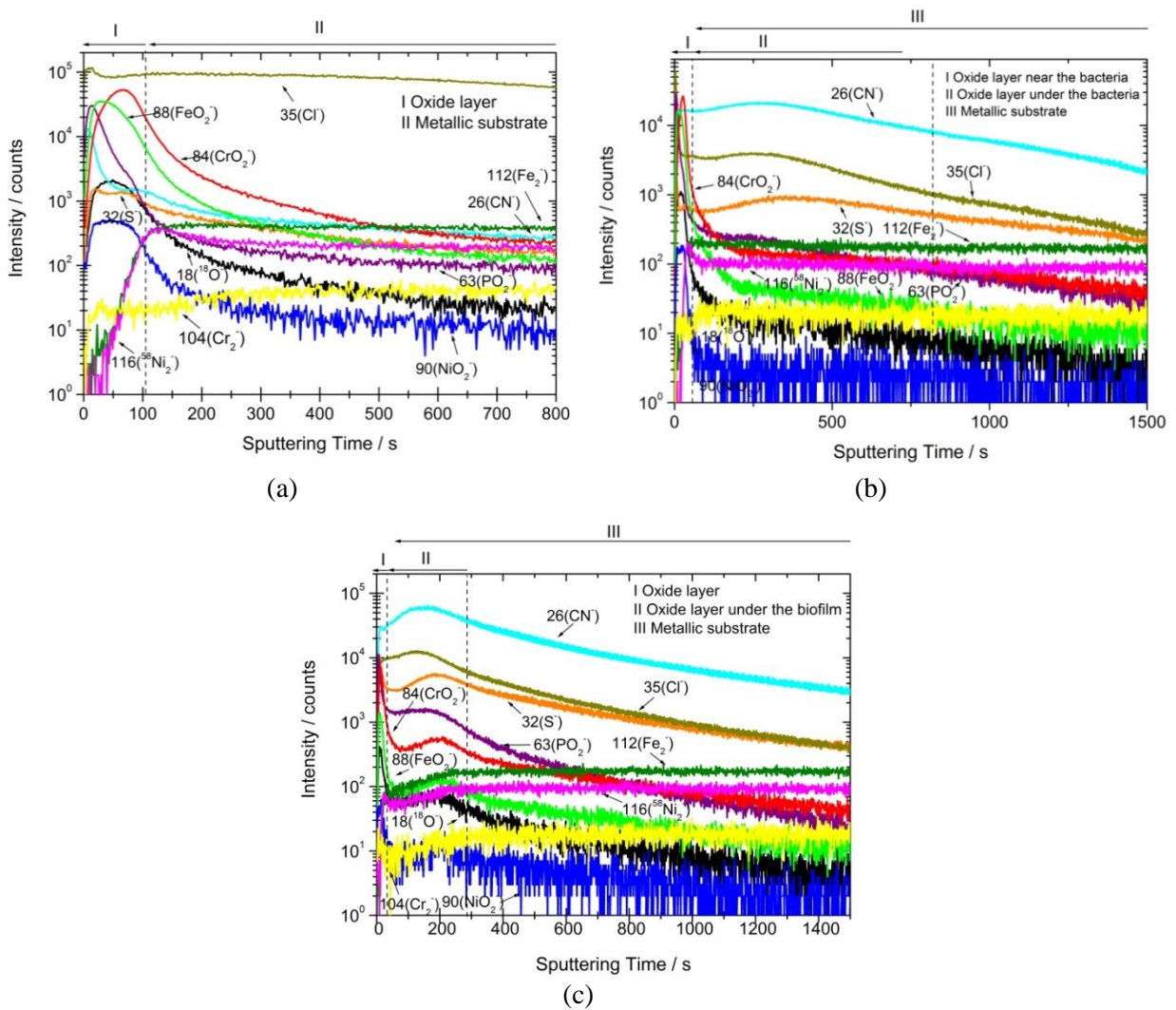


Figure B. 4: Characteristic Time-of-Flight Secondary Ions Mass spectrometry (ToF-SIMS) depth profiles (negative ions) of 304L stainless steel: (a) negative control without treatment (dehydration and fixation procedure; sputtered surface area of $300 \times 300 \mu\text{m}^2$), (b) *E. coli* 1 h exposure, and (c) *E. coli* biofilm (sputtered surface area of $700 \times 700 \mu\text{m}^2$).

Ratios between the maximum intensity of the oxidized Fe and Cr signals (FeO_2^- and CrO_2^-) were also calculated in the two different regions detected on the ToF-SIMS depth profile, corresponding to the oxide non-covered and the oxide under the bacteria and/or biofilm, in order to detect changes in the Fe and Cr composition in the oxide layer (Table B.6). The results indicate that after 1 h of exposure to *E. coli*, the content of Fe in the oxide film decreases with respect to the content of Cr, in the oxide located under the biofilm and/or bacteria. On the other hand, in the case of the sample after biofilm growth test, the oxide film seems to be even more enriched in Cr than the one observed after 1h of exposure to *E.coli* bacteria. The modification of the composition of the oxide film under the bacteria can be the result of the consumption of the Fe contained in the oxide film by the bacteria (Fe is an essential nutriment for the *E.coli* bacteria), since *E.coli* bacteria use a variety of systems to acquire iron from the surrounding environment (*E.coli* is known as a siderophore bacteria). Comparing the results obtained in the presence of bacteria with the result observed for the negative control (ratio = 0.66), it is observed that after 1 h of exposure to the bacteria, the ratio of the area not covered is similar to the ratio of the negative control. Furthermore, after 24 h (sample after biofilm growth) the ratio of this non-covered area is much lower, indicating an influence of the bacteria located close to these areas.

Table B. 6: Ratios between the maximum intensities of the FeO_2^- and CrO_2^- signals obtained from the ToF-SIMS measurements for 304L stainless steel after 1 h of exposure to *E. coli* and the biofilm growth test.

	Oxidized Fe/Oxidized Cr	
	Oxide not covered by bacteria	Oxide under biofilm and/or bacteria
<i>E. coli</i> 1h	0.63	0.34
<i>E. coli</i> biofilm	0.20	0.26

B.3. Titanium

The following core levels were recorded: Ti 2p, Ni 2p, O 1s, C 1s, and N 1s. As mentioned in Chapter V, the Ti 2p_{3/2} core level spectra can be decomposed in 4 peaks attributed to the different oxidation states of Ti. The peak located at the binding energy of 453.6 ± 0.2 eV corresponds to Ti^0 , 455.2 ± 0.1 eV to Ti^{+2} , 457.2 ± 0.1 eV to Ti^{+3} and 458.9 ± 0.2 eV to Ti^{+4} . However, due to an overlapping of the contribution of Ti^0 in Ti 2p_{1/2} with Ti^{+4} in Ti 2p_{3/2} the

whole Ti 2p core level was decomposed (Figure B.5 (a)). It is observed that in all the cases the presence of the metal component (Ti^0 at ~ 453.6 eV) is observed. Additionally, the decomposition of the different peaks evidences the presence of the suboxides (Ti^{+2} and Ti^{+3}), and not only Ti^{+4} . Nevertheless, the major contribution corresponds to Ti^{+4} , associated with the formation of TiO_2 , characteristic of the passive layer usually formed on Ti.

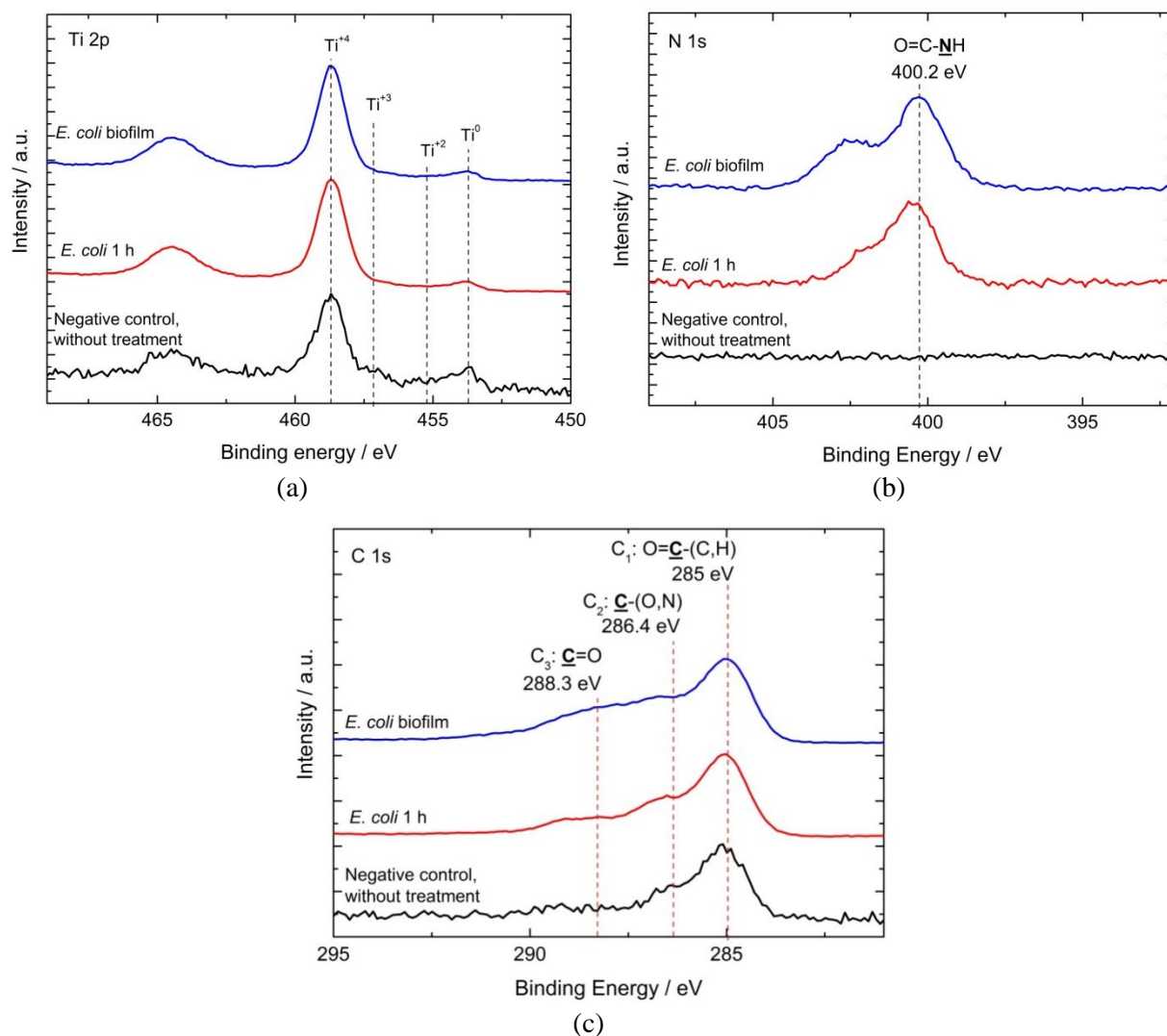


Figure B. 5: X-ray photoelectron spectroscopy (XPS) (a) Ti 2p core level spectra (b) N 1s core level spectra and (c) C 1s core level spectra of Ti: negative control without treatment (without dehydration fixation procedure), 1 h of exposure to *E. coli* and *E. coli* biofilm. The intensity is expressed in arbitrary unit (a.u.).

The N 1s spectrum recorded after 1 h of exposure to *E. coli* after biofilm growth (Figure B.5 (b)) exhibits the major symmetric peak, centred at ~ 400 eV, as expected for non-protonated nitrogen like in the amine or amide groups of proteins. Furthermore, the second component

observed at higher binding energy is present in both cases probably due to protonated nitrogen, *e.g.* ammonium ion, as for 304L stainless steel. The C 1s signal obtained in the same conditions is shown in Figure B.5 (c). It can be fitted with the three characteristic contributions: C₁, at a binding energy of 285.0 eV, C₂, at a binding energy of 286.4 eV, and C₃, at a binding energy of 288.3 eV.

Table B.7 shows the composition of suboxides and TiO₂ forming the oxide layer, as well as the oxide layer thickness calculated considering the total oxide as TiO₂. No significant differences were observed in the suboxides composition. However, it is observed that the highest oxide layer thickness is observed for the *E. coli* biofilm sample, followed by the negative control and *E. coli* 1h. The lowest oxide layer thickness was observed in the negative control without treatment.

Table B. 7: Oxide layer composition (oxidation state), and oxide layer thickness estimated by assuming that the total oxidized Ti (Ti⁺⁴, Ti⁺³ and Ti⁺²) corresponds to Ti⁺⁴.

	Oxide layer composition / at. %			Oxide layer thickness / nm
	Ti ⁺⁴	Ti ⁺³	Ti ⁺²	
Negative control without treatment	82	11	7	3.4
<i>E. coli</i> 1 h	85	12	3	4.5
<i>E. coli</i> biofilm	87	8	5	5.6

The carbon/nitrogen atomic ratios were calculated from the C 1s and N 1s XPS core level spectra, and the values were compared to those atomic ratios obtained experimentally in previous works for *E. coli* K-12. According to Table B.8, some deviations can be observed with respect to the reference values, especially for the sample with a biofilm, which may be explained by the presence of exopolymers on the surface, produced by the bacteria.

Table B. 8: Atomic ratios calculated from the XPS N 1s and C 1s core level spectra recorded for Ti after 1 h of exposure to *E. coli* and the biofilm growth test.

	C ₁ /N _{total}	C ₂ /N _{total}	C ₃ /N _{total}
Reference values for <i>E. coli</i> K-12¹	6.10	3.08	1.30
<i>E. coli</i> 1h	10.35	4.33	1.72
<i>E. coli</i> biofilm	8.03	4.07	2.68

Figure B.6 shows the ToF-SIMS depth profiles (negative ions) obtained with Ti. As in the case of 70Cu-30Ni alloy and 304 L stainless steel, the profiles obtained for the negative control without treatment were recorded on a sputtered area of $300 \times 300 \mu\text{m}^2$, whereas the others were recorded on a sputtered area of $700 \times 700 \mu\text{m}^2$.

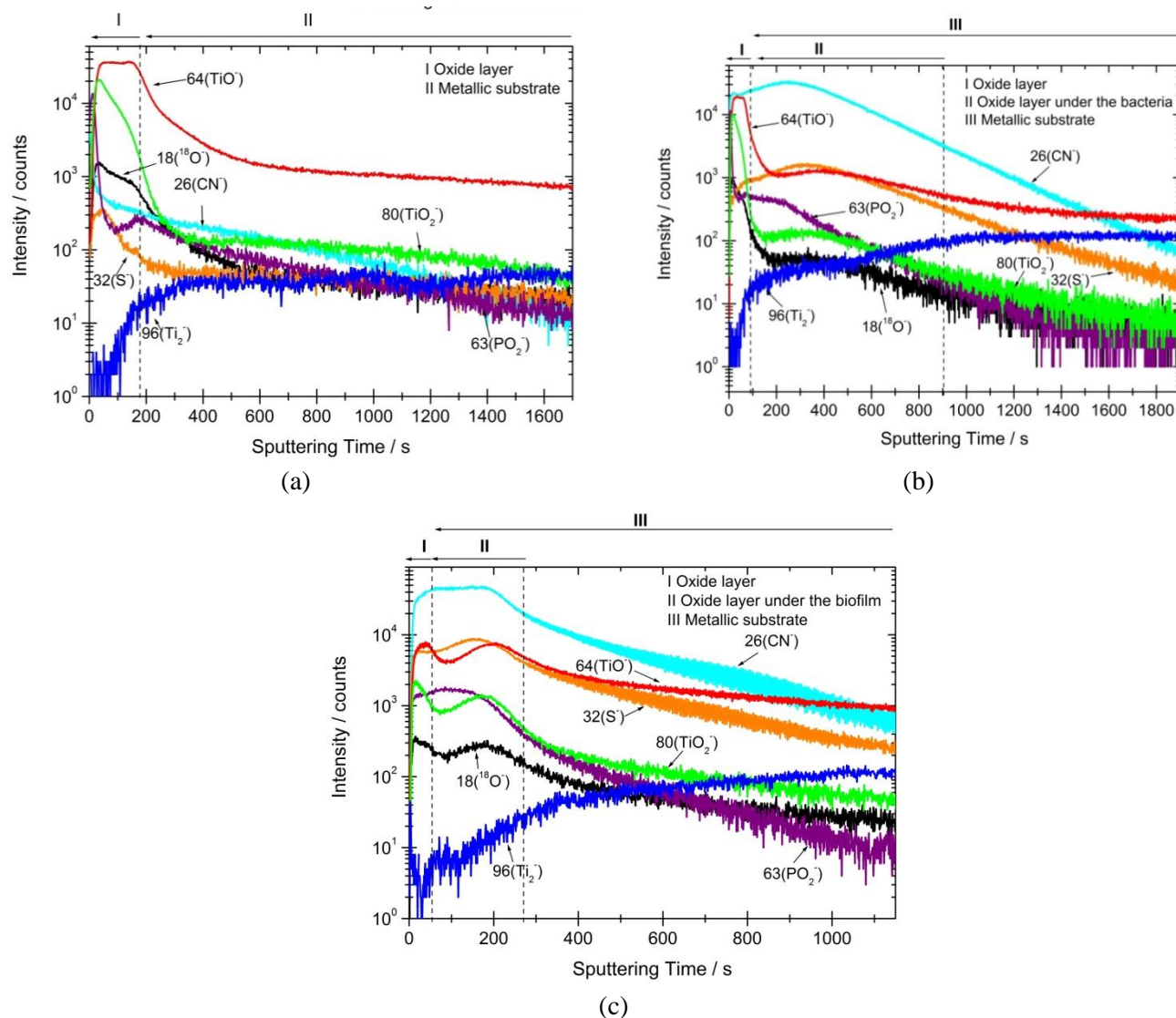


Figure B. 6: Characteristic Time-of-Flight Secondary Ions Mass Spectrometry (ToF-SIMS) depth profiles (negative ions) of Ti: (a) negative control without treatment (dehydration and fixation procedure; sputtered surface area of $300 \times 300 \mu\text{m}^2$), (b) *E. coli* 1 h exposure, and (c) *E. coli* biofilm (sputtered surface area of $700 \times 700 \mu\text{m}^2$).

Figure B.6 (a) illustrates the profile obtained for the negative control without treatment. This profile shows the presence of two regions. A first region corresponding to the oxide layer of Ti^{+4} and the suboxides, being the Ti^{+4} always mainly in the outer part of the oxide. The second region corresponds to the metallic substrate. Figure B.6 (b) and (c) show the depth profiles of

the sample after 1 h of exposure to *E. coli* and after *E. coli* biofilm growth, respectively. As in the case of 304L stainless steel, three main regions can be distinguished whatever the conditions. The first region evidences the area non-covered by the EPS and/or bacteria. The second region is evidenced by the decrease of all oxidized signals concomitantly with the increase of the metallic substrate signal (~100 s of sputtering). A slight increase (shoulder) of the oxidized signals is observed on the profile recorded after exposure to bacteria. This slight increase of the oxidized signals (~300 s and ~200 s of sputtering for Ti sample exposed 1 h and 24 h to bacteria, respectively) is assigned to the oxide film that remains under the bacteria that were attached to the surface. Finally, the third region is related to the metallic substrate. As previously discussed on 70%Cu – 30%Ni and 304L stainless steel samples, the increase of the S^- , PO_2^- and Cl^- signal just before the wave observed on the oxidized signals, and associated to the oxide under the bacteria, also indicates that these species are involved in the bacteria adhesion.

B.4. Organic layer

The purpose of this section is to characterise the organic film present on the surface of 70Cu-30Ni alloy, 304L stainless steel, and Ti, without having the contribution of the bacteria.

The main biomolecule contributions can be distinguished and, therefore, the composition can be estimated in terms of proteins, polysaccharides and lipids (see details in Chapter IV, V and Annex A). The elemental molar concentrations, obtained from XPS spectra, were converted into weight percentages of these chemical entities (g/100 g of adlayer).

In order to estimate the biomolecules composition of the biofilm present on the surfaces, some assumptions had to be done. It has been mentioned before that the water used for the experiments was probably contaminated, and thus, it was considered that all the organic compounds already present on the water was consumed by the bacteria. This would mean that the C and N signals coming from XPS data are attributed to the bacteria and the biofilm. A second assumption to be done is that the amount of bacteria is the same after 1 h and after 24 h (biofilm growth test). This was probed for the 316 stainless steel in a previous work (data not published), but it has to be proved for 304L stainless steel and Ti. This assumption is probably wrong for 70Cu-30Ni alloy, due to the biocide effect of Cu, and, thus, only the results of the negative control are presented below.

Finally, if we consider that after 1 h of exposure to *E. coli*, all the C and N (organic) detected by XPS corresponds to the bacteria (low EPS produced after 1 h compared to 24 h), then it is possible to subtract the contribution of C and N corresponding to the bacteria in the sample after 24 h (biofilm growth test), and, in this way it would be possible to determine the biomolecules composition of the biofilm.

Figure B.7 illustrates the XPS results, after subtraction of the C and N contribution corresponding to bacteria, and converted into weight percentages in the form of a ternary composition diagram for the samples after the biofilm growth test. The corners of this triangle represent 100 wt % of amide, 100 wt % of CH₂ and 100 wt % of additional carbon and oxygen (C_{add} + O_{add}). In table B.9 are compared the biomolecules composition of the three different materials for the negative control and for the biofilm sample without the bacteria contribution.

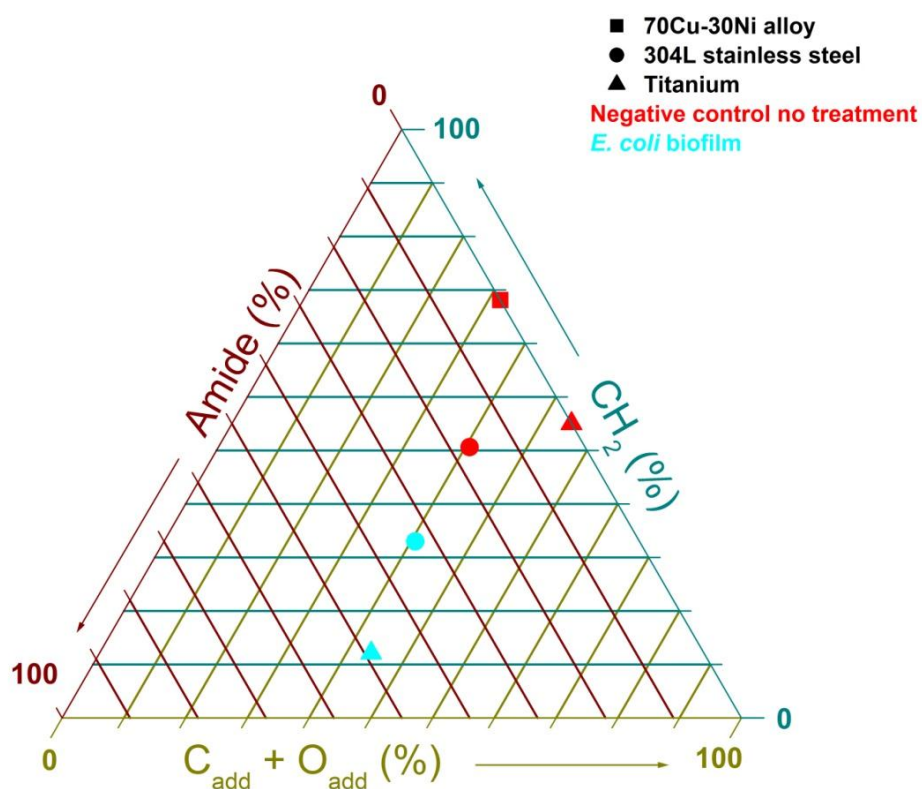


Figure B. 7: Biomolecules composition of the surfaces for the negative control and after the biofilm growth test considering the subtraction of the bacteria contribution. Relative mass concentration of amide (HC-NH-(C=O)), hydrocarbon CH₂, and other oxygen-containing molecules (C_{add} + O_{add}), including polysaccharides. 70Cu-30Ni alloy, 304L stainless steel and Ti.

Table B. 9: Biomolecules composition of surface. Relative mass concentration of amide (HC-NH-(C=O)), hydrocarbon CH₂, and other oxygen-containing molecules (C_{add} + O_{add}), including polysaccharides. Atomic composition of the surface oxide layer calculated from XPS data recorded for 70Cu-30Ni alloy, 304L stainless steel and Ti after biofilm growth test.

	% Amide			% CH ₂			% C _{add} + O _{add}		
	70Cu-30Ni alloy	304L stainless steel	Ti	70Cu-30Ni alloy	304L stainless steel	Ti	70Cu-30Ni alloy	304L stainless steel	Ti
Negative control without treatment	0	17	0	71	46	50	29	37	50
<i>E.coli</i> biofilm	-	33	49	-	30	11	-	37	40

The presence of proteins was minimal in the negative control without treatment for all the metallic materials; whereas hydrocarbons, related to lipids, were the highest components in 70Cu-30Ni alloy and 304L stainless steel. Similar contribution of hydrocarbon and additional carbon and oxygen were found in the case of Ti.

Comparing the 304L stainless steel and Ti samples containing biofilm, it is observed in Figure B.7 that 304L stainless steel is located almost in the middle of the triangle, indicating equal contribution of proteins, hydrocarbons (like lipids) and additional carbon and oxygen (commonly related to polysaccharides). On the other hand, Ti contains higher amount of proteins, followed by additional carbon and oxygen, and finally lipids.

If these results are compared to those obtained with TB EPS extracted from *Pseudomonas NCIMB 2021*, it is observed that similar results are observed in the case of 304L stainless steel, where similar percentages of proteins and hydrocarbons (38 % amide and 37% CH₂) and slightly lower additional carbon and oxygen concentration (25 %) were found

In the case of Ti in the presence of TB EPS of *Pseudomonas NCIMB 2021*, proteins are also dominant in the adlayer (51 % amide), and the contributions of hydrocarbons (27 % CH₂) and additional carbon and oxygen (22 % C_{add} + O_{add}) are similar.

B.5. Discussion and conclusions

For 70Cu-30Ni alloy it was observed that only in the case of the negative control without treatment (without dehydration and fixation procedure) and after 1 h of exposure to *E. coli*, the oxide layer thickness could be calculated (2.4 and 2.6 nm respectively) whereas the oxide layer was very thick in the case of the samples exposed to the biofilm growth test. Besides, the content of oxidized nickel is decreased in the presence of bacteria and biofilm, the lowest amount of oxidized Ni being found for the sample after biofilm growth. The amount of Cu⁺² compounds is the highest in the presence of the biofilm whereas no Cu⁺² compounds are found in the negative control. Results obtained by ToF-SIMS, where ratios between the maximum intensity of the oxidized Cu and Ni signals (CuO₂⁻ and NiO₂⁻) were calculated in the different regions detected on the ToF-SIMS depth profile (corresponding to the oxide non-covered by the bacteria and the oxide under the bacteria), indicate that after exposure to *E. coli*, the content of Cu in the oxide layer is higher with respect to the content of Ni, compared to the oxide non-covered.

Additionally, ToF-SIMS results evidenced the presence of three main areas on the 70Cu-30Ni surface after 1 h of exposure to *E.coli*. The first area is assigned to a mixed Cu and Ni oxide layer non-covered by bacteria or biofilm. Then the second area is assigned to the oxide covered by EPS that partially covers the metallic substrate. Finally, the third area is assigned to the oxide film remaining under the bacteria fixed on the surface of the 70Cu-30Ni alloy. A similar distribution can be observed in the case of the sample after the biofilm growth except that the substrate is fully covered by the EPS.

It would be interesting to perform further experiments in order to correlate the Cu^{+2} increase and the known biocide effect of Cu on the bacteria.

Contrary to what is observed in the case of 70Cu-30Ni alloy, in 304L stainless steel and Ti is evidenced the presence of bacteria on the surface after 1 h of exposure to *E. coli* and after the biofilm growth test. Therefore, the effect of the organic compound coming from the contaminated water was not strongly observed in the case of 304L stainless steel and Ti. Besides, the bacteria seem to have an effect on the oxide layer thickness of Ti, which increase with the presence of bacteria and the exposure time.

ToF-SIMS results indicated that after 1 h of exposure to *E. coli*, the content of Fe in the oxide film decrease with respect to the content of Cr, in the oxide located under the biofilm and/or bacteria, whereas in the case of the sample after biofilm growth test, the content of Fe and Cr in the oxide film remain almost invariable in both cases (non-covered and covered by the bacteria and/or biofilm).

Furthermore, enrichment on Cr is observed when comparing the exposure time to *E. coli*. It has been shown in a previous work with 316 stainless steel that *E. coli* reduce Fe^{+3} in Fe^{+2} , and that Fe^{+2} goes then to the solution, which could be an explanation to this Cr enrichment.

ToF-SIMS results also evidenced, in both conditions, the presence of two main areas on the surface: a) an area non-covered by the EPS and/or bacteria, and b) an area assigned to the oxide film that remains under the bacteria that are fixed on the surface. Similar results were obtained in the case of Ti.

Finally by ToF-SIMS it was demonstrated that S, Cl, P species were located at the bacteria/oxide interface in the three materials indicating that these species could be involved in the adhesion of the bacteria on the oxide covering the metallic substrate.

On the other hand, the composition of the biofilm produced by the bacteria depends on the nature of the metallic substrate. More proteins were observed on Ti than on the 304L stainless steel and this is also observed in the case of the TB EPS extracted from *Pseudomonas NCIMB 2021*, previously studied. However, the composition of the biofilm depends on the kind of bacteria used.

Further experiments need to be done in order to confirm the results obtained and eliminate the assumptions considered for the analysis of these data.

List of Figures**Chapter I**

Figure I. 1: Classification of cooling water systems [1].	2
Figure I. 2: Classification of heat exchangers [7].	3
Figure I. 3: Interrelation between the different problems in cooling circuits [1].	6
Figure I. 4: Bacterial interaction in biofilms [25], [26].	11
Figure I. 5: Classification scheme of living organisms.	13
Figure I. 6: Classification of bacteria according to their cell wall structure: gram positive/gram negative.	14
Figure I. 7: Microbial growth curves.	15
Figure I. 8: EPS matrix: a) types of physico-chemical interactions present in the EPS matrix; b) EPS categorization [55], [60].	19
Figure I. 9: Different conformations of bovine serum albumin (BSA).	29

Chapter II

Figure II. 1: Disk electrodes, cut from real condenser tubes, and sample holder used for the measurements in static conditions, and under flow and stirring.	32
Figure II. 2: Rotating ring electrode (RRE) used for the measurements in well-controlled hydrodynamics.	33
Figure II. 3: Schematic drawing of the used EPS extraction procedure [87].	36
Figure II. 4: (a) <i>Pseudomonas</i> NCIMB 2021 culture after 3 days of growth and before the EPS extraction; (b) separation of loosely bound EPS from tightly bound EPS after the centrifugation step.	37
Figure II. 5: (a) Filtration of the supernatant obtained after centrifugation; (b) dialysis step using Spectra/Por 3.5 kDa dialysis tubing.	38
Figure II. 6: a) Cell pellet obtained after centrifugation; and b) tightly bound EPS during Dowex treatment.	38
Figure II. 7: Purification and concentration of tightly bound EPS using Amicon tubes.	39
Figure II. 8: Pie chart illustrating the weight percent of biomolecules for: (a) TB EPS and (b) LB EPS.	40

Figure II. 9: Schematic drawings of different cell configurations: a) 2-electrode; b) 3-electrode; and c) 4-electrode cell design.	41
Figure II. 10: Different electrochemical cells used in this work: a) static conditions, b) under flow and stirring and c) using the rotating ring electrode.	43
Figure II. 11: EC-Lab SP-200 system from Bio-Logic.	44
Figure II. 12: Sinusoidal AC potential with the current response phase shifted.	48
Figure II. 13: Lissajous plots for a system with potential perturbation amplitude dE	48
Figure II. 14: Graphical representations commonly used in EIS: a) Nyquist plot, and b) Bode plots [26].	50
Figure II. 15: Diagrams of the Auger process (left) and the photoelectric process (right).	54
Figure II. 16: Schematic drawing of an XPS spectrometer.	55
Figure II. 17: Schematic drawing of the secondary ion emission process initiated by the impact of the primary ions [113].	58
Figure II. 18: Schema illustrating the sputter-depth process.	60

Chapter III

Figure III. 1: (a) Cathodic and (b) anodic polarisation curves of 70Cu-30Ni after 1 h of immersion at E_{corr} in aerated artificial seawater and filtered natural seawater. Scan rate: $0.5 \text{ mV}\cdot\text{s}^{-1}$	64
Figure III. 2: Experimental impedance diagrams in the complex plane (Nyquist diagrams) of 70Cu-30Ni plotted at E_{corr} after 1 h of immersion in artificial seawater and filtered natural seawater.	65
Figure III. 3: (a) SEM image; and EDS analysis of the 70Cu-30Ni tube just after polishing: (b) Cu and Ni distribution, (c) Cu distribution, and (d) Ni distribution.	66
Figure III. 4: Layer model assumed for the analysis of XPS data (mixed oxide layer covering the metallic substrate).	67
Figure III. 5: (a) X-ray photoelectron spectroscopy (XPS) Cu $2p_{3/2}$ core level spectra, and (b) Cu $L_3M_{45}M_{45}$ Auger lines of 70Cu-30Ni after polishing, after 1 h of immersion at E_{corr} in static aerated artificial seawater and in filtered natural seawater. The intensity is expressed in arbitrary unit (a.u.).	71
Figure III. 6: X-ray photoelectron spectroscopy (XPS) Ni $2p_{3/2}$ core level spectra of 70Cu-30Ni alloy after polishing, after 1 h of immersion at E_{corr} in static aerated artificial seawater and in filtered natural seawater. The intensity is expressed in arbitrary unit (a.u.).	72

Figure III. 7: Characteristic Time-of-Flight Secondary Ions Mass Spectrometry (ToF-SIMS) depth profile (negative ions) of 70Cu-30Ni after 1 h of immersion at E_{corr} in static aerated artificial seawater (ASW).....	73
Figure III. 8: Characteristic Time-of-Flight Secondary Ions Mass Spectrometry (ToF-SIMS) depth profile (negative ions) of 70Cu-30Ni after 1 h of immersion at E_{corr} in static aerated filtered natural seawater (FNSW).	74
Figure III. 9: Anodic polarisation curves of 70Cu-30Ni after 1 h of immersion at E_{corr} in aerated artificial seawater, in static conditions and under flow and stirring. Scan rate: 0.5 mV.s ⁻¹	75
Figure III. 10: Experimental impedance diagrams in the complex plane (Nyquist diagrams) of 70Cu-30Ni plotted at E_{corr} after 1 h of immersion in aerated artificial seawater, in static conditions and under flow.	76
Figure III. 11: (a) X-ray photoelectron spectroscopy (XPS) Cu2p _{3/2} core level spectra, and (b) Cu L ₃ M ₄₅ M ₄₅ Auger lines of 70Cu-30Ni after polishing, after 1 h of immersion at E_{corr} in aerated artificial seawater in static conditions and under flow and stirring. The intensity is expressed in arbitrary unit (a.u.).....	77
Figure III. 12: XPS Ni 2p _{3/2} core level spectra of 70Cu-30Ni alloy after polishing, after 1 h of immersion at E_{corr} in aerated artificial seawater in static conditions and under flow and stirring. The intensity is expressed in arbitrary unit (a.u.).	77
Figure III. 13: Characteristic Time-of-Flight Secondary Ions Mass Spectrometry (ToF-SIMS) depth profile (negative ions) of 70Cu-30Ni after 1 h of immersion at E_{corr} in aerated artificial seawater under flow and stirring.	78
Figure III. 14: Cathodic polarisation curves of 70Cu-30Ni after 1 h of immersion at E_{corr} in aerated artificial seawater, using the rotating ring electrode at three different rotation speeds (40, 160 and 640 rpm) and in static conditions. Scan rate: 0.5 mV.s ⁻¹	83
Figure III. 15: Cathodic polarisation curves of 70Cu-30Ni rotating ring electrode at 160 rpm, after 1 h of immersion time at E_{corr} in: i) aerated artificial seawater (scan rate: 0.5 mV.s ⁻¹), ii) aerated artificial seawater (steady-state curve), and iii) filtered natural seawater (scan rate: 0.5 mV.s ⁻¹).....	84
Figure III. 16: Anodic polarisation curves of 70Cu-30Ni rotating ring electrode at three different rotation speeds (40, 160 and 640 rpm), after 1 h of immersion at E_{corr} in: (a) aerated artificial seawater, and (b) aerated filtered natural seawater. Scan rate: 0.5 mV.s ⁻¹	85
Figure III. 17: Experimental impedance diagrams in the complex plane (Nyquist diagrams) of 70Cu-30Ni rotating ring electrode at three different rotation speeds (40, 160 and 640 rpm), after 1 h of immersion at E_{corr} using the in: (a) aerated artificial seawater, and (b) aerated filtered natural seawater.	86
Figure III. 18: Anodic polarisation curves of 70Cu-30Ni alloy and Al brass after 1 h of immersion at E_{corr} in static aerated FNSW time. Scan rate of 0.5 mV.s ⁻¹	89

Figure III. 19: Equivalent electrical circuits to model the 70Cu-30Ni/ASW and 70Cu-30Ni/FNSW systems: (a) general circuit, (b) simplified circuit taking into account experimental cathodic polarisation curves, and (c) circuit used to analyse the HF loop of experimental impedance diagrams. R_e is the electrolyte resistance, CPEdl a constant phase element related to the double layer, R_i^a the anodic charge transfer resistance, $Z_{\theta,D}^a$ an impedance that illustrates anodic mass transport and partial blocking effect by CuCl, R_{tc} the cathodic charge transfer resistance, Z_D^c a cathodic impedance that illustrates O_2 mass transport, and W_c the cathodic Warburg impedance.	90
Figure III. 20: Experimental impedance data (imaginary part of the impedance as a function of frequency) of 70Cu-30Ni alloy obtained at E_{corr} after 1 h of immersion in: (a) aerated artificial seawater, and (b) aerated filtered natural seawater; in static conditions and using the rotating ring electrode at three different rotation speeds (40, 160 and 640 rpm). Same data as in Figure III.17.....	92
Figure III. 21: Experimental impedance data (derivative curves calculated from Figure III.20) of 70Cu-30Ni alloy obtained at E_{corr} after 1 h of immersion in: (a) aerated artificial seawater, and (b) aerated filtered natural seawater; in static conditions and using the rotating ring electrode at three different rotation speeds (40, 160 and 640 rpm). Same data as in Figure III.17.....	93
Figure III. 22: High frequency loops of Nyquist diagrams obtained for 70Cu-30Ni at E_{corr} after 1 h of immersion in aerated: (a) ASW in static conditions, (b) ASW with the RRE at 40 rpm, (c) ASW with the RRE at 160 rpm, (d) ASW with the RRE at 640 rpm, (e) FNSW in static conditions, (f) FNSW with the RRE at 40 rpm, (g) FNSW with the RRE at 160 rpm, and (h) FNSW with the RRE at 640 rpm. Experimental curves and fit of the impedance model presented in Figure III.19(c) to the data. Same data as in Figures III.17.....	98
Figure III. 23: Comparison of the corrosion current density values calculated from Eq III.35 with $z = 1$ and $\alpha = 0.5$, for 70Cu-30Ni alloy after 1h of immersion in ASW or FNSW, in static condition and using the rotating ring electrode.	101
Figure III. 24: Models of the surface layers deduced from combined X-ray photoelectron spectroscopy (XPS) and Time-of-Flight Secondary Ions Mass Spectrometry (ToF-SIMS) results for 70Cu-30Ni: (a) just after polishing; (b) after 1 h of immersion at E_{corr} in static ASW; (c) after 1 h of immersion at E_{corr} in static FNSW; (d) after 1 h of immersion at E_{corr} in ASW under flow and stirring.	103
Chapter IV	
Figure IV. 1: (a) Cathodic and (b) anodic polarisation curves of 70Cu-30Ni after 1 h of immersion at E_{corr} in static aerated artificial seawater, without BSA and with 20 mg.L ⁻¹ of BSA. Scan rate: 0.5 mV.s ⁻¹	107
Figure IV. 2: Experimental impedance diagrams in the complex plane (Nyquist diagrams) of 70Cu-30Ni plotted at E_{corr} after 1 h of immersion in static aerated artificial seawater, without and with 20 mg.L ⁻¹ of BSA.	108
Figure IV. 3: Layer model assumed for the analysis of XPS data (organic layer -BSA- covering the mixed oxide layer formed on the metallic substrate).	109

- Figure IV. 4: (a) X-ray photoelectron spectroscopy (XPS) Cu 2p_{3/2} core level spectra and (b) Cu L₃M₄₅M₄₅ Auger lines of 70Cu-30Ni alloy after 1 h of immersion at E_{corr} in static aerated artificial seawater, without and with 20 mg.L⁻¹ of BSA. The intensity is expressed in arbitrary unit (a.u.). 110
- Figure IV. 5: X-ray photoelectron spectroscopy (XPS) Ni 2p_{3/2} core level spectra of 70Cu-30Ni after 1 h of immersion at E_{corr} in static aerated artificial seawater, without and with 20 mg.L⁻¹ of BSA. The intensity is expressed in arbitrary unit (a.u.). 111
- Figure IV. 6: Characteristic Time-of-Flight Secondary Ions Mass Spectrometry (ToF-SIMS) negative depth profile of 70Cu-30Ni after 1 h of immersion at E_{corr} in static aerated artificial seawater with 20 mg.L⁻¹ of BSA. 112
- Figure IV. 7: (a) N 1s and (b) C 1s core level spectra of 70Cu-30Ni after 1 h of immersion at E_{corr} in static aerated artificial seawater with 20 mg.L⁻¹ of BSA. Solid line: experimental spectra; dashed line: peak decomposition. The intensity is expressed in counts per second (CPS). 113
- Figure IV. 8: (a) X-ray photoelectron spectroscopy (XPS) Cu 2p_{3/2} core level spectra, and (b) Cu L₃M₄₅M₄₅ Auger lines of 70Cu-30Ni after polishing and after 1 h of immersion at E_{corr} in aerated artificial seawater with 20 mg.L⁻¹ of BSA (static and under flow and stirring). The intensity is expressed in arbitrary unit (a.u.). 114
- Figure IV. 9: XPS Ni 2p_{3/2} core level spectra of 70Cu-30Ni after polishing and after 1 h of immersion at E_{corr} in aerated artificial seawater with 20 mg.L⁻¹ of BSA (static and under flow and stirring). The intensity is expressed in arbitrary unit (a.u.). 115
- Figure IV. 10: Characteristic time-of-flight secondary ions mass spectrometry (ToF-SIMS) negative depth profiles of 70Cu-30Ni after 1 h of immersion at E_{corr} in aerated artificial seawater with 20 mg.L⁻¹ of BSA, under flow and stirring. Sputtering surface area: 700 x 700 μm². 116
- Figure IV. 11: (a) N 1s and (b) C 1s core level spectra of 70Cu-30Ni after 1 h of immersion at E_{corr} in aerated artificial seawater with 20 mg.L⁻¹ of BSA under flow and stirring. Solid line: experimental spectra; dashed line: peak decomposition. The intensity is expressed in counts per second (CPS). 117
- Figure IV. 12: Cathodic polarisation curves of 70Cu-30Ni after 1 h of immersion at E_{corr} , in aerated artificial seawater with 20 mg.L⁻¹ of BSA using the rotating ring electrode at three different rotation speeds (40, 160 and 640 rpm) and in static conditions. Scan rate: 0.5 mV.s⁻¹. 119
- Figure IV. 13: Anodic polarisation curves of 70Cu-30Ni after 1 h of immersion at E_{corr} , in aerated artificial seawater with 20 mg.L⁻¹ of BSA using the rotating ring electrode at three different rotation speeds (40, 160 and 640 rpm) and in static conditions. Scan rate: 0.5 mV.s⁻¹. 120
- Figure IV. 14: Experimental impedance diagrams in the complex plane (Nyquist diagrams) of 70Cu-30Ni rotating ring electrode at three different rotation speeds (40, 160 and 640 rpm) after 1 h of immersion at E_{corr} in aerated artificial seawater with 20 mg.L⁻¹ of BSA. 121

- Figure IV. 15: Cathodic polarisation curves of 70Cu-30Ni after 1 h of immersion at E_{corr} in static ASW in the absence and in the presence of biomolecules (BSA, TB EPS, LB EPS) with a proteins concentration of 20 mg.L⁻¹. Scan rate: 0.5 mV.s⁻¹..... 123
- Figure IV. 16: Anodic polarisation curves of 70Cu-30Ni after 1 h of immersion at E_{corr} in ASW in the absence and in the presence of biomolecules (BSA, TB EPS, LB EPS) with a protein concentration of 20 mg.L⁻¹. Scan rate: 0.5 mV.s⁻¹..... 123
- Figure IV. 17: Experimental impedance diagrams in the complex plane (Nyquist diagrams) of 70Cu-30Ni after 1 h of immersion at E_{corr} in ASW in the absence and in the presence of biomolecules (BSA, TB EPS, LB EPS) with a proteins concentration of 20 mg.L⁻¹. 124
- Figure IV. 18: (a) X-ray photoelectron spectroscopy (XPS) Cu 2p_{3/2} core level spectra, and (b) Cu L₃M₄₅M₄₅ Auger lines of 70Cu-30Ni alloy after 1 h of immersion at E_{corr} in static ASW in the presence of tightly bound EPS (TB EPS) or loosely bound EPS (LB EPS), with a protein concentration of 20 mg.L⁻¹. The intensity is expressed in arbitrary unit (a.u.)..... 125
- Figure IV. 19: X-ray photoelectron spectroscopy (XPS) Ni 2p_{3/2} core level spectra of 70Cu-30Ni alloy after 1 h of immersion at E_{corr} in static ASW in the presence of tightly bound EPS (TB EPS) or loosely bound EPS (LB EPS), with a protein concentration of 20 mg.L⁻¹. The intensity is expressed in arbitrary unit (a.u.). 126
- Figure IV. 20: Characteristic Time-of-Flight Secondary Ions Mass Spectrometry (ToF-SIMS) negative depth profiles of 70Cu-30Ni after 1 h of immersion at E_{corr} : (a) in ASW with tightly bound EPS (TB EPS) with a proteins concentration of 20 mg.L⁻¹ (sputtering area: 300 x 300 μm²); (b) in ASW with loosely bound EPS (LB EPS) with a proteins concentration of 20 mg.L⁻¹ (sputtering area: 700 x 700 μm²). 127
- Figure IV. 21: (a) N 1s and (b) C 1s core level spectra of 70Cu-30Ni alloy after 1 h of immersion at E_{corr} in static ASW in the presence of tightly bound EPS (TB EPS) or loosely bound EPS (LB EPS), with a proteins concentration of 20 mg.L⁻¹. The intensity is expressed in arbitrary unit (a.u.). 128
- Figure IV. 22: Experimental impedance data (imaginary part of the impedance as a function of frequency) of 70Cu-30Ni obtained at E_{corr} after 1 h of immersion in aerated artificial seawater: (a) in static conditions in the absence and in the presence of biomolecules (BSA, TB EPS, LB EPS) with a protein concentration of 20 mg.L⁻¹; and (b) with 20 mg.L⁻¹ of BSA in static conditions and using a rotating ring electrode at three different rotation speeds (40, 160 and 640 rpm). Same data as in Figures IV.14 and IV.17. 131
- Figure IV. 23: Experimental impedance data (derivative curves calculated from Figure IV.22) of 70Cu-30Ni obtained at E_{corr} after 1 h of immersion in aerated artificial seawater: (a) in static conditions in the absence and in the presence of biomolecules (BSA, TB EPS, LB EPS) with a proteins concentration of 20 mg.L⁻¹; and (b) with 20 mg.L⁻¹ of BSA in static conditions and using a rotating ring electrode at three different rotation speeds (40, 160 and 640 rpm). 131
- Figure IV. 24: Nyquist diagrams obtained for 70Cu-30Ni at E_{corr} after 1 h of immersion in aerated: (a) static ASW in the presence of 20 mg.L⁻¹ of BSA, (b) static ASW in the presence of TB EPS with 20 mg.L⁻¹ of proteins, (c) static ASW in the presence of LB EPS with 20

mg.L⁻¹ of proteins, and ASW with 20 mg.L⁻¹ of BSA using the RRE at (d) 40, (e) 160 and (f) 640 rpm. Experimental curves and fit of the impedance model presented in Figure III.19 (c) of Chapter III. Same data as in Figures IV.14 and IV.17. 132

Figure IV. 25: Comparison of the corrosion current density values calculated from Eq. III.39 with $z = 1$ and $\alpha = 0.5$, for 70Cu-30Ni alloy after 1 h of immersion in ASW without and with biomolecules, in static conditions and using the rotating ring electrode. 137

Figure IV. 26: Models of the surface layers deduced from combined X-ray photoelectron spectroscopy (XPS) and time-of-flight secondary ions mass spectrometry (ToF-SIMS) data for 70Cu-30Ni after 1 h of immersion at E_{corr} in: (a) static ASW with 20 mg.L⁻¹ of BSA; (b) static ASW in the presence of TB EPS with a proteins concentration 20 mg.L⁻¹; (c) static ASW in the presence of LB EPS with a proteins concentration of 20 mg.L⁻¹; and (d) ASW under flow and stirring with 20 mg.L⁻¹ of BSA. 138

Figure IV. 27: Plot of molar concentrations determined by XPS: (a) C_{3288.3} vs N_{org}, (b) C_{2286.4} vs N_{org}, c) O₅₃₃ vs C_{2286.4}-N_{org}, and d) C_{1285.0} vs C_{tot}-2*N_{org}. 70Cu-30Ni samples immersed 1 h at E_{corr} in ASW with 20 mg.L⁻¹ of BSA, in static conditions (ASW + BSA) and under flow and stirring (ASW + BSA FS), in static ASW in the presence of TB EPS (ASW + TB EPS) or LB EPS (ASW + LB EPS), with a proteins concentration of 20 mg.L⁻¹, and in static FNSW. Dashed lines: 1:1 relation. 140

Figure IV. 28: Composition of biomolecules adsorbed on 70Cu-30Ni alloy. Relative mass concentration of amide (HC-NH-(C=O)), hydrocarbon CH₂, and other oxygen-containing molecules (C_{add} + O_{add}), including polysaccharides. 70Cu-30Ni samples immersed 1 h at E_{corr} in ASW with 20 mg.L⁻¹ of BSA, in static conditions (ASW + BSA) and under flow and stirring (ASW + BSA FS), in static ASW in the presence of TB EPS (ASW + TB EPS) or LB EPS (ASW + LB EPS), with a protein concentration of 20 mg.L⁻¹, and in static FNSW..... 143

Chapter V

Figure V. 1: Cathodic polarisation curves of Ti after 1 h of immersion at E_{corr} in static aerated ASW, in the absence and in the presence of biomolecules (BSA, TB EPS) with a protein concentration of 20 mg.L⁻¹. Scan rate: 0.5 mV.s⁻¹. 146

Figure V. 2: Anodic polarisation curves of Ti after 1 h of immersion at E_{corr} in static aerated ASW, in the absence and in the presence of biomolecules (BSA, TB EPS) with a protein concentration of 20 mg.L⁻¹. Scan rate: 0.5 mV.s⁻¹. 147

Figure V. 3: Experimental impedance diagrams in the complex plane (Nyquist diagrams) of Ti after 1 h of immersion at E_{corr} in static aerated ASW, in the absence and in the presence of biomolecules (BSA, TB EPS) with a protein concentration of 20 mg.L⁻¹. 148

Figure V. 4: Anodic polarisation curves of 304L stainless steel after 1 h of immersion at E_{corr} in static aerated ASW. Scan rate: 0.5 mV.s⁻¹. 149

Figure V. 5: Cathodic polarisation curves of 304L stainless steel after 1 h of immersion at E_{corr} in static aerated Cl⁻-free solution (0.24 M Na₂SO₄ + 0.002 M NaHCO₃), in the absence and in the presence of biomolecules (BSA, TB EPS) with a protein concentration of 20 mg.L⁻¹. Scan rate: 0.5 mV.s⁻¹. 150

- Figure V. 6: Anodic polarisation curves of 304L stainless steel after 1 h of immersion at E_{corr} in static aerated Cl^- -free solution ($0.24 \text{ M Na}_2\text{SO}_4 + 0.002 \text{ M NaHCO}_3$), in the absence and in the presence of biomolecules (BSA, TB EPS) with a protein concentration of 20 mg.L^{-1} . Scan rate: 0.5 mV.s^{-1} 151
- Figure V. 7: Experimental impedance diagrams in the complex plane (Nyquist diagrams) of 304L stainless steel after 1 h of immersion at E_{corr} in static aerated Cl^- -free solution ($0.24 \text{ M Na}_2\text{SO}_4 + 0.002 \text{ M NaHCO}_3$), in the absence and in the presence of biomolecules (BSA, TB EPS) with a protein concentration of 20 mg.L^{-1} 152
- Figure V. 8: Layer model assumed for the analysis of XPS data of Ti: (a) TiO_2 oxide layer covering the metallic substrate, and (b) organic layer covering the oxide layer formed on the metal. 153
- Figure V. 9: X-ray photoelectron spectroscopy (XPS): (a) decomposition of the Ti 2p core level spectra (1 h of immersion at E_{corr} in static aerated ASW), and (b) comparison of Ti 2p core level spectra of Ti after polishing and after 1 h of immersion at E_{corr} in static aerated ASW, in the absence and in the presence of biomolecules (BSA, TB EPS) with a proteins concentration of 20 mg.L^{-1} . The intensity is expressed in (a) counts per second (CPS) or (b) arbitrary unit (a.u.). 156
- Figure V. 10: Characteristic Time-of-Flight Secondary Ions Mass spectrometry (ToF-SIMS) depth profiles (negative ions) of Ti (a) after polishing, and after 1 h of immersion at E_{corr} in static aerated: (b) ASW, (c) ASW with 20 mg.L^{-1} of BSA, and (d) ASW with TB EPS (protein concentration: 20 mg.L^{-1}). 158
- Figure V. 11: (a) N 1s and (b) C 1s XPS core level spectra of Ti after 1 h of immersion at E_{corr} in static aerated ASW, in the presence of biomolecules (BSA, TB EPS) with a protein concentration of 20 mg.L^{-1} . The intensity is expressed in arbitrary units (a.u.). 159
- Figure V. 12: Characteristic Time-of-Flight Secondary Ions Mass spectrometry (ToF-SIMS) depth profiles (negative ions) of 304L stainless steel (a) after polishing, and after 1 h of immersion at E_{corr} in static aerated: (b) Cl^- -free solution, (c) Cl^- -free solution with 20 mg.L^{-1} of BSA (sputtered surface area of $1000 \times 1000 \mu\text{m}^2$), and (c) Cl^- -free solution with TB EPS (protein concentration of 20 mg.L^{-1} ; sputtered surface area of $700 \times 700 \mu\text{m}^2$). 161
- Figure V. 13: Layer model assumed for the analysis of XPS data of 304L stainless steel considering: (a) a duplex oxide layer formed on the metallic substrate, with an outer Fe_2O_3 layer and an inner Cr_2O_3 layer, and (b) organic layer covering the duplex oxide layer formed on the metallic substrate. 163
- Figure V. 14: X-ray photoelectron spectroscopy (XPS) (a) Cr $2p_{3/2}$ and (b) Fe $2p_{3/2}$ core level spectra of 304L stainless steel after polishing and after 1 h of immersion at E_{corr} in static aerated Cl^- -free solution, in the absence and in the presence of biomolecules (BSA, TB EPS) with a protein concentration of 20 mg.L^{-1} . The intensity is expressed in arbitrary unit (a.u.). 164
- Figure V. 15: (a) N 1s and (b) C 1s core level spectra of 304L stainless steel after 1 h of immersion at E_{corr} in static aerated Cl^- -free solution in the presence BSA and TB EPS, with a protein concentration of 20 mg.L^{-1} . The intensity is expressed in arbitrary unit (a.u.). 166

- Figure V. 16: Models of the surface layers deduced from combined X-ray photoelectron spectroscopy (XPS) and time-of-flight secondary ions mass spectrometry (ToF-SIMS) results for Ti (a) just after polishing, and after 1 h of immersion at E_{corr} in static aerated (b) ASW, (c) ASW with 20 mg.L^{-1} of BSA, and (d) ASW in the presence of TB EPS with a protein concentration of 20 mg.L^{-1} 167
- Figure V. 17: Models of the surface layers deduced from combined X-ray photoelectron spectroscopy (XPS) and time-of-flight secondary ions mass spectrometry (ToF-SIMS) results for 304L stainless steel (a) just after polishing, and after 1 h of immersion at E_{corr} in static aerated (b) Cl^- -free solution, (c) Cl^- -free solution with 20 mg.L^{-1} of BSA, and (d) Cl^- -free solution in the presence of TB EPS with a protein concentration of 20 mg.L^{-1} 168
- Figure V. 18: Experimental impedance diagrams in the complex plane (Nyquist diagrams) of (a) Ti after in ASW and (b) 304L stainless steel in Cl^- -free solution, plotted at E_{corr} after 1 h of immersion and in the passive domain after 1 h of immersion at E_{corr} followed by 30 min of polarisation. 170
- Figure V. 19: Cathodic polarisation curves without ($|j|$) and with correction for the anodic contribution ($|j - j_a, \text{pl}|$) of (a) Ti and (c) 304L stainless steel; and zooms of the corrected curves for (b) Ti and (d) 304L stainless steel. Experiments performed after 1 h of immersion at E_{corr} in static aerated ASW (Ti) or Cl^- -free solution (304L stainless steel), in the absence and in the presence of biomolecules (BSA, TB EPS) with a protein concentration of 20 mg.L^{-1} . Scan rate: 0.5 mV.s^{-1} 171
- Figure V. 20: Experimental impedance data (imaginary part of the impedance as a function of frequency) of (a) Ti in ASW and (b) 304L stainless steel in Cl^- -free solution, plotted at E_{corr} after 1 h of immersion in static conditions, in the absence and in the presence of biomolecules (BSA, TB EPS) with a protein concentration of 20 mg.L^{-1} . Same data as in Figures V.3 and V.7. 172
- Figure V. 21: Equivalent circuit to model the Ti/ASW and 304L stainless steel/ Cl^- -free solution systems at E_{corr} , with R_s the electrolyte resistance, and PLM the power-law model accounting for the passive layer. 174
- Figure V. 22: Resistivity profiles of (a) Ti and (b) 304L stainless steel, calculated from the parameters values by application of Eq. V.15. 176
- Figure V. 23: Plot of molar concentrations determined by XPS: (a) $\text{C}_{3288.3}$ vs N_{org} , (b) $\text{C}_{2286.4}$ vs N_{org} , (c) O_{533} vs $\text{C}_{2286.4} - \text{N}_{org}$, and (d) $\text{C}_{1285.0}$ vs $\text{C}_{tot} - 2 * \text{N}_{org}$. Ti samples immersed 1 h at E_{corr} in static aerated ASW with 20 mg.L^{-1} of BSA (ASW + BSA), and in the presence of TB EPS (ASW + TB EPS) with a protein concentration of 20 mg.L^{-1} . Dashed lines: 1:1 relation. 177
- Figure V. 24: Plot of molar concentrations determined by XPS: (a) $\text{C}_{3288.3}$ vs N_{org} , (b) $\text{C}_{2286.4}$ vs N_{org} , (c) O_{533} vs $\text{C}_{2286.4} - \text{N}_{org}$, and (d) $\text{C}_{1285.0}$ vs $\text{C}_{tot} - 2 * \text{N}_{org}$. 304L stainless steel samples immersed 1 h at E_{corr} in static aerated Cl^- -free solution with 20 mg.L^{-1} of BSA (Cl^- -free solution + BSA), and in the presence of TB EPS (Cl^- -free solution + TB EPS) with a protein concentration of 20 mg.L^{-1} . Dashed lines: 1:1 relation. 178
- Figure V. 25: Biomolecules composition of the surfaces. Relative mass concentration of amide (HC-NH-(C=O)), hydrocarbon CH_2 , and other oxygen-containing molecules ($\text{C}_{add} +$

O_{add}), including polysaccharides. Ti samples immersed 1 h at E_{corr} in static aerated ASW with 20 mg.L⁻¹ of BSA (ASW + BSA), and in the presence of TB EPS (ASW + TB EPS) with a protein concentration of 20 mg.L⁻¹; and 304L stainless steel samples immersed 1 h at E_{corr} in static aerated Cl⁻-free solution with 20 mg.L⁻¹ of BSA (Cl⁻-free solution + BSA), and in the presence of TB EPS (Cl⁻-free solution + TB EPS) with a protein concentration of 20 mg.L⁻¹.
..... 180

Annex B

Figure B. 1: X-ray photoelectron spectroscopy (XPS) (a) Cu 2p_{3/2} core level spectra (b) Cu L₃M₄₅M₄₅ Auger lines (c) Ni 2p_{3/2} core level spectra (d) N 1s core level spectra and (e) C 1s core level spectra of 70Cu-30Ni alloy: negative control without treatment (without dehydration fixation procedure), 1 h of exposure to *E. coli* and *E. coli* biofilm. The intensity is expressed in arbitrary unit (a.u.)..... 205

Figure B. 2: Characteristic Time-of-Flight Secondary Ions Mass Spectrometry (ToF-SIMS) depth profiles (negative ions) for 70Cu-30Ni alloy (a) negative control without treatment (dehydration and fixation procedure; sputtered surface area of 300 × 300 μm²), (b) *E. coli* 1 h exposure, and (c) *E. coli* biofilm (sputtered surface area of 700 × 700 μm²). 208

Figure B. 3: X-ray photoelectron spectroscopy (XPS) (a) Fe 2p_{3/2} core level spectra (b) Cr 2p_{3/2} core level spectra (c) Ni 2p_{3/2} core level spectra (d) N 1s core level spectra and (e) C 1s core level spectra of 304L stainless steel: negative control without treatment (without dehydration fixation procedure), 1 h of exposure to *E. coli* and *E. coli* biofilm. The intensity is expressed in arbitrary unit (a.u.)..... 210

Figure B. 4: Characteristic Time-of-Flight Secondary Ions Mass spectrometry (ToF-SIMS) depth profiles (negative ions) of 304L stainless steel: (a) negative control without treatment (dehydration and fixation procedure; sputtered surface area of 300 × 300 μm²), (b) *E. coli* 1 h exposure, and (c) *E. coli* biofilm (sputtered surface area of 700 × 700 μm²). 213

Figure B. 5: X-ray photoelectron spectroscopy (XPS) (a) Ti 2p core level spectra (b) N 1s core level spectra and (c) C 1s core level spectra of Ti: negative control without treatment (without dehydration fixation procedure), 1 h of exposure to *E. coli* and *E. coli* biofilm. The intensity is expressed in arbitrary unit (a.u.). 215

Figure B. 6: Characteristic Time-of-Flight Secondary Ions Mass spectrometry (ToF-SIMS) depth profiles (negative ions) of Ti: (a) negative control without treatment (dehydration and fixation procedure; sputtered surface area of 300 × 300 μm²), (b) *E. coli* 1 h exposure, and (c) *E. coli* biofilm (sputtered surface area of 700 × 700 μm²). 217

Figure B. 7: Biomolecules composition of the surfaces for the negative control and after the biofilm growth test considering the subtraction of the bacteria contribution. Relative mass concentration of amide (HC-NH-(C=O)), hydrocarbon CH₂, and other oxygen-containing molecules (C_{add} + O_{add}), including polysaccharides. 70Cu-30Ni alloy, 304L stainless steel and Ti. 219

List of Tables
Chapter I

Table I. 1: Types of corrosion [28].	8
Table I. 2: Theoretical models for describing bacteria-substrate interactions	17
Table I. 3: Components content in EPS.	20
Table I. 4: Most famous exopolysaccharides present inside biofilms.....	21
Table I. 5: Amino acid composition of BSA [16].	27
Table I. 6: Effect of pH on the conformation of serum albumin.....	28

Chapter II

Table II. 1: Chemical compositions of the studied metallic materials.	33
Table II. 2: Composition of EPS extracted from the marine strain <i>Pseudomonas NCIMB 2021</i>	40

Chapter III

Table III. 1: Transmission functions $T(E_{kin})$ of the Escalab 250 energy analyzer, provided by Thermo Electron Corporation.	68
Table III. 2: Inelastic mean free paths λ in nm – Taken from the QUASES-IMFP-TPP2M... 68	
Table III. 3: Photo-ionization cross sections σ_X at 1486.6 eV.	68
Table III. 4: Binding energy and kinetic energy of Cu $2p_{3/2}$ XPS peak and Auger line, respectively, for Cu species [12], [117]–[122].....	69
Table III. 5: Corrosion potential values for 70Cu-30Ni alloy after 1 h of immersion in artificial seawater (ASW), and filtered natural seawater (FNSW), in static conditions and using a RRE at three different rotation speeds (40, 160 and 640 rpm).	82
Table III. 6: Comparison between the limiting current densities at -0.75 V vs SCE taken from Figure III.14 (corresponding to the second step of dissolved oxygen reduction reaction with transfer of 4 electrons), and the theoretical values calculated from Eq. III.19.	83
Table III. 7: Experimental frequency range taken into account for the regression, parameters values (electrolyte resistance R_e , anodic charge transfer resistance R_t^a , constant of the cathodic Warburg impedance k_c , and CPE parameters α and Q) obtained from the regression of the equivalent circuit presented in Figure III.19(c) to experimental impedance data shown in Figure III.17, and effective capacitance C_{eff} associated with the CPE calculated from Eq. III.32.....	97

Table III. 8: Comparison of the corrosion current values obtained from R_t^a , by application of Eqs. III.39 and III.40, and from the cathodic polarisation curve (first plateau current density).	100
---	-----

Chapter IV

Table IV. 1: Inelastic mean free paths λ in nm – Taken from the QUASES-IMFP-TPP2M.	110
Table IV. 2: Atomic ratios calculated from the XPS N 1s and C 1s core level spectra recorded for the BSA powder and for 70Cu-30Ni after 1 h of immersion at E_{corr} in static aerated artificial seawater, without and with 20 mg.L ⁻¹ of BSA.	113
Table IV. 3: Atomic ratios calculated from the XPS N 1s and C 1s core level spectra recorded for the BSA powder, and for 70Cu-30Ni after 1 h of immersion at E_{corr} in aerated artificial seawater under flow and stirring, without and with 20 mg.L ⁻¹ of BSA.	117
Table IV. 4: Corrosion potential values for 70Cu-30Ni alloy after 1 h of immersion in artificial seawater with 20 mg.L ⁻¹ of BSA, in static conditions and using a RRE at 3 different rotation speeds.	118
Table IV. 5: Current densities at -0.75 or -0.95 V vs SCE, corresponding to the second step of dissolved oxygen reduction (transfer of 4 electrons), taken from Figure III.16 (a) and IV.12.	119
Table IV. 6: Corrosion potential (E_{corr}) values for 70Cu-30Ni alloy after 1 h of immersion in ASW without and with biomolecules (proteins concentration: 20 mg.L ⁻¹).	122
Table IV. 7: Binding energy of elements in chemical functions of biochemical compounds [106].	129
Table IV. 8: Atomic ratios calculated from the XPS N 1s and C 1s core level spectra recorded for the BSA powder and for 70Cu-30Ni after 1 h of immersion at E_{corr} in static aerated artificial seawater in the presence of TB EPS or LB EPS, with a protein concentration of 20 mg.L ⁻¹	129
Table IV. 9: Experimental frequency range taken into account for the regression, parameters values (electrolyte resistance R_e , anodic charge transfer resistance R_t^a , constant of the cathodic Warburg impedance k_c , and CPE parameters \square and Q) obtained from the regression of the equivalent circuit presented in Figure III.19 (c) of Chapter III to experimental impedance data shown in Figures IV.14 and IV.17, and effective capacitance C_{eff} associated with the CPE calculated from Eq. III.32.	133
Table IV. 10: Comparison of the corrosion current density values obtained from R_t^a , by application of Eq III.39 and III.40, and from the cathodic polarization curves.	136

Chapter V

Table V. 1: Corrosion potential (E_{corr}) of Ti after 1 h of immersion in static aerated ASW, without and with biomolecules (protein concentration: 20 mg.L ⁻¹).	146
--	-----

Table V. 2: Corrosion potential (E_{corr}) of 304L stainless steel after 1 h of immersion in static aerated Cl^- -free solution, without and with biomolecules (protein concentration: 20 mg.L^{-1}). 150

Table V. 3: Transmission functions $T(E_{kin})$ of the Escalab 250 energy analyzer, provided by Thermo Electron Corporation. 154

Table V. 4: Inelastic mean free paths λ in nm – Taken from the QUASES-IMFP-TPP2M. . 155

Table V. 5: Photo-ionization cross sections σ_X at 1486.6 eV. 155

Table V. 6: Oxide layer composition (oxidation state), and oxide layer thickness estimated by assuming that the total oxidized Ti (Ti^{+4} , Ti^{+3} and Ti^{+2}) corresponds to Ti^{+4} . Ti after polishing and after 1 h of immersion at E_{corr} in static aerated ASW, in the absence and in the presence of biomolecules (BSA, TB EPS) with a protein concentration of 20 mg.L^{-1} 156

Table V. 7: Atomic ratios calculated from the XPS N 1s and C 1s core level spectra recorded for the BSA powder and for Ti after 1 h of immersion at E_{corr} in static aerated artificial seawater, in the presence of BSA or TB EPS with a protein concentration of 20 mg.L^{-1} 159

Table V. 8: Transmission functions $T(E_{kin})$ of the Escalab 250 energy analyzer, provided by Thermo Electron Corporation. 163

Table V. 9: Inelastic mean free paths λ in nm – Taken from the QUASES-IMFP-TPP2M. . 163

Table V. 10: Photo-ionization cross sections σ_X at 1486.6 eV. 163

Table V. 11: Oxide layer thickness and elemental composition beneath the oxide layer estimated by considering a duplex oxide layer: 304L stainless steel after polishing and after 1 h of immersion at E_{corr} in static aerated Cl^- -free solution, in the absence and in the presence of biomolecules (BSA, TB EPS) with a protein concentration of 20 mg.L^{-1} 165

Table V. 12: Atomic ratios calculated from the XPS N 1s and C 1s core level spectra recorded for the BSA powder and for 304L stainless steel after 1 h of immersion at E_{corr} in static aerated Cl^- -free solution, in the presence of BSA or TB EPS with a protein concentration of 20 mg.L^{-1} 166

Table V. 13: α and Q CPE parameters estimated graphically from Eqs. III.25 and III.26. Same data as in Figures V.3 and V.7. 172

Table V. 14: Parameters values for Ti obtained from the regression of the equivalent circuit presented in Figure V.22 to experimental impedance data shown in Figure V.3. 175

Table V. 15: Parameters values of 304L stainless steel obtained from the regression of the equivalent circuit presented in Figure V.22 to experimental impedance data shown in Figure V.7. 176

Chapter VI

Table VI.1: Summary of main conclusions of this work.....186

Annex A

Table A. 1 : Calculation sheet for converting marker concentrations (molar percentage of relevant element, excluding hydrogen) into mass concentration (%) of model constituents in an organic phase. 200

Annex B

Table B. 1: Chemical composition and thickness of the surface oxide layer calculated from XPS data recorded for 70Cu-30Ni after experiments. 206

Table B. 2 : Atomic ratios calculated from the XPS N 1s and C 1s core level spectra recorded for the 70Cu-30Ni alloy after 1 h of exposure to *E. coli* and the biofilm growth test. 207

Table B. 3: Rations between the maximum intensity of the CuO_2^- and NiO_2^- signals obtained from the ToF-SIMS experiments of 70Cu-30Ni alloy after 1 h of exposure to *E. coli* and the biofilm growth test. 209

Table B. 4: Chemical composition of the surface film calculated from XPS data recorded for 304L stainless steel after experiments. 211

Table B. 5: Atomic ratios calculated from the XPS N 1s and C 1s core level spectra recorded for 304L stainless steel after 1 h of exposure to *E. coli* and the biofilm growth test. 212

Table B. 6: Rations between the maximum intensity of the FeO_2^- and CrO_2^- signals obtained from the ToF-SIMS experiments for 304L stainless steel after 1 h of exposure to *E. coli* and the biofilm growth test. 214

Table B. 7: Oxide layer composition (oxidation state), and oxide layer thickness estimated by assuming that the total oxidized Ti (Ti^{+4} , Ti^{+3} and Ti^{+2}) corresponds to Ti^{+4} 216

Table B. 8: Atomic ratios calculated from the XPS N 1s and C 1s core level spectra recorded for Ti after 1 h of exposure to *E. coli* and the biofilm growth test. 216

Table B. 9: Biomolecules composition of surface. Relative mass concentration of amide (HC-NH-(C=O)), hydrocarbon CH_2 , and other oxygen-containing molecules ($\text{C}_{\text{add}} + \text{O}_{\text{add}}$), including polysaccharides. Atomic composition of the surface oxide layer calculated from XPS data recorded for 70Cu-30Ni alloy, 304L stainless steel and Ti after biofilm growth test. 220

Effet de l'adsorption de biomolécules sur les couches d'oxydes développées sur des matériaux métalliques utilisés dans les systèmes d'eau de refroidissement

Résumé : Cette thèse, réalisée en collaboration avec le partenaire industriel RSE S.p.A (Italie), s'inscrit dans le cadre du projet européen BIOCOR ITN. Les matériaux métalliques habituellement utilisés dans les circuits de refroidissement de centrales électriques peuvent être affectés par la biocorrosion induite par la formation d'un biofilm. L'objectif de ce travail était d'étudier l'influence de l'adsorption de biomolécules, qui est l'étape initiale de formation du biofilm, sur le comportement électrochimique et la composition chimique de surface de trois matériaux métalliques (alliage 70Cu-30Ni, acier inoxydable 304L et titane) en milieu marin. Dans un premier temps, les interactions entre une protéine modèle, l'albumine de sérum bovin (BSA), et la surface de ces matériaux ont été étudiées. Ensuite, des substances polymériques extracellulaires (EPS) étroitement liées (TB) et faiblement liées (LB) à la surface cellulaire, qui jouent un rôle fondamental dans les différentes étapes de formation, maturation et maintenance du biofilm, ont été extraites à partir de la souche marine *Pseudomonas NCIMB 2021* et leurs effets sur les couches d'oxydes ont été aussi évalués. Pour ce faire, des mesures électrochimiques (potentiel de corrosion E_{corr} vs temps d'immersion, courbes de polarisation et spectroscopie d'impédance électrochimique (EIS)) réalisées pendant les toutes premières étapes de formation des couches d'oxydes (1 h d'immersion) ont été combinées à des analyses de surface par spectroscopie de photoélectrons induits par rayons X (XPS) et spectrométrie de masse d'ions secondaires à temps de vol (ToF-SIMS). En comparaison de l'alliage 70Cu-30Ni en eau de mer artificielle (ASW) statique sans biomolécules, pour lequel une couche duplex épaisse (couche externe de Cu_2O redéposé et couche interne de nickel oxydé) est montrée, la présence de BSA, TB EPS et LB EPS conduit à une couche mixte d'oxydes (cuivre et nickel oxydés) d'épaisseur plus faible. En présence de biomolécules, la couche d'oxydes est recouverte d'une couche organique adsorbée, principalement composée de protéines. Un modèle est proposé pour analyser les données d'impédance obtenues à E_{corr} . Les résultats montrent un ralentissement de la réaction anodique par les biomolécules (BSA, TB EPS et LB EPS) et un effet d'inhibition de la corrosion par les LB EPS et dans une moindre mesure par la BSA. Aucun effet néfaste n'est mis en évidence en présence de TB EPS. D'autre part, l'effet des TB EPS et de la BSA sur la passivation du Ti dans ASW et de l'acier inoxydable 304L dans une solution sans chlorure a été étudié. A partir des données d'impédance, les profils de résistivité au sein des couches d'oxydes peuvent être tracés. Pour les deux matériaux, les couches d'oxydes sont plus protectrices avec la BSA et moins protectrices avec les TB EPS en comparaison de celles obtenues sans biomolécules. Enfin, les biomolécules n'induisent aucune différence significative de composition et d'épaisseur des couches d'oxydes.

Mots-clés : alliage 70Cu-30Ni, acier inoxydable 304L, titane, BSA, EPS, biocorrosion, EIS, XPS, ToF-SIMS

Effect of biomolecules adsorption on oxide layers developed on metallic materials used in cooling water systems

Abstract: This thesis was carried out in the frame of the BIOCOR ITN European project, in collaboration with the industrial partner RSE S.p.A. (Italy). Metallic materials commonly used in cooling systems of power plants may be affected by biocorrosion induced by biofilm formation. The objective of this work was to study the influence of biomolecules adsorption, which is the initial stage of biofilm formation, on the electrochemical behaviour and the surface chemical composition of three metallic materials (70Cu-30Ni alloy, 304L stainless steel and titanium) in seawater environments. In a first step, the interactions between a model protein, the bovine serum albumin (BSA), and the surface of these materials were investigated. Secondly, tightly bound (TB) and loosely bound (LB) extracellular polymeric substances (EPS), that play a fundamental role in the different stages of biofilm formation, maturation and maintenance, were extracted from *Pseudomonas NCIMB 2021* marine strain, and their effects on oxide layers were also evaluated. For that purpose, electrochemical measurements (corrosion potential E_{corr} vs time, polarization curves and electrochemical impedance spectroscopy (EIS)) performed during the very first steps of oxide layers formation (1 h immersion time) were combined to surface analysis by X-ray photoelectron spectroscopy (XPS) and time-of-flight secondary ions mass spectrometry (ToF-SIMS). Compared to 70Cu-30Ni alloy in static artificial seawater (ASW) without biomolecules, for which a thick duplex oxide layer (outer redeposited Cu_2O layer and inner oxidized nickel layer) is shown, the presence of BSA, TB EPS and LB EPS leads to a mixed oxide layer (oxidized copper and nickel) with a lower thickness. In the biomolecules-containing solutions, this oxide layer is covered by an adsorbed organic layer, mainly composed of proteins. A model is proposed to analyse impedance data obtained at E_{corr} . The results show a slow-down of the anodic reaction in the presence of biomolecules (BSA, TB EPS and LB EPS), and a corrosion inhibition effect by LB EPS and to a lesser extent by BSA. No detrimental effect is evidenced with TB EPS. On the other hand, the effect of TB EPS and BSA on the passivation behaviour of Ti in ASW and of 304L stainless steel in chloride-free solution was studied. From EIS data, resistivity profiles within oxide films can be plotted. For both materials, oxide layers are more protective with BSA and less protective with TB EPS compared to the solution without biomolecules. At last, biomolecules induce no significant differences in oxide layer composition and thickness.

Key words: 70Cu-30Ni alloy, 304L stainless steel, titanium, BSA, EPS, biocorrosion, EIS, XPS, ToF-SIMS